4-2-2018

Mobility of Nano-Particles in Rock Based Micro-Models

Jagannath Upadhyay
Louisiana State University and Agricultural and Mechanical College

MOBILITY OF NANO-PARTICLES IN ROCK BASED MICRO-MODELS

A Dissertation

Submitted to the Graduate Faculty of the
Louisiana State University and
Agricultural and Mechanical College
in partial fulfillment of the
requirements for the degree of
Doctor of Philosophy

in

The Department of Mechanical and Industrial Engineering

by
Jagannath Upadhyay
B.Sc. in Mechanical Engineering, Louisiana State University, 2012
May 2018

Acknowledgments

First and foremost, I am grateful to my adviser, Professor Dimitris E. Nikitopolous, for his incredible support and his trust in me. This work has been greatly benefited in oil and gas industries, advanced energy consortium and microfabrication industries due to his unparallel vision in a new era of microfabrication, understanding of microscale fluid dynamics in complex rock based micro-model, and his constant encouragement and support in exporing new ideas throughout my PhD. He has provided endless support and guidance along with enough freedom to work independently throughout the course of my PhD.. I would like to thank my committee members Professor Dorel Moldovan, Professor Ram Devireddy and Professor Karsten E. Thompson for their time, guidance and support throughout my PhD. I would also like to thank dean representative Thomas Corbitt for his support. I would like to extend sincere gratitude to Dr. Daniel Park, in particular, for his endless support in microfabrication and many hours of insightful conversation in microfluidic experiments and manufacturing that helped me gain knowledge in microfabrication.

This research project was funded and supported by the Advanced Energy Consortium, so I would like to gratefully acknowledge them. I would also like to express my gratitude to the Department of Mechanical and Industrial Engineering for the financial support throughout my PhD. I would like to thank and acknowledge the Louisiana Optical Network Iniative (LONI) and High Performance Computing (HPC) systems at Lousiana State University for computational resources.

I am thankful to my fellow research group members at LSU, Kasra F. Hesary and Jace Boudreaux for various discussions on simulation, experiments, numerous jokes, lunch breaks, coffee breaks and all the fun we have in a window free office as well as in a new building during these years. I would like to thank Dr. Eamonn D. Walker for our numerous conversations on simulation, teaching courses and helping me to review my dissertation. I would also like to thank all my other friends who have helped me directly and indirectly during my PhD. journey.

I would also like to share my appreciation for Gurmeet, Hardeep, Navi, Sukhi and Inderbir for their support, love, hospitality, and for making us (my wife and I) feel at home during all these years in Baton Rouge.

I am always indebted to my parents Chandramani and Saraswati for their endless patience, unparalleled support, encouragement, joys and never-ending love on all parts of my life. I am also grateful to my sisters: Sita, Madhu and Tara for their unwavering support and love.

Last but not least, my heartful and deepest appreciation goes to my beloved better half, Namoona, for her endless, unconditional love, support, and encourangement. Every moment we shared, from low to high points, have helped me to reach to this part of my life.

Table of Contents

Abstract

A confocal micro-particle image velocimetry (C-μPIV) technique along with associated post-processing algorithms is detailed for obtaining three dimensional distributions of nano-particle velocity and concentrations at select locations of the 2.5D (pseudo 3D) Poly(methyl methacrylate) (PMMA) and ceramic micro-model. The designed and fabricated 2.5D micro-model incorporates microchannel networks with 3D wall structures with one flat observation wall which resembles fourteen morphological and flow parameters to those of fully 3D actual reservoir rock (Boise Sandstone) at resolutions of 5 and 10 μm in depth and 5 and 25 μm on plane. In addition, an in-situ, non-destructive method for measuring the geometry of low and high resolution PMMA and ceramic micro-models, including its depth, is described and demonstrated. The flow experiments use 860 nm and 300 nm fluorescence-labeled polystyrene particles, and the data is acquired using confocal laser scanning microscopy. Regular fluorescence microscopy is used for the in-situ geometry measurement along with the use of Rhodamine dye and a depth-to-fluorescence-intensity calibration, which is linear. Monochromatic excitation at a wavelength of 544 nm (green) produced by a HeNe continuous wave laser was used to excite the fluorescence-labeled nanoparticles emitting at 612 nm (red). Confocal images were captured by a highly sensitive fluorescence detector photomultiplier tube. Results of detailed three dimensional velocity, particle concentration distributions, and particle deposition rates from experiments conducted at flow rates of 0.5 nL/min, 1 nL/min, 10 nL/min and 100 nL/min are presented and discussed. The three dimensional micro-model geometry reconstructed from fluorescence data is used as the computational domain to conduct numerical simulations of the flow in the as-tested micro-model for comparisons to experimental results using dimensionless Navier-Stokes model. The flow simulation results are also used to qualitatively compare with velocity distributions of the flowing particles at selected locations. The comparison is qualitative because the particle sizes used in these experiments may not accurately follow the flow itself given the geometry of the micro-models. These larger particles were used

for proof of concept purposes, and the techniques and algorithms used permit future use of particles as small as 50 nm.

Chapter 1
Introduction

1.1 Role of Nanotechnology in Petroloeum Industry

Along with the increase in the world population over the past few decades, the world energy demand is increasing accordingly. The energy demand has increased more than 100 % over two decades and will increase by another one-third of the energy consumed today by 2030. Figure 1.1 shows the world's primary energy demand by sources. More than three-fourths of the world's energy demand comes from petroleum and fossil fuels. Although it have low energy efficiency, its inexpensive, and portable nature make it impractical to replace petroleum products and fossil fuels with other supplement sources. Oil, natural gas and coal are the main sources of energy that dominate energy demand globally. Figure 1.2 shows energy consumption by different parts of the world. More than one-third of the energy is consumed in North America, of which USA is the highest. Energy demand is also increasing in developing nations like India, China and other nations with high increases in population. Energy demand for Asian and Oceanian countries has increased significantly (*e.g.* more than triple) over the past three decades as shown in Figure 1.2.

Over the past few decades, nanotechnology has been used in oil and gas industries for drilling muds, in primary and assisting production, and refining and distributing oil and gas [3]. Nearly two-thirds of the oil remains in the reservoir due to lack of existing advanced technology [4]. However even with current state-of-the-art technologies, oil and gas companies are not able to comprehend the characterization of hydrocarbons in new locations[3].

Through nanotechnology, one can understand process of oil and gas extraction, oil and water separation, as well as transport mechanism of nano-particles at the molecular level, which in fact enhance oil recovery from reservoirs[5]. In other word, injecting nano-sensors into reservoirs improves the understanding of fluid transport behavior in harsh

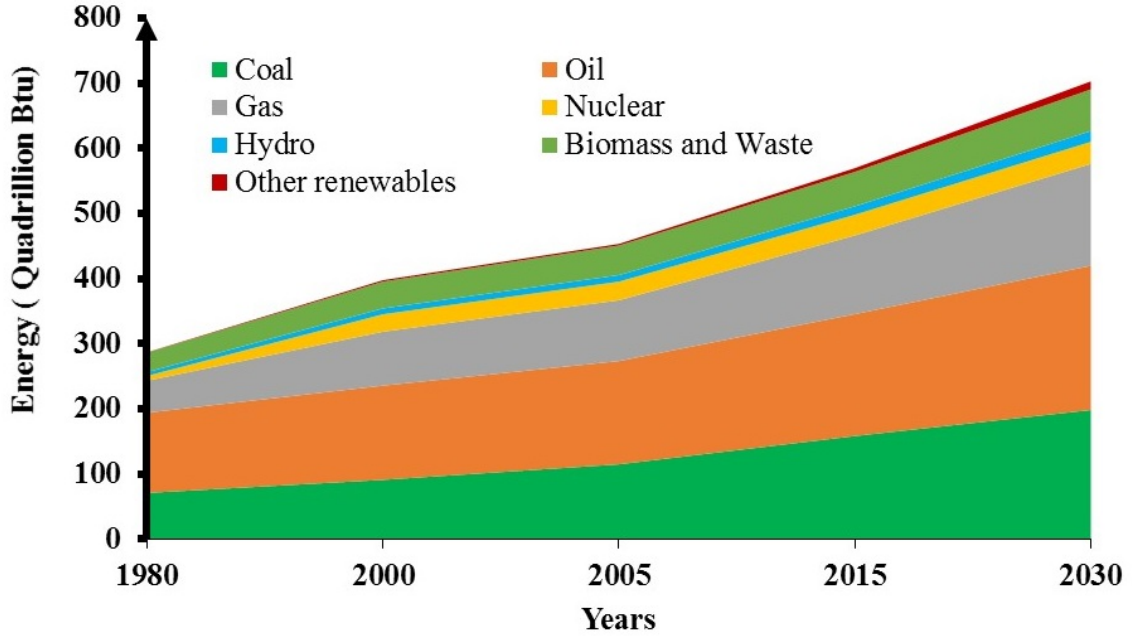

Figure 1.1: World Primary Energy Demand[1]

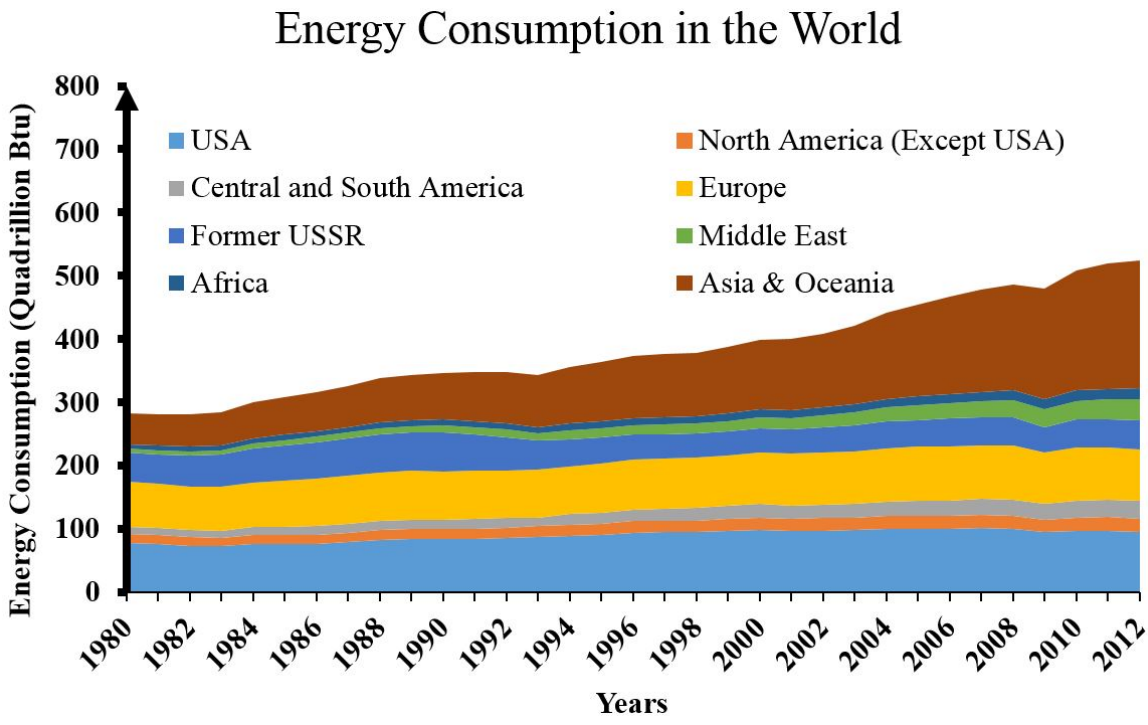

Figure 1.2: Energy Consumption by different parts of the world[2]

environments. A combination of nano-fabricated particles with fluids also known as "Smart fluids" are widely used to enhance fluid properties like drag reduction, binders for sand consolidation, gels, wettability alteration, and anti-corrosive coatings, and it has become one of the primary technologies for oil and gas companies [5, 6, 7, 8]. Moradi *et al.* has presented a novel method called nanofluid alternating gas injection in order to increase the efficiency of oil recovery from oil-wetted carbonated reservoirs[9]. Experimental results illustrate that adding nano-particles to fluid alters the wettability of the solid-liquid surface of the reservoir rock[9, 7]. Various flooding scenarios have been studied by Ragab *et al.* which show injected nano-particle are effective and have increased the efficiency of oil recovery from reservoirs over traditional methods[10].

In harsh conditions (*e.g.*: high temperature, high pressure), most of the measuring tools are incompetent for reliable measurements of oil flow fields, temperature, and electro-magnetic fields, so an alternative way of measuring those parameters is necessary[5]. Han *et al.* has demonstrated porosity and a very small presence of clay in shaly sandstones can significantly reduce elastic moduli, as a result affecting compression and shear velocity in sandstones[11]. In order to improve the functionality of all the nano-particles, nano-sensors or any smart fluids, one must understand fluid transport, nano-particles' retention as well as their behavior in high temperature, and high pressure multiphase environments. For accurate measurements and understanding of smart fluid in reservoirs, one has to conduct measurements in real porous rock (see for example [12]). Conducting an experiment in real rock is not only expensive but also challenging due to limited resolution. To facilitate all these measurements, one has to develop inexpensive reservoir-on-chip in such a way that it can preserve 3D features of relevant tortuous geometry of pore-throat pathways along with an observation window. The 2.5D micro-model which has been developed by our research group, serves as a replica of 3D actual rock (see [13]) for measuring 3D velocity distributions, particles concentration of nano-particles of different size and nano-particles deposition [14].

1.2 Fluid and Nano-Particles Transport

Microfluidics

Microfluidics is a branch of science and technology which deals with manipulation and analysis of tens of microliters to hundreds of nanoliters of a fluid with relevant applications within engineering, physics, biology, chemistry, nanotechnology, biochemistry, genomics, proteomics, pharmaceuticals, biodefence and other disciplines[15]. Microfluidic technology has emerged as a powerful tool in recent decades because of its capability to carry out complex protocols of chemical processing [16]. Due to its inexpensive and portable nature, it has become a toolbox for the technological arena, which offers solutions to most of the emerging problems in the context of Lab-on-Chip [16].

Microfluidics technology has tremendous applications in the oil and gas industries, whether in sub-surface operation or analysis of fluid properties. It provides not only economical and environmental gain to the oil and gas industries, but also super resolution of multiphase flow transport mechanism in reservoirs [17]. Reservoir rock consists of heterogeneous pore-size throats and fluid transport mechanisms are strongly dependent on geometrical and topological properties of the pores and properties of the displaced fluid[18]. Since most of the oil and gas are trapped inside the petroleum reservoir rock, it is vital to understand oil and gas transport behavior in reservoir rock to enhance the production of oil and gas from the reservoir. In order to fully understand the phenomena of oil and gas recovery, one has to fully incorporate geometrical, as well as flow, parameters that resemble reservoir rock into reservoir-on-chip.

Physical understanding of micro-scale fluid transport mechanisms provides better understanding of fluid transport in macroscopic scale. Most of the flows in microfluidics are laminar; as the reynolds number is often less than 1 or in the order of unity, steady, and fully developed pressure driven, which make microfluidics so important in electrophoresis as well as diffusion separation of phases[15, 19]. Zhang *et al.* has presented kinematics of nano-particles in microchannels to understand mechanisms, and underlying physics

of nano-particles in inertial microfluidic systems [20]. To comprehend displacement of oil/water interface/meniscus in the pore network, Gunda *et al.* have designed a complete microfluidic chip termed as "Reservoir-on-Chip" which represents naturally occurring oil and gas natural porous structures [21]. Similarly, Robert *et al.* have also used microfluidic technology for measuring gas-oil ratio of reservoir fluids. Gas-oil ratio, a key parameter used in reservoir simulation, describes phase behavior in oil and gas equilibrium [22]. In another laboratory experiment, Nilsson *et al.* developed an inexpensive microfluidic sandstone device to study the effect of fluid rheological properties in enhanced oil recovery [23]. In a recent experimental study, Porter *et al.* have used 3D tomography images to represent pore spaces along with fracture geometries to outline the benefit of flow and transport study in porous media for future development of subsurface energy resource technologies [24].

The current state-of-the-art technology in microfabrication has made it possible to fabricate a microfluidic device with complex 2D and 3D structures that resembles actual rock, to understand transport mechanisms in porous media. Preserving morphological as well as fluidic behavior in actual rock base micro-models is challenging. To address mobility of nano-particles in reservoir rock, our research group has developed a 2.5D micro-model which matches fourteen morphological and flow parameters to those of fully 3D actual reservoir rock (Boise rock sandstone) to study fluid transport mechanisms in reservoirs (for more detail see [13, 25]).

Nano-particles Transport in Rock-based Micro-model

Nano-particle injection into reservoirs has become a foundation for upstream oil and gas industries to enhance oil recovery from reservoirs. Brownian effects usually contribute to slippage of nano-particles near solid walls, which results in migration of crude oil and enhanced nano-particles flow in porous media. In other word, nano-particles decrease the contact angle of the aqueous solution and increase water wettability in the reservoir, which enhance displacement of oil from the reservoir rock [26]. Particle retention in reservoir rock

plays a significant role in the enhancement of oil recovery, which is subsequently affected by particle size and surface properties of the particles [27].

Experimental results depict that use of apposite concentration of nano-particles in a fluid decreases surface tension in surfactant solution and influences the surfactant adsorption process and oil wettability[28]. Injection of brine solution can alone recover 49 percent of heavy oil whereas injecting two pore volumes of nano-particles and brine solution can improve heavy oil recovery up to 80 percent in sandstone cores [29]. Another in-situ experiment in Berea sandstone also demonstrates, use of appropriate nanofluid along with high salinity brine solution can improve crude oil displacement from the reservoir[30].

To properly understand behavior (mobility, retention, absorption and interaction with rock walls) of nano-particles in harsh environments like in a reservoir, one needs to execute experiments in actual rock-based micro-model "Reservoir-on-Chip" while preserving 3D features of reservoir rock. Study of nano-particles mobility in reservoir provides detailed understanding of nano-particle interaction with high salinity fluid, interaction with reservoir walls, deposition and retention of nano-particles in reservoir rocks. Once the mobility of nano-particles is fully understood in the reservoir-based micro-model, one can incorporate nano-particle effects in pore scale simulations to better estimate oil and gas recovery from the reservoirs.

1.3 Thesis Overview

Advanced Energy Consortium is a consortium which focuses on research involving energy resources, especially oil and gas. AEC was established with the mission of facilitating pre-competitive research in micro/nano technology material and sensors that can create positive change in petroleum and gas recovery from existing as well as new reservoirs. The main goal of this consortium is to develop high-tech intelligent subsurface micro/nano-sensors to aid in characterizing 3D space of the reservoir and improve existing as well as new hydrocarbons extraction. With past years of research activities, AEC has made advancements in designing subsurface nano-sensors, developing various injection/detection

strategies along with understanding the governing factors that command particle mobility in the reservoir. However, AEC has faced challenges in addressing field trails, inability to control particle environments as well as scaling up with technology transfer. In order to address those issues, one has to understand nano-particles mobility in a physical surrogate of reservoir rock. Studying and executing nano-particle experiments in rock-based surrogate will directly address coating and designing of nano-particles which can be used in enhanced oil recovery as well as provide a benchmark for micro/nano sensors that can be used later in addressing 3D space characterization of the reservoir rock.

My Contributions

My main contribution towards the current research project is to conduct experimental study of nano-particles using confocal microscopy to quantify 3D nano-particle transport in a physical surrogate of reservoir rock for understanding the physics of nano-particles as well as establishing a benchmark for validation of pore level simulation in reservoir surrogate. My research contributions to the above endeavor are:

1. A Novel non-destructive, inexpensive and reliable method of in-situ geometry extraction is proposed and demonstrated to extract 3D in-situ geometry of 2.5D rock based micro-models for pore level multiscale computation flow analysis.

2. An experimental study of nano-particle in rock-based 2.5D (low resolution, high resolution PMMA and ceramic) physical micro-model exploring physics of nano-particles transport and quantifying velocity, concentration and deposition rate in 3D. This provides a foundation for validating pore-level multiscale computational flow and particle transport models.

3. A Novel method of image-patching algorithm is proposed and validated in order to measure nano-particles velocity as well as particle concentration in complex porous media with uniform grid and extended field of view.

4. A combination of image processing algorithms are assembled and applied to micro-

particle image velocimetry (μ-PIV). A new particle segregation algorithm is proposed and demonstrated for distinguishing dynamic particles from raw images in order to improve μ-PIV data.

1.4 Organization

The current research has focused on quantifying nano-particles transport in a physical surrogate derived from optimizing fourteen morphological as well as flow parameters of the original Boise sandstone. The research presented here is primarily focused on two topics (1) developing measurement techniques in quantifying nano-particles velocity, concentration and deposition as well as developing inexpensive, non-destructive and reliable 3D geometry extraction technique to extract in-situ geometry for computational flow analysis, and (2) experimental measurement of nano-particle transport in 2.5D low-resolution and high-resolution PMMA micro-model, and ceramic micro-model.

In chapter 2 various micro-fabrication techniques along with a brief introduction of design and optimization of 2.5D micro-model of micro-model are presented. In chapter 3 experimental procedure and experimental set up along with image acquisition of a 2.5D micro-model is presented. In chapter 4, a novel non-destructive, inexpensive and reliable in-situ geometry extraction technique is presented and demonstrated. In chapter 5, a novel method of image-patching algorithm is proposed and validated to extend the field of view of confocal micro-PIV system. Necessary algorithms in order to achieve thin optical thickness plane and particle segregation are presented and demonstrated in chapter 6. In chapter 7, experimental results of nano-particles velocity, concentration and deposition rates at different local areas in low-resolution 2.5D micro-model are presented. In chapter 8, experimental results of nano-particles velocity, concentration and deposition rates at different local areas in a ceramic 2.5D micro-model are presented. In chapter 9, a new technique of 3D geometry extraction is proposed and demostrated for high-resolution 2.5D PMMA micro-model. The experimental results of nano-particles velocity, concentration and deposition rates at different local areas in a high-resolution (the same as the original

CT scan resolution) 2.5D micro-model are also presented.

Chapter 2
Micro-Fabrication of Low-Resolution Boise Rock-Based Micro-Models

2.1 Introduction

Creating miniature structures of micro- and nano-scales have become a necessity for highly industrialized and developed countries for betterment of life. Initially, semiconductor industries were involved in micro- and nano-fabrication to fabricate electronic devices such as integrated circuits, transistors and capacitors using silicon-based materials so that many electronic components can be fitted into a small compartment [31]. As long as people use space efficiently, micro-fabrication technology will become an important tool for advanced development in technology[32]. Since the transistor was invented, silicon has become a mainstay not only for microelectronics, but also for micro-mechanics because of its novel properties: mechanical strength, semi-conduction (can act as p-type as well as n-type), and easy fabrication of a single crystal from a large crystal[33]. Three main steps are typically involved in micro-fabrication process: addition, subtraction and multiplication of the materials. I have briefly discussed about these various micro-fabrication techniques used in micro-fabrication of a 2D and 2.5D structures. The main goal of this chapter is to describe how a 2.5D micro-model is created from a CT scan images of Boise Sandstone.

2.2 Micro-fabrication Techniques

Lithography, Electroplating and Molding (LIGA)

International Business Machines (IBM) was the first industry to use electrodeposition and x-ray lithography to fabricate high aspect ratio metal structure plated with 20 μm thick gold [31]. Later, it was expanded by adding molding technique to x-ray lithography technique by "Karlsruhe Nuclear Research Laboratory", Germany to introduce the LIGA fabrication process. Figure 2.1 shows the various steps of LIGA process for fabricating

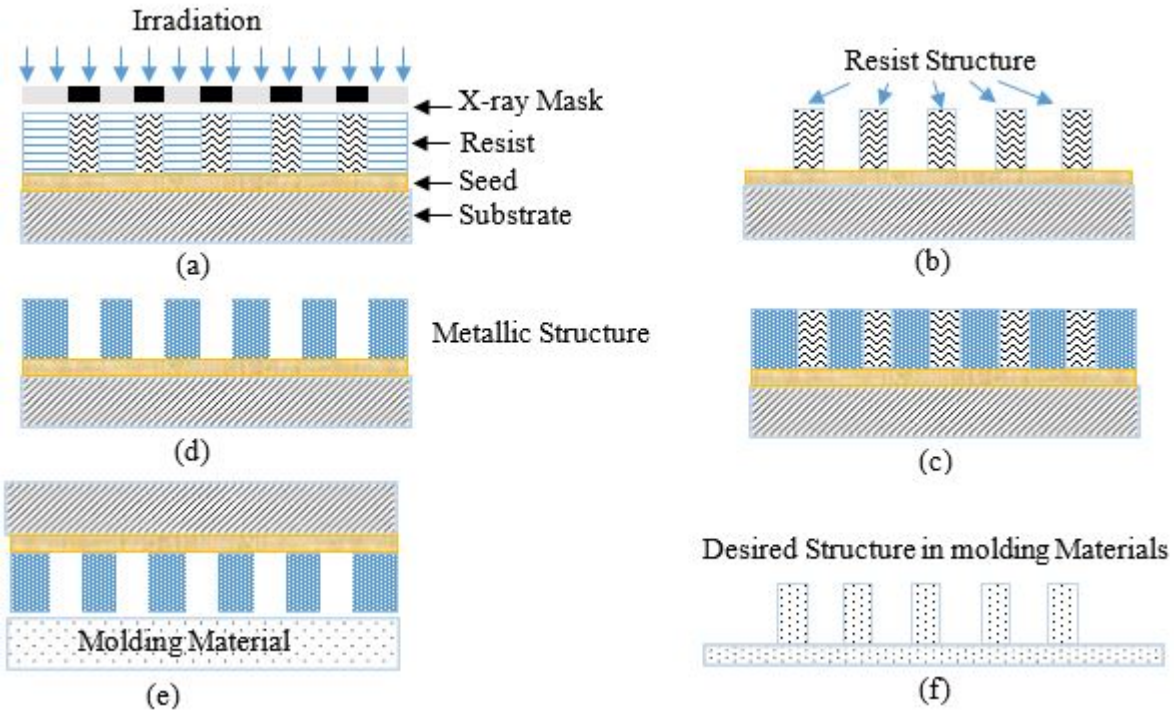

Figure 2.1: Process involved in LIGA (a) Irradiation (b) Development (c) Galvanoforming or electroforming (d) Metallic Mold Formation (e) Molding Process (f) Unmolding and Plastic Structure Formation

micro-structures in plastic templates. As of today, LIGA based research has been conducted in various laboratories around the world to fabricate very high aspect ratio as well as high resolution structures, which are used in biochemical filtering process, biomechanical analysis, DNA analysis, electronic devices and physical understanding of nano-particles' behavior.

X-ray masking is one of the crucial and difficult part of lithography process. Usually, an x-ray mask consists of a thin membrane of some low atomic number element which is highly sensitive to light and has high transmissivity[31]. An x-ray mask should be tough, have high exposure endurance without any distortion as well as easily align with respect to the sample. The x-ray mask consists of all the imprinting structures and reflects them into a resist, once a resist is exposed to the x-ray. A resist is a thin layer of polymer coated in a substrate that is used to transfer micro/nano-structures on it. An x-ray resist is highly sensitive material towards the x-ray and resistance toward dry and wet etching. The

resist should be a good adhesive with substrate and compatible with electroforming process [34]. The resist acts as memory for all imprinted structures until the development process. Development is a process where unexposed/exposed material is dissolved depending on positive or negative resist. The undissolved resist delivers required micro structures on the substrate. Once the development process is completed, an electroforming process is required to create a mirror template of the micro-structure, necessary for molding. Electroforming or galvanoforming is a mirror replication of the master photoresist mold by depositing metal on the substrate. Metal can be deposited on the substrate by using electroless metal deposition or electrodeposition. Electroless metal deposition is a metal deposition process which involves chemical means of metal deposition without using external power supply or eroding electrodes. In electronic industries, for electronic devices such as integrated circuits (IC) and other devices with high aspect ratios, electroless deposition is used to produce high structural integrity devices [34]. Electrodeposition is a common method of depositing metal in dielectric substrate by using electric field. The substrate is usually coated with an adhesive conductive layer made of chromium, titanium, along with seed layer of gold, platinum, copper, iron etc to adhere the resist layer with adhesive layer. Before electroforming, the adhesive layer (*e.g.* Cr, Ti, etc.) is etched, so that the seed layer is exposed to a buffer solution with a continuous electric field. Once the electroforming process is completed, the resist and substrate, along with the seed layer are etched using wet and dry etching process. Upon completion of etching, the metallic mold acts as a mirror template for prototype structures. Molding is the last process of imprinting desired structures in soft materials using different molding techniques such as hot embossing, reaction injection molding, soft molding, casting, or injection molding. Each molding technique has its own advantages and disadvantages. Sandia National Laboratories at Livermore and Center for Advance Microstructures and Devices (CAMD) at Louisiana State University in Baton Rouge are the most active research groups involved in using the LIGA process [31]. Here, in this chapter, we will briefly focus on those techniques which were used or had potential

to be used in the micro-fabrication of Boise rock-based micro-models.

Mechanical Micromachining

Mechanical micromachining is the cheapest method of fabricating high aspect ratio microstructures of complex geometry by using diamond coated cutting tools [35, 36]. The micromachining process has been used for decades and is suitable to fabricate micro 3D products where roughness and dimension precision is within tens of nanometer [36, 37, 32]. Along with industrial revolution, ultraprecision metal cutting is used by manufacturing companies to manufacture optical parts with top notch surfaces as well as geometrical quality [38].

Mechanical micromachining is a flexible fabrication process which is applied to a wide range of materials [37]. This process involves removal of chips which includes conductor, dielectric, brittle and ductile materials by using machining tools in the form of conglomerates of atoms [36]. Material removal rate in mechanical micromachining is comparatively lower than conventional macro-scale machining. Unlike in conventional macro-scale machining, formation of an undeformed chip, as a result of tool edge radius, is in the range of a few nanometers to a few microns [39, 40]. When the material removal thickness is less than critical minimum chip thickness, elastic deformation occurs. As a result, no material is removed from the work piece. If the material removal thickness is greater than critical minimum chip thickness, no undeformed chip is observed and the depth of cut is removed from the work piece [41]. Therefore, a relation exists between tool radius and minimum thickness depending on the tool cutting edge radius and removal material from the work piece. Although it is very difficult to find minimum chip thickness of the material, some researchers have estimated minimum chip thickness by means of finite element methods or by experiments [42]. Liu *et al.* has demonstrated how undeformed chip thickness influences chip formation mode, which is greatly dependent on depth of cut, feed rate and cutting tools geometry [43]. Multiphase microstructure of the material plays significant role in micromachining as depth of cut is on the same order of magnitude as the grain size

Table 2.1: List of Polymers used in Micromolding [31, 47]

Acronym	Full Name	Temperature(^{0}C) Stability	Properties	Structure
COC	Cyclo-olefin copolymer	140	High transparency	Amorphous
PA	Polyamide	80-120	Chemical and temperature resistivity	Semicrystalline
PC	Polycarbonate	130	High transparency	Amorphous
PEEK	Polyetheretherketone	250	High temperature resistivity	Semicrystalline
PET	Polyethylene terephthalate	110	Transparent low friction	Amorphous/ Semicrystalline
PMMA	Polymethylmethacrylate	80	High transparency	Amorphous
POM	Polyoxymethylene	90	Low friction	Semicrystalline
PP	Polypropylene	110	Mechanical Properties	Semicrystalline
PS	Polystyrene	80	Transparent	Amorphous
PSU	Polysulfone	150	Chemical and temperature resistivity	Amorphous
PVC	Polyvinylchloride	60	Low cost	Amorphous
PVDF	Polyvinylidenedluoride	150	Chemical inert, piezoelectric	Semicrystalline

and cutting tool's edge radius [41, 44]. Chip formation and cutting forces are significantly affected by multiphase microstructures of the work piece material [45]. The work piece experiences vibration as well as a fluctuating cutting force due to various plastic deformation of multiphase microstructure [42]. Most of the material properties such as life span of the material, corrosion resistance, crack initiation and propagation, fatigue resistance, creep life, wear and tear, and friction during use are affected by surface finish and surface integrity of the material [44]. Equally notable, burr formation is also an outcome of material plastic deformation produced due to shearing process at work piece edges [46].

Currently, micro-mold inserts are produced by using mechanical micromachining (micromilling) for mass production of plastic chips by mean of hot embossing process [44]. By using this technique, negative features are imprinted in the desired plastic materials.

Micro-Molding

Micro-molding is one of the low-cost mass production micro-fabrication techniques, which involves production of non-electronic micro-devices from thermoplastic materials [47]. It has been commonly used to reproduce low cost as well as high aspect ratio microstructures in polymers from a master piece. Molded materials can vary from soft plastic materials such as PC, PMMA *etc.* to hard and brittle materials like polysulfone (PSU). Table 2.1 shows a list of polymer materials used in current state of micro-molding technology. Depending on application, one can select a suitable polymer from Table 2.1 to fabricate low cost and disposable micro-devices.

- **Injection Molding**

Injection molding is a variotherm process which involves injection of thermoplastic materials into a closed, evacuated, and heated mold cavity [48]. The mold cavity is heated above the glass transition temperature of molding polymers and viscous polymer is injected, filling the mold cavity. Complete filling of high resolution mold requires low viscosity resin so that high resolution structure can be replicated into the polymer. Figure 2.2 shows the basic principles of injection molding to produce micro-devices.

- **Reaction Molding**

Reaction injection molding is similar to injection molding with two or more varieties of polymers. The end product can be a thermoplastics or a thermosetting material depending on the reaction of two species. Due to longer curing/chemical reaction time, the final product takes longer to produce than the product fabricated by injection molding technique. Integration of UV (Light) in reaction injection molding techniques has enhanced curing time of the chemical reaction which results in rapid prototyping of the product. Photo-induced reaction molding is highly dependent on amount of resin, its composition, and radiation strength [48].

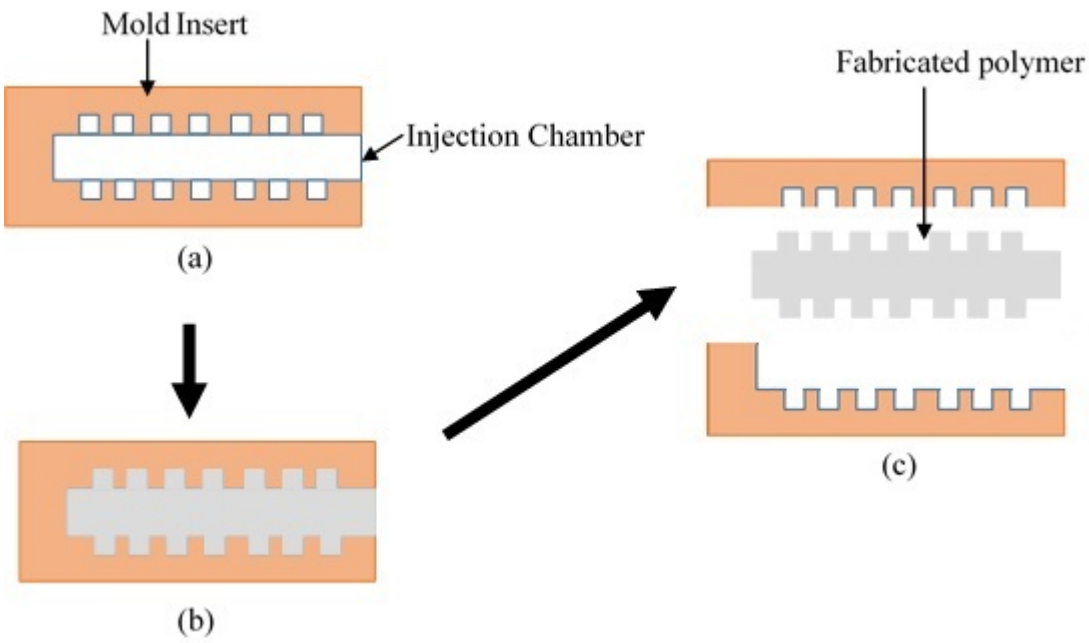

Figure 2.2: Injection Molding Process:(a) Mold Insert is heated above glass transition temperature (b) Viscous polymer is injected through injection chamber (c) Polymer is pressurized and demolding of polymer takes place after cooling the mold insert chamber.

- **Injection Compression Molding**

Injection compression molding is a combination of two techniques which involves hot embossing and injection molding to produce better quality micro-devices compared to injection molding itself [49]. This technology has been a boom for micro-fabrication industries to enhance dimension control on the sub-micron scale. It has also been introduced to overcome heating of polymer using a tool which increases the stress concentration around the sharp edge of the polymer. Injection compression molding usually consists of a compression control system which controls pressurized gas in the compression chamber. The thin plastic polymer is injected through a small hole into the semi-closed chamber where a mold is inserted. Then the chamber is closed and pressed into microstructures. This technique is widely used to produce CDs, DVDs and other sub-micron devices that are very sensitive in dimension.

- **Hot Embossing**

Because of low cost, effective reproducibility, and high-volume production, micro-fabrication of polymers has become an alternative to silicon or glass-based micro-fabrication [50, 51]. Hot embossing of thermoplastic polymers is one of the promising micro-fabrication technologies in MEMS to produce optically transparent, high compatibility, high aspect ratio products with a wide range of polymers. The expensive side of this technology is creating a master stamp using LIGA or micro-machining. Once the master stamp is created in silicon, nickel, or other stamp materials, hot embossing is relatively inexpensive to mass produce replica of the master piece. In hot embossing process, a substrate is sandwiched between the upper master mold and a lower metal plate at elevated temperature just above the glass transition temperature of the substrate. A hot embossing machine also consists a force frame which delivers force to sandwich the substrate between plates. Before initializing the system, the master mold is mounted in the heating plate, which consists of heating and cooling channels. Similarly, the substrate is placed on the lower plate, equipped with a heating-cooling system. The cooling system has a high heat capacity fluid, which is circulated through the cooling channels during the cooling process of the lower and upper plates of the embossing machine. The upper and lower plates are heated separately in a vacuum chamber just above the glass transition temperature and the mold is brought in contact with the substrate and a controlled force is applied to emboss the master pattern in the substrate. The master mold and substrate remain in contact with each other at elevated temperature for a few seconds to a few minutes depending on material properties of the substrate. Due to different thermal expansion coefficients of the mold insert and substrate, the thermal cycle should be as small as possible in order to minimize thermal stress in the substrate [50]. Once the system has reached low temperature cycle, the substrate is separated from the master mold insert and desired features are embossed in the substrate. Various successful experiments have been reported in biomedical/microfluidic and micro optical as well as MEMS in chemistry or life science fields. One of the recent

reports shows successful replication of 5 μm features in PMMA substrate using the hot embossing technique[52]. A study shows that accuracy of the imprinted features increases with the increase in the applied force [51]. With this micro-fabrication technology, high aspect ratio features are fabricated commercially to lower the cost of production for polymer micro components [50].

2.3 X-Ray Micro-Computed Tomography

X-ray micro-computed tomography (X-ray μCT) is a non-destructive 3D x-ray imaging technique that allows manufacturers to generate 3D object from 2D projections of a 3 dimensional object. X-ray tomography consists of a x-ray source and a detector "scintillator". The basic principles of x-ray μCT depends on the absorption of x-rays in material and projections of 2D images [53]. X-ray absorption in the material behaves in a logarithmic manner and depends on the distance travelled by light through the material [54]. Using a synchrotron source for radiation in x-ray μCT significantly improves image quality as well as reduces data collection time. The use of monochromatic beams increase signal to noise ratio, which results in no hardening effect [55]. The synchrotron x-ray produces high photon flux, which is used in precise mapping of internal structures of the sample along with fast data acquisition with high resolution [55].

Collimated x-ray beams emitted from the x-ray synchrotron source, which are more powerful than conventional X-ray sources, are passed through an object and a detector converts the x-ray light into visible light, which is then converted into current by means of photo-diode [53] or coupled with CCD camera. The signals received by photo-diode are analyzed by a computer and converted into a digital image. The sample rotates with small angle increments to acquire a series of multiple 2D projected images. Later, the series of acquired 2D images are used to reconstruct a 3D image of an object. A filter back projection algorithm is used to reconstruct a voxel based 3D image of an object [56]. Error and limitations of the reconstructed 3D image depend on the reconstruction algorithm.

2.4 Boise Rock Sandstone

Most of the oilfields lie in the heart of sandstone rock. Sandstone rock is a highly porous and permeable sedimentary rock that is composed of minerals, quartz and organic materials. Most of the sandstone rocks consist of smaller grains, pieces of rocks, and remains of skeleton, which are cemented together by clay and silica. Because of its porosity and permeability, oil and gas migrates from one location to another location, hence sandstones rock generally serves as a reservoir for oil and gas production. Boise rock sandstone is a kind of sandstone which is mostly found in the oil and gas reservoir. Boise rock sandstone is obtained from Prof. Steven Bryant at University of Texas Austin to study topology and mobility of nano-particles inside the Boise sandstone rock. Michael has studied morphological as well as flow key parameters of Boise rock sandstone in his thesis. He later designed and optimized a micro-model that resembles fourteen different morphological and flow parameters of an actual 3D scan image of Boise rock [25]. The Boise rock based micro-model was designed and fabricated by our research group and is used in this project to understand mobility of nano-particles inside the rock-based micro-model.

Optimization and Design of 2.5D Micro-model of Boise Rock Sandstone

Micro-model design and optimization was performed by Bou-Mikael and a detail description can be found in his Master thesis, titled "Design and Optimization of 2.5 Dimension Porous Media micro-model for Nanosensor Flow Experiments".

Using x-ray μCT at Center for Advanced Microstructures and Devices (CAMD) at LSU, a sample of Boise sandstone rock of 2.03 mm x 2.03 mm x 2.03 mm section was imaged and a 400^3 voxel image was extracted to generate a micro-model. Seven different parameters (pore coordination number, inscribed pore diameter, inscribed pore volume, inscribed pore throat diameter, pore throat aspect ratio, throat length, and hydraulic diameter) were used to statistically characterize the network morphology of the Boise rock sample. Similarly, good agreement of capillary pressure curves between micro-model and

original Boise rock shows similar multiphase flow in the micro-model and the original rock. Two-point correlation function is a method of statistical quantification of permeability and resistivity of porous media structure, which is also described in detail in his thesis. Two-point correlation function was also considered while designing the micro-model and results have been reported in his thesis. Detailed comparisons of fourteen different key parameters of micro-CT scan of boise rock sandstone and the designed 2.5D micro-model have been reported and published by Bou-Michael in his thesis and Park *et al.* in IMECE conference 2012[25, 13].

Depth averaging techniques and CFD simulation were used to design and replicate CT scan Boise rock sandstone into reservoir-on-chip with depth variation. A depth averaging tool allows us to map pores and throats of real rock core in close vicinity to project and create a 2.5D micro-model with varying floor elevation along a planar observation window. Third dimension (depth) variation in reservoir-on-chip provides us realistic model of Boise rock sandstone with additional geometric complexity and realistic pore networks of actual reservoir rock. An optimized 2.5D micro-model was designed using depth averaging and a series of flow based as well as morphology based parameters (for detail see Bou-Mikaels master thesis [25] and [13]) that best represents original Boise rock sample with the same flow characteristics.

Figure 2.3a shows a 3D image generated by multiple stacks of 2D projected images of a real Boise rock sandstone scanned at 5.07 μm/pixel. Figure 2.3b is an extracted binary image from original μCT scan images prior to manipulation, and it was used in CFD simulation using in house Stokes flow simulation to determine flow characteristics. Figure 2.3c shows a subset of slice images of finite thickness which was used in optimizing depth and in designing the 2.5D micro-model. Similarly, Figure 2.3d and Figure 2.3f are high resolution (5 μm) and low resolution (25 μm) micro-model designs respectively. Color region in Figures 2.3d and 2.3f shows fluidic domain whereas 2.3e and 2.3g shows qualitative CFD simulation results in high and low resolution 2.5D micro-models

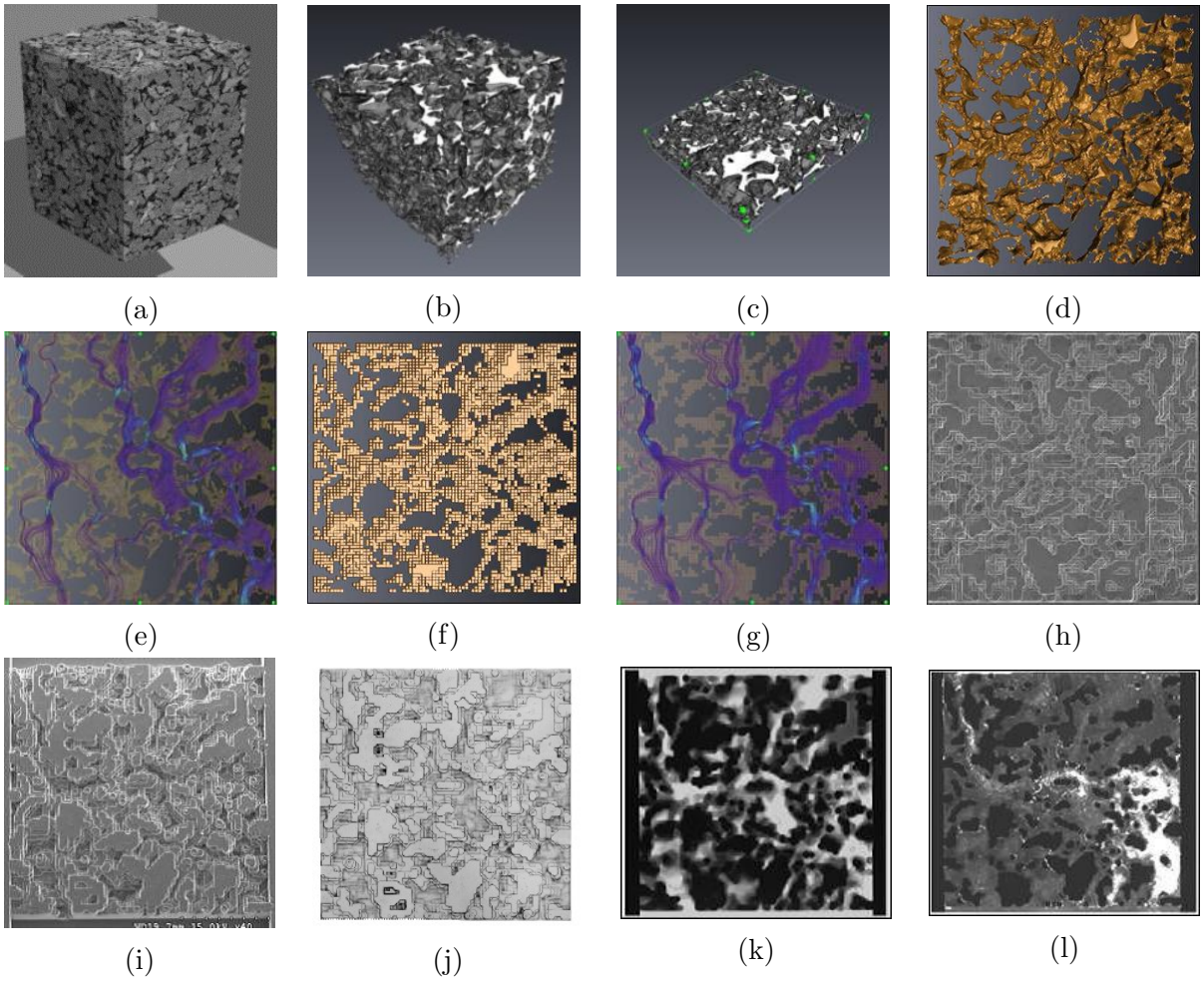

Figure 2.3: Design of 2.5D micro-model (a) original X-ray μCT image (b) Image extracted from μCT prior to manipulation (c) a slice of 3D image with finite thickness for depth averaging (d) high resolution (5 μm) 2.5D micro-model (e) qualitative results of CFD simulation in high resolution micro-model (f) low resolution (25 μm) 2.5D micro-model (g) qualitative results of CFD simulation in low resolution micro-model (h) SEM image of low resolution 2.5D micro-model master mold (brass) (i) SEM image of low resolution 2.5D micro-model PMMA sample (j) Microscopy image of low resolution PMMA micro-model filled with deionized water prior to dye experiment (k) Microscopy image low resolution PMMA micro-model filled with rhodamine dye B (l) Microscopy image of low resolution PMMA micro-model during nano-particle flow experiment[a].

[a]Reprinted with permission from "Design and Fabrication of Rock Based micro-model" by Daniel Park *et al.*, 2012,Paper No. IMECE2012-88501 by ASME

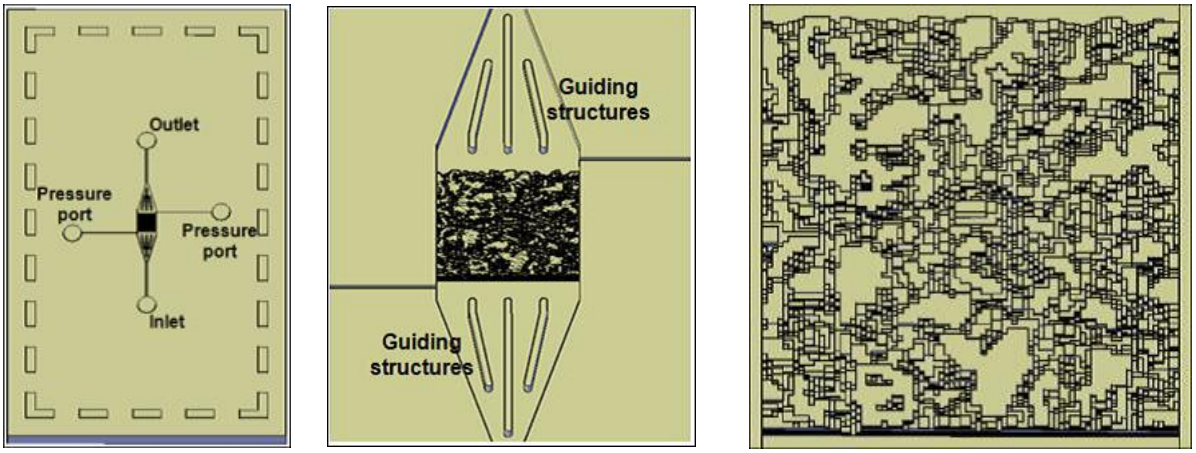

(a) (b) (c)

Figure 2.4: Schematic views of (a) low resolution PMMA Micro-Model (b) Close up view of PMMA micro-model showing fluid guiding channels (c)Close up view of 13 different layers design and footprint of 2 x 2 mm^2 of Boise Rock Sandstone[a].

[a]Reprinted with permission from "Design and Fabrication of Rock Based micro-model" by Daniel Park *et al.*, 2012,Paper No. IMECE2012-88501 by ASME.

respectively. Figure 2.3h is a SEM image of a low resolution machined brass mold insert, which is used as a master template to fabricate mirror pattern in the 2.5D PMMA micro-model. Figure 2.3i shows SEM image of the fabricated 2.5D PMMA micro-model which represents mirror structures of the Boise rock based master mold insert. This fabricated micro-model is covered with 250 μm thick PMMA sheet using thermal fusion bonding [13]. Figure 2.3j shows a microscopic image of PMMA filled with deionized water prior to dye experiment. Figure 2.3k is an image of the 2.5D PMMA micro-model filled with rhodamine dye B that resembles flow pattern of flow simulation in μCT scan Boise rock sandstone. Figure 2.3l shows nano-particles injection experimental results in a fabricated PMMA micro-model.

Figure 2.4a shows the final version of the low resolution of PMMA micro-model, after hot embossing process. A flow guiding channel was added to the system so that uniform flow can enter through guiding channel as shown in Figure 2.4b. Figure 2.4c shows 13 different layers of micro-model for nano-particle experiment. Hence, the design of the 2.5D rock-based micro-model fulfil the necessity of third dimension and adds geometrical

complexity similar to reservoir rock to study nano-particle flow inside reservoir. The nano-particle experiment conducted in the 2.5D micro-model not only aids in understanding flow dynamics in reservoir but also provides a platform to test new field application nano-particles to enhance oil and gas recovery in petroleum industries.

Chapter 3
Experimental Set Up and Image Acquisition

3.1 Experimental Setup

Prior to particle experiment, the PMMA micro-model sample is bonded with a thin flat (250 μm) PMMA sheet using a thermal fusion method [57]. The inlet and outlet nanoports are connected to the PMMA micro-model using adhesive. After curing adhesive, the PMMA micro-model is placed on the stage of the inverted confocal microscope, so that coverslip of the micro-model is faced down. Once the nanoports are connected, the adhesive is allowed to cure for 24 hours to achieve its full strength. The PMMA sample is held firmly on the stage of the microscope using adhesive tape, prior connecting the connecting tubes to the inlet and outlet of the micro-model. One one-sixteenths inch tubes is used to connect the inlet port of the micro-model and the syringe.

3.2 Air Bubble Removal

Prior to water injection into the PMMA micro-model, all the tubes and glass syringes are cleaned with deionized water and ethanol. Ultra-pure ethanol (99.99 %), supplied by ThermoFisher Scientific Inc., is mixed with deionized water in the ratio of 2:9. As a result, the viscosity of the liquid mixture (water-ethanol) decreases and helps in removing air bubbles trapped inside the complex geometry of PMMA micro model. Due to the low viscosity and comparatively high wettability of the water-ethanol to the PMMA surface, the liquid pushes air bubbles out of the micro-structure. Initially, the water-ethanol is injected into the micro-structure using a pulling mechanism. The mixture is pulled from inlet to outlet for 30 mins, so that large trapped air bubbles are removed without debonding PMMA micro film. Once most of the large air bubbles trapped inside the micro-structure are released, a pushing mechanism plays a significant role in removing micro air bubbles that are trapped around the corners of the microstructure. During the pushing mechanism,

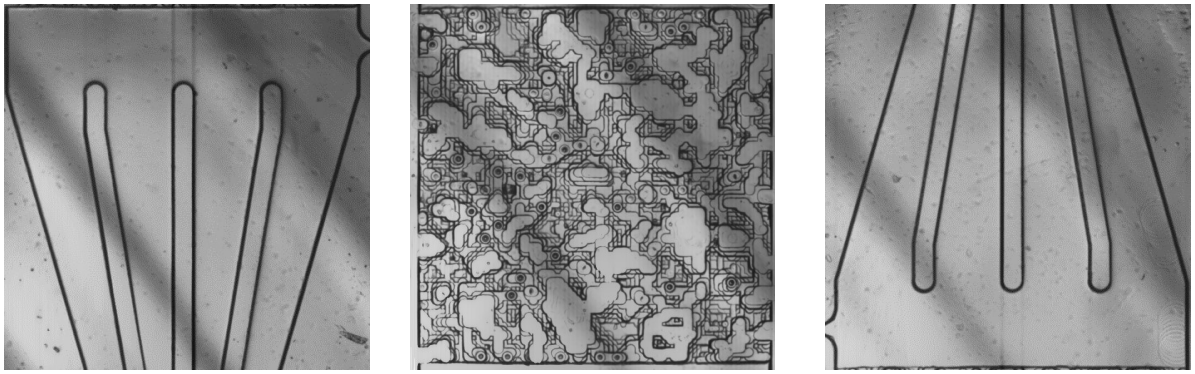

(a) (b) (c)

Figure 3.1: Low (25 μm) resolution 2.5D PMMA micro-model flooded with de-ionized water illustrating most of the air bubbles trapped inside the micro-model is removed from it. (a) shows image of inlet fluid guiding channel, while (b) shows image of 2.5D 2 x 2 mm^2 Boise Rock-Based structure of the micro-model and (c) shows image of outlet fluid guiding channels

a syringe pump along with a 25 milliliter air tight glass syringe is used to push water-ethanol at a constant volumetric flow rate of 25 μl/min for an hour and then the flow rate is decreased to 10 μl/min until micro-air bubbles are completely released from the micro-model. Once all air bubbles are completely removed, de-ionized water is injected via syringe pump at a constant volumetric flow rate of 10 μl/min for a day in order to remove the alcohol effect on the surface of the micro-model.Most of the air bubbles trapped inside the micro-model at room temperature are removed from the micro-model as shown in Figure 3.1. Figure 3.1a shows the inlet guiding channel filled with de-ionized water, while Figure 3.1b shows rock-based structures filled with de-ionized water, and Figure 3.1c shows the outlet guiding channel filled with de-ionized water.

3.3 Confocal Micro Particle Image Velocimetry (C-μPIV)

The confocal micro-PIV consists of an Olympus FluoView-1000 (FV1000) laser scanning confocal microscope (IX81; Olympus, Tokyo Japan) which delivers efficient and high resolution multi-dimensional images. FV1000 is incorporated with real time visualization as well as targeted laser simulation of nano-particle response. FV1000 includes a laser unit,

scanner and detection unit, and optical system.

Laser Unit

The laser unit consists of two types of laser; diode and gas laser. Diode lasers are highly stable, durable and cost efficient. In our system, we have a single diode laser which produces 635 nm wavelength monochromatic light. Gas lasers consists of various gases including: HeNe, Helium, and Ar in which electric current is passed to produce coherent light. Multi-line argon (Ar) along with Helium Neon (HeNe) lasers are also incorporated in our laser unit, which can produce 458 nm, 488 nm, 515 nm and 543 nm wavelength monochromatic light. A single fiber is used to connect the laser unit to the main scanner FV 1000 unit. The laser unit is facilitated with a natural air cooling system in order to produce continuous monochromatic light with various systems. Figure 3.2 shows a schematic drawing of the light path in confocal laser scanning system (FV 1000). The number indicated in the laser unit defines the wavelength of monochromatic light. As the laser is activated, monochromatic light passes through the scanning unit (SU) and dichroic mirror to eliminate all wavelengths of light except the desired wavelength of light. Once the excited wavelength of light passes through the objective lens, it excites fluorescent particles and light emitted by fluorescent particles is passed through the dichroic mirror and pinhole to the detector units.

Detectors

A confocal unit consists of a highly sensitive fluorescence detector Hamamatsu Photo-multiplier R7862 tube with an adjustable pinhole (diameter 50 μm to 800 μm) along with highly reflective silver coated galvanometer scanning mirrors in order to increase signal-to-noise (S/N) ratio [58]. Two PMTs (photo multiplier tube) are integrated with a confocal system which allow us to activate multiple detection units simultaneously. Each detection unit can capture a 64 pixels x 64 pixels to 4096 pixels x 4096 pixels, 24 bit image. Each channel (also known as detection unit) consists of various filters and has to select base on the emission wavelength of light to capture reflected signal from the sample. For our

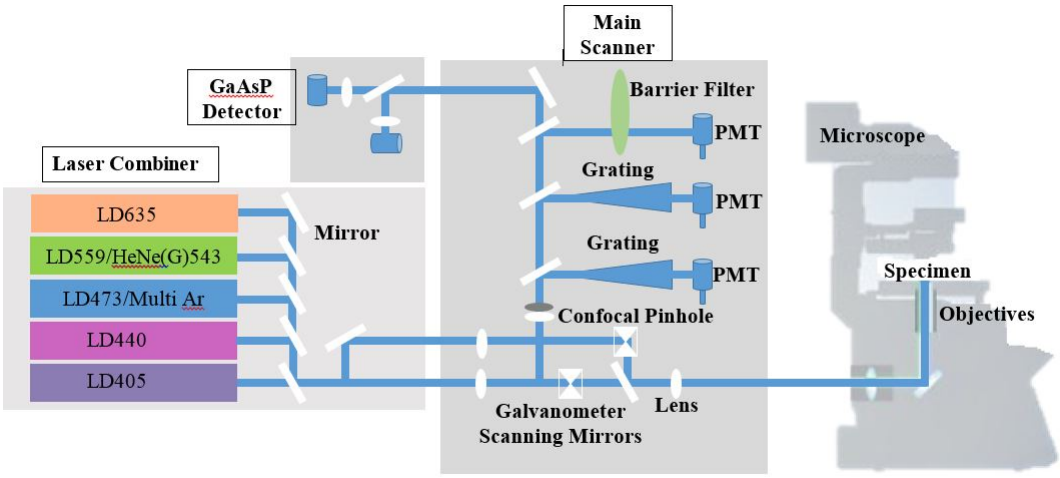

Figure 3.2: A schematic drawing of light path in FluoView 1000 Confocal Laser Scanning Microscope[58].

experiment, we used red and green fluorescent microspheres, made of polystyrene. A red fluorescent polystyrene particle has an average excitation wavelength of 542 nm (green) and an average emission wavelength of 612 (red) nm light. Similarly, a green fluorescent microsphere has an average excitation wavelength of 468 (blue) nm and an average emission wavelength of 508 nm (green) wavelength light. Once the signal is detected and captured by the PMTs, it is transferred to a storage device in the form of a tagged image file format (tiff) image.

3.4 Dye Injection

Dye is a colored substance that has high affinity to be dissolved in water. Here, in our experiment, we have used laser grade 99+% pure Rhodamine B, supplied by Acros Organics (a part of Thermos Fisher Scientific) as a dye to provide color to the water for visualization and depth measurement. Once air bubbles are completely removed from the micro-model, 100 ppm (1 mg in 10 ml deionized water) of Rhodamine B is dissolved completely in deionized water and allowed to diffuse homogeneously for a day. Once the Rhodamine dye is prepared and ready to inject into the micro-model, it is filtered with 200 nm filter paper in order to remove undissolved residue of Rhodamine B as well as other unknown impurities if present in the solution. Once the solution is filtered, the Rhodamine dye is

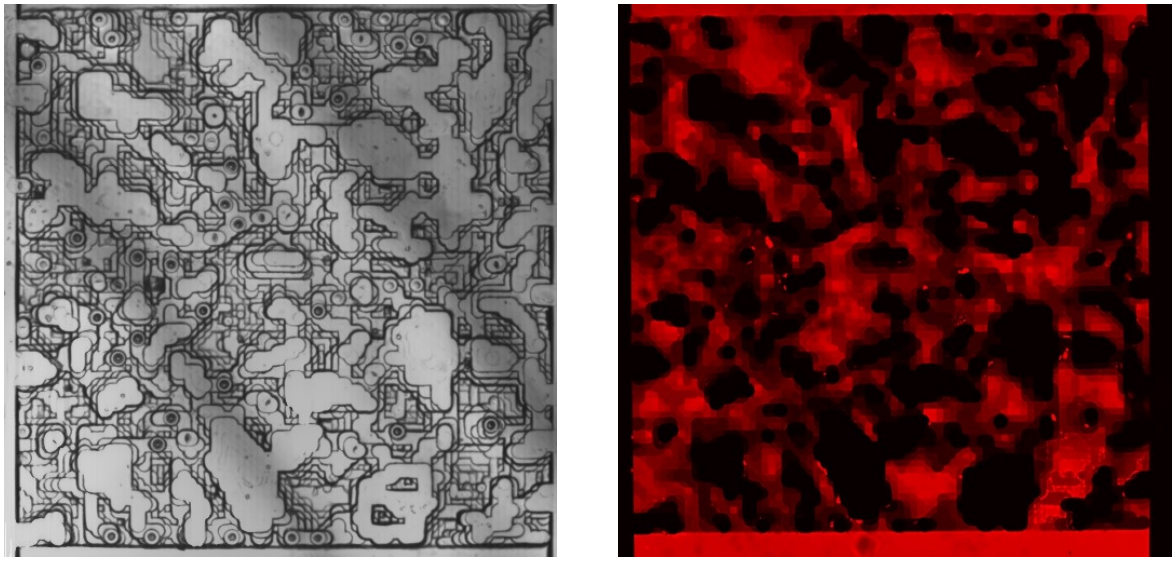

(a) (b)

Figure 3.3: Low (25 μm) resolution PMMA Boise rock base micro-model showing (a) bright field image of micro-model flooded with de-ionized water (b) fluorescence image flooded with rhodomine dye.

filled in a 5 mL gas sealed glass syringe without any air and the syringe is connected to the inlet of the micro-model using one-sixteenth inch tubing. The Rhodamine dye solution is injected through the micro-model using syringe pump at a constant volumetric flow of 10 μL/min to displace de-ionized water from the micro-model. Once the micro-model is completely filled with Rhodamine dye solution, dye injection process is continued for 30 minutes. Thus, a continuous flow of Rhodamine solution delivers homogeneous solution of Rhodamine dye inside the micro-model in order to avoid local dye gradient. Figure 3.3a shows a 2.5D PMMA brightfield image flooded with de-ionized water whereas Figure 3.3b shows a 2.5D PMMA micro-model flooded with the Rhodamine dye solution.

3.5 Experimental Fluid

A fluorescent microsphere suspended in de-ionized water with trace amounts of surfactant and preservative is used in our experiment. Fluorescent microspheres were supplied by Thermo Fisher Scientific. Trace amounts of surfactant and preventive used in the solutions helps to inhibit aggregation and stability of those nano-particles in the fluid solution. Initially, the fluorescent microsphere is packed with suspended aqueous solution at 1 % solids

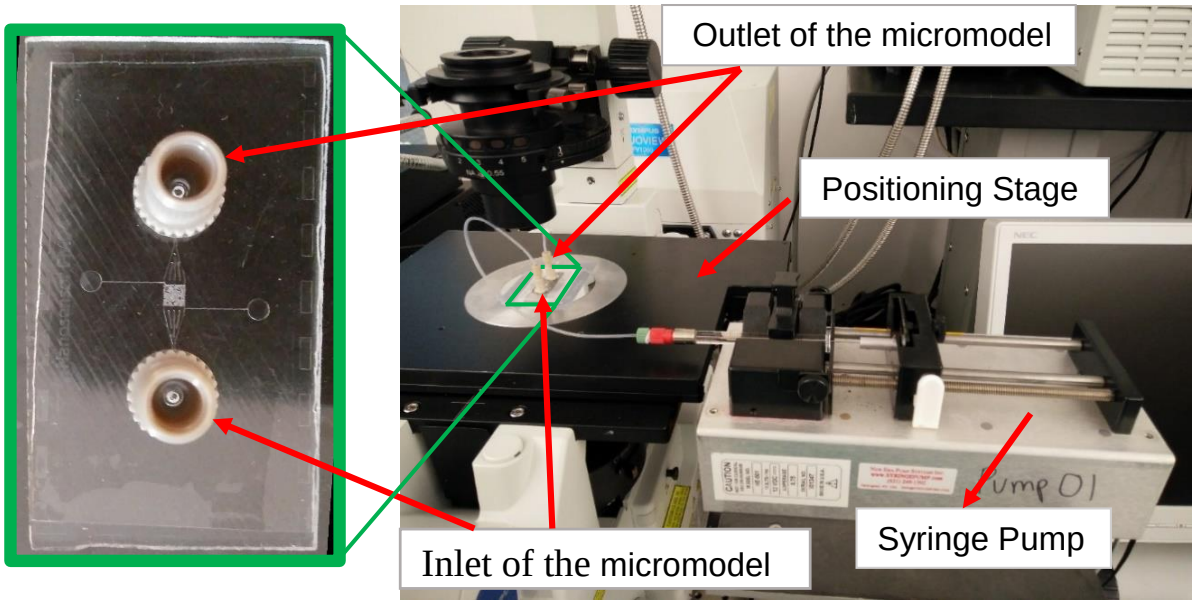

Figure 3.4: Experimental setup of the confocal microscope for particle flow experiments in PMMA micro-model. Left figure shows complete rock based micro-model illustrating inlet and outlet ports.

by weight and further diluted in deionized water according to the experimental requirement.

3.6 Nano-Particles

Suspended nano-particles are made of polystyrene and dyed with red and green fluorescent dyes. Polystyrene nano-particles are dyed using a polymer matrix instead of surface dye in order to preserve the dye for a longer time. Polystyrene nano-particles used in this project vary from 51 nm to 860 nm (usually called 900 nm). Those nano-particles supplied by Thermos Fisher Scientific, are electrically neutral and neutrally buoyant. They have refractive index of 1.59 and density of 1.06 gm/cm^3.

3.7 Syringe Pump

The syringe pump is the driving source of fluid into the micro-model. NE 501 and NE 502 series syringe pump, supplied by New Era Pump System (www.syringepump.com), were used in our experiment. All the syringe pumps used in the experiment are fully computer controllable. Motor stall detection was installed in the syringe pump system

in order to avoid any breakage of the system. The NE 501 has a maximum operation speed of 510.05 mm/min and a minimum speed of 0.4205 mm/hr whereas NE 502 has a maximum operational speed of 22.447 mm/min and a minimum speed of $8.408e^{-3}$ mm/hr. The NE 501 has a maximum pumping rate of 1699 ml/hr whereas the NE 502 has a maximum pumping rate of 74.76 ml/hr using B-D 60 cc syringe. Similarly, the NE 501 has minimum pumping rate of 0.73 μl/hr whereas the NE 502 has a minimum pumping rate of 14.59 nL/hr using a B-D 1 cc syringe. Figure 3.4 shows the laboratory set up for particle injection experiment where the inlet port is connected to syringe and outlet is connected to open container via one-sixteenth inch tube. The nano-particle fluid is injected through inlet port using syringe pump as shown in Figure 3.4. A confocal microscope is used to acquire images of nano-particles flowing through the micro-model at various depths. Once all the images of nano-particles were acquired, post image processing was performed to quantify nano-particle transports in the micro-model.

Chapter 4
In-Situ Geometry Extraction

The objective of this chapter is to describe and present the inexpensive, non-destructive and reliable novel method of in-situ geometry extraction of the complex 2.5D micro-model. In this chapter, we discuss detailed procedures to extract depth to pixel intensity calibration, which provides a third dimension along with two dimensional fluorescence image of in-situ micro-model. Thus a 3D in-situ geometry can be reconstructed based on Fluorescence Image of a 2.5D PMMA micro-model.

4.1 Experimental Setup and Procedure

Prior to the dye experiment, the 2.5D micro-model is bonded with 250 μm PMMA film and all nanoports are installed in the micro-model using strong and fast acting cyanoacrylate adhesive (also known as Super Glue). During installation of the nanoports in the micro-model, a thin circular rubber ring is used in order to avoid contact between liquid and adhesive. Once inlet and outlet nanoports are installed in the micro-model, the glue is allowed to cure for a day in order to optimize bonding between the PMMA micro-model and nanoports. After completion of the air bubbles removal process (as stated in chapter 3), 100 ppm of laser grade 99+ % pure Rhodamine B dye solution is injected into the 2.5D micro-model at a constant volumetric flow rate of 10 μL/min using a syringe pump and a 5 mL syringe. Once the Rhodamine B dye solution completely displaced the de-ionized water, the dye injection process continued for half an hour in order to maintain homogeneous solution in the micro-model. Once the dye is homogeneously disseminated all over the micro-model, a monochromatic laser beam is passed through the micro-model to illuminate the fluorescent dye. The 543 nm monochromatic laser wavelength light excites fluorescent dye and emitted 612 nm wavelength red light from the dye is captured by the photo-multiplier tube. Figure 4.1a shows a bright field image of the micro-model filled with de-ionized water and fluorescence image of the micro-model filled with fluorescence dye.

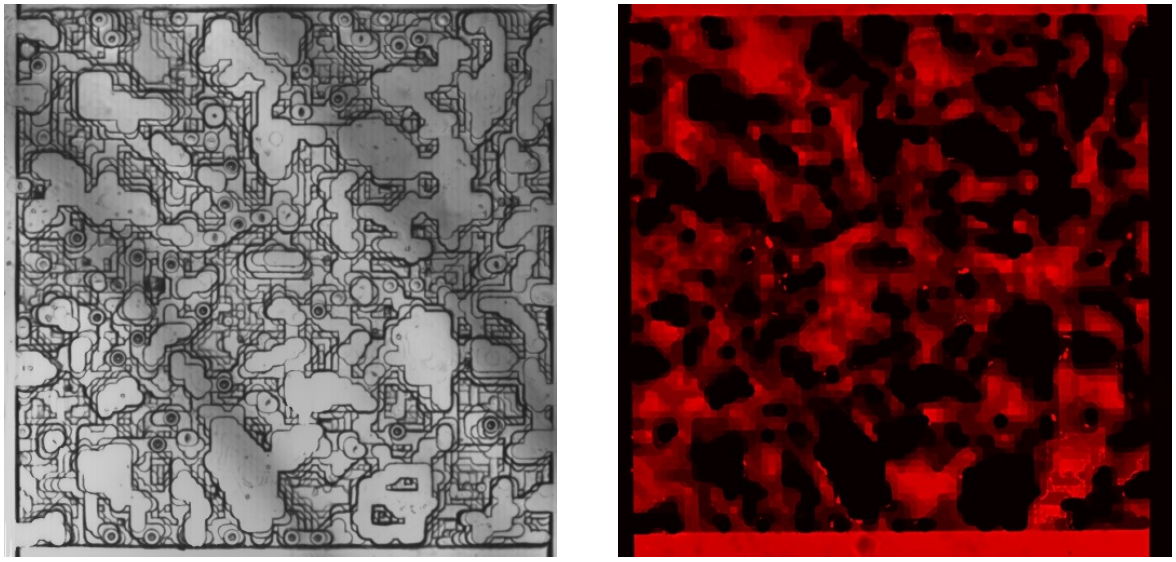

(a) (b)

Figure 4.1: Low (25 μm) resolution PMMA (a) filled with de-ionized water after air removal process (b) flooded with rhodamine dye solution.

4.2 Calibrated Depth

Five different locations were chosen to measure depth using a high Numerical Aperture (NA) water immersion objective lens (20 x WI 0.95 NA). Each region of interest has a different shape and size along with distinguishable depth. Each ROI has at most thirteen different depth layers. Depth of each structure was measured using a confocal microscope. A detail description of depth measurement of one of the ROIs from 2.5D micro-model is presented in this section.

Region of interest I is a portion of Boise rock-based micro-model, and it is one of the fast moving throats of the system. The structure indicated by letter A shown in Figure 4.2a indicates one of the 13^{th} layer structure of the micro-model. The average depth was measured as 9.57 microns with reference to inner of the flat observation window. Similarly, letter B shown in Figure 4.2b represents one of the 12^{th} layer structures of the micro-model and the average depth is 20.20 microns. Letter C shown in Figure 4.2c indicates one of the 11^{th} layer structures of the micro-model and the average depth of the structure indictated by letter C is 30.60 microns. Similarly, average depth of the structures

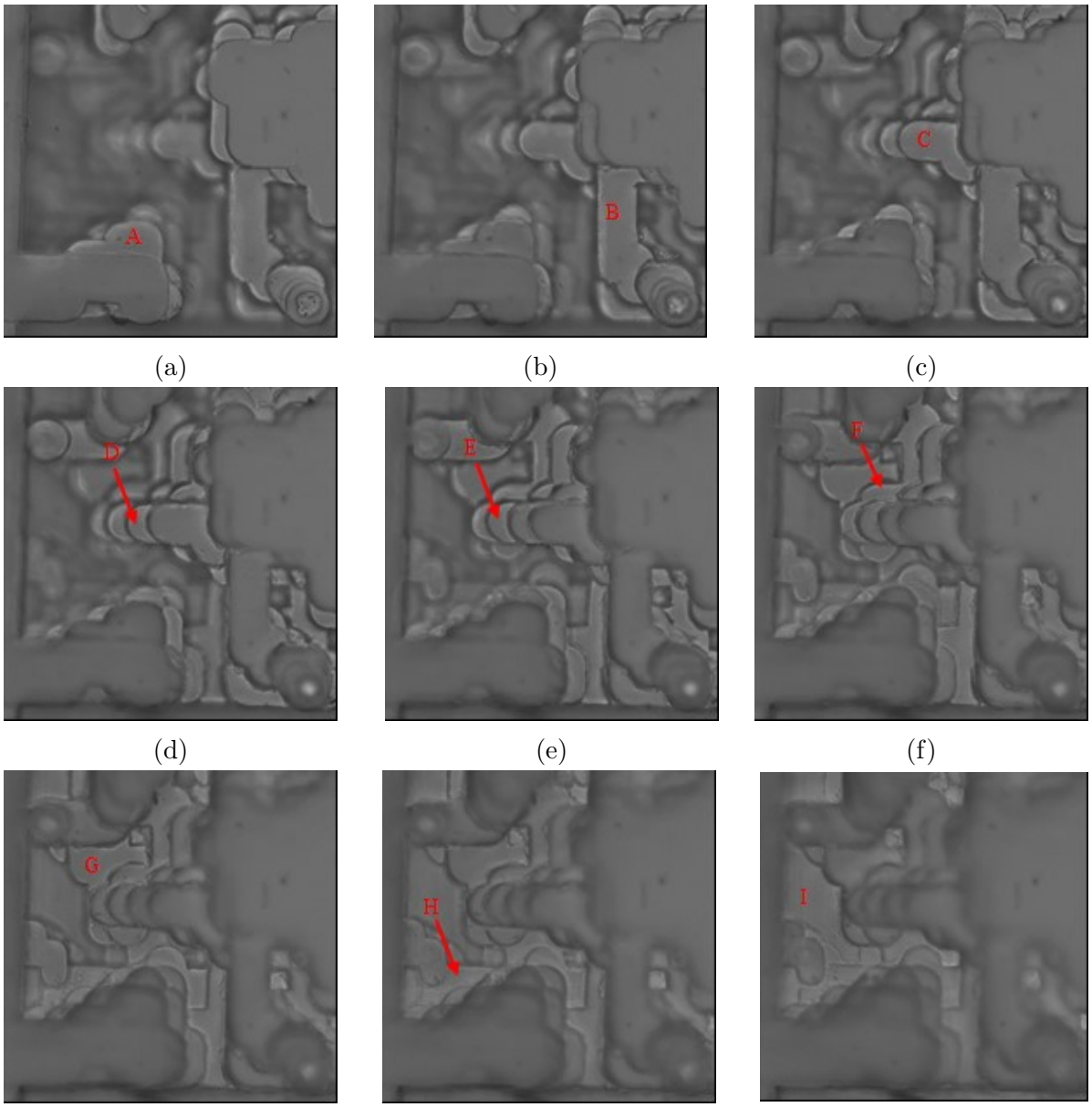

(a) (b) (c)

(d) (e) (f)

(g) (h) (i)

Figure 4.2: Local depth measurement of various structures of region of interest I of the micro-model. Structures indicated by alphabatical letters measure from inner wall of the observation window have an average depth of (a) 9.57 μm,(b) 20.20 μm, (c) 30.60 μm, (d) 39.26 μm, (e) 49.58 μm, (f) 60.65 μm, (g) 69.02 μm, (h) 77.52 μm, and (i) 91.23 μm.

indicated by letters D, E, F, G, H, and I shown in Figure 4.2d - 4.2i were mesured as 39.26 μm, 49.58 μm, 60.65 μm, 69.02 μm, 77.52 μm, and 91.23 μm respectively.

4.3 Image Analysis

Fluorescence image of the Boise rock-based micro-model flooded with fluorescence dye was captured using a low Numerical Aperture (NA) objective lens by confocal microscope and recorded as digital image. Each digital image acquired by the photo multiplier tube is analyzed using MATLAB. Resolution of an image depends on the acquisition conditions such as objective lens, lateral optical zoom, sensitivity of the photo multiplier tube (PMT) and laser power of the confocal microscope. Fluorescence image, recorded as a true image in confocal system, consists of three different color channels: red, blue and green. The red channel of the 24 bit true image registered fluorescence signal emitted from fluorophores (rhodamine dye) whereas other channels registered as zero signal. In the digital image, pixel intensity indicates illuminated light intensity of the fluorophore, once fluorosphore is exited with exicitation wavelength monochromatic light. The Red channel consists of 8 bits of fluorescence information and it is segmented from the true color image (24 bit image) for further pixel intensity analysis.

Based on the calibration depth measurement of numerous structures of 2.5D micro-models, fluorescence intensities from the respective regions are extracted and analyzed. Figure 4.3 illustrates the schematic process of correlating fluorescence intensity with measured structural depth of the micro-model. Letter "A" shown in the image at top left corner of Figure 4.3 indicates one of the local depth measured locations of the micro-model. The square with a red border in the right top image of Figure 4.3 indicates measured depth location represented by letter "A" in fluorescence image of micro-model, and digital number in Figure 4.3 represents fluorescence intensity of the square box of location "A". Similarly, fluorescence intensities of all other measurements at their respective locations were extracted and analyzed. Dim bright color in the fluorescence image of the micro-model represents shallow depth whereas bright color indicates deeper channel. Pixel intensity of

fluorescence dye at a specific depth varies depending on the roughness of the surface of the structure. The higher the surface roughness, greater the fluctuation in pixel intensity. Therefore, average pixel intensity is assigned after averaging a minimum of thirty six pixels for each calibrated depth location.

4.4 Correlation between Calibrated Depth and Pixel Intensity

The fluorescence image was fully analyzed, and all pixel intensities of measured depths of the micro-model were extracted. The pixel intensity versus calibrated depth is shown in Figure 4.4. In Figure 4.4, the Y-axis represents fluorescence intensity emitted by fluorescence dye and thin PMMA coversheet measured in pixel intensity whereas their respective calibrated depths are represented in the X-axis. As depth increases, pixel intensity increases in similar form. Figure 4.4 shows fluorescence intensity is directly proportional to the measured depth of the structure of the micro-model. Because of fluorescence signal emitted from PMMA thin coversheet, the measured pixel intensity is higher than the actual fluorescence intensity emitted by fluorescence dye. Fluorescence signal emitted from the thin PMMA coverslip range from seven to nine pixel intensity, with an average of approximately eight pixel intensity. A linear correlation model with zero y intercept was used to fit data. Figure 4.4 illustrates that a linear relationship exists between pixel intensity and calibrated depth with more than 98% correlation factor and repeatability. Figure 4.5 represents pixel intensity to depth calibration after eliminating fluorescence signal from the PMMA coversheet which is also linear with more than 99% correlation and repeatability. Based on the relationship between fluorescence intensity and calibrated depth, one can predict the depth of any location in the micro-model with a maximum axial resolution of 0.55 microns per pixel. The calibration coefficient was used to quantify depth over the entire micro-model domain and acts as the third dimension in the 2D image.

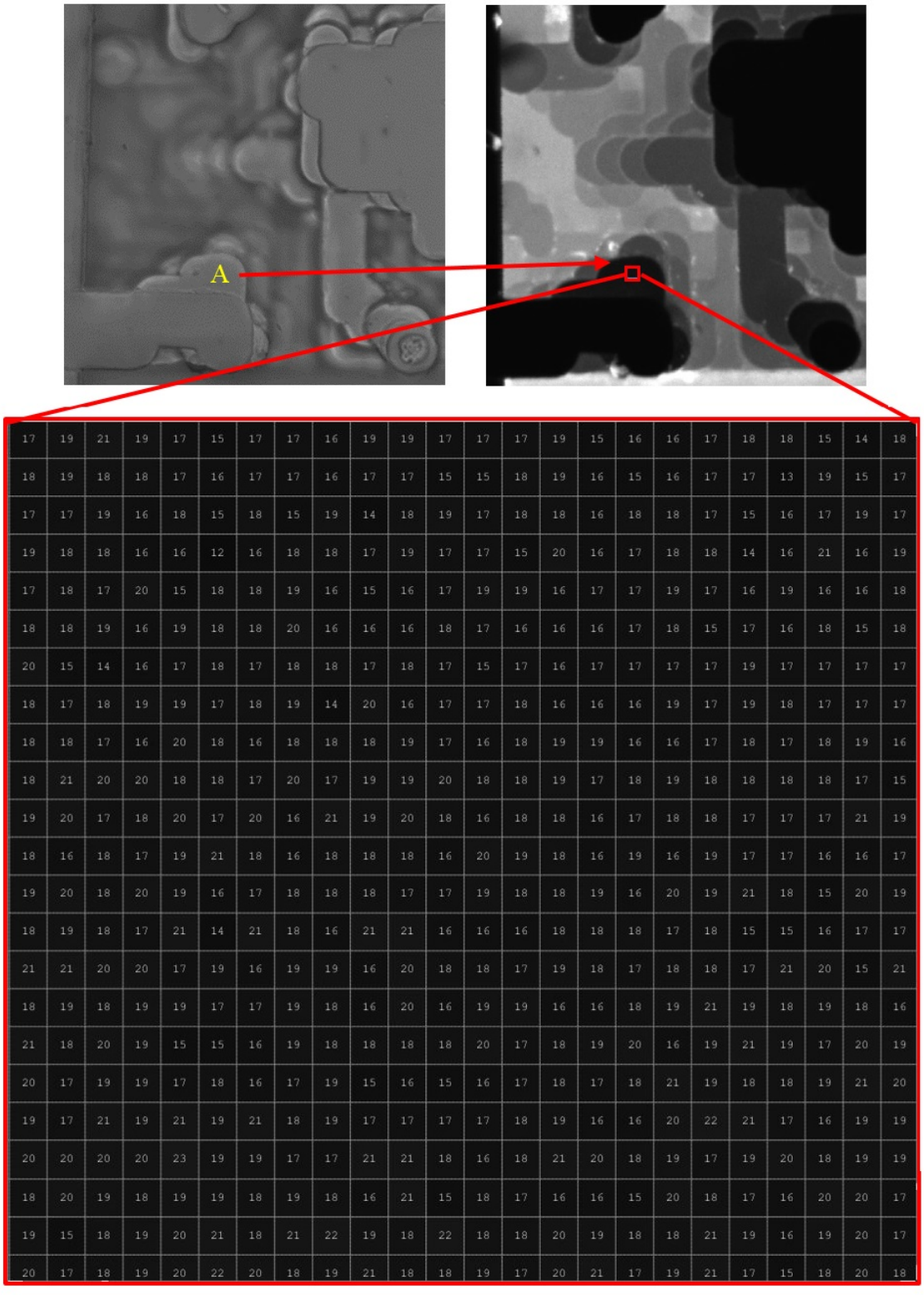

Figure 4.3: Calibration depth measurements. (a) shows microscope image of a focused location A. The calibrated depth is measured by using confocal microscope with high numerical aperture objective lens (20 x 0.95 WI). (b) shows fluorescence signal of a portion of location A. (c) illustrates detail fluorescence intensity of the fluorescence dye at location shown in (b).

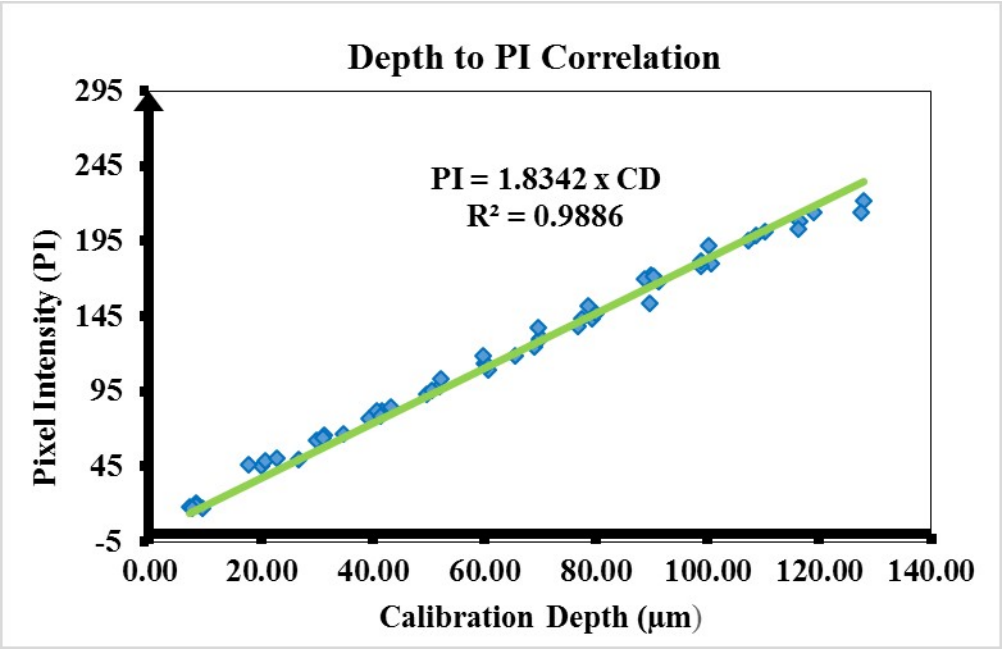

Figure 4.4: Depth Correlation between Pixel Intensity and Calibrated Depth before eliminating Fluorescence signal illuminating from PMMA coverslip.

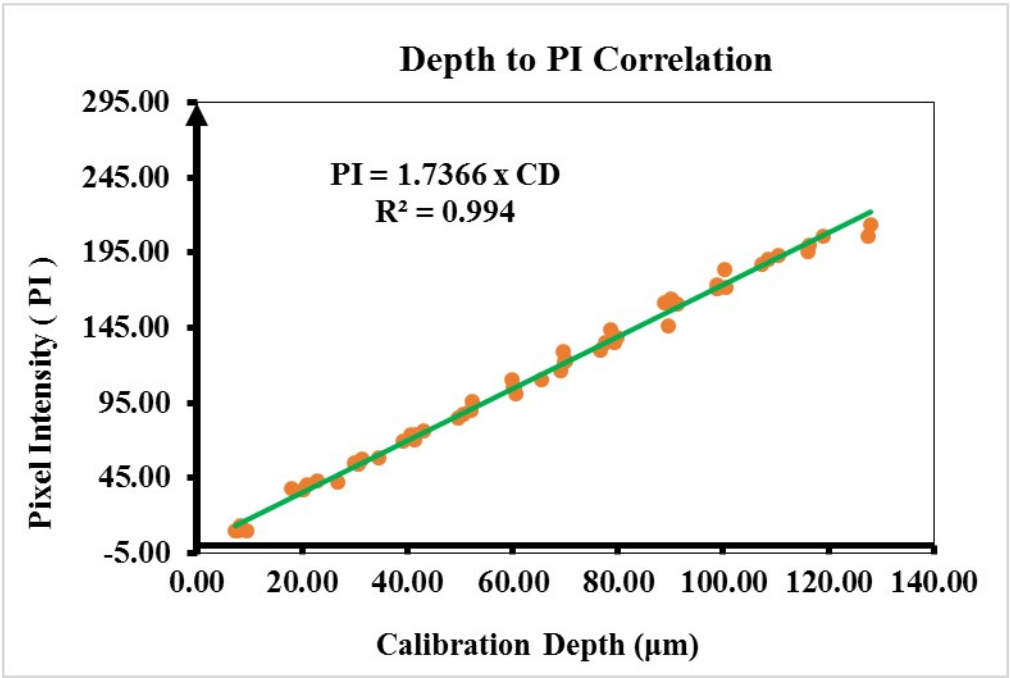

Figure 4.5: Depth Correlation between Pixel Intensity and Calibrated Depth after eliminating Fluorescence signal illuminating from PMMA coverslip.

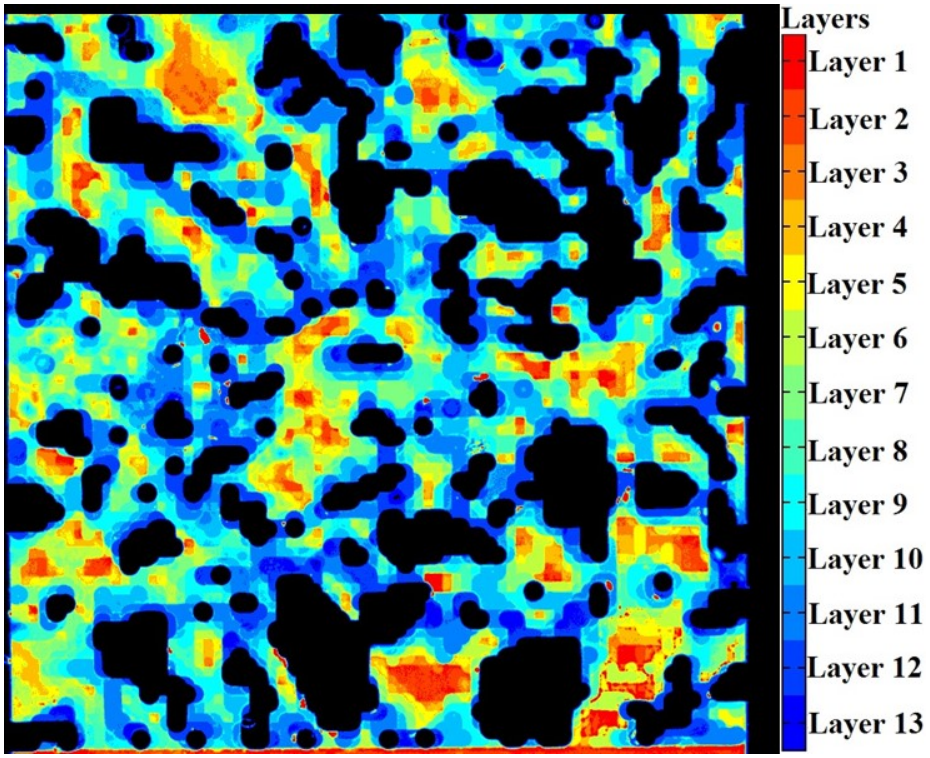

Figure 4.6: Depth Colormap generated from Fluorescence image and calibrated depth to pixel intensity correlation for Micro-Model.

4.5 Image Segmentation

Based on the linear relationship between Pixel Intensity and Calibration depth, fluorescence image is segmented into 5 micron-resolution depth images in order to compare with X-ray CT scan as well as initial CAD drawing based on the fourteen different flow parameters. Segmented images are further post-processed to reduce random noise by eliminating less than 50% of the structural components in the images and compared with the CAD drawing. Individual segmented images are compared with x-μCT scan images obtained by Godfrey Mills (Dr. Wilson Research Group). Figures in appendix A show segmented images of fluorescence images at an interval depth of 5 micron, before and after filter was applied and compared with x-μCT scan images. Figures in appendix A show a comparison of geometry extraction of rock-based micro-model using two different techniques. μCT scan has maximum resolution of 2.5 μm as well as approximately 6 μm depth of field whereas the fluorescence based technique has 0.55 μm axial depth resolution. Fluorescence

based technique is an inexpensive as well as non-destructive method of in-situ geometry extraction of 2.5D micro-model compared to X-μCT scan. The main disadvantage of using fluorescence-based technique is that one of the observation walls must be transparent for visualization in order to extract 3D geometry of the 2.5D micro-model.

4.6 Full-scale Image Reconstruction

Reconstruction of whole 3D geometry of the 2.5D micro-model is performed to replicate the in-situ experimental micro-model device to perform full-scale fluidic flow simulation. Prior to the construction of the full image of a micro-model, each image and position of the image acquired in the system must be calibrated with the physical micro-model. Once, the position of the images are calibrated, construction of segmented images of the micro-model flooded with Rhodamine dye is performed. Full micro-model device was imaged into five segments with appropriate amount of overlapping regions in the system. Once those images' positions are noted including edge matching between images, construction of the full-scale micro-model image is completed. Figure 4.7 shows a schematic procedure of constructing a full-scale micro-model image from segmented images of the micro-model.

4.7 CAD Geometry

A full-scale fluorescence image provides two dimensional geometry while linear calibration facilitates third dimension of in-situ Boise rock-based micro-model. 3D structures of fluorescence image of the 2.5D micro-model are extracted, and converted into stereolithography or "stl " files using a triangulation method. Initially, Guillaume Bidan developed in-house code for "stl" conversion from a 3D fluorescence image using MATLAB. Later, it was modified and redeveloped. Hence, three dimensional geometry is created from a single full-scale fluorescence-based image. Figure 4.8 shows a full-scale three dimensional in-situ computer-aided-design(CAD) of the 2.5D micro-model generated from a full-scale fluorescence image.

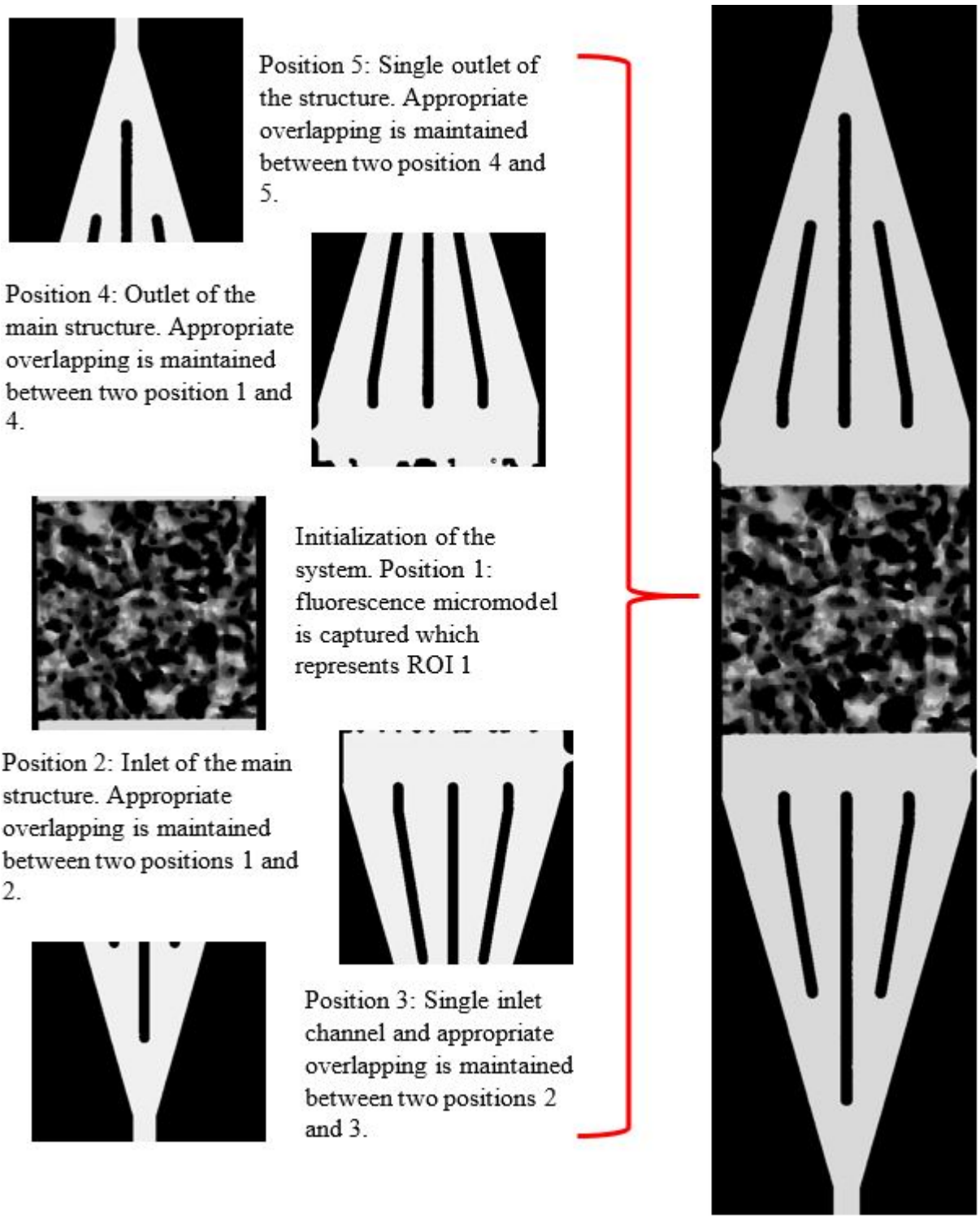

Figure 4.7: Schematic procedure of reconstructing full-scale micro-model from segmented images captured by the laser scanning confocal microscope.

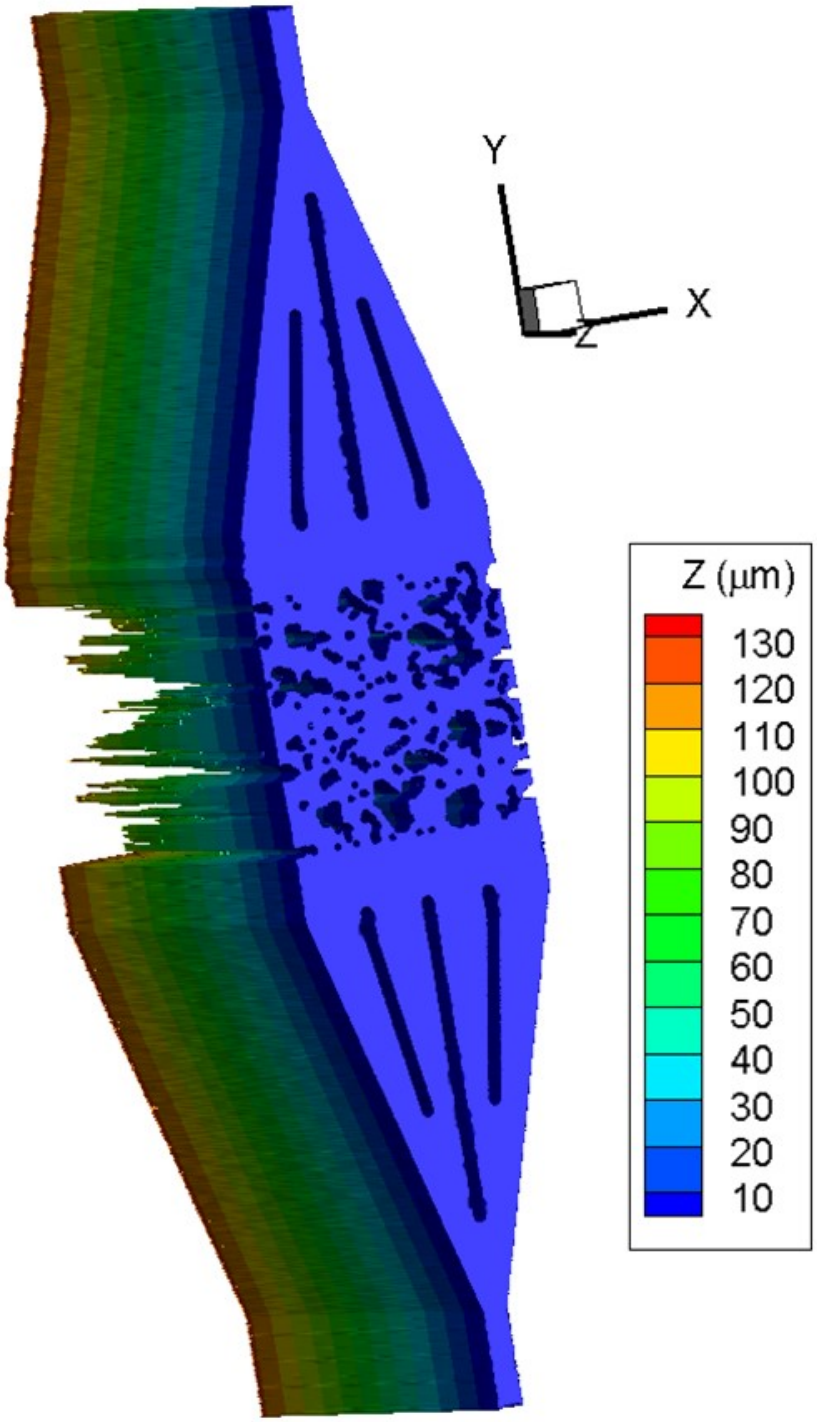

Figure 4.8: In-situ 3D computer aid design (CAD) of 2.5D micro-model generated using full-scale Fluorescence Micro-model image and depth-PI correlation.

4.8 Conclusion

In this chapter, we have introduced and investigated a novel depth measurement technique along with 3D in-situ geometry extraction from the fluorescence image with sub-microns preciseness in the lateral as well as axial direction. The novel technique presented in this chapter is a non-destructive, economical, convenient and precise technique of reconstructing experimental devices for computational flow simulation. This technique has numerous advantages over μCT scanning; considering μCT scanning has comparatively low-resolution and higher depth of field, and μCT is expensive whereas fluorescence-based techinque is an inexpensive and convenient technique.

Reconstruction of in-situ 3D geometry depends on the microscope configurations ; *i.e.* laser power, objective lens, sensitivity of PMT, and pinhole. The experimental results presented in this chapter illustrated that confocal fluorescence microscopy can be used in precise sub-micron measurement of microfluidics devices. In summary,

1. Shallow depth emits lower fluorescence signals while the deepest channel emits higher fluorescence signals.

2. The fluorescence intensity emitted from a micro-model is linearly proportional to the depth of the micro-model

3. Using confocal fluorescence microscopy, one can precisely measure sub-micron depth along with sub-micron resolution in lateral direction of any 2.5D (one coverslip should be flat for visualization) micro-model.

4. Fluorescence-based depth measurement is an inexpensive, convenient, as well as non-destructive method of depth measurement of 2.5D micro-model/micro-device.

5. Three dimensional as experimented micro-model is created with sub-micron accuracy for further computation fluid analysis in the experimented micro-model.

Chapter 5
Image Patching Algorithm

The main objective of this chapter is to present a novel approach of measurement technique and image processing for particle image velocimetry to synthesize a large domain from sequential discretized sub-regions with precise measurement and maintaining statistical integrity of the experimental data. Instead of segmenting a large micro-model into sub-regions and affixing the results together, the current methodology we propose in this chapter is a more accurate and reliable method of synthesizing a large domain from discretized sub-regions to calculate the velocity field and ensure consistent grid size at overlapping regions. This methodology is more robust, as it preserves all the information from sub-regions of the micro-model and is more efficient to synthesis large domain velocity fields.

5.1 Methodology

The proposed methodology consists of two main preprocessing steps before particle image velocimetry is performed. In the first step, a 2D image acquisition is performed with accurate positioning of sub-regions in the micro-model. Images from multiple sub-regions are registered and a universal domain or region is created from multiple sub-regions of interest. Based on the location of each region of interest (ROI), acquired images are patched back to the universal domain. All other regions besides the patch region of interest in the universal domain is a "dark region" or zero signal region.

5.2 Image Acquisition

Image acquisition plays a significant role in image alignment of acquired images to produce an extended field of view in the micro-model. Figure 5.1 shows a schematic method of image acquisition during fluidic experiment to create extended field of view.

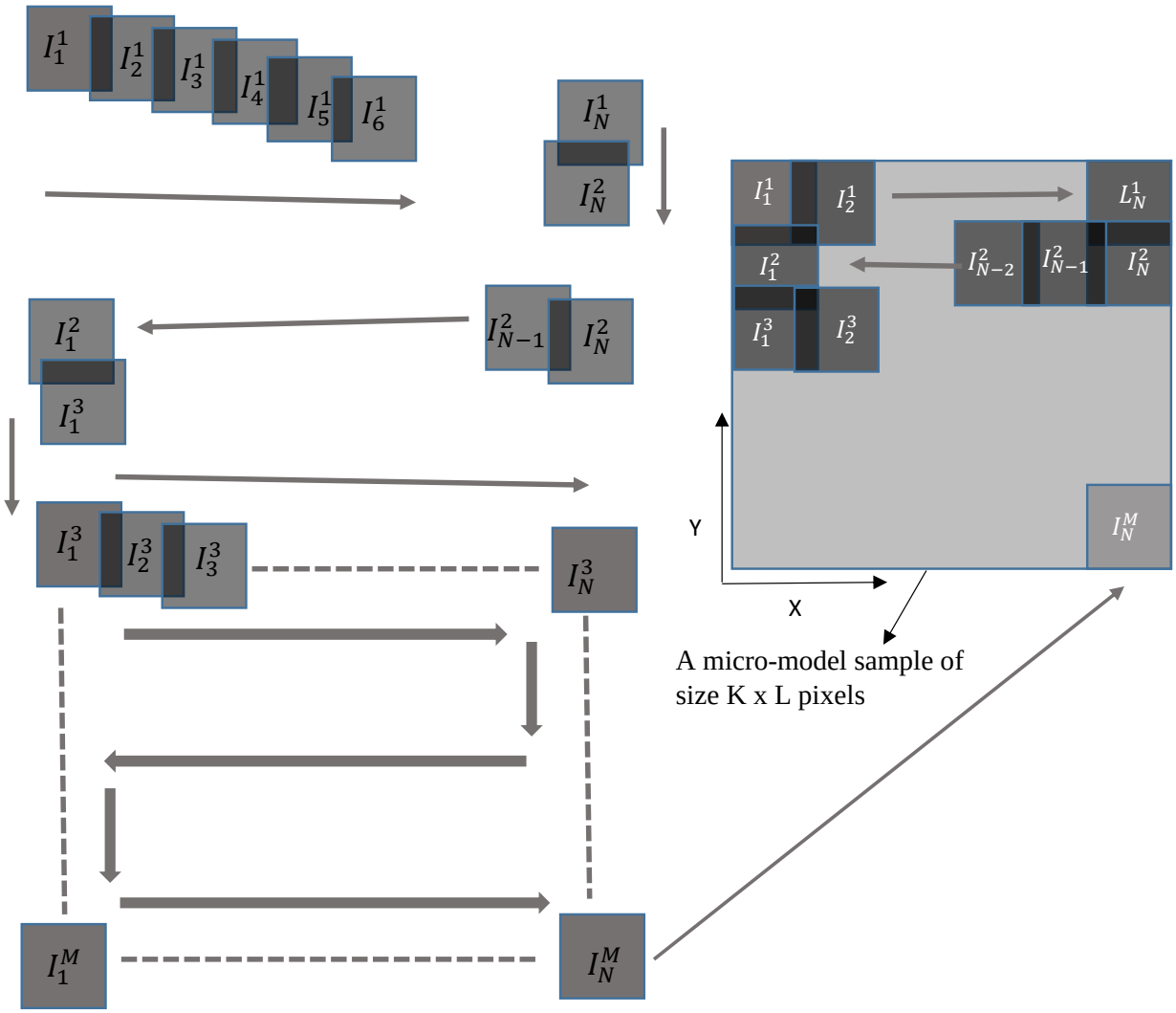

Figure 5.1: Schematic stretch showing the procedure of image acquisition of an entire micro-model.

Position Initialization

This is the first step of image acquisition of sub-region in a micro-model which defines the initial position of acquired images based on the location of ROIs in the micro-model. Image I_1^1 as shown in Figure 5.1 represents the image of a ROI of the micro-model and acts as a reference for all other images in the micro-model. The size of image "I" is optimized based on the capability of the confocal microscope to capture nano-particles images in order to perform particle image velocimetry as well as quantification of particle concentration. Overlapping regions between two sequential locations (ROIs) aids in alignment of two images from two different sequential ROIs and acts as a continuum bridge between vector fields created by two independent pairs of images from two sequential ROIs during particle image velocimetry.

Sequential Image Acquisition along +X Direction

To capture images along the +X direction in the micro-model as shown in Figure 5.1 at a fixed vertical location Y_1, the camera is shifted by ΔX horizontal distance from the original position to record images represented as "I_2^1" of region of interest 2 of same row in the micro-model. Hence, all the particle information of region of interest 2 of row 1 is recorded in image "I_2^1". Similarly, the camera is again shifted by another ΔX horizontal distance from the previous location to record image of region of interest 3 with an overlapping region "O_h" . This process is continued until images "I_N^1" are recorded for ROI N of the first row of the micro-model.

Shifting in Vertical Position I

After successful image acquisition of the N^{th} column of the first row, the camera is shifted $-\Delta$Y direction from previous location to shift from Y_1 to Y_2 in the micro-model with an overlapping region "O_v" as shown in Figure 5.1. This phenomenon shifts the acquisition of images from one row to another row.

Sequential Image Acquisition along −X Direction

The camera is shifted $-\Delta$X horizontal distance in the X direction from location I_N^2 to I_{N-1}^2 in the micro-model. I_N^2 represents the Nth ROI of row 2 and I_{N-1}^2 represents (N-1)th ROI of row 2. Once all the information of location (N-1)th ROI of row 2 is recorded in the image I_{N-1}^2, the camera is again shifted by $-\Delta$X horizontal direction from the previous location to record images of next location. This process is repeated until I_1^2 location of the micro-model is recorded.

Shifting in Vertical Position 2

After recording particles information at location I_1^2 the camera is shifted $-\Delta$Y from previous location in order to shift image acquisition from one row to another row. The above processes are repeated until all the information of ROI I_N^M is recorded from the micro-model.

5.3 Image Processing

Prior to particle image velocimetry, image processing includes two major steps: creation of a universal domain and transformation of the particle information from individual discretized regions of interest into the universal domain.

To illustrate the concept of algorithm 5.1, I have sketched four regions of interest which I assumed are captured by the confocal microscope as shown in Figure 5.2. Suppose A represents a set of all the pixel information of location A in the micro-model. Similarly B, C, and D also represent all digital images of their respective locations within the micro-model. The universal image is also known as universal domain, which is created by union of all sequential images recorded based on the location of sub-domains in the micro-model. Vertices abcd represent image of location A and a'b'c'd' represent projection of region of interest A onto the universal image based on the location during image acquisition of the micro-model. Similarly, efgh represent vertices of region of interest B and e'f'g'h' corresponds vertices of region of interest B in the universal domain. Based on the locations of all the sub-domains of the micro-model, all the acquired images were superimposed and

the area of the universal domain is determined by equations 5.1 and 5.2. A universal domain provides a full representation of the observation location which consists of several region of interest, to be studied for all the fluidic as well as nano-material characterization in the micro-model.

Algorithm 5.1 Creation of Universal Domain(Image)

We have considered a simple rectangular case to create an extended field of view in the micro-model. Consider a 2D sequential set of images I=$\{I_1^1, I_2^1, I_3^1, \cdots I_N^M\}$, a rectangular universal image is created based on the position of the image acquired by the confocal system. Each image of size R x S is recorded by the confocal system from each ROI of the micro-model. $O_h\{(i,j) \mid (i,j)\epsilon\mathbb{Z}, i \leq a, j \leq b\}$ represents a horizontally overlapped area between two horizontally overlapped images while $O_v\{(i,j) \mid (i,j)\epsilon\mathbb{Z}, i \leq c, j \leq d\}$ represents a vertically overlapped area. The maximum size of the horizontally overlapped two regions is given by a x b where a is the length and b is the width of the overlap region. Similarly, the maximum size of the vertically overlapped two regions is given by c x d where c is the length and d is the width of the overlap region. The final size (L x W) of the universal image is given by:

$$L = N \times R - (N-1) \times a \tag{5.1}$$

$$W = M \times S - (M-1) \times d \tag{5.2}$$

where L,N,R,W,M,S,a,d are scalar quantities. N is the total number of images acquired in horizontal direction whereas M is the total number of images acquired in the vertical direction by the confocal system in order to reproduce an extended field of view. Once, the final dimension of the universal image is computed, the universal image is created with zero signal.

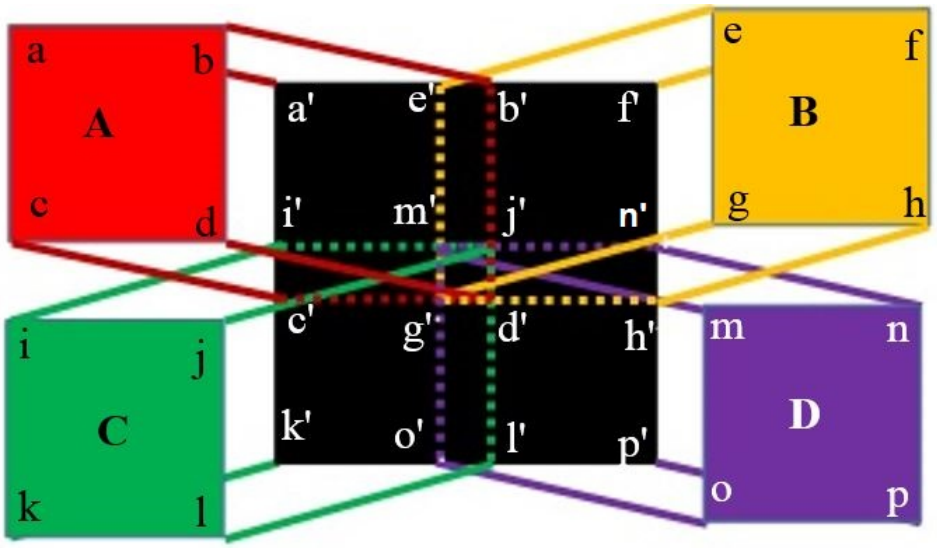

Figure 5.2: Creation of Universal Domain showing the projection of four different Region of Interests (ROIs).

Algorithm 5.2 Individual Image Registration in Universal Domain

For individual image registration into the universal image, we build a method of patching an individual image into the universal image by creating a position function. A position function is generated for each individual sub-domain of the micro-model based on the location of the image in the micro-model. All individual images are passed through the position function to create an extended field of view for each sub-domain. The position function takes individual images as an input and transforms all particle information into the universal domain along with the location of an individual image in the extended field of view. For each individual image, all the particle information is recorded in pixels in three different channels *i.e.* red , green or blue. In the case of gray scale, all the particle information is recorded as a gray scale value. A position function preserves location as well as the particle information of the acquired image into the universal image. Because of zero signal in the universal image, there is no alteration on particle information during individual image transformation into universal image. Hence, this methodology preserves all the particle information of the individual image in the universal image. To illustrate Figure 5.3 shows all the particle information of regions of interest A and B are transferred into universal image using a position function.

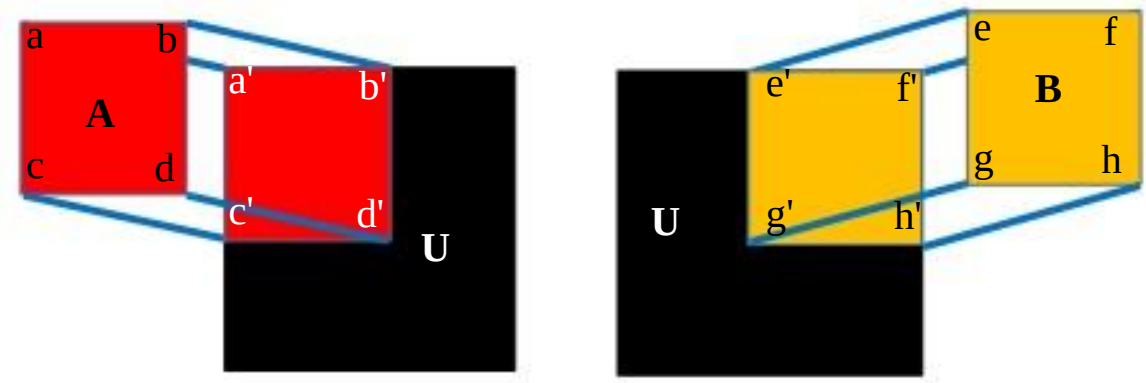

Figure 5.3: Transformation of particle information from Region of Interest A and B into Universal Image "U" respectively.

Algorithm 5.1 and 5.2 assemble an infinite number of regions of interest (ROIs) in theory to an create an extended field of view (also known as observation location) with continuum grids in any experiment where extended field of view is required.

5.4 Particle Image Velocimetry (PIV) Processing

Each raw image is divided into small interrogation windows for PIV analysis. Before PIV analysis, a mask is created in such a way that it masks only the non-signal region of the raw images. Masking the non-signal regions during the PIV process reduces computation workload significantly. The non-masked region is processed using a cross-correlation algorithm to determine the velocity field. The uniform grid size enables us to average all the velocity vectors at the same node at overlapping regions as well as attain a seamless continuous velocity field in the extend field of view. The extended field of view contains nano-particle transport information of an observation location, which consists of numerous discretized regions of interest depending on image acquisition.

5.5 Experiment and Results

Image Acquisition

A rock-based PMMA micro-model is used for investigating the velocity field in an extended field of view. Prior to particle experiment, a series of air removal processes take

place in order to remove air trapped inside the micro-model by wetting the inner surface of the PMMA micro-model with diluted ethanol solution. Once gas was removed from the PMMA micro-model, the particle experiment was performed at a constant volumetric flow rate of 100 nL per minute with deionized water seeded with 860 nm fluorescence particles to investigate particle transport in 264.96 x 264.96 μm^2 observation location. A water immersion objective lens with 2 mm working distance with 20X magnification and a numerical aperture of 0.95 was used to visualize particles flowing inside the micro-model. Monochromatic light of wavelength 543 nm produced by HeNe laser was used to illuminate fluorescence particles. The illuminated light was captured by a highly sensitive PMT and transferred to a storage device. To create an extended field of view, nine different image fields were acquired to cover a 264.96 x 264.96 μm^2 field of view as shown in Figure 5.4. Each image consists of 256 x 256 pixels with 3 channels of 8 bits gray scale to cover 105.984 x 105.984 μm^2 area of a micro-model. For each region of interest of a micro-model, a total of 450 independent images were acquired. Initially, nano-particles flowing in 105.984 x 105.984 μm^2 were recorded in image "I" and image "I" acted as a reference position for all other image acquisitions. A maximum horizontal overlapping area of 26.496 x 105.984 μm^2 ($\approx$25 % of total area of an image area) was considered and the stage was shifted 79.488 μm in the horizontal direction to capture all the information of location II. Similarly, the stage was again shifted by 79.488 μm horizontally to capture flowing nano-particles at location III. To capture image at location IV the stage was shifted by -79.488 μm in vertical direction from previous location III. In a similar manner, nine different image fields were captured to the extend field of view to 264.96 x 264.96 μm^2. As shown in Figure 5.4, a maximum horizontal overlapping area of 26.496 μm x 105.984 μm between I and II, II and III, IV and V, V and VI, VII and VIII, VIII and IX was maintained. Similarly, a maximum vertical overlapping area of 105.984 x 26.496 μm^2 was maintained between I and VI, II and V, III and IV, IV and IX, V and VIII, VI and VII.

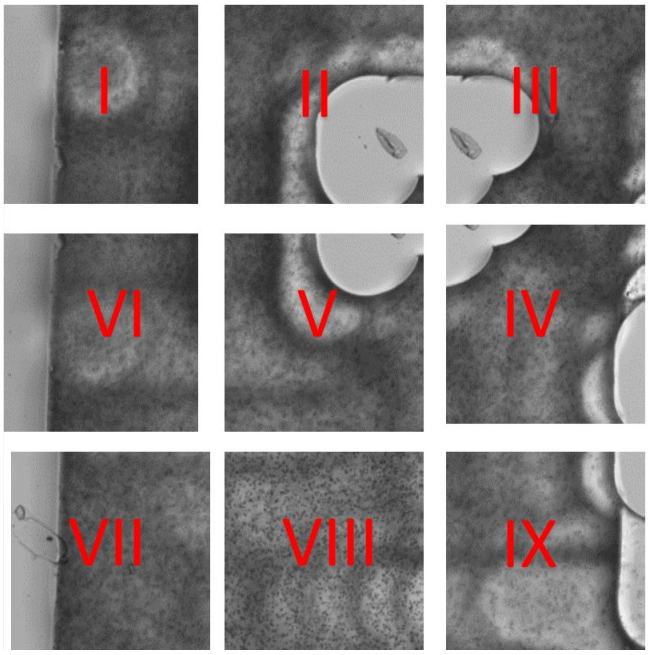

(a)

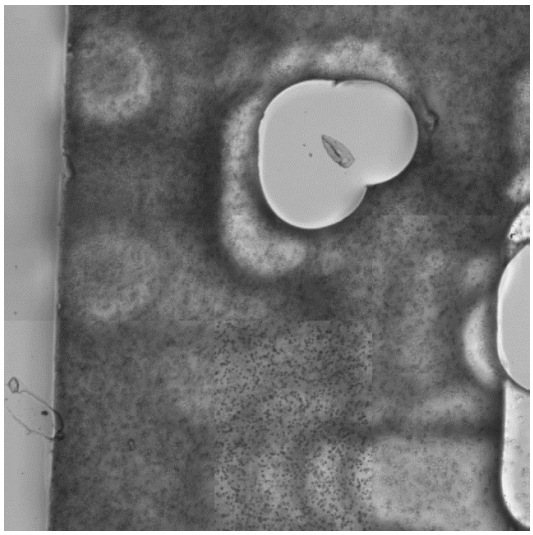

(b)

Figure 5.4: Flow Experiment in Boise Rock based Micro-model showing (a) nine different discretized region of interest (ROIs) captured by confocal microscope and (b) assembly of nine different ROIs to create a single observation location (Extended Field of View).

Alignment Accuracy

As a result, nine different image fields were successfully aligned to reconstruct a 264.96 x 264.96 μm^2 image. The reconstructed image of the observation location consists all the information of each individual domain. Reconstructing a brightfield image provides final dimension of the observation location and acts as verification tool to verify the dimension of the universal image. Based on the reconstruction of nine different image fields, the measurement of a universal image is 640 x 640 pixels in the digital dimension which corresponds to 264.96 x 264.96 μm^2. Figure 5.4a shows consecutive bright field images captured by the confocal microscope with 25 % overlapping with each other. Qualitatively, Figure 5.4b evaluates assembly of nine different images from nine different locations, where the image indicates good alignment as well as transformation of all individual image information into the reconstructed brightfield image. The maximum error in alignment is less than $\pm$ 0.207 μm, corresponding to less than 1 percent of the individual image. This error is due to

sub-pixel calibration between physical and digital dimensions. The error due to alignment is small and has minimum influence in PIV. Hence, the error can be neglected.

Patching Data from Individual Image in Universal Domain

First of all, the universal image is divided into 640 x 640 arrays of pixels which corresponds to the dimension of the nine assembled ROIs. Before patching an individual image, each universal image is considered as a zero signal image(*i.e.* black image). Figure 5.5a shows consecutive raw images acquired by the confocal system for individual region of interest in the micro-model. Fluorescence signals emitted from nano-particles are digitized into an array of pixels; each image consists of 256 x 256 pixels. Figure 5.5b shows sketch of information transformation of an individual raw image of a region of interest into the universal image using position function of that region of interest. Since the position function passes position of the individual region of interest into the universal image, it does not alter any signal captured from nano-particles which is illustrated in Figure 5.5b.

Particle Image Velocimetry (PIV)

The cross-correlation is performed into two passes; the first pass consists of a 64 x 64 pixel interrogation window while the second pass consists of a 32 x 32 pixels interrogation window with 50 % overlapping to compute velocity fields of each individual universal image. During PIV processing, the size of the interrogation window defines the grid size of the universal image. Hence, for a uniform grid size, an interrogation window of the first pass as well as second pass of all universal images should remain constant at a fixed plane.

Before computing a velocity field, a rectangular mask of 256 x256 pixels is generated and inversion of masking is applied to the entire universal image. Henceforward, non-signal regions of interest in the universal image are masked, and the particle information regions of interest are processed to compute velocity fields of the individual domain. Masking of the non-signal region eliminates computational cost without altering data size in the computed velocity field. Each region of interest consists of 449 pairs of images acquired by the confocal system which correspond to 449 universal image pairs in each location. Figure 5.6 shows

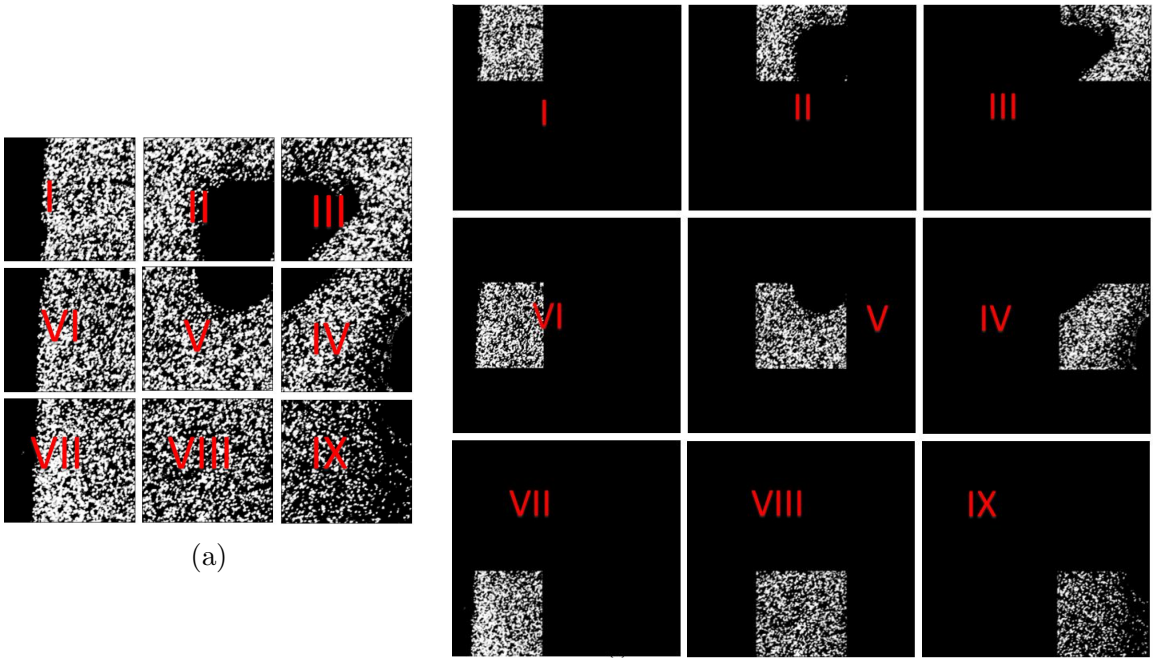

(a)

(b)

Figure 5.5: (a)Sequence of raw image from nine different region of interests. Each image represents 256 x 256 pixels raw images captured by confocal system that contains particle information from respective region of interests (ROIs), (b) transformation of particles infomation into universal domain without losing particle information.

successive vector fields of nano-particles flowing at nine different region of interests of the micro-model. Each velocity field at different ROIs shown in Figure 5.6 consists of a uniform velocity grid. Velocities at each node from nine different ROIs are computed to obtain an average extended velocity field. An average nodal velocity represents the averaging of non-zero data. So, zero nodal velocity does not contribute while computing average and standard deviation. Figure 5.7 shows nodal velocity averaging from nine different ROIs to compute a single extended velocity field. Data at each overlapping region from two or more locations is also averaged, which increases the sampling number and decreases statistical error in the measurement. The number of data sample increases with the increase in overlapping number of regions. The maximum possible sample size for a vector is four times the number of sample vectors in each discretized region of interest. As the sample size increases the expected deviation of nodal measured velocity from its actual mean decreases as the square root of number of sample size. As a result, the statistical integrity of the data in overlapping region increases with the increase in the number of overlapped regions in the extended field. Figure 5.7 also shows the seamless velocity field of nine different regions of interest (ROIs) into a single assembled region of interest with a 6.624 μm span-wise and stream-wise velocity vector spacing. Seamless velocity fields are only possible because of the novel measurement and image processing technique described in this chapter. The size of the interrogation window plays a significant role in velocity resolution as well as computing seamless velocity field in an extended field of view. The spacing between two vectors are constant throughout the velocity field, and no evidence suggests that nine different locations were used to cover the observation location by observing a single extended velocity field.

5.6 Conclusion

A combination of confocal micro-PIV along with the measurement and image patching algorithm described in this chapter provides a novel method of extending the field of view of particle image velocimetry without losing any particle information from individual dis-

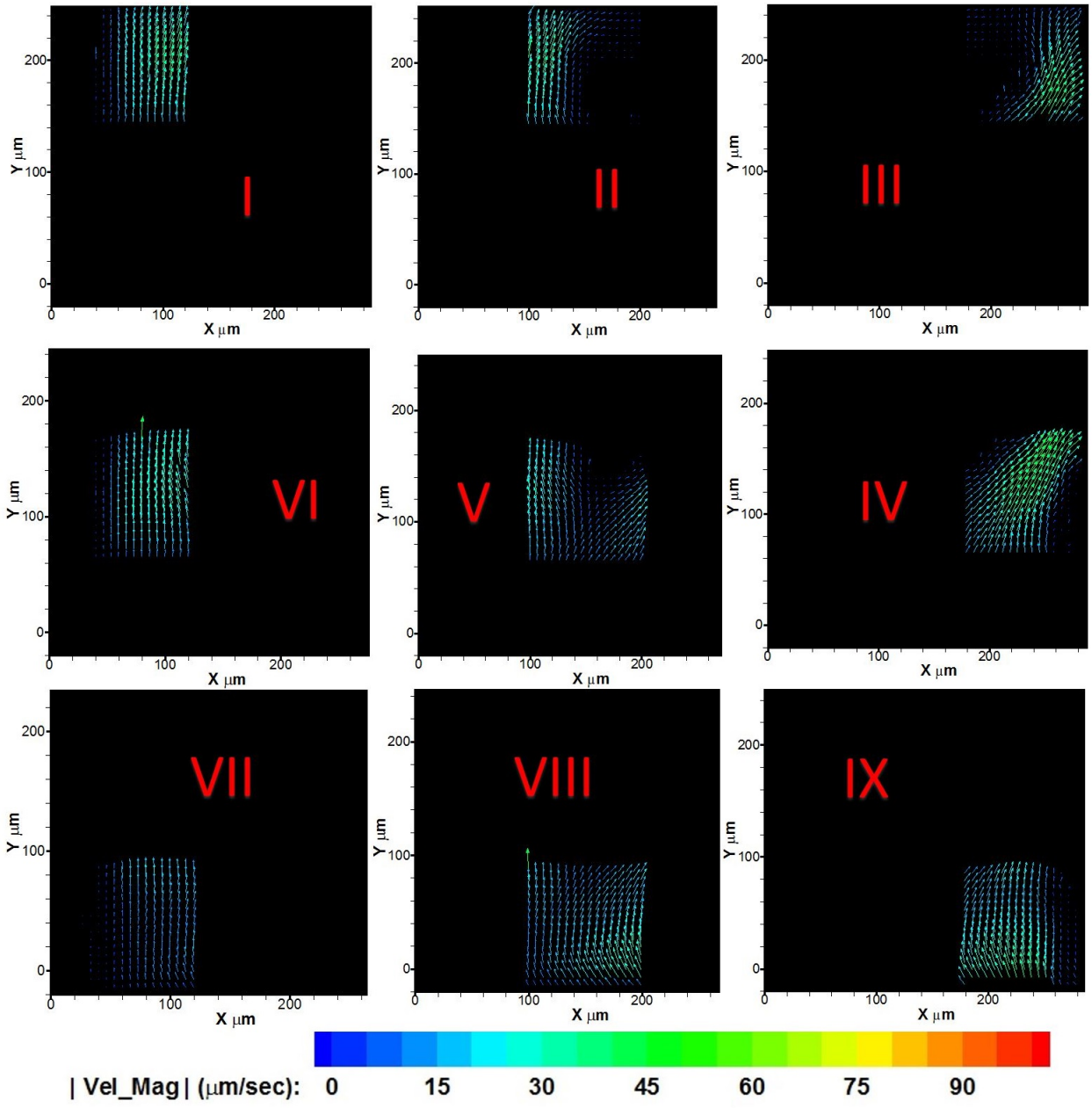

Figure 5.6: Sequential micro-PIV results from nine individual discretized region of interests.

cretized regions of interest in a micro-scale flow. Regular confocal micro-PIV is unable to acquire a large field of view as it is limited by the numerical aperture and magnification of the objective lens. An experimental technique for image acquisition as well as image processing was successfully demonstrated for the quantitative characterization of nano-particle transport in microfluidic devices, forming an extended field of view. The experimental result shown in Figure 5.7 illustrates that the C-μPIV system along with measurement and image patching algorithm is powerful technique to extend a continuous seamless velocity field in a complex geometry. The size of the observation location depends on the number of discretized regions of interest used to cover it. The extended field of view carries all the information of nano-particles from all individual images and a continuous seamless velocity vector field is generated to characterize transport behavior of nano-particles in observation location of a complex micro-model. Numerous digitized region of interest cannot produce an extended seamless, uniform velocity field that covers observation location of the micro-model by itself. Although the post processing of data from individual discretized regions of interest can extend the velocity field to cover larger observation locations, it cannot assure a uniform, continuous, seamless velocity field of the observation location. Therefore, the image patching algorithm described in this chapter provides a convenient way of synthesizing a single extended velocity field from sequential discretized region of interest images with high accuracy which accounts for less than 1 percent error due to sub-pixel alignment. To the best of our knowledge, this is the first image process method which extends field of view based on a sequential discretized regions of interest. The final measurement of the observation location is dependant on the number of overlapping region of interests, the size of overlapping areas of regions of interest, and the size of individual region of interest. Therefore, seamless and continuous velocity vectors can be easily achievable with sufficient overlapping areas between two sequential locations, and the size of the observation location can be extended indefinitely in theory depending on instrument capability.

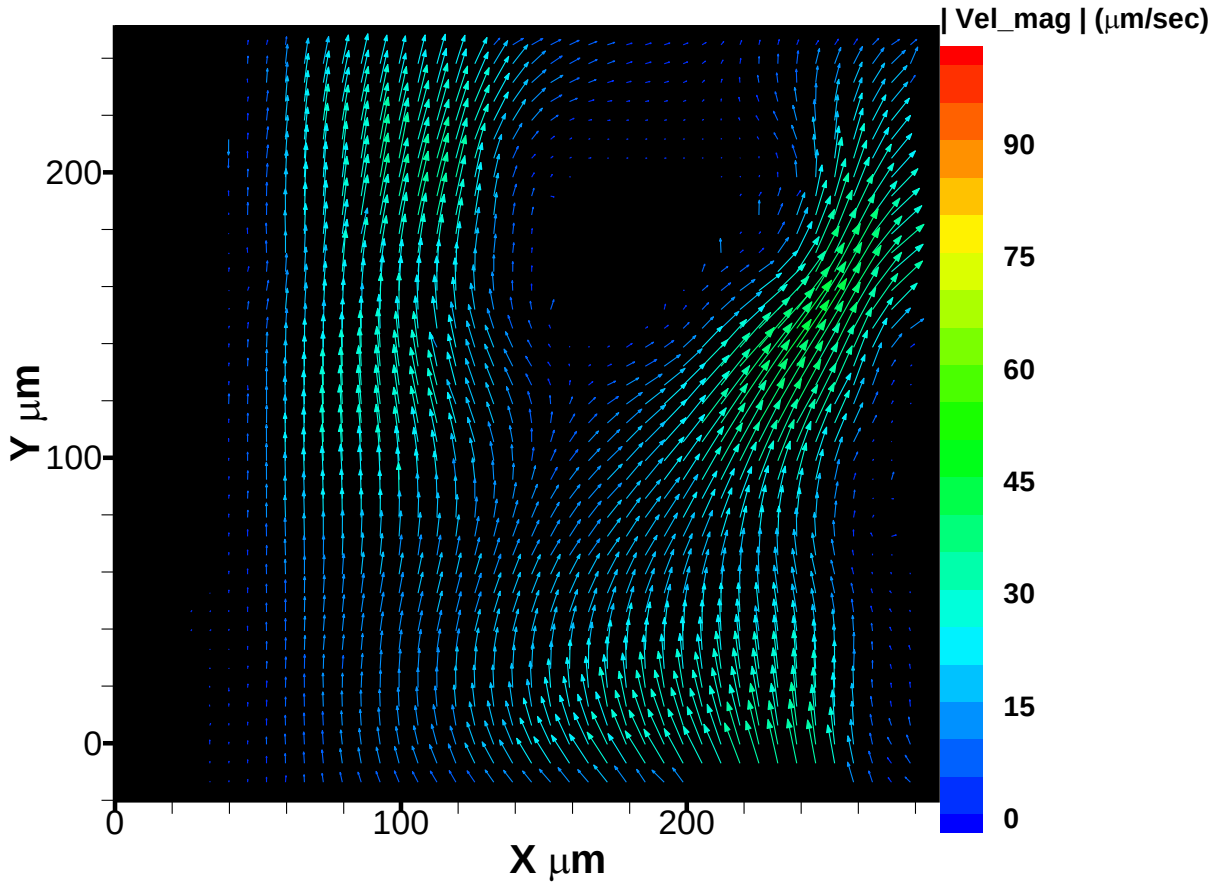

Figure 5.7: Seamless velocity fields generate from nine different region of interest into a single extended field of view with uniform resolution of vector field.

Chapter 6
Image Post-Processing for Confocal Micro-PIV*

The goal of this study is to improve and minimize the effects of out-of-focus particles flowing through the microfluidic devices with a sub-micron depth of focus. Although a confocal system has high capability to acquire a particle image from a thin focal plane, it is not adequately thin for high resolution 3D measurements of particle transport, which necessitates post-image processing to eliminate out-of-focus particles from the focal plane to attain high resolution velocity field in 3D. In this chapter, we have proposed and assembled image processing algorithms to eliminate out-of-focus particles flowing in a micro-model to minimize focal plane thickness. Post-image processing includes a combination of background noise elimination, high pass filter and neighborhood connective algorithms(proposed). We have also briefly discussed the interlace effect of odd and even scans of laser scanning confocal microscope.

6.1 Introduction

The confocal microscope was introduced by Minsky in 1957 at Harvard University and patented in 1998 [59], which significantly improved lateral and axial resolution in microscopic imaging [60]. The confocal microscopy system is an unlikely conventional microscopy system, due to its capability to discriminate out-of-focus planes by limiting the pinhole aperture diameter of the system. Figure 6.1 shows a schematic diagram of the basic concept of the confocal microscope in which light emanating from out-of-focus planes is blocked by operating pinhole diameter. Due to its thin in-focus optical slicing capability, it has allowed us to reconstruct a 3D structure without destroying specimens. As indicated in Figure 6.1, out-of-focus light (purple and red dotted lines) emitted from specimens are

*some of the materials are republished with permission from "3D Measurements of Nano-Particle Transport in Complex 2.5D Micro-Models, by Jagannath Upadhyay, Daniel S. Park, Karsten E. Thompson and Dimitris E. Nikitopoulos, Paper No. IMECE2015-50635 by ASME

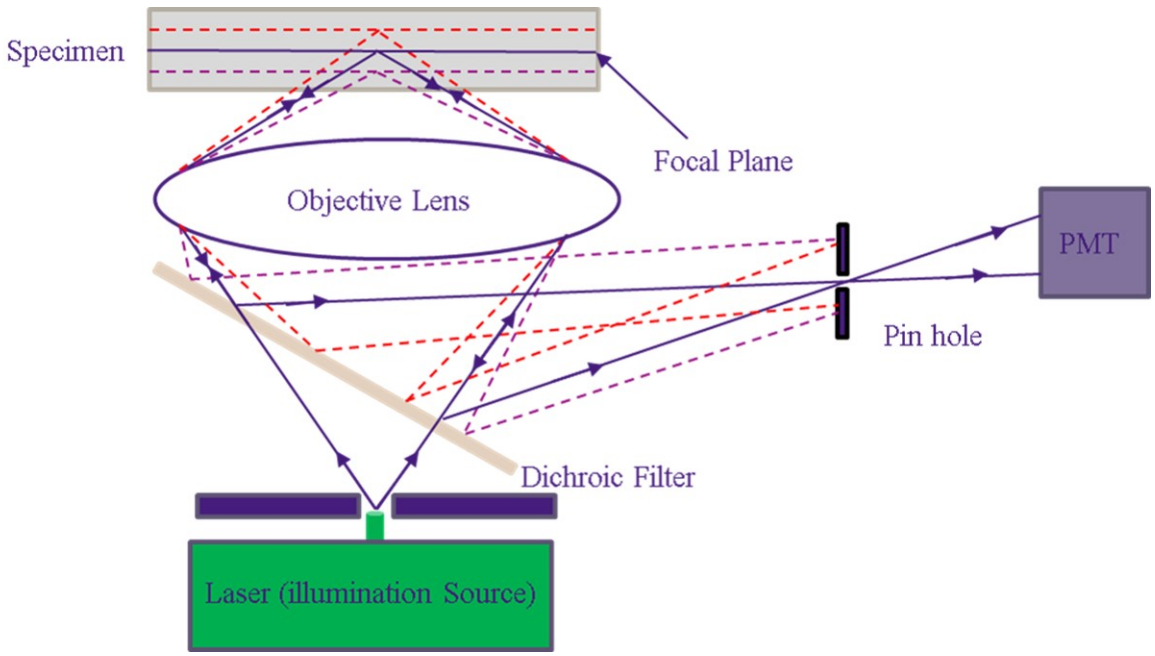

Figure 6.1: A schematic drawing illustrating principle of laser scanning confocal Microscopy using a pinhole to eliminate out-of-focus plane.

blocked by the pinhole aperture, which results in low photon transmission in the sensor. With a decrease in pinhole diameter, a small portion of light is detected by photo detector, hence limiting the thickness of the focal plane. Similarly, a wide opening of the pinhole allows the confocal system to be in wide field (WF) condition to transmit an enormous amount of photons through the pinhole, which results in thicker focal plane, collimated image rather than a convergent image and acts as conventional microscope. So, pinhole diameter plays a decisive role in confocal microscopy by determining the optical thickness of the specimens.

6.2 Optical Thickness

Optical thickness is defined as the thickness between two significantly focused planes above and below the focal plane of the system. Because of the pinhole aperture, a thin optical sectioning of a specimen is achieved by scanning a focus beam of fluorescent light emitted by the specimen. Various experimental as well as analytical approaches were performed to determine quantitative optical properties as well as depth discrimination in confocal microscopy [61, 59, 60, 62]. According to the study conducted by Wilhelm *et al.*,

optical slice thickness in confocal system is given by this following equation:

$$FWHM_{depth} = \begin{cases} \sqrt{(\frac{0.88*\lambda_{em}}{n-\sqrt{n^2-NA^2}})^2 + (\frac{\sqrt{2}*n*PD}{NA})^2} & 1AU < PD < \infty \\ \frac{0.64*\bar{\lambda}}{n-sqrtn^2-NA^2} & PD < 0.25AU \end{cases} \tag{6.1}$$

where $\mathrm{FWHM_{depth}}$ is the axial full width at half maximum, n is the refractive index, NA is the numerical aperture of the objective lens, λ_{em} is the emission wavelength, $\bar{\lambda}$ is the mean wavelength of the excitation and emission wavelength, AU is Airy Disc Unit and PD is the pinhole diameter divided by total magnification of the system in microns.

FWHM is defined as the difference between two extreme points of a function where the dependable variable is equal to half of the maximum value of independent variable in a normal distribution. In other words, $\mathrm{FWHM_{depth}}$ is the optical thickness between two cut off fluorescent signals which are at half value of the maximum fluorescent signal (Normally maximum fluorescent signal is at focal plane) of a point spread function (PSF) of illuminating light source. Equation 6.1 for large PD is also known as optical slice thickness in a geometrical optical confocal microscope, as geometrical pinhole diameter plays significant role in determining optical thickness. As the pinhole diameter gets smaller, less than 0.25 AU, the pinhole acts as wave optics and pinhole size effects are neglected, so it is also known as optical thickness in wave-optical confocal microscope. In a wave-optical confocal microscope, the axial resolution is equivalent to optical thickness of the focal plane. Similarly, Wilson *et al.* has also discussed the optical sectioning or depth discrimination property in detail and a new analytical formulae has been proposed to determine optical thickness of the focal plane [62]. In his paper, he relates optical thickness of the plane with pinhole diameter, emission wavelength and characteristics of the objective lens in a confocal microscope. A new analytical cubical approximation equation which is in good

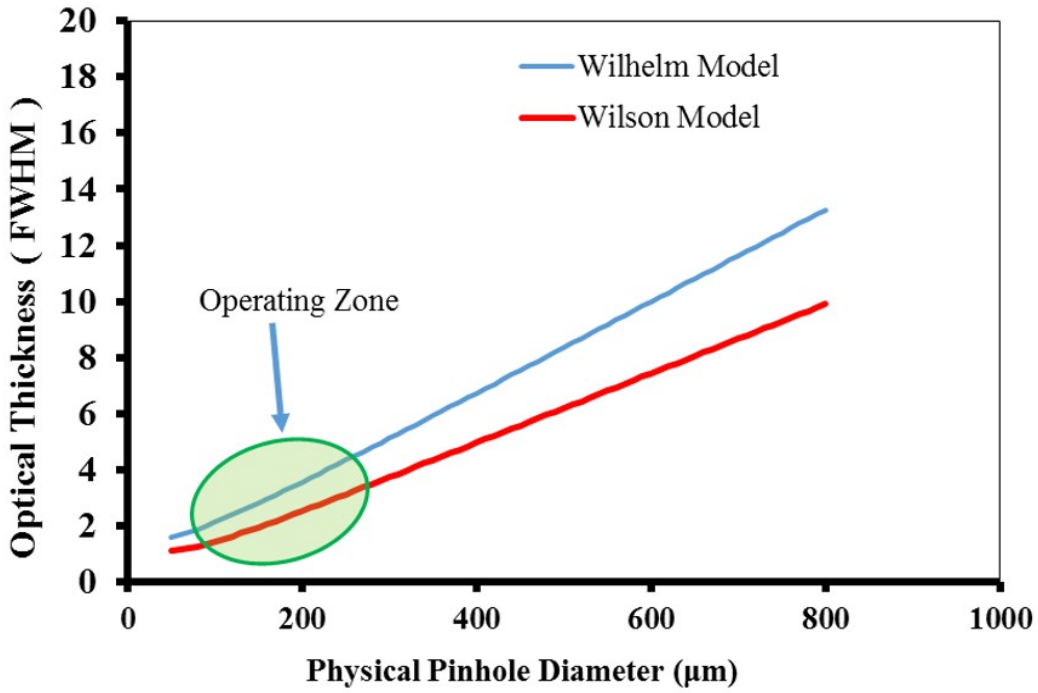

Figure 6.2: A graph showing a relationship between optical thickness of the focal plane and physical pinhole diameter of the confocal microscopy using two different models[63, 62].

agreement with the calculated family of curves is given by Equation 6.2.

$$FWHM_{depth} = 0.67 \frac{\lambda_{em}}{n - \sqrt{n^2 - NA^2}} \sqrt[3]{1 + 1.47 * PD_{AU}^3} \tag{6.2}$$

where PD_{AU} is pinhole diameter in Airy Disc Unit.

Although a confocal microscope is very capable of producing a very thin beam of light emitting from the focal plane with a tremendous amount of photons rejecting by pinhole aperture, it is impossible to get an adequate fluorescence signal from a negligibly thin focal plane with current optical technology. Figure 6.2 presents a relationship between pinhole diameter and calculated optical slice thickness of a geometric-optical confocal microscope for an objective lens 20 x Water immersion 0.95 NA with an optical zoom of 6x on pinhole diameter. Table 6.1 presents experimental parameters used to study nano-particles transport at various observation locations of Boise rock-based micro-models are listed below.

Table 6.1: Experimental parameters used to study nano-particles transport in Boise rock-based micro-model.

Excitation Wavelength (μm)	0.543
Emission Wavelength (μm)	0.612
Refractive Index(n)	1.33
Numerical Aperture (NA)	0.95
Overall Magnification	20 x 6
Airy Unit (AU)	0.697
Pinhole Diameter(PD) (μm)	50-200
Optical Thickness ($FWHD_{depth}$) (μm)	1.58-4.34

Depending on the size of the particle and sensitivity of the PMT, the pinhole diameter ranged from 50μm - 200μm in our experiment. The emitted fluorescence intensity of the fluorescence labeled nano-particles depends on their size and the excitation power of the laser. It is better to increase the sensitivity of the PMT rather than increasing the power of the laser source. As pinhole diameter increases, optical thickness increases, which leads to bias measurement of velocity at a specified focal plane. So, it is necessary to minimize optical focal thickness and the image of the out-of-focus particles influencing correlation for velocity measurement. Figure 6.3 shows how the numerical aperture of the objective lens, plays a significant role in determining optical thickness of the focal plane using the Wilhelm model [63]. As the numerical aperture increases, the resolving power increases, which results in reduction of the optical thickness of the focal plane.

Besides advanced optical technology, various research has been performed on post-image processing in order to improve the velocity measurement on the focal plane. Most of the image processing involves reduction of depth of correlation (DoC) [64, 65, 66, 67]. Depth of correlation is the depth of the volume from which emitted particles signals contribute to cross correlation analysis during particle image velocimetry. Larger depth of correlation leads to bias in velocity measurement of a non-zero axial velocity gradient. All the post-processing involves filtering of particle appearance in image along with the distance from the object plane. We have presented the most powerful and simple image post processing

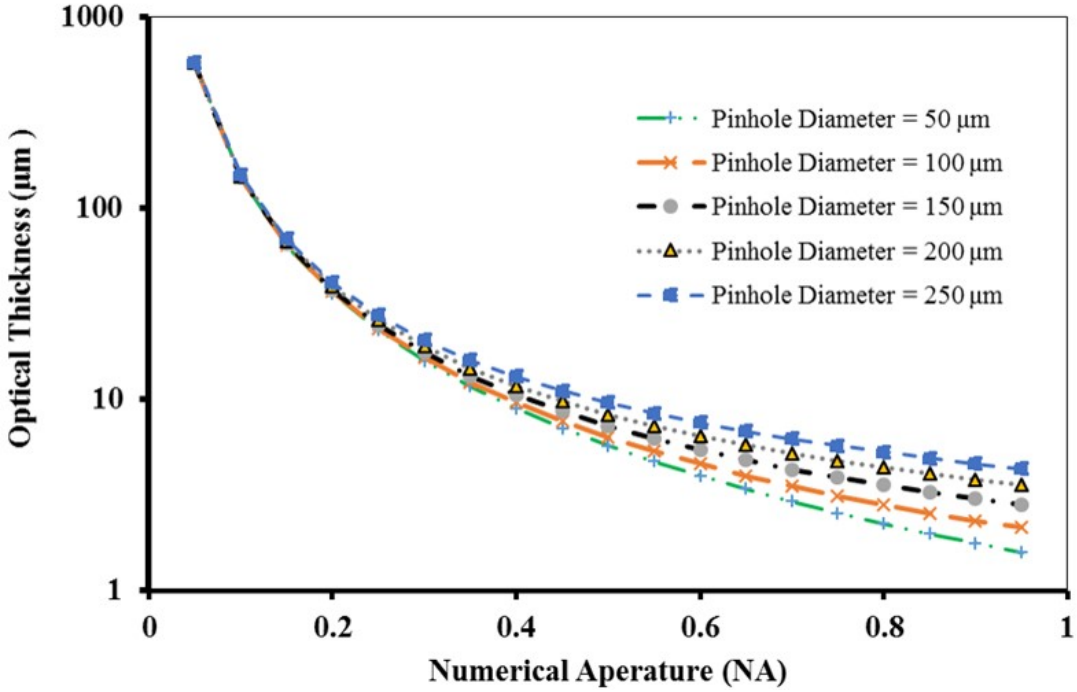

Figure 6.3: A graph showing an effect on calculated optical thickness of the focal plane due numerical aperture of objective lens in confocal microscopy with various pinhole diameter (n=1.33, λ_{em}=543 nm 20x objective lens, 6x optical zoom)[63].

technique in this chapter which will allow us to eliminate particle appearance in the image above and below the focal plane.

6.3 Post-Image Processing

In this section, we have proposed and assembled various image processing algorithms to eliminate out-of-focus particles captured along with in-plane particles flowing in the measurement plane. Image processing involves de-interlacing of scanned images, background elimination of non-dynamics particles in the micro-PIV system, elimination of out-of-focus particle from the in-plane image, and pixel connectivity also called "neighborhood connectivity" to determine particle authenticity flowing in the in-plane.

De-interlacing

The process of minimizing visual defects due to interlacing of two fields (in our case even and odd lines scan) and combining them into a single frame is known as de-interlacing. Figure 6.4 shows two different ways of image acquisition in our laser scanning confocal

system. We will be more focused on bidirectional scanning of the image acquisition as shown in Figure 6.4b due to its capability to scan faster than the other as shown in Figure 6.4a. Due to bidirectional line scan, overlying of odd and even scans result in "combing" artifact or interlacing effect in the full frame image. Figure 6.5 shows jagged edges when two odd and even pixels do not line up in a single frame.

Numerous de-interlacing algorithms like line averaging (LA), edge based line average(ELA), novel intra deinterlacing(NID), directional interpolation and motion compensation algorithm (DIMC), motion compensation (MC) and so on have been using to improve interlaced images/videos in television and video on personal computers [68, 69, 70, 71, 72]. Out of these de-interlacing algorithms, line averaging accomplishes overcoming the interlacing effect in our confocal images with an expense of mislaying half of the particles information. So, to overcome mislaying particle information as well as interlacing of confocal images, we have proposed a directional shifting algorithm which is slightly different than the ELA algorithm in terms of interpolation between two scan fields. In ELA, directional correlation is used to determine the missing line using linear interpolation whereas in our case, we use bidirectional field information of two fields and shift one directional field information horizontally to overcome interlacing without interpolating two fields. Detail of the directional shifting algorithm to overcome interlacing of laser scanning confocal microscope images is presented in algorithm 6.1.

- **Directional Shifting Algorithm**

The main motivation of this algorithm is to retain all the pixels' information from both odd and even scans of the interlaced images. This method as listed below describes shifting of one of the line scan fields towards left/right depending on the reverse direction of interlace. It should be noted that all the information from the field scan is retained and used to create a single deinterlaced image. Figure 6.7 shows results of the shifting algorithm, where pixelation of line scan is reduced and contains all the pixelated information of the full frame image. The main advantage of this algorithm is to preserve all the information

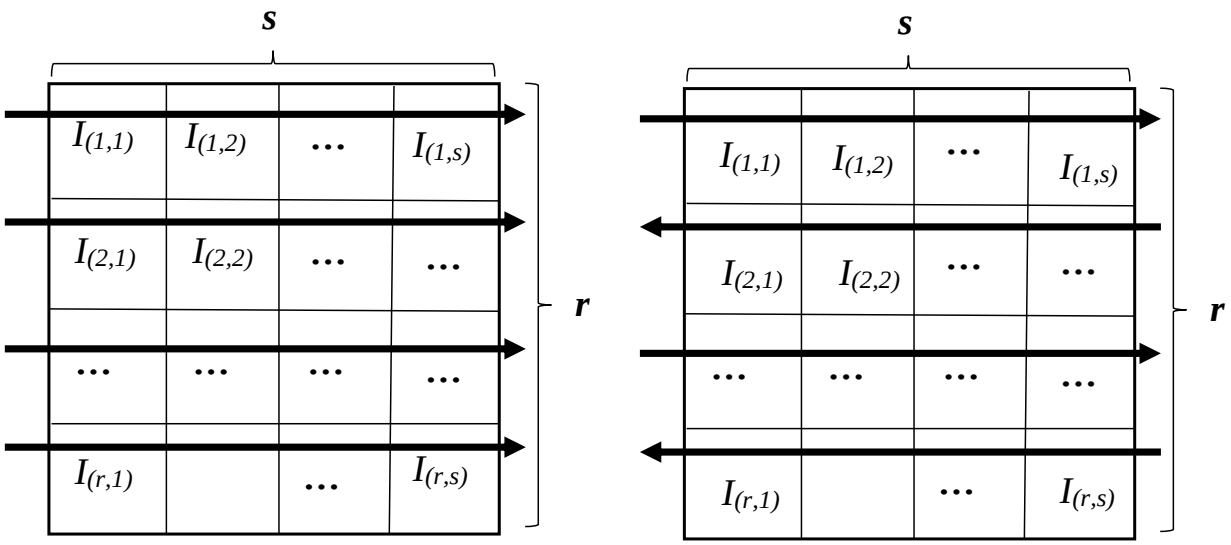

Figure 6.4: Direction of laser scanning method in confocal laser scanning microscope (a) unidirectional scanning (b) bidirectional scanning.

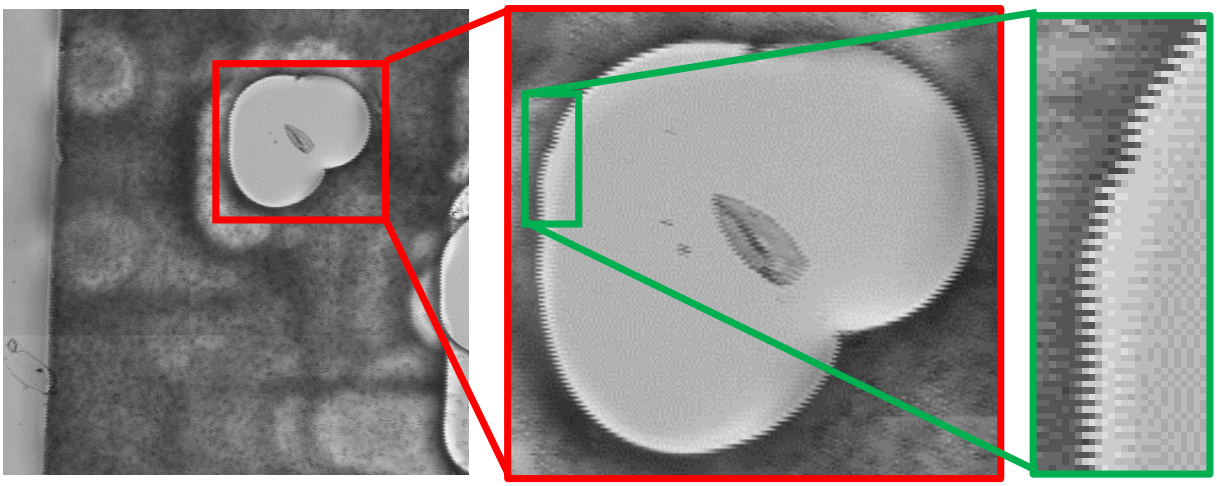

Figure 6.5: Image captured by Confocal Laser Scanning Microscope, raw image (left) without de-interlacing, close up view of a structure of left image (center) and zig-zag pattern as seen along the edge of the image structure(right).

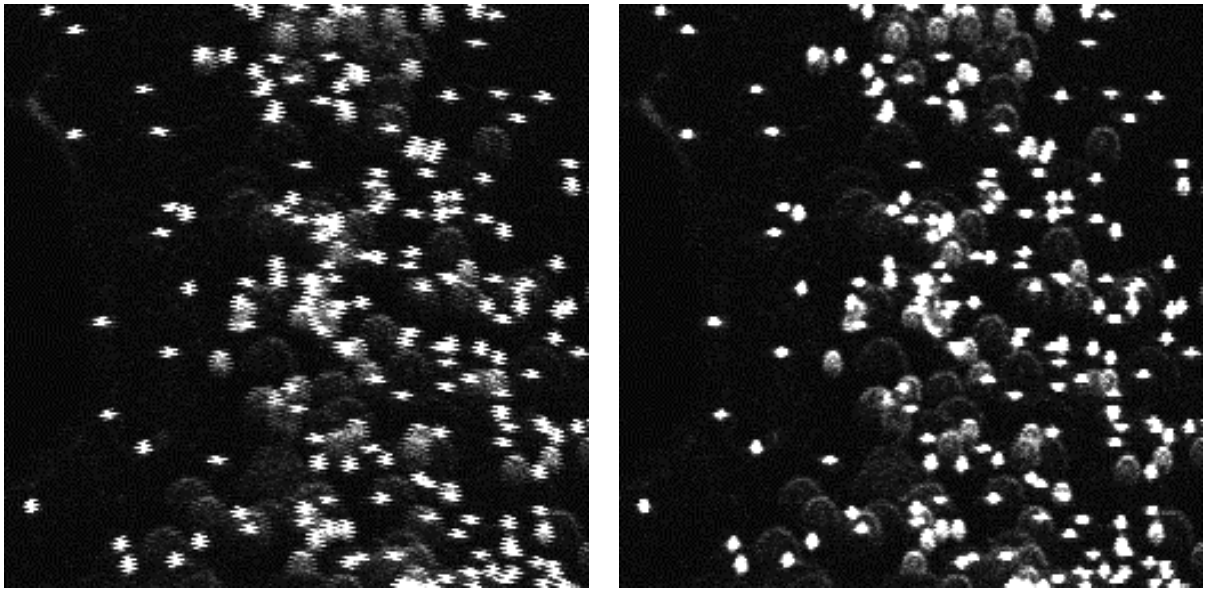

(a) (b)

Figure 6.6: Raw image of nanoparticles flowing in the micro-model captured by laser scanning confocal system, (a) before correcting interlacing effect and (b) after correcting interlacing effect. Because of interlacing, the particle shape has been distorted and recorded as non-circular shaped particles.

of the image resolution while the cons of this algorithms is that it requires all odd and even scan information of the image in order to reconstruct the full frame image.

Algorithm 6.1 Directional Shifting Algorithm

$$\text{I(i,j)}= \begin{cases} I(i,j) & \text{if i is odd} \\ I(i \pm n, j) & n \in \mathbb{Z}, \text{if i is even} \\ or & \\ I(i \pm n, j) & n \in \mathbb{Z}, \text{if i is odd} \\ I(i,j) & \text{if i is even} \end{cases}$$

- **How does de-interlacing play a significant role in Micro-PIV?**

The main objective of using deinterlaced images in micro-PIV is to improve correlation between two time framed images. The higher correlated images the better the micro-PIV result. Because of the deinterlacing, the number of statistically valid vectors increases drastically as shown in Figure 6.8. Figures 6.8a and 6.8b show average velocity fields

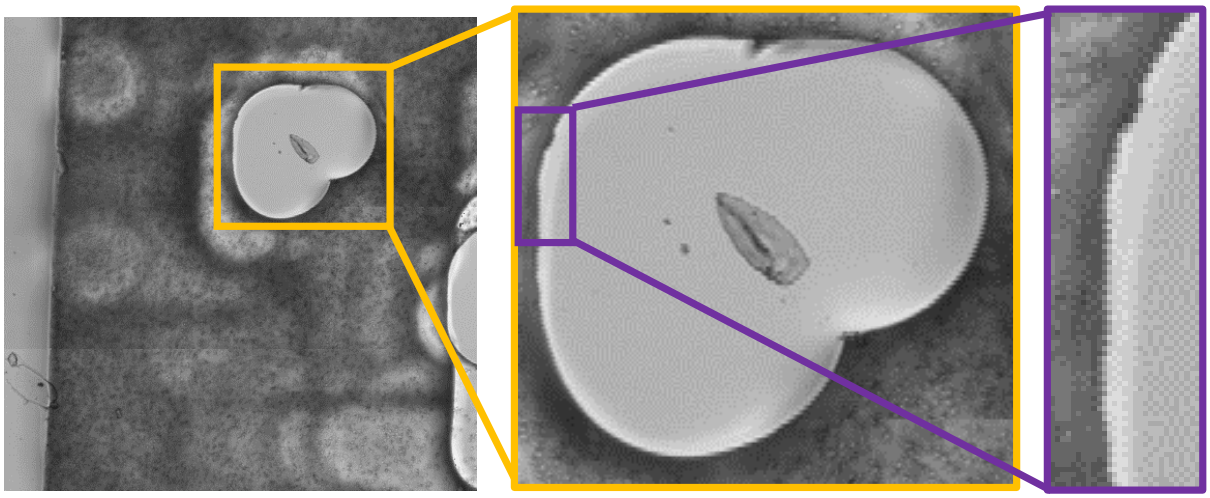

Figure 6.7: (left)Image generated using directional shifting algorithm, (center) close up view of a structure of left image,(right)no zig-zag pattern observed on the edge of the image structure after image processing.

calculated using interlaced and deinterlaced images. Although the two velocity fields shown in Figure 6.8a and 6.8b do not vary significantly from each other, the statistical sampling to calculate the average velocity of each location represented by a vector is significantly improved by using deinterlaced images as shown in Figure 6.8c and Figure 6.8d. A particle in deinterlacing image represents the actual particle shape where as a particle in an interlace image produces an aliasing effect on the particle shape. The larger the number of valid vectors, the lower the statistical error in the measurement of the system. So, average velocity for a steady state flow calculated from a large valid sample provides more accuracy towards its mean velocity field than if the average velocity field were calculated with a low sample size data. A larger sampling minimizes deviation of the velocity field from its actual mean value.

Background Elimination

This section presents registration of non-dynamic particles from N sequential images along with their precise coordinates. Once non-mobile particles are registered using the background image registration algorithm described below, the non-dynamic particles are subtracted from the raw images to eliminate all stationary particles from mobile particles

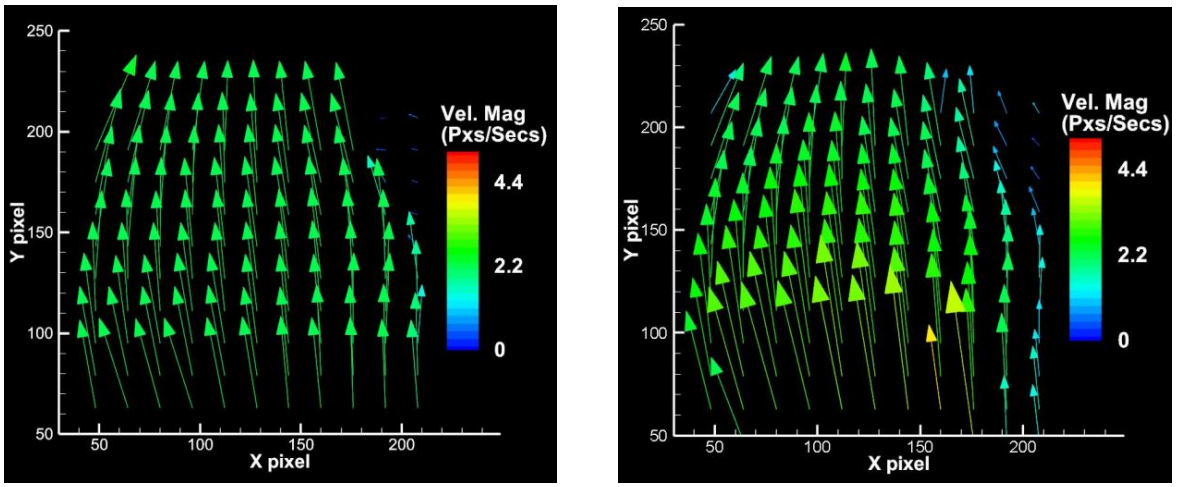

(a)

(b)

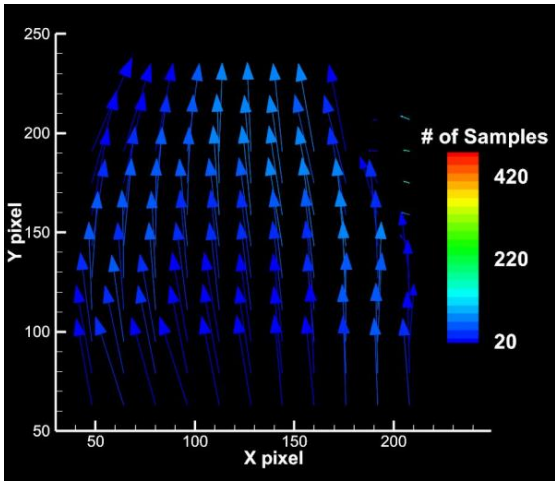

(c)

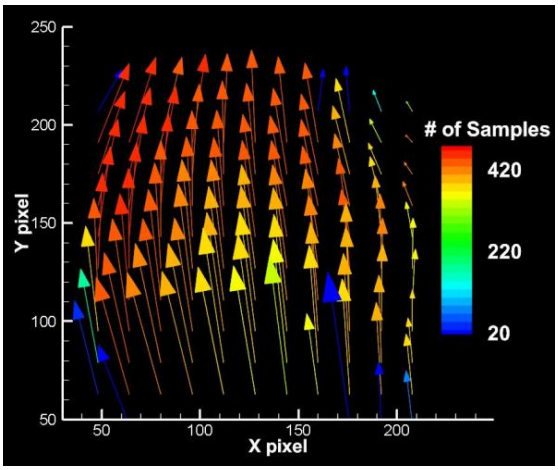

(d)

Figure 6.8: Micro-PIV showing (a) velocity field when using interlaced images (b) velocity field when using deinterlaced images (c) number of correlated samples out of 449 image pairs when using interlaced images (d) number of correlated samples out of 449 image pairs when using deinterlaced images.

captured by highly sensitive PMT. For our purpose, to register as a non-mobile particle, the following criteria have been applied to all images recorded by confocal microscope.

1. The particles must be stationary at that position for at least 29 secs. 29 secs is chosen because of instrumental limitation in capturing continuous images.

2. Particle intensity must be equivalent to the threshold particle intensity of the nano-particle flowing through the micro-model.

Background image registration from N sequential images is given by Equation 6.4 [14, 73].

$$B_{ij} = \frac{1}{N} \sum_{n=1}^{N} \sum_{i=1}^{r} \sum_{j=1}^{s} (I_{ij})_n \tag{6.3}$$

$$BI_{ij} = \begin{cases} 0 & if B_{ij} < f \\ B_{ij} & B_{ij} \geq f \end{cases} \tag{6.4}$$

where I_{ij} represents pixel intensity at (i, j) location of an image, and [r s] represents size of the image, f is called "threshold intensity" of the particle to be recognized as a valid particle, and N represents the total number of images acquired by the confocal system during one continuous scan.

The number of images acquired by the confocal system should be sufficiently large in order to avoid influence of moving particles in the system. Equation 6.3 represents an average background image registered as of N sequential images. Equation 6.4 applies a high pass filter to eliminate moving particles registered in the background image. Once the background image generated by Equation 6.4 is deducted from the raw digitized images, most of the unnecessary steady background noise as well as non-dynamic particles are eliminated from the raw images. Figure 6.9a shows one of the raw images from 450 sequential images captured by the confocal system while Figure 6.9b shows background images constructed from 450 sequential images captured by confocal system. Since the particles are flowing in close proximity of the coverslip, there is higher chance of adsorbing

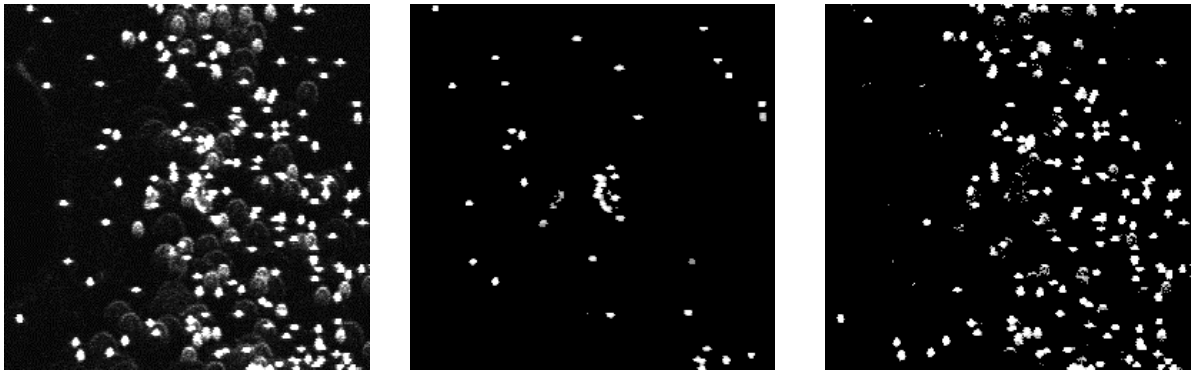

(a) (b) (c)

Figure 6.9: (a) One of 450 sequential raw image (b) Reconstructed background image from 450 sequential images (c) One of the 450 sequential images after background elimination[14].

particles on the coverslip. Figure 6.9b shows adsorbed particles along the coverslip during particle flow in the micro-model. Figure 6.9c shows image of dynamic particles flowing inside micro-porous media as well as noise from fluorescence signals illuminating from out of the focal plane particles. This technique eliminates all the fluorescence particles adsorbed on the side wall as well as coverslip of the 2.5D micro-model and uniform noise generated by PMT.

High Pass Filter Algorithm

Digital images acquired by the confocal system contain particles illuminating fluorescence signals from in-focus as well as out-of-focus particles. With the current art-of-technology in optics, it is adequately impossible to capture fluorescence signals from a negligibly thin focal plane, facilitates a necessity of Post-image processing to minimum depth of correlation of PIV images. The idea of a high pass filter algorithm comes from the image intensity distribution of a fluorescence particle in the axial direction. Since image intensity of a particle behaves as a point spread function, a Gaussian particle intensity can be constructed at a focal plane.

To illustrate, Figure 6.10a shows a sketch of particles A, B, C flowing in different XY planes. Similarly, the image intensity shape for particles A, B and C are sketched in Figure 6.10b. Since the image intensity of the particles follows Gaussian distribution at their focal

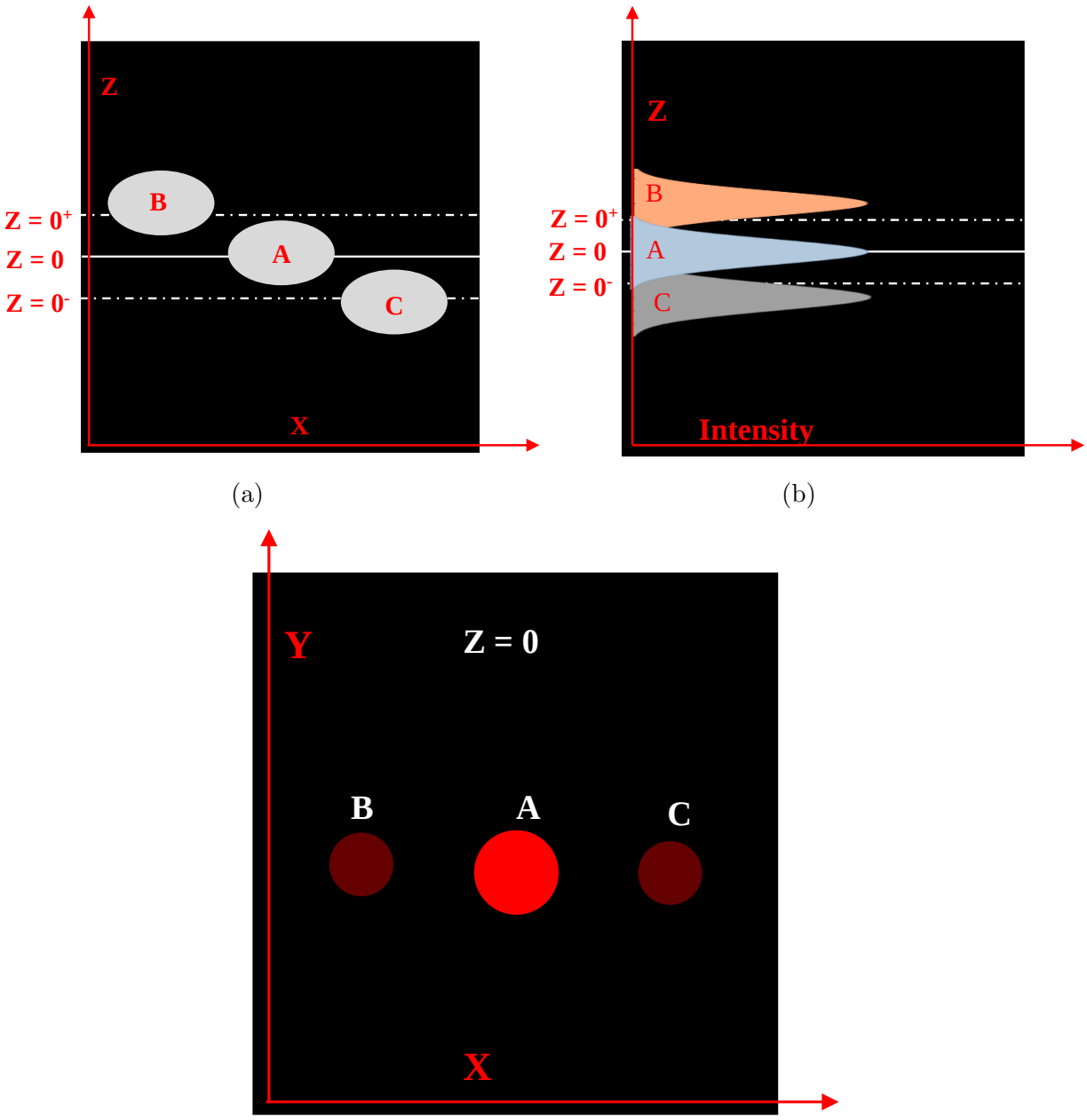

Figure 6.10: A schematic drawing of (a) particles in XZ plane at various focal planes (b) image intensity shape (also known as point spread function) of particles projected in XZ plane (c) A,B,C particles recorded in XY plane when observing from Z = 0 plane.

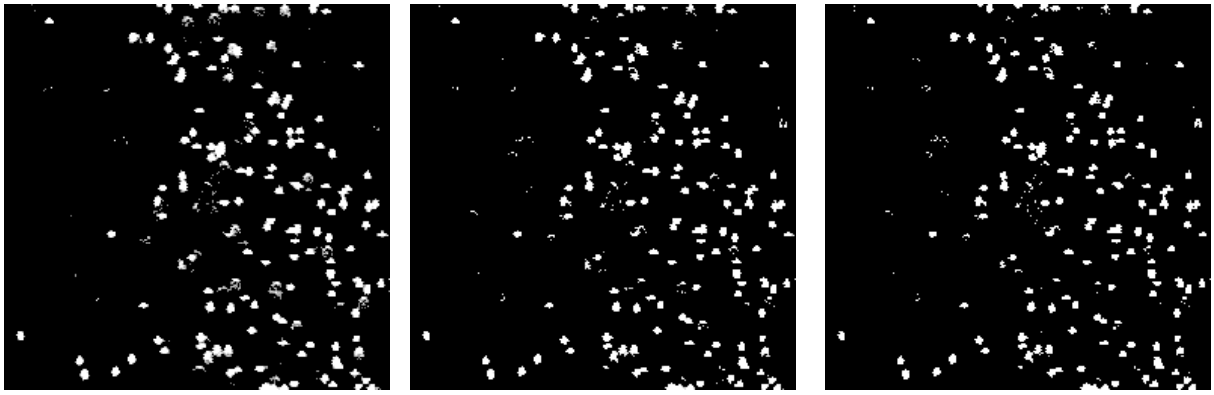

(a) (b) (c)

Figure 6.11: Image generated after non-dynamic particles are removed and a threshold filter of (a) 130 PI (b) 200 PI and (c) 220 PI applied to the raw image.

planes, there is a threshold range where image intensity of the particle at a specific focal plane influences its presence in the image. Because of this Gaussian distribution behavior in particle intensity and thick optical focal plane of confocal microscope, particles flowing in the out-of-focus planes ($Z = 0^-$, and $Z = 0^+$) are also captured by confocal system at the focal plane $Z = 0$, which is illustrated by a schematic 2D projection of those particles in Figure 6.10c. The High Pass Filter Algorithm described in Algorithm 6.2 eliminates all the particles flowing in out-of-focus planes from raw images in a specific focal plane. The threshold intensity "f" in the Algorithm 6.2 determines the optical thickness of the focal plane and is subjective to the user.

Algorithm 6.2 High Pass Filter

```
for i ← 1 → r do
  for j ← 1 → s do
    if I(i, j) < f then
      I(i, j) = 0
    else
      I(i, j) = I(i, j)
    end if
  end for
end for
```

The larger the threshold intensity, the thinner the optical thickness of the focal plane. This algorithm minimizes bias error due to out-of-focus particles in micro-PIV. Figure 6.11 shows an image constructed when high pass filters of 130 PI, 200 PI and 220 PI are applied

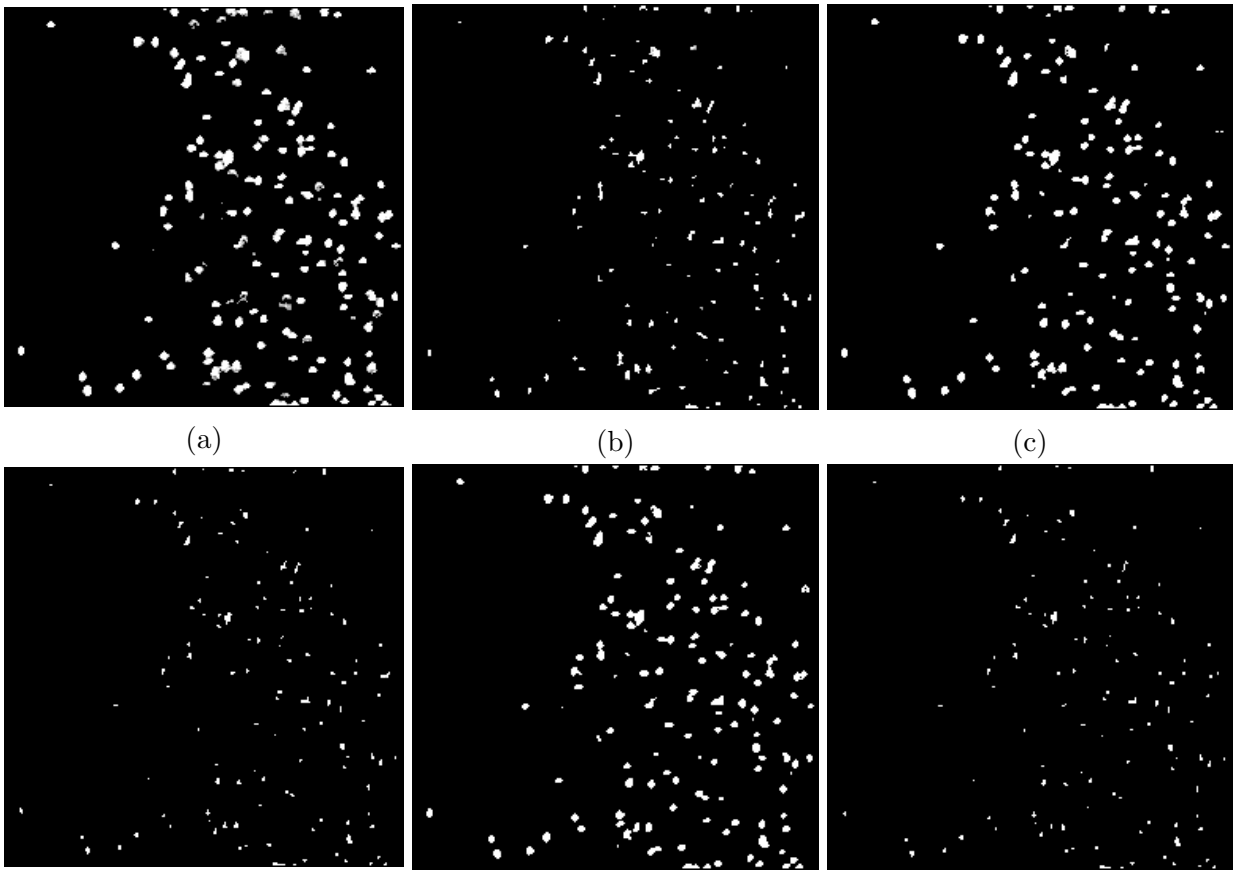

Figure 6.12: Post processed images after applying background elimination,(a) high pass filter of 130 PI, deinterlacing and PC of 4 (b) high pass filter of 130 PI, deinterlacing and PC of 8 (c) high pass filter of 200 PI, deinterlacing and PC of 4 (d) high pass filter of 200 PI, deinterlacing and PC of 8 (e) high pass filter of 220 PI, deinterlacing and PC of 4 (f) high pass filter of 220 PI, deinterlacing and PC of 8.

to a background subtracted raw image. Figure 6.11c shows more in-focus particle images at the focal plane than Figure 6.11a and Figure 6.11b. Hence, this demonstrates that filtration is subjective and elimination of out-of-focus particle image depends on the requirement of the micro-PIV system. The variation in particle size observed in the images shown in Figure 6.11 indicates some nano-particles are flowing in different depth but within the measured in-plane plane. A small-sized particle image indicates nano-particles flowing slightly away from in-plane depth compared to large particle image. So, a thin optical thickness still exists but the in-plane optical thickness is maintained below 2.5 microns in order to measure 2D PIV images at a rate of 5 μm per slice.

Pixel Connectivity

This is a proposed novel method to validate and register authentic particles flowing in a plane. Pixel connectivity is defined as the minimum number of pixels connected to a single pixel that surrounds it in order to validate a pixel as a part of a particle image. This method eliminates unconnected noise generated from PMT as well as fluorescence solution.

Algorithm 6.3 Pixel Connectivity

$$\text{I(i,j)}= \begin{cases} I(i,j) & \sum_{k=i-1}^{i+1}\sum_{l=j-1}^{j+1} bi(k,l) \geq PC, k = 2,3,4,...,r-1, l = 2,3,4,...,s-1 \\ 0 & \sum_{k=i-1}^{i+1}\sum_{l=j-1}^{j+1} bi(k,l) < PC, k = 2,3,4,...,r-1, l = 2,3,4,...,s-1 \end{cases}$$

First of all, the gray scale image attained after eliminating background noise and unfocused particles from the system, it is converted into a binary image using image segmentation. Any pixel intensity higher than particle threshold "f " as defined in Algorithm 6.2 is recorded as a white pixel(1 value) in binary image "bi", where PC is pixel connectivity. Figure 6.12 shows the effect of pixel connectivity on the processed image. Most of the unconnected pixel intensity illuminated from fluorescence solution and PMT noise are eliminated and fluorescence signal illuminating from dynamic fluorescence particle are recorded in the retained in the image.

6.4 Conclusion

In this chapter, we have investigated the influence of various image processing techniques on micro-PIV image in order to eliminate adsorbed particles and reduce optical focal thickness in order to improve depth of correlation in micro-PIV. We have also presented an efficient method of reducing optical focal thickness as well as separation of adsorb particles from dynamic fluorescence particles in order to improve micro-PIV. We have also presented an effective method of deinterlacing interlaced laser scanned images. In summary,

1. A background elimination technique described here eliminates all the steady noise illuminating from non-dynamic particles as well as steady PMT noise.

2. The high pass filter presented in this chapter increases depth of correlation of PIV images and reduces optical focal thickness by assigning threshold pixel intensity.

3. The effect of interlacing in micro-PIV images is described in this chapter and a directional shifting algorithm is proposed in correcting interlaced images of laser scanning confocal micro-PIV systems.

4. A novel pixel connectivity technique is proposed for reducing unconnected noise in the system in-order to improve quality of the recorded fluorescence particles in the micro-PIV system.

Chapter 7
3D Measurement of Nano-Particles Transport in Low Resolution (25 μm) 2.5D Micro-Model

This chapter presents confocal micro particle image velocimetry measurement of velocity 3D distributions, 3D concentration and deposition of neutrally buoyant and electrically-neutral fluorescent nano-particles flowing through such complex 2.5D (25 μm) low resolution micro model domains, which is derived from a real Boise sandstone sample optimally matching fourteen key parameters. These measurements provide a basis for validation of molecular/particle/pore scale models, which assist in developing and exploring the physics of nano-particle transport through porous media. Also, it contributes to assess the role of effects such as the Segrè-Silberberg, hydrodynamic trapping on particle mobility and deposition, and material interaction (adsorption) mechanisms. The nano-particles flowing through the 2.5D micro-model are visualized through a confocal laser scanning microscope, whereas particle image velocimetry is used to obtain three dimensional velocity distribution at a local region of interest. 3D inlet velocity profiles of mean velocity, 3D inlet particle concentration distribution, along with synthesis of data from multiple regions of interests (ROIs) are used to determine the measured velocity fields and 3D particle concentration over an entire observation location in 2.5D micro-model are presented in this chapter. Also, nano-particle behavior and deposition of nano-particles on the inner wall of regions of interest (ROIs) of a 2.5D micro-model are presented in this chapter.

7.1 Introduction

Particle image velocimetry (PIV) is a powerful tool in experimental fluid mechanics to measure a whole field, instantaneous scalar as well as vector fields instead of measuring point-wise flow velocity in an observation domain[74, 75]. PIV is a well-established technique to generate a quantitative velocity field in macro- as well as micro-fluid systems

[76, 74, 75, 77]. Before PIV was introduced, hot wire anemometry and laser Doppler velocimetry were used in fluid mechanics to measure pointwise velocity and lack of relevant spatial information in the flow field. PIV systems consist of mainly three basic components: seeding particles also known as "flow tracer", an illumination source such as a laser, a fluorescence lamp, and an imaging system such as CCD camera, PMTs *etc.*. Flow tracer particles must be sufficiently small as well as neutrally buoyant, so that they faithfully flow the flow path of the fluid without interrupting the flow field and are large enough to scatter sufficient light for recording and damping browning motion[77, 62]. Melling has studied suitable tracer particle size for faithful flow tracking in gas as well as in liquids[78]. Tracer particles are illuminated using a fluorescent light source or a laser source to create a thin sheet of light illuminating from tracer particles. The illuminated light from tracer particles is recorded by an imaging system and velocity vectors are analyzed by using a double frame cross-correlation algorithm. Over the past few decades, various flow measurement techniques have been developed to understand three dimensional flow fields in complex geometries. A few of the highlights are presented in this section on measurement of three dimensional velocity distributions using numerous techniques in characterizing porous media and flow fields.

A laser scanning confocal microscope (LSCM) has been used in reconstruction as well as characterization of microgeometry of porous geologic and engineering materials that includes porosity and brittle failure in low porous rock under triaxial loading. Based on image acquisition by a confocal system, Fredrich has developed an automatized 3D mesh generator for numerical pore-scale flow simulation [79]. A new particle tracking technique has been introduced to track three dimensional, three component velocity of micro-particles using encoded ring structure of the micro-particle images. This technique uses a series of calibrated images of micro-particles at known positions from the focal plane to generate calibration curve that relates radius of the encoded outer ring to the axial distance of the micro-particle. Based on the calibration curve, out-of-focus particles are eliminated and in-

plane particles are used to compute 3D3C velocity using particle tracking algorithms [80]. Similarly, Klein presented the 3D3C velocity field in PDMS microchannel using a high speed Nipkow spinning disk confocal microscopy PIV and Particle Tracking Velocimetry (PTV) system [81]. Sang Joon describes measurement of three dimensional velocity fields using stereoscopic micro-PTV, defocusing micro-PTV and holographic micro-PTV to visualize as well as reveal basic physics of microscale flow[82, 83, 84]. Kim *et al.* has used tomographic PIV and 3D PTV to compare flow velocity in a confined shear driven 200 μm height and 2 mm diameter droplet over a moving surface at Reynold's number 200 [73, 85]. A volumetric three dimensional flow structure and 3D velocity distribution inside a moving droplet in a microchannel was studied by Kinoshita *et al.* using high speed confocal micro-PIV that lead to a finding of a complex circulating flow inside the droplet[86]. Besides, confocal micro particle image velocimetry system can be used in vitro study of pure water, physiological saline containing 9% or 17% human red blood cells seeded with 1 micron (0.15 % by volume) fluorescent solid microspheres to deduce statistical behavior (RMS) of the flow due to hematocrits present in plasma[87, 88]. Ooms *et al.*has used a digital holographic microscope to measure 3D flow field in T-shaped micromixers [89]. Min *et al.* has developed a micro-nano hybrid PIV system to measure 3D3C near, as well as far field velocity simultaneously with the use of total reflection fluorescence microscopy and three hole particle tracking velocimetry[90]. This technique was used to precisely measure wall shear stress in a 2D micro scale Poiseuille flow. Infrared micro-PIV has been applied in measuring flow fields in silicon-based MEMS with micron scale resolution [91]. Sen *et al.* has used a combination of PIV and PTV to study pore scale flow in a microglass porous media (pore size 10-50 μm) packed with 200 μm microspheres [92]. In order to investigate transport mechanisms of interstitial flow, Ogawa *et al.* has carried out magnetic resonance imaging (MRI) technique to measure 3D local velocity in cylindrical porous media packed with crushed glass and spherical beads[93]. Similarly, Romanenko *et al.* has conducted 3D velocity measurements in sedimentary rock cores using MRI and

APGSTE-SPRITE method to gain insight of the flow patterns in complex real reservoir porous media samples. Although this technique provides low spatial resolution, it can still serve as fundamental validation for simulations such as those carried out by Bijeljic *et al.* by employing Navier-Stokes equations and a streamline simulation approach to compute flow field in millimeter sized micro-CT images of porous media[94, 12]. Most of the physical mechanism is still unknown in micro-nano scale fluid flow, so these intensive experimental studies of micro-nano flow bring insight into micro-nano flows. Silva *et al.* has studied surface roughness effects on micro-flow in a microchannel using micro-PIV and compared experimental results with a computational model in a microchannel [95]. Similarly, another micro-PIV was conducted to gain insight on the effect of drag reduction in a slip flow of a hydrogel surface using micro-PIV[96]. All the significant measurements of nano-particles in numerous diverse fields aid in understanding and enhancing performance in the oil/gas industries, drug delivery, and predicting empirical models over conventional models of fluid flow in micro-nano scale. All these observations lead to proposing new developing theories or to validating proposed mechanisms in nanofluids [97].

7.2 Data Analysis

A combination of post-image-processing techniques described in chapters 5 and 6 as well as image deformation interrogation and C-μPIV are used to compute velocity fields of a particle flow in one of the observation locations at nineteen different depths are presented in detail in this chapter. Insight 4G, supplied by TSI Inc., is used to compute the velocity vector field. Other measurements of particle flow at various observation locations are presented in the appendices B, C and D.

Before proceeding to data analysis, all raw images acquired by the PMT of the confocal system are exported as "tiff" images. Those images are processed with numerous post image processing techniques as described in chapter 6 to eliminate non-dynamics noise as well as adsorbed nano-particles on the inner walls of the solid boundaries from raw images. Post-image-processing of those raw images increases reliability of dynamic particles and

statistical sampling number of correlated images as it improves depth of correlation of those images while performing cross correlation to compute the velocity vector. After post image processing of each image of 256 x 256 pixel resolution, corresponding to 105 μm x 105 μm (for 20 x 0.95 NA WI objective lens) in physical dimensions, is processed with an image-patching algorithm to increase the field of view based on the position of the images captured from discretized regions of interest to cover the particle flow domain. The cross correlation between two images is performed in two passes, first pass consists of 64 x 64 pixels interrogation window while the second pass consists of 32 x 32 pixels with 50 % overlapping between interrogation windows and a maximum displacement of 0.49 of an interrogation window to obtain instantaneous as well as ensemble average velocity fields.

7.3 Statistical Analysis

From instantaneous velocity fields, an ensemble average velocity field is calculated. To calculate mean velocity and standard deviation of each grid point from N pairs of instantaneous vector fields, a MATLAB script was written based on the equation below:

$$\bar{u}_{ij} = \frac{1}{N}\sum_{n=1}^{N}(u_{ij})_n \tag{7.1}$$

$$\bar{v}_{ij} = \frac{1}{N}\sum_{n=1}^{N}(v_{ij})_n \tag{7.2}$$

$$\bar{\sigma}_{u,ij} = \sqrt{\frac{1}{N-1}\sum_{n=1}^{N}(u_{ij} - \bar{u}_{ij})_n^2} \tag{7.3}$$

$$\bar{\sigma}_{v,ij} = \sqrt{\frac{1}{N-1}\sum_{n=1}^{N}(v_{ij} - \bar{v}_{ij})_n^2} \tag{7.4}$$

$\bar{u}_{\mathrm{ij}}$ represents spatial horizontal velocity components and $\bar{v}_{\mathrm{ij}}$ represents spatial vertical velocity component of the particle flow field. Similarly, $\bar{\sigma}_{\mathrm{u,ij}}$ and $\bar{\sigma}_{\mathrm{v,ij}}$ represent spatial horizontal and vertical standard deviation of the velocity respectively. Mean velocities are calculated based on the number of valid samples "N" instead of the number of pairs of snapshots.

Velocity Convergence

Velocity convergence is required in order to ensure that the ensemble average velocity field from 449 pairs of instantaneous velocity fields statistically converges and represents an accurate velocity field of the flow. Based on the experiment, at most 449 instantaneous velocity vector fields are available for each region of interest to calculate error percentage. In most of the overlapping regions, generated by overlapping two or more region of interests have at most 1796 instantaneous velocity fields. There are many sources of errors that we encountered in micro-PIV and some of those errors come from experimental conditions like non-uniform particle size as well as seeding and some come from loss of particle pairs, varying intensities, noise and sub-pixel fitting [98, 99, 100, 101]. In order to measure accurately, one has to increase the number of samples so that the statistical error is minimized to an acceptable range. The error in the horizontal component, vertical components, and magnitudes of the velocity are given by the equations below:

$$\bar{U}_{error} = |\frac{\bar{V}_{x,n} - \bar{V}_{x,m}}{\bar{V}_{x,n}}| \tag{7.5}$$

$$\bar{V}_{error} = |\frac{\bar{V}_{y,n} - \bar{V}_{y,m}}{\bar{V}_{y,n}}| \tag{7.6}$$

$$\bar{U}_{mag,error} = |\frac{\bar{V}_{n} - \bar{V}_{m}}{\bar{V}_{n}}| \tag{7.7}$$

Figure 7.1a shows the convergence error for velocity along the flow direction in an inlet channel. Similarly, Figure 7.1b shows convergence error for velocity along the X direction and while Figure 7.1c shows convergence error along the Y direction in particle flow area. Figure 7.1d shows convergence error for the velocity magnitude in particle flow area. As the number of snapshots increases, statistical error decreases as shown in Figure 7.1, since the velocity magnitude required more sampling than u and v velocity to reach a statistically acceptable average velocity. Figure 7.1d shows at least 250 pairs of snapshots are required to reach 10 % error of the mean velocity with 449 pairs of solutions and above 300 pairs

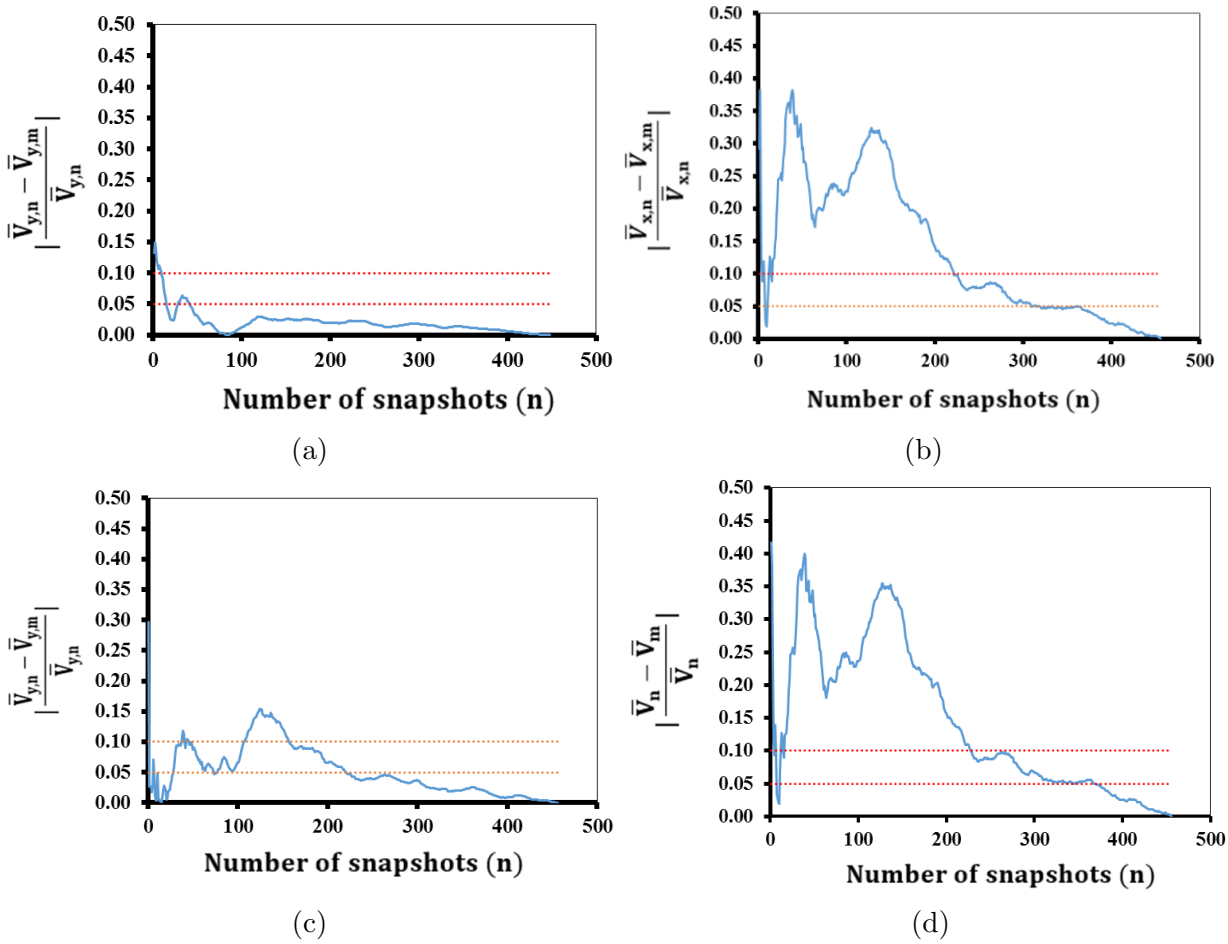

Figure 7.1: Convergence of velocity (a) $\bar{V}_{\text{error}}$ in inlet section (b) $\bar{U}_{\text{error}}$ in Region of interest (c) $\bar{V}_{\text{error}}$ in Region of interest (d)$\bar{V}_{\text{mag,error}}$ in Region of interest.

snapshots reduce statistical error to 5 % to the mean velocity calculated from 449 pairs of snapshots. Although increasing snapshots increases accuracy of the measurement, it also increases data acquisition time with a decrease in computational performance of the system.

Velocity Refinement and Elimination

Few sampling numbers and high random motion can cause spurious vectors in a velocity field which do not represent accurate flow field of the system. Few bias velocity vectors can create inaccurate solutions in the flow field. So, it is necessary to eliminate those spurious vectors in the velocity field base on the statistics of the system. We have proposed a statistical method that eliminates unrelated spurious vectors from a flow field, hence

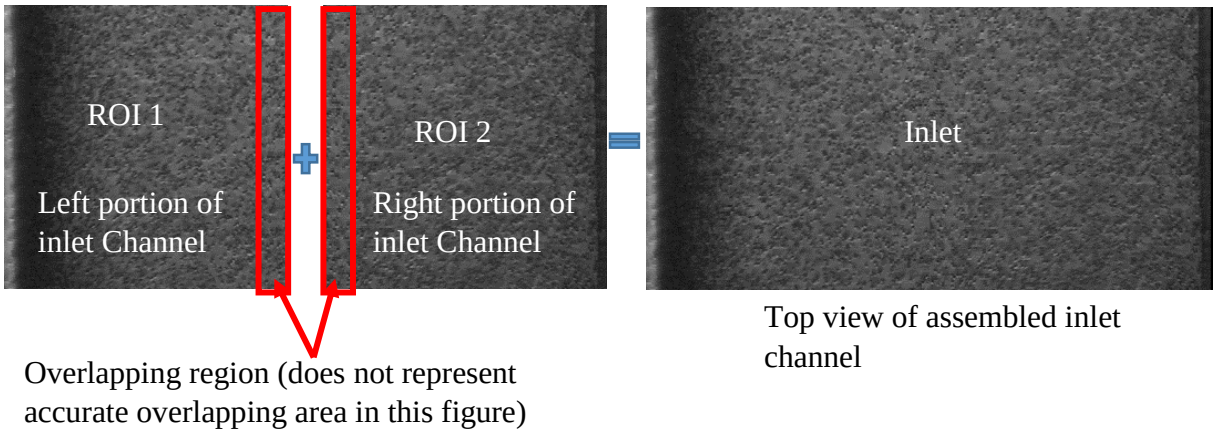

Figure 7.2: Single inlet channel of Boise Rock-Based micro-model. Two overlapping ROIs were used to cover the inlet channel. Each ROI is 105 x 105 μm^2.

representing an accurate flow field. First of all, spatial velocity fields must consist of at least n number of sampling and each vector must be within 95 % confidential interval of the flow system. Applying these criteria in order to validate a vector field eliminates unrelated bias vectors generated due to error sources mentioned in section 7.3.1.

7.4 Mean Behavior at Inlet

Mean velocity profiles are generated by ensemble-averaging of 449 instantaneous velocity fields from each region of interest. Figure 7.2 shows a assembly of two region of interests to fully cover a single inlet channel of a Boise rock-based micro-model. Based on the ideal model, the inlet channel is designed as 200 μm wide by 130 μm deep, but due to manufacturing variability, the nominal measurement of inlet channel was found to be 200 μm wide by 120 μm deep. The micro-model inlet channel is designed in such a way to ensure fully developed flow in a straight channel. Measurements are performed in two different sequential orders. First, all the measurements were taken from one (left ROI as shown in Figure 7.2) half of the inlet channel to cover 120 μm depth and then measurements were performed on the second (right ROI in Figure 7.2) half of the inlet channel so that it covers all 120 μm deep inlet channel as shown in Figure 7.2. The experimental fluid (de-ionized water seeded with 860 nm fluorescence particles) enters through a single chan-

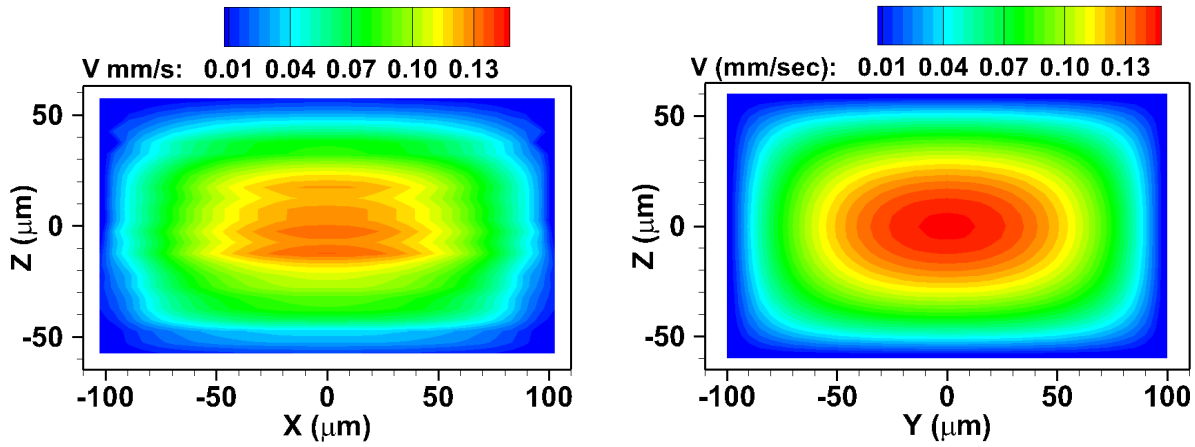

(a) (b)

Figure 7.3: Velocity distribution (a) Experimental (b) Analytical in a cross section of an inlet channel of 2.5D PMMA low resolution micro-model. Experimental conditions –Polystyrene fluorescent 860 nm particles; net flow rate 100 nL/min; particle concentration of 9.54 particles/pL (0.32% by volume).

nel. Ensemble average velocity over 449 pairs of an instantaneous velocity field along with analytical results are presented in this section. Before proceeding more in detail, Figure 7.3 compares the velocity magnitudes of the particle experiment and analytical solution over cross section area of the 2.5D micro-model inlet, which reveals good agreement between analytical solution and particle experiment.

Flow through the inlet channel is studied using 860 nm polystyrene particle (9.54 partilcles/pL concentration or 0.32 % by volume) coated with fluorescence dye at a flow rate of 100 nL/min. Experiments at various depth were studied and compared with the analytical solution of fluid flow in a rectangular channel. Figure 7.4 represents lateral velocity profiles of nano-particles and compared with analytical velocity profiles of the single phase fluid flowing in a rectangular channel, close to observation window proceeding to bottom of the rectangular channel with an increment of 5 μm. Z = 0 μm represents the first observation of nano-particle flowing close to coverslip (observation window) and acts as a reference plane for all other measurements in inlet channel. Here, "V" denoted in y axis represents velocity magnitude of nano-particles and fluid flow along flow direction (Y direction). Each velocity profile at different depths behaves similarly (parabolic) but differs in velocity magnitude

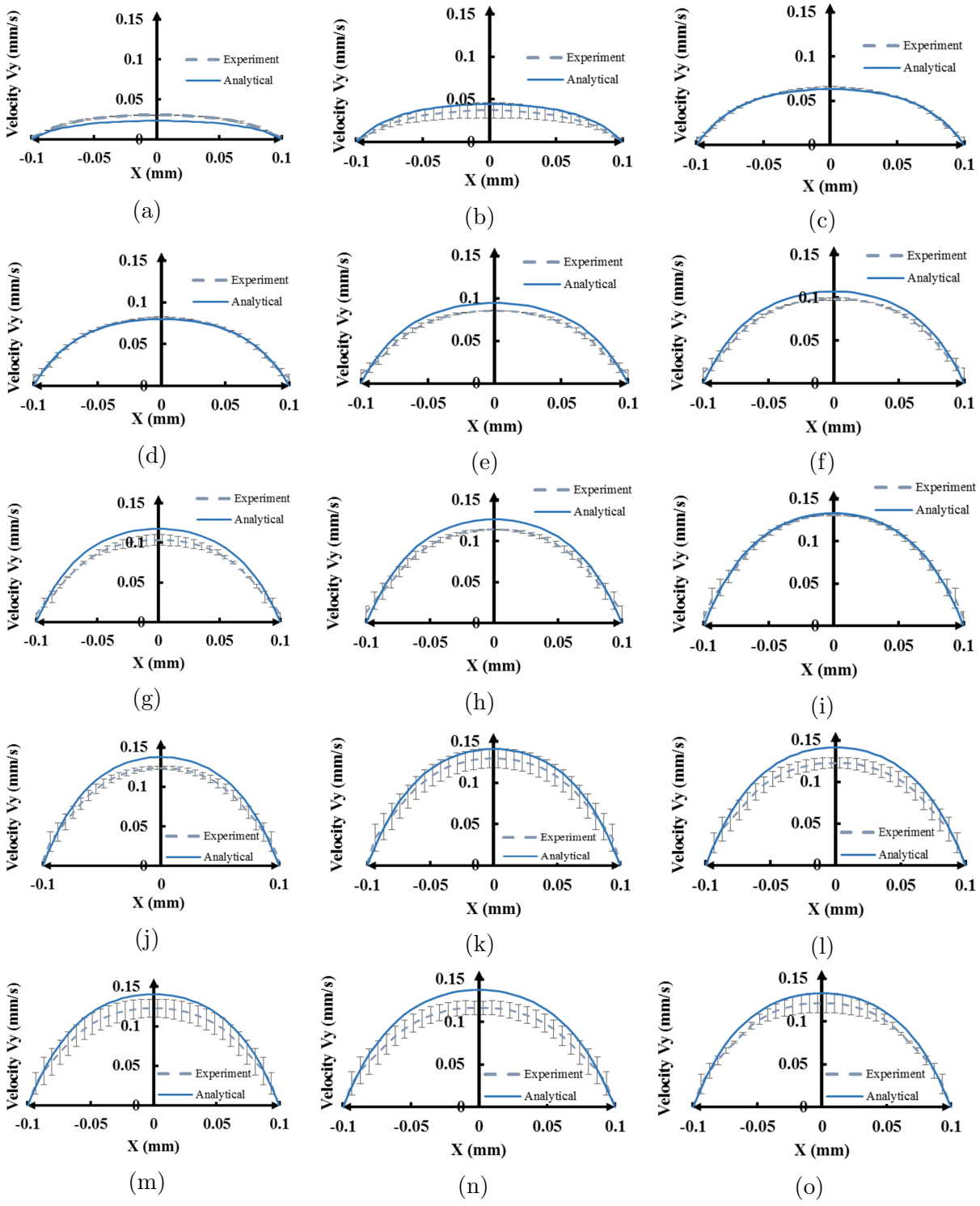

Figure 7.4: Comparison of measured velocity profiles (dotted line) with analytical velocity profiles (solid line) at various depth (a-w) in an increment of 5 μm. Experimental conditions –Polystyrene fluorescent 860 nm particles; net flow rate 100 nL/min; particle concentration of 9.54 particles/pL (0.32% by volume)(figure cont'd.).

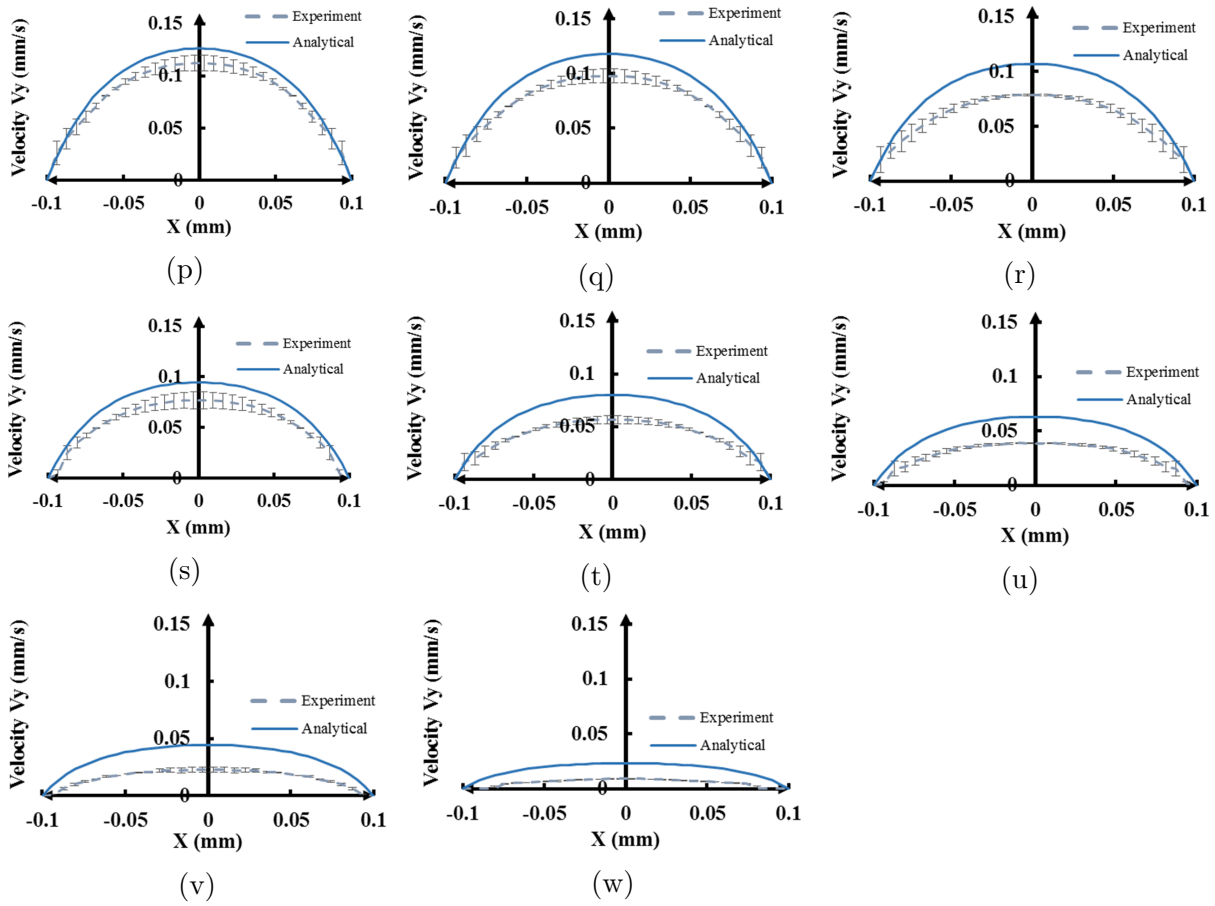

Figure 7.4: Comparison of measured velocity profiles (dotted line) with analytical velocity profiles (solid line) at various depth (a-w) in an increment of 5 μm. Experimental conditions –Polystyrene fluorescent 860 nm particles; net flow rate 100 nL/min; particle concentration of 9.54 particles/pL (0.32% by volume).

flowing at different depths. The velocity magnitude increases from the observation window (Z = 0 μm plane) to mid-plane of the inlet and velocity amplitude decreases as we move further deep from mid-plane to the bottom of the inlet channel. This behavior is well studied and follows in accordance with characteristics of internal laminar flow in a rectangular channel. The maximum velocity amplitude of the profile, measured experimentally, varies slightly with the analytical velocity profile of the system. The maximum velocity amplitude occurs at the mid plane of the channel. As we move further away from the observation window and close to bottom wall of the inlet channel, measured velocity amplitude differs significantly with the theoretical velocity profile as shown in Figure 7.4t-w. The difference in measured and analytical velocity profile near bottom wall of the channel describes prominent effects of wall roughness generated during the demolding process. As bottom wall roughness is not accounted in the analytical solution, which results in higher velocity amplitudes near the wall compared to measured velocity. If a particle to wall interaction model is incorporated in the analytical solution, it may result in comparable velocities near the wall.

7.5 3D Velocity Distributions

Figure 7.5 shows an interior observation location of a Boise rock-based micro-model where 3D measurements of velocity distributions, particle concentration and particle deposition in selected regions were measured. The observation location as shown in Figure 7.5 was chosen because of the principle flow path and flow dominance in the micro-model. It is observed that the velocities measured in this location are close to the highest velocity as expected from prior experiments as well as CFD simulation while designing the Boise rock-based micro-model (see chapter 2 as well as [25, 13] for more details). Nine different regions of interest were used in order to capture the observation location and chapter 5 detailed image patching to synthesize single observation location. The data acquisition procedures have been optimized and a protocol is laid out in chapter 3 and 5, so that measurements cover earlier stage of nano-particles flow in the micro-model focusing on selected

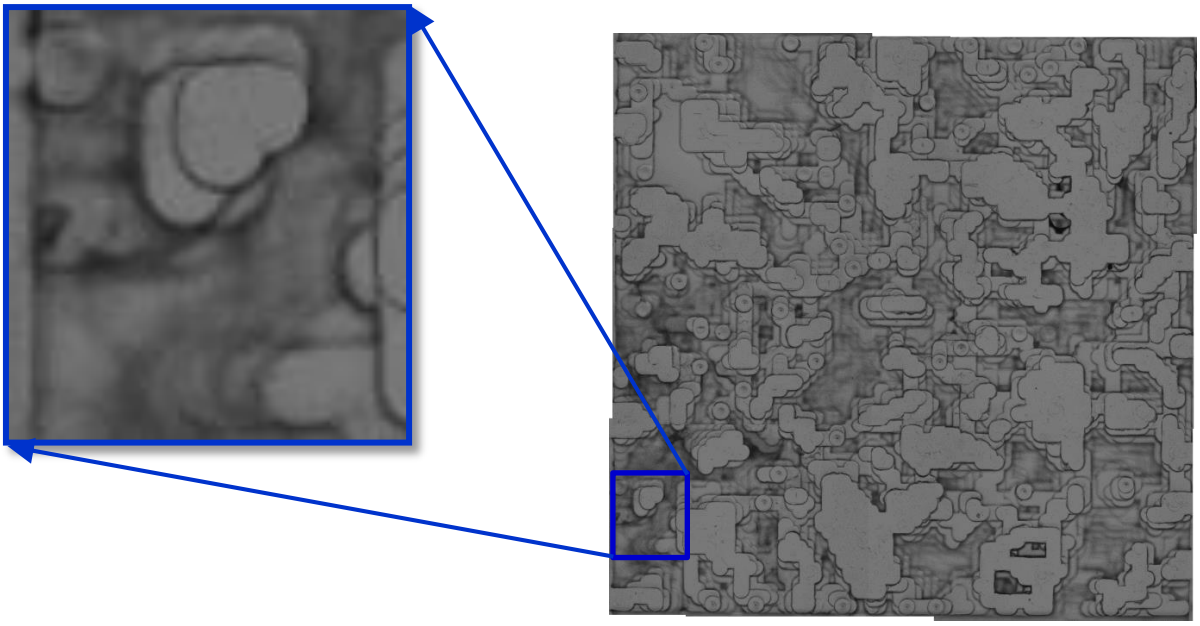

Figure 7.5: Interior observation location of Boise rock based micro-model. Nine overlapping region of interests, each measured as 105 x 105 μm^2, were used to cover internal observation location

observation location with high spatial resolution velocity field and particle concentration. Each region of interest covers 105 x 105 μm^2 of 2 mm x 2 mm rock-based structures of a 2.5D PMMA micro-model. Experimental fluid seeded with 860 nm polystyrene particles (concentration 0.32% by volume; 9.54 particles/pL) coated with fluorescence dye was injected at a flow rate of 100 nL/min. The 3D velocity measurements of the observation location shown in Figure 7.5 are presented in Figure 7.6. Figure 7.6 shows all depths of velocity distribution starting from close to the observation window (Z = 0 μm) proceeding in 5 μm resolution all the way to the highest depth of the observation location. The spatial resolution is approximately 6.6 μm x 6.6 μm x 5.0 μm. Color-code of each vector represents planar(xy) velocity magnitude normalized by streamwise inlet velocity U_0, superposed into a brightfield image of focused observation location at corresponding depth. In this result, Z = 0 μm represents a reference depth characterized by initial observation of nano-particles flowing close to the coverslip (observation window) and acts as a reference plane for all other measurements. The velocity magnitude increases from the observation window to

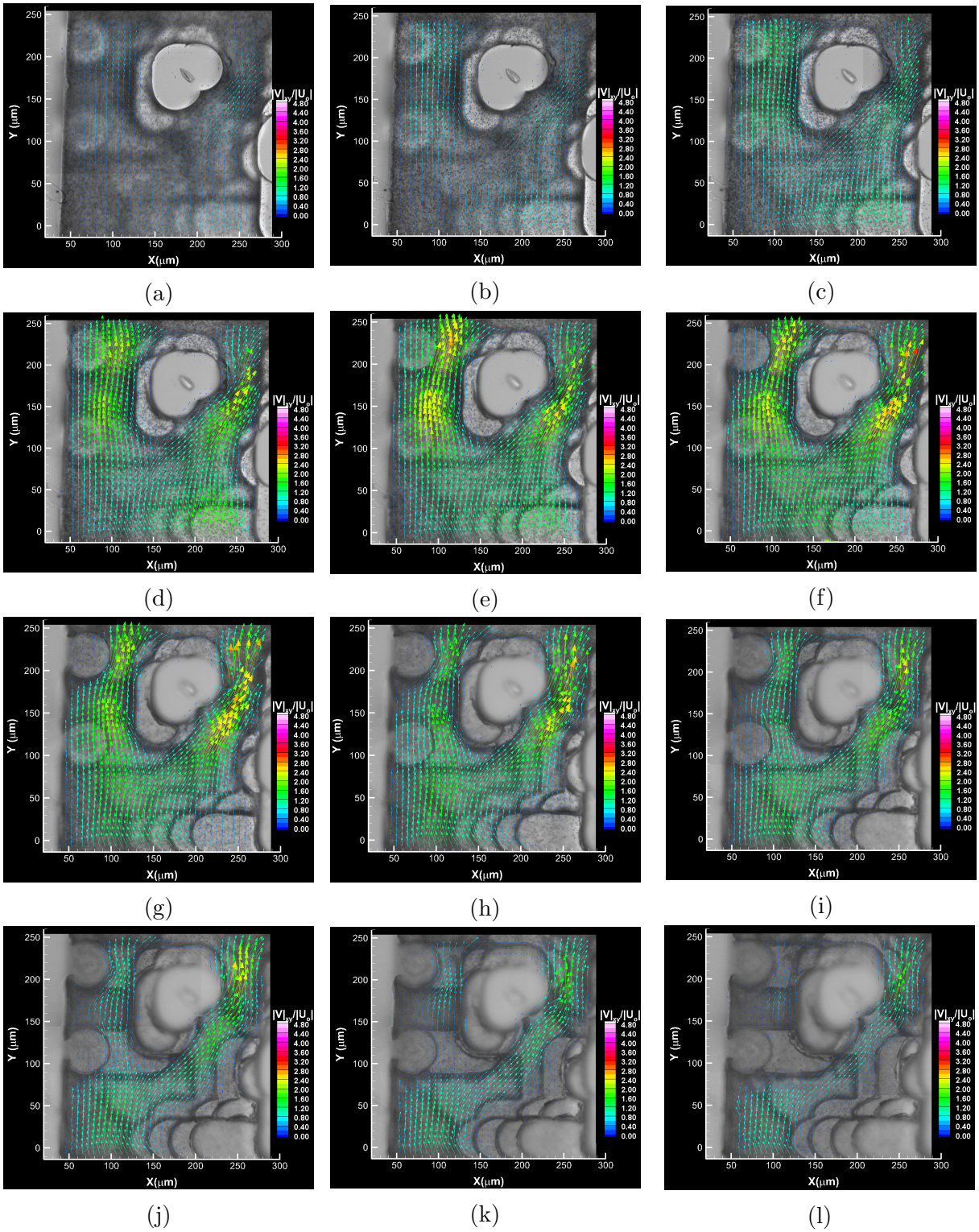

Figure 7.6: Sequence of images illustrating the depth-wise velocity distribution from observation location of Boise rock-based micro-model as indicated in Figure 7.5. Depth is measured from inside wall of the observation starting Z = 0 μm (a) progressing in 5 μm increments through (s), which is bottom of the micro-model at Z = 90 μm. Experimental conditions as same as inlet condition (figure cont'd.).

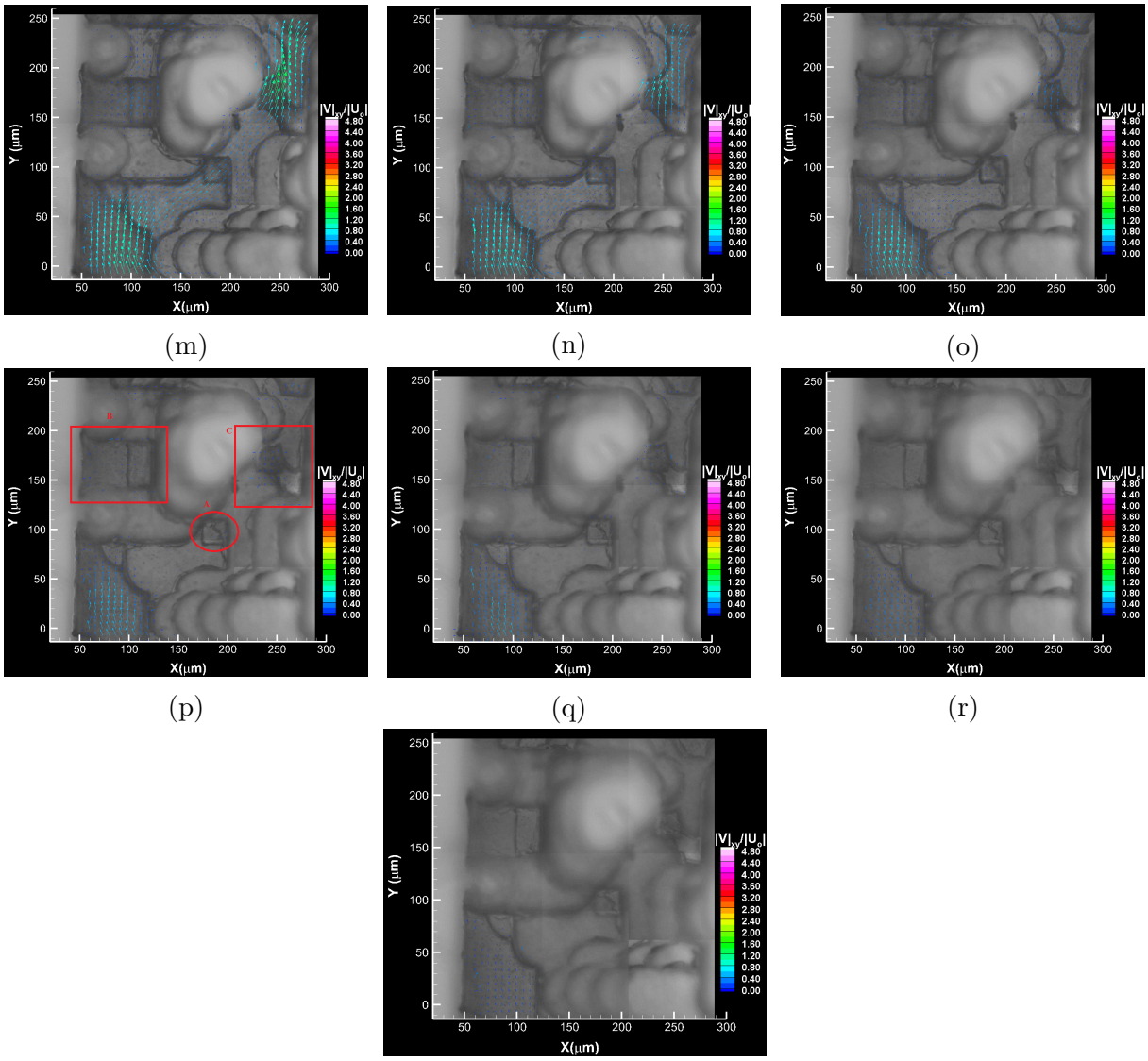

Figure 7.6: Sequence of images illustrating the depth-wise velocity distribution from observation location of Boise rock-based micro-model as indicated in Figure 7.5. Depth is measured from inside wall of the observation starting Z = 0 μm (a) progressing in 5 μm increments through (s), which is bottom of the micro-model at Z = 90 μm. Experimental conditions as same as inlet condition.

the mid-plane and gradually decreases from mid-plane to the bottom of the observation location. Depth-wise highest velocities are observed at a depth of 20 μm to 35 μm, which is almost half of the depth between the first two throat depths. The right throat is narrower (approximately twice) than the left throat. The highest velocities are observed on the right throat because of the smaller cross-sectional area while connected to the same inlet and outlet pressures. The measured velocities on the right throat are biased to lower velocities because particles' velocities exceed maximum displacement resolution used to obtain a high resolution uniform velocity grid. Some of the velocity vectors are in erratic directions because of low sampling particle data on that spatial location. Non-uniform velocity distributions near walls indicate the wall roughness created while demolding PMMA from its master brass mold. The inlet region of the micro-model has dominantly lower velocity than the narrow throat because of a larger cross-sectional area compared to the throat. A velocity close to the wall tends to zero which is an outcome of no-slip condition near walls. A velocity distribution close to the observation window tends to have a higher velocity than the velocity at equidistant from bottom walls. This is because of the dominance of flow path in the system. Figure 7.6 shows most of the flow dominance occurs in between first 5-6 layers as the pore volume close to the observation window is much larger than the bottom part of the micro-model. Hence, it represents a principal flow path (the pathway where the flow is maximum compared to others) of the system. As we move deeper into the observation location, nano-particles flow is limited by the outlet throat size of the observation location. At a depth of Z = 55 μm, the left throat is disconnected to the inlet, which slows down the flow on the left side of the observation location. Due to flow restriction toward the left portion of the observation location, a maximum flow on the right portion of the observation location is observed in order to preserve mass flow in the system. As we move close to Z= 65 μm depth inlet and outlet are planarly discontinued. Beyond the depth of Z = 80 μm, all the flow is restricted in a small domain near the inlet region. Nano-particles trapped on the central region represented by a red circle named "A" in Figure 7.6p exhibit

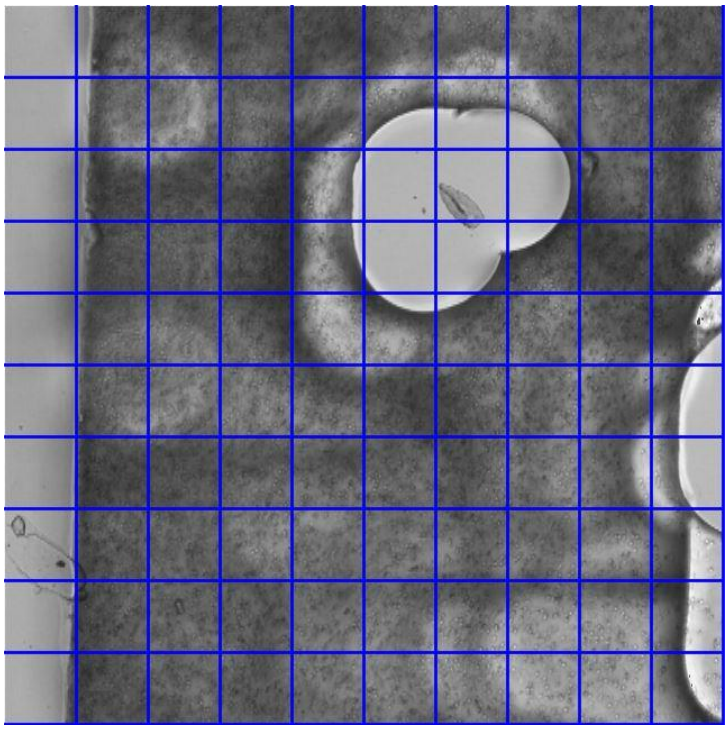

Figure 7.7: Illustration of discretization of bright field image of an observation location into 100 square. Each square measures 26.50 x 26.50 μm^2

as random and non-uniform walk where differential pressure is negligible within the void structure. Rectangular red marks named "B" and "C" in Figure 7.6p represent void areas with no planar flow connectivity and nano particles flowing in those areas also show random walk as there is no significant pressure gradient to overcome random motion of those particles at the plane of observation.

7.6 Discretization and Image Processing

Raw images captured from nine regions of interest are synthesized to obtain a 265 x 265 μm^2 single field image by using image patching algorithm as described in Chapter 5. Each single field image is further discretized into 100 equal parts; each measures as 26.50 x 26.50 μm^2. All the particles flowing in each discretized region are calculated using a MATLAB script. Each discretized region consists of particles flowing on it, providing a spatial resolution to the particle concentration of the observed region. Figure 7.7 is the illustration of discretization of a bright field image into 100 equal parts.

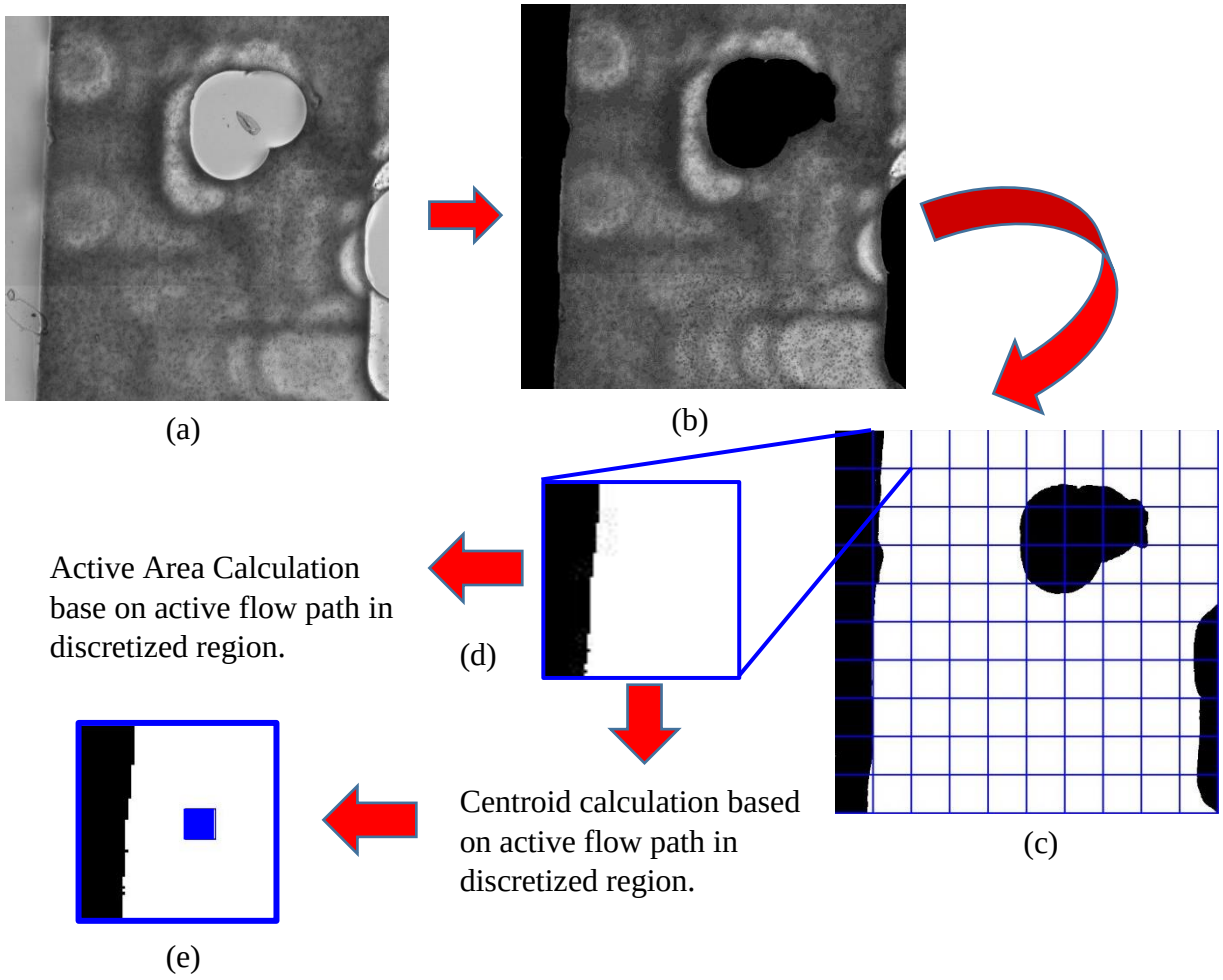

Figure 7.8: Schematic illustration of active area and centroid calculation for each discretized region. (a) Bright field image (b) image showing non active flow area with dark color (c) conversion of image (b) to binary image (d) close up view of one discretized region (e) discretized region showing areal centroid of the active flow region.

7.7 Active Area and Centroid Calculation

It is necessary to calculate an active area (area where particles are viable to flow) in order to measure particle concentration per unit pore volume. Before proceeding in the area calculation, all inactive parts, where nano particles cannot flow, are segmented as dark regions in bright field image bases on nano-particle experiment. The brightfield image is converted into a binary image where pixels are registered as black ("0") or white ("1"). Once the brightfield image is converted into a binary image, it is discretized into 100 equal 26.5 x 26.5 μm^2 parts. Base on active flow path in the discretized region, each active area

and centroid is calculated. Figure 7.8 shows a schematic illustration of active area and centroid calculation for each discretized region.

$$Area(A) = \sum_{i=1}^{n} A_i \tag{7.8}$$

$$\bar{X} = \frac{\sum_{i=1}^{n} x_i A_i}{\sum_{i=1}^{n} A_i} \tag{7.9}$$

$$\bar{Y} = \frac{\sum_{i=1}^{n} y_i A_i}{\sum_{i=1}^{n} A_i} \tag{7.10}$$

where A_i is binary area ("0" of "1") in pixel of a digital discretized image, ($\bar{X}$,$\bar{Y}$) is the centroid of the discretized active area A in the flow field.

7.8 Particle Concentration

Inlet

Inlet particle concentrations per unit pore volume were measured in 3D and Figure 7.9 shows measurements of 3D particle concentration at 24 measured depths. At each depth, the particle concentration was extracted at 8 spanwise locations covering 200 μm and 4 streamwise locations spanning 100 μm. Each position in the scatter plot, determined based on the active flow path in the discretized region, offers $\approx$ 25 μm lateral resolution which allows us to measure 3D particle concentration profiles in the inlet. The color map represents particle concentration per unit pore volume in the discretized location. A high degree of uniformity of particle distribution in streamwise is an evidence of a self-similar solution, as expected. The uniform particle distribution adds confidence that the measurement is consistent and reliable. Reasonable uniform particle distribution is observed along the spanwise direction except close to the wall. Particle concentration per unit pore volume seems larger at the edge of the inlet side walls because of low pore volume of discretized regions close to the wall, although it has lower particle concentration compared to the central location, which can be illustrated in Figures 7.9c and 7.9d. The depth-wise particle

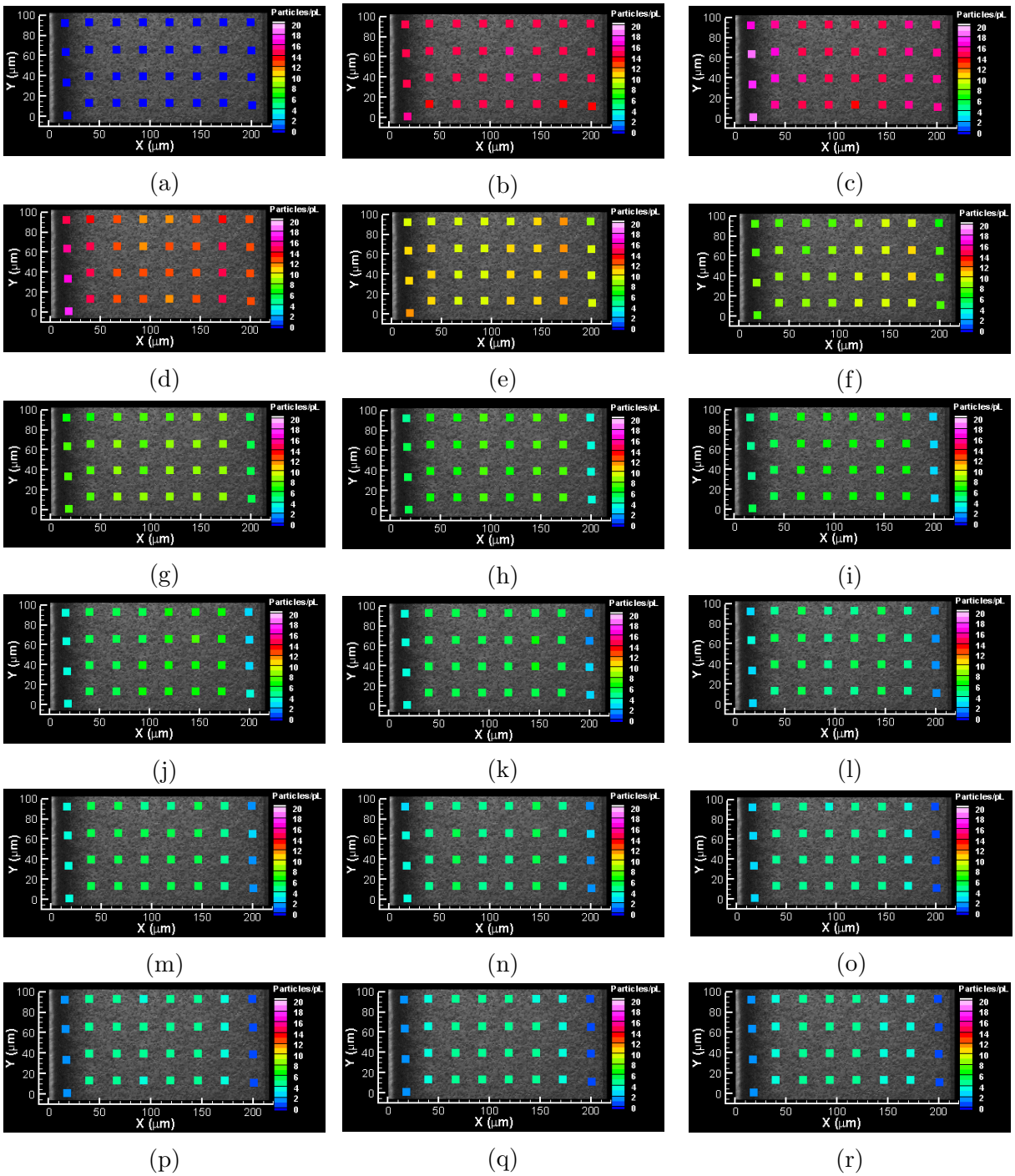

Figure 7.9: Illustration of depth-wise particle concentration distribution in the inlet channel starting depth "Z = 0 μm" inside of the observation window proceeding to bottom of the inlet channel with an increment of 5 μm. Experimental condition are same as velocity measurement at inlet and (a) represents particle concentration per unit pore volume very close to observation window "Z= 0 μm" and acts as reference plane, progressing deeper to the bottom of the channel (x) "Z= 115 μm" (figure cont'd.).

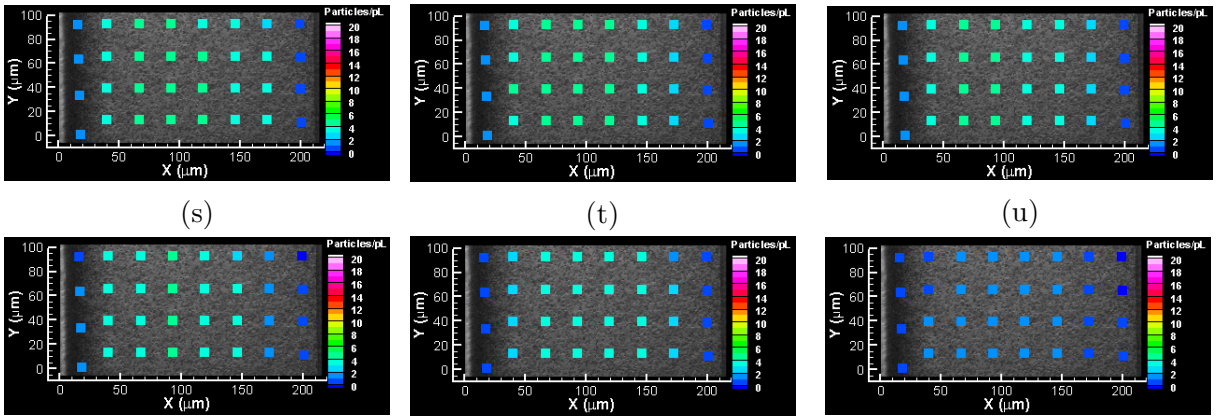

(s) (t) (u)

(v) (w) (x)

Figure 7.9: Illustration of depth-wise particle concentration distribution in the inlet channel starting depth "Z = 0 μm" inside of the observation window proceeding to bottom of the inlet channel with an increment of 5 μm. Experimental condition are same as velocity measurement at inlet and (a) represents particle concentration per unit pore volume very close to observation window "Z= 0 μm" and acts as reference plane, progressing deeper to the bottom of the channel (x) "Z= 115 μm".

distribution varies with highest particle concentration per pore volume at Z = 15 μm, away from the observation window. As we move deeper into the channel, the particle concentration declines very gradually down to the bottom of the inlet channel. Based on the velocity profiles, the particle concentration is supposed to be the highest at the mid plane of the inlet channel but the highest particle concentration occurs close to the observation window. As flow is injected through the nano-port connector opposite to the observation window, it has to turn a sharp right angle in order to proceed flow into inlet channel. This might create flow impingement in the system and may favor initial higher particle concentration near the observation window.

Internal Observation Location

Figure 7.10 represents particle concentration profiles at all depths starting with Z= 0 μm proceeding in 5 μm depth increment all the way to the highest depth of the location "Z = 90 μm". Similar to the inlet, each grid point is superimposed to a bright-field image representing a particle concentration flowing through varying active area. The maximum area of an active domain is 26.5 x 26.5 μm^2. The color code indicates particle concentration

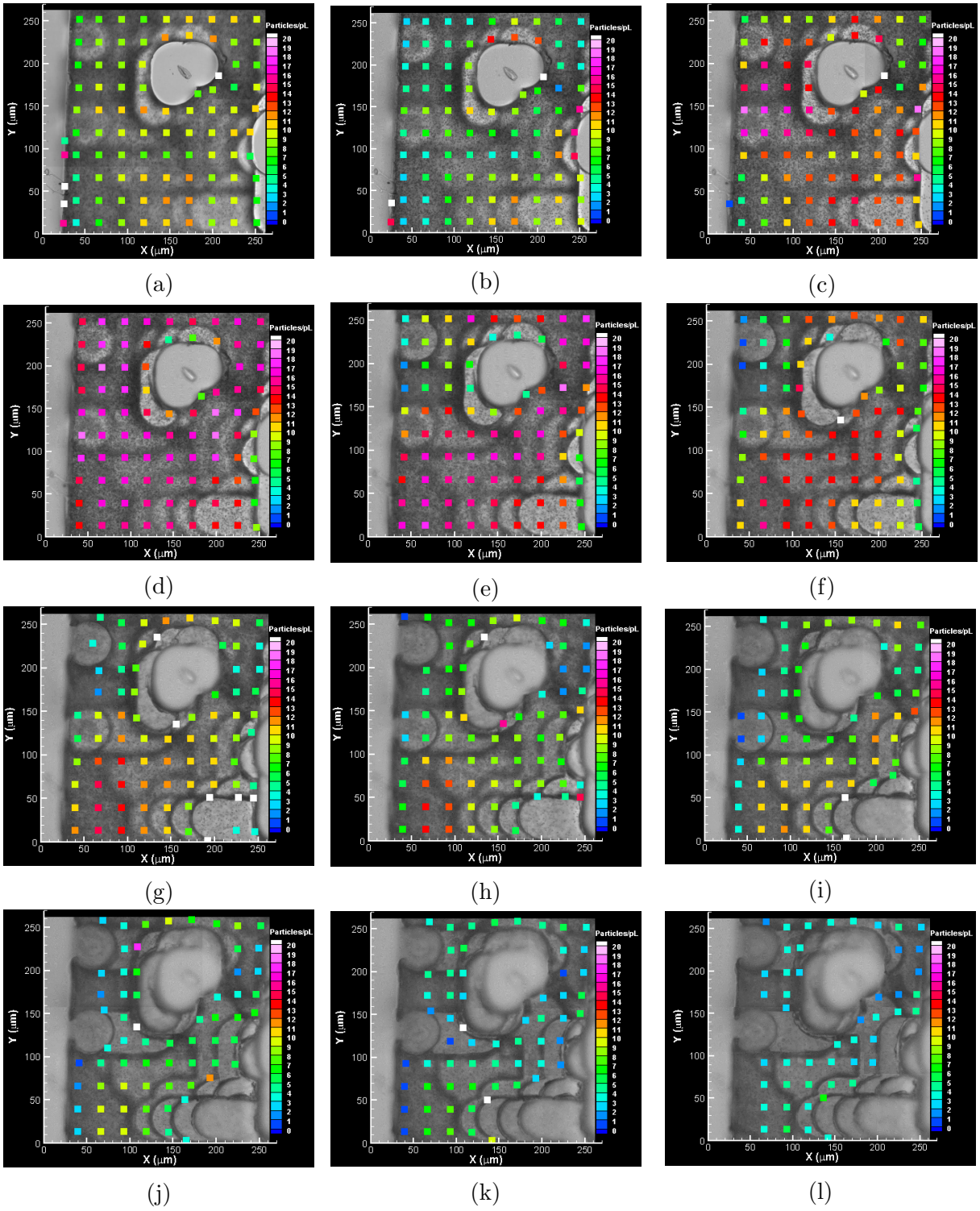

Figure 7.10: Illustration of depth-wise particle concentration distribution at internal observation location starting depth "Z = 0 μm" inside of the observation window proceeding to bottom of the inlet channel with an increment of 5 μm. Experimental condition are same as velocity measurement at inlet and (a) represents particle concentration per unit pore volume very close to observation window "Z= 0 μm" and acts as reference plane, progressing deeper to the bottom of the channel (s) "Z= 90 μm" (figure cont'd.).

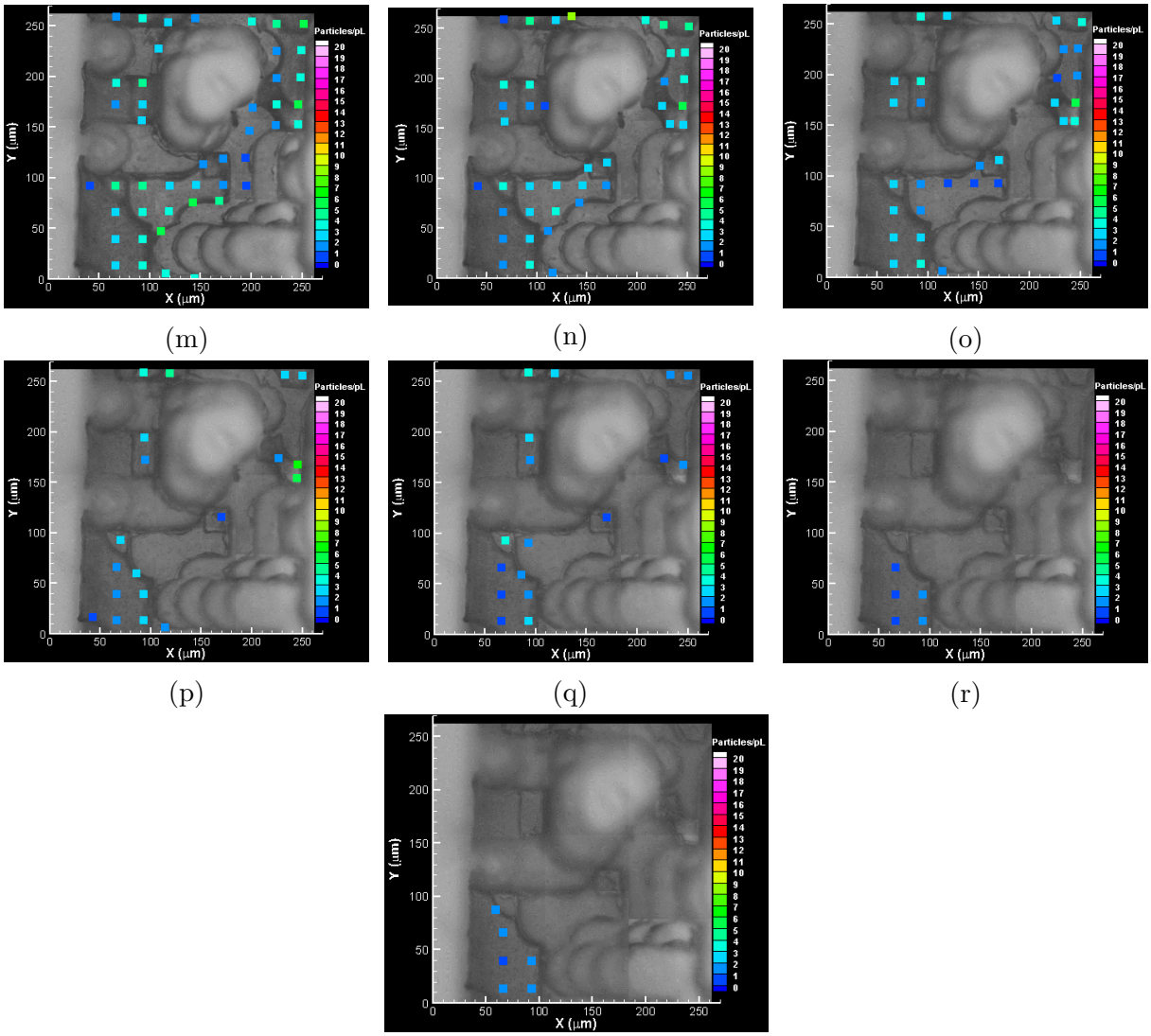

Figure 7.10: Illustration of depth-wise particle concentration distribution at internal observation location starting depth "Z = 0 μm" inside of the observation window proceeding to bottom of the inlet channel with an increment of 5 μm. Experimental condition are same as velocity measurement at inlet and (a) represents particle concentration per unit pore volume very close to observation window "Z= 0 μm" and acts as reference plane, progressing deeper to the bottom of the channel (s) "Z= 90 μm".

per unit pore volume in discretized locations. The highest particle concentrations in the observation location are observed at active principal flow paths in the system. A higher peak particle concentration is observed within the depth of 10-15 μm from the observation window, similar to that of the inlet particle concentration. As we move deeper into the location, particle concentration also declines accordingly after the depth of Z = 20 μm. Lower particle concentration is observed close to non-moving wall boundaries of the micro-model. From Figure 7.6 and Figure 7.10, there seems to be a relationship between velocity and particle flowing concentration, but this remains to be proven yet. Higher velocity regions seem to have higher particle concentrations at same planes and depths of the system. Particle concentration close to the bottom wall has lower concentration and behaves in a similar fashion with velocity distribution. Particles flowing close to the bottom walls have less connected porous structures compared to top wall, resulting in lower particle concentration. Although particles flowing equidistant from the top and the bottom wall, the flow and particle concentration are dominant close to top wall because of higher connected porous structures as well as the principal flow path of nano-particles in the system. There are fewer flow impediments close to the top wall (near the observation window) compared to the bottom wall which affects the particle flow in the system. Numerous pockets are present as we move close to the bottom wall, which aid in flow resistance in the system. A deep pocket acts as trapping zone in which particles tend to experience Brownian motion and divert from ideal particles which signify a fluidic flow path as shown in Figure 7.6p. Due to random motion behavior, those particles trapped in the packet represent repetition of the same particles counts in 450 images. The possibility to have lower particle concentration in a pocket region is due to negligible convectional force and flow solely depends on diffusion force in those pocket areas. The pressure gradient along axial plane is negligible and has negligible effect on the particle diffusion in those pocket regions.

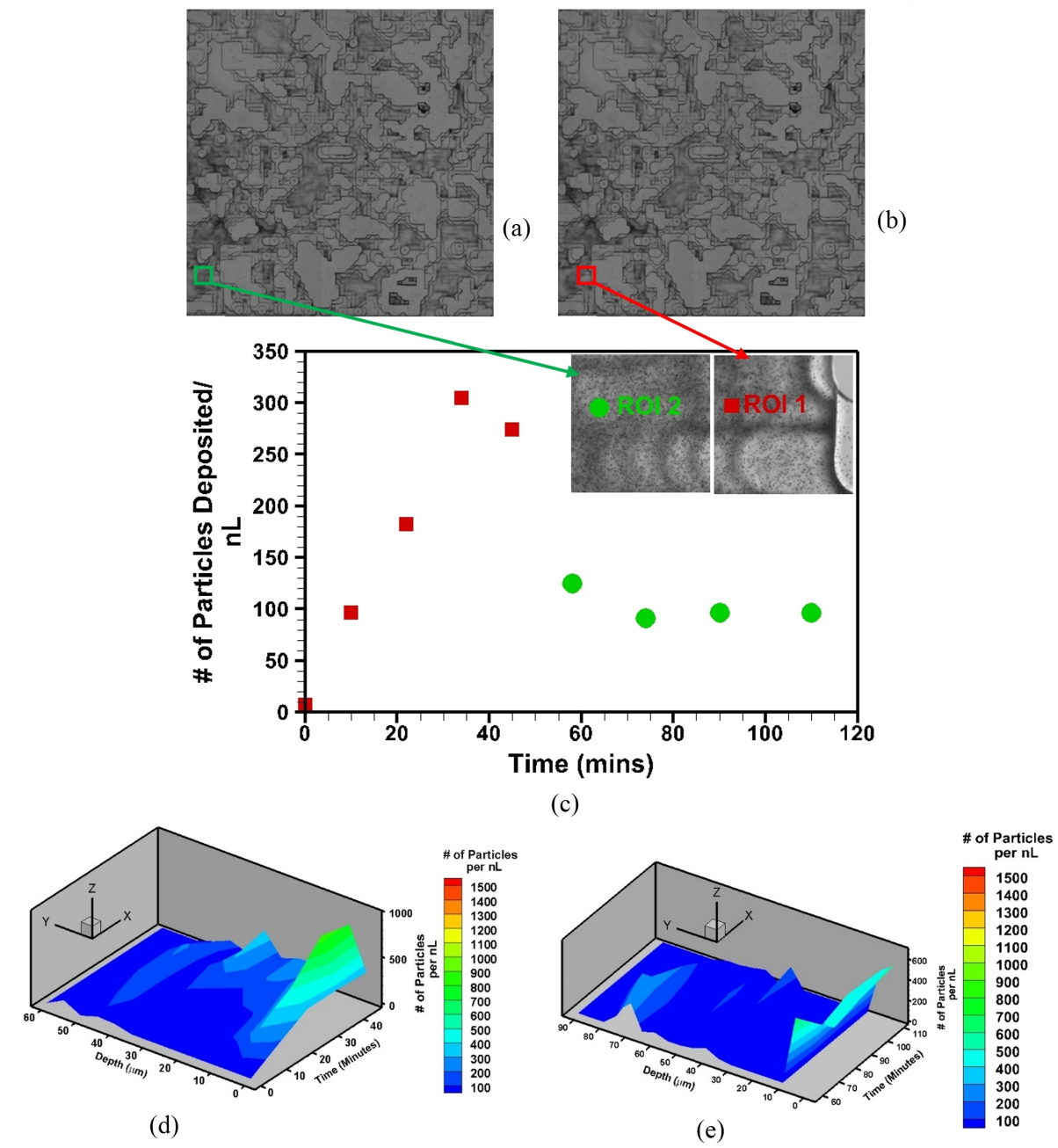

Figure 7.11: (a), (b) show region of interest where particle deposition measurements were taken. (c) shows particle deposition in all walls of two different ROIs within the observation location indicated in the Figure (a) and (b), and (d) and (e) show detail deposition of nanoparticles at different planes over period of time. Experimental conditions –Polystyrene fluorescent 860 nm particles; net flow rate 100 nL/min; particle concentration of 9.54 particles/pL (0.32% by volume).

7.9 Particle Deposition

Figure 7.11 shows a sample of deposition evolutions over time measured at two of the partially overlapped region of interests. The deposition includes deposition on all walls and represented in number of deposited particles per volume basis. The reference volume is the volume filled with fluid of each region of interest. Region of interest I (ROI-I) is a shallower region compared to region of interest II (ROI-II) as illustrated by Figure 7.11d and 7.11e. Region of interest I shows initial $\approx$ 45 mins deposition rate after the injected particle reached to the entrance region of rock-based structures of the micro-model at the flow rate of 100 nL/ min. Particles start depositing rapidly in the ROI-I for first 30 minutes and particle deposition starts declining after 30 minutes in region of interest I; a sign of deposition slowdown. Figure 7.11d shows number of deposited particles per volume at various planes of ROI-I shown in Figure 8.17b over a period of time. Most of the nano-particles are deposited on the coverslip compared to any other planes in the ROI-I. This indicates that particle deposition are predominant on a flat coverslip than the side and bottom walls.

After completion of capturing initial nano-particle deposition phenomenon at ROI-I, the stage was moved left of ROI-I to capture nano-particle deposition phenomenon at ROI-II. ROI-II is deeper than ROI-I and partially overlapped with ROI-I. Initial nano-particle deposition data at region of interest II was acquired approximately 55 minutes after the injected particles reached to the entrance region of rock-based structures of micro-model. Figure 7.11e shows the number of deposited particles per unit volume at various planes of ROI-II. Although particle data was collected after approximately 55 mins, it shows a constant deposition of 100 particles/nL regardless of time period. This indicates that simultaneous deposition and detachment of nano-particles occurs after approximately 55 mins at ROI-II. The lower particles deposition per unit pore volume at ROI-II compared to ROI-I, seems to have lower deposition per unit volume because of comparatively large fluid volume rather than reduced particles deposition. Similar to ROI-I, most of the nano-

particles are deposited on the coverslip compared to any other planes in the ROI-II and particle deposition is more predominant on the flat coverslip than the side and bottom walls. The larger contact surface area of nano-particles with PMMA smooth coverslip and viscous layer may be the effect on higher deposition rate on cover slip than side walls and bottom wall of the micro-model. This indicates that particle deposition is more vigorous during the earliest injection period and is not constant throughout the injection period.

7.10 Computational Model

To simulate the flow in 3D in-situ geometry, extracted using the in-situ geometry extraction technique described in chapter 4, a computational fluid dynamics program, ANSYS FLUENT 15.0, is used. The governing equation for pressure driven flow is non dimensionlized and numerically solves steady state Navier-Stokes equations. This section will cover details of numerical simulation of flow in 3D in-situ geometry and comparision of the velocity field with the experimental result.

Governing Equations

The governing equation used for pressure driven flow in pore space geometry are the steady state Navier-Stokes equation and continuity equation.

$$\nabla \cdot u = 0 \tag{7.11}$$

$$(u \cdot \nabla)u = -\frac{\nabla P}{\rho} + \nu \nabla^2 u \tag{7.12}$$

In the above equations, u= u(x), and P=P(x) are the dimensional Cartesian velocity vector and pressure respectively. ρ and ν represents fluidic properties: density and kinematic viscosity respectively. The dimensional equations are transformed into non-dimensional quantities using following non-dimensional parameters.

$$x^* = \frac{x}{L_c}$$

$$u^* = \frac{u}{U_0}$$

$$P^* = \frac{P}{\rho U_0^2}$$

The non-dimensional Navier Stoke and continuity equations are:

$$\nabla^*.u = 0 \tag{7.13}$$

$$(u^*.\nabla^*)u^* = -\nabla^* P^* + \frac{1}{Re_{L_c}}\nabla^{*2}u^{*2} \tag{7.14}$$

In the above equations, u* and P* are non dimensional Cartesian velocity vector and pressure respectively, where as Re_{L_c} is Reynolds number of the flow in the porous medium, and L_c is the characteristic length of the micro-model.

Mesh

The 3D in-situ geometry is discretized using a tetrahedral patch independent method. This method creates a volume mesh from the closed geometry and extracts a surface mesh from the boundaries. The patch-independent method ignores gaps below the critical mesh size. This is the direct approach of extracting volume from the closed complex geometry and creating mesh surface from the volume. Figure 7.12 shows mesh generated for a full scale Boise rock-based micro-model extracted from in-situ geometry. After a grid independence check through grid node doubling the unstructured grid used for the simulations using the experimental micro-model geometry was of the order of 12M nodes.

Results

The CFD simulation results were compared with experimental results at the observation location shown in Figure 7.5 are presented in Figure 7.13. In the figure the velocity contours shown at each depth on the left are the simulated ones, while on the right are the measured contours with velocity vectors superimposed. The comparison is very good overall with the exception of the highest velocity regions where the limited ability to cap-

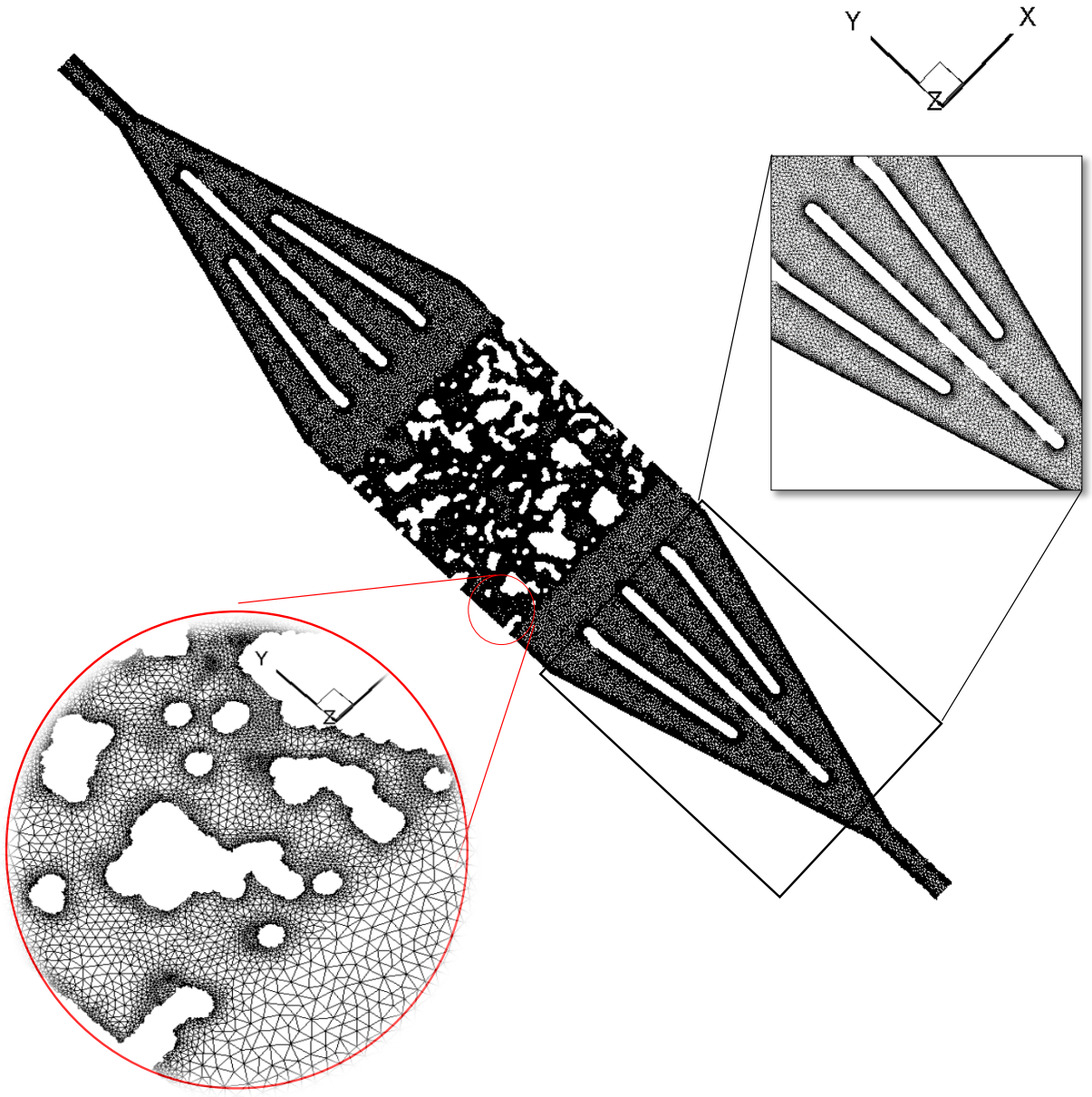

Figure 7.12: Unstructured tetrahedral mesh of an experimental geometry (PMMA Boise Rock-Based Micro-model).

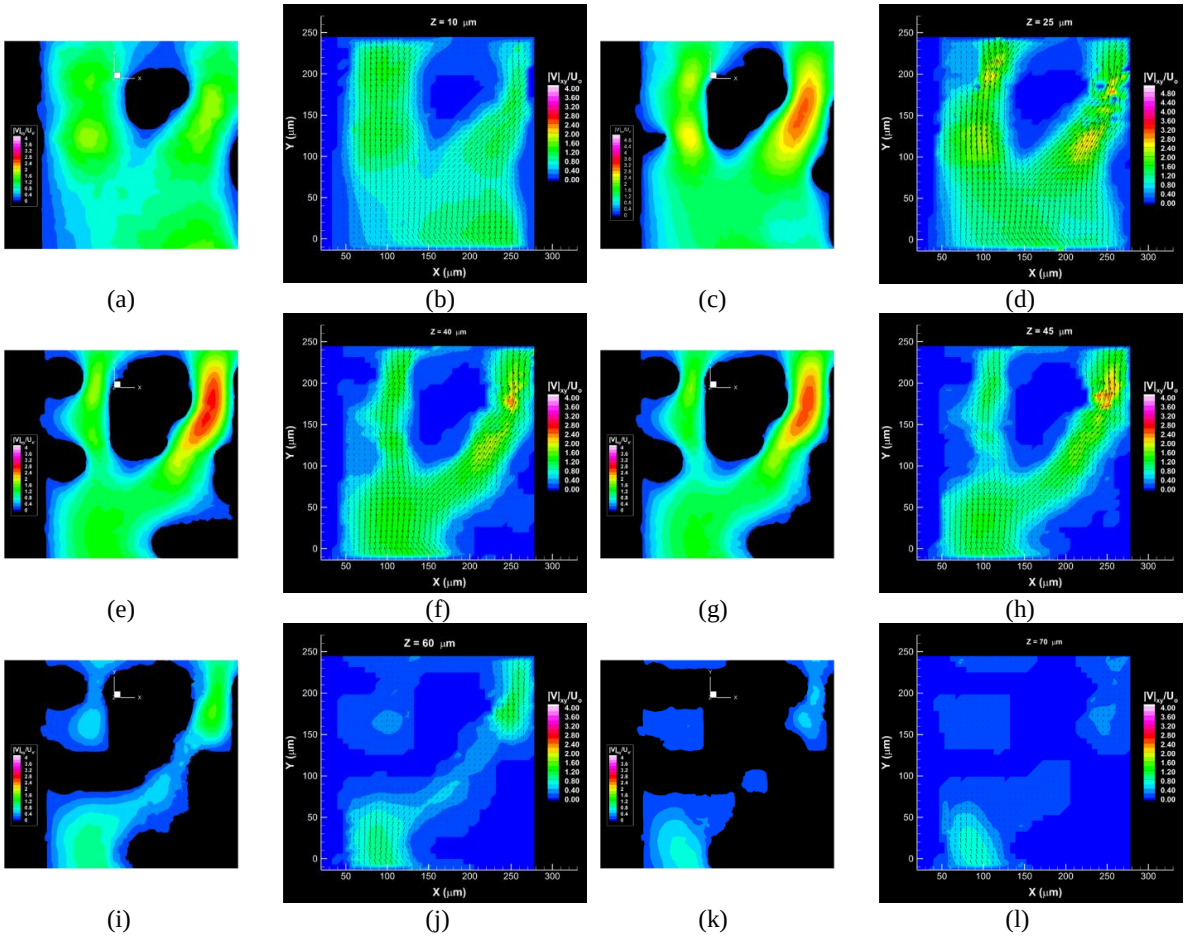

Figure 7.13: Comparison of Computational Fluid Dynamics simulation results (a, c, e, g, i, k) to experimental measurements (b, d, f, h, j, l) at various depths at the experimental observation region. Contours shown are of the velocity magnitude of the fluid for the simulation and of the particles for the experiment. The simulation was carried out over the entire micro-model geometrical domain as measured in-situ using the fluorescence technique with experimental inlet conditions. Experimental conditions as Figure 7.4.

ture the highest velocities in the experiment is evident (right throat). In addition, some differences are evident near solid boundaries because in the experiments it is the velocity of particles that is recorded while the simulation produces fluid velocities. For example, looking at the upper left corner of the contour plots of Figure 7.13c and Figure 7.13d, it is evident that the velocities over the surface of the blocking protrusion on the left side are higher in the simulation relative to the experiment. The protrusion is visible in black at the deeper plane of Figure 7.13e and Figure 7.13f. This difference is natural because particles measured in the experiment interact with, and are slowed down by, the top wall of the protrusion, and illustrates the importance of taking into account particle-fluid-wall interaction in the simulations. It should be noted that experimental velocity contours at the fringes of the observation region are not reliable because the contouring is biased by the lack of information in these bounding areas. The overall agreement is good between these results from the CFD simulation of the flow over the entire micro-model domain and the local experimental particle velocity distributions. This is true in terms of validating the methods used to tailor the experiments for consistency with simulations regarding the geometry of the micro-model domain and the required inlet conditions. They provide a solid basis for comparisons of experiments and simulations of particle mobility using the pore-scale models developed by our group and others.

7.11 Conclusion

In this chapter, a series of new imaging techniques along with post processing techniques introduced in chapter 5 and 6 have been employed to examine nano-particles motion in a low resolution rock based 2.5D micro-model. Micro-particle image velocimetry is used to measure the velocity distribution along with inbuilt mobile particle separation from the raw image algorithm explained in chapter 6 is also engaged to measure high resolution velocity distribution in the micro-models. All of these measurements were performed in 3D using a confocal fluorescence microscope system. Experimental procedures have been optimized so that the maximum area of observation location can be covered to capture

particles flowing in the micro-model. 3D measurements of nano-particles flowing in one of the observation locations from the principal flow path consists of 9 ROIs, which were synthesized using image patching algorithm explained in chapter 5 to cover particle flow domain, is presented in this chapter. We have successfully captured a flow field of the inlet channel as well as the behavior of nano-particles at different observation locations. A sample of nano-particle velocity fields, concentration and deposition evolutions over a period of time at an observation location are presented in this chapter. The experiment results illustrated that a confocal micro-particle image velocimetry (C-μPIV) system along with algorithms developed for post-image-processing can be used to quantify a 3D distribution of nano-particle concentrations and velocity fields in a steady state laminar flow inside a complex Boise- rock-based porous media with pore size less than 25 μm. The velocity fields along with nano-particle concentrations and particle deposition over time were successfully studied at different planes in different pore structures, which provides insights of nano-particles transport mechanisms in porous media. 3D measurements of nano-particle transport in the rest of the observation locations from principal flow path are also presented and explained in appendices B, C and D. CFD simulations results were compared with experimental results of one of the observation location shown in Figure 7.5 and a very good overall velocity comparision is found. Some of the highest velocity regions were unable to compare one to one due to the limitations of the confocal micro-PIV system whereas overall good agreement between these results provide a solid basis for flow distribution over the entire micro-model domain. Pressure distribution as well as velocity distribution over an entire low resolution in-situ 3D as experimented micro-model are presented in appendix E.

Chapter 8
3D Measurement of Nano-Particles Transport in 2.5D Ceramic Micro-Model*

This chapter presents 3D measurements of velocity, concentration and particle deposition in 2.5D ceramic rock-based micro-models of neutrally buoyant and electrically-neutral fluorescent nano-particles flowing through complex and an opaque 2.5D ($\approx$ 20 μm resolution) ceramic micro-model, which is derived from a Boise sandstone sample optimally matching fourteen key parameters, by using a confocal microscope. The ceramic micro-model is composed of alumina, alkali borosilicate glass powder, and thermoplastic binders such as PEG 6000 and PEG 200 that acts as surrogate for Boise rock sandstone. A detailed procedure of the microfabrication can be found in Khurshida Sharmin's dissertation [102]. Besides geometric, and fluidic-dynamic consistency of the 2.5D micro-model, the ceramic micro-model also allows us to investigate 3D flow as well as acts as a test bed for nano sensors developed by AEC and delivery agents in harsh experimental conditions like high temperature, and high pressure similar to reservoir conditions. These measurements provide insight of the particles interaction with the ceramic micro-model along with exploring the physics of nano-particles in ceramic base micro-models. The polystyrene nano-particles are used in visualizing a flow field inside the ceramic micro-model. In this chapter, we have described and presented 3D velocity distribution, 3D particle concentration distribution and particle deposition on the inner walls of selected regions of interest of 2.5D ceramic micro-model.

*some of the materials are republished with permission from "Fabrication and Flow Visualization for 2.5D Rock-Based Ceramic micro-models by Daniel S. Park, J. Upadhyay, J. K. Sharmin, J. F. Robbins, I. Schoegl, K. E. Thompson, and D. E. Nikitopoulos, Paper No. IMECE2017-71630 by ASME and "Flow Visualization and 3D Measurements of Nanoparticle transport in Rock-Based 2.5D Micro-Models" by Jagannath Upadhyay, Daniel S. Park, Khurshida Sharmin, Ingmar Schoegl, Karsten E. Thompson, and Dimitris E. Nikitopoulos, Paper No. IMECE2017-71698 by ASME

8.1 Introduction

A solid understanding of the physics behind multiphase flow in ceramic porous media is important for applications such as oil recovery, geological CO_2 sequestration, fuel cells, nuclear devices, chemical reaction and nano-particle transport. Use of a ceramic micro-model is of interest because of its novel properties like thermal, chemical resistance, dielectric and piezoelectric properties that cannot be met by thermoplastic materials or metals [103]. Molding of powder based ceramic materials is one of the cheapest as well as easiest methods of microfabrication, but the microfabrication of the ceramic based micro-model is challenging because methods for development, design and production of ceramic micro-model have not been fully established. Various design and fabrication techniques have been proposed, but production and microfabrication of microstructures is still lacking within the current state of ceramic microfabrication.

Particle image velocimetry is applied to measure a field instantaneous scalar and vector fields of nano-particles flowing in the ceramic micro-model devices. 3D velocity distribution, 3D particle concentration and deposition rate are of importance to understand how nano-particles interact in a non-plastic, rough ceramic micro-model, which provides insight in understanding the physics of nano-particles on a microscale as well as incorporating it into a microscale modeling scaled up to a field scale simulation. Once all the interactive phenomenon are well understood, it will aid not only in microscale modeling but also in improving higher hierarchy modeling (pore scale to field scale) for better understanding of flow in the reservoir. In this chapter, we have quantified as well as extracted flow information of nano-particles flowing in a ceramic Boise rock-based micro-model. Experimental data presented in this chapter opens a new era of understanding physics of nano-particles in a 2.5D opaque ceramic micro-model which aids in modeling real application base flow simulation not only in the oil and gas industry but also in understanding transient chemical reactions of multiple species in chemical resistant platforms. Besides, this capability of fluorescence based 3D in-situ geometry extraction of a complex 2.5D ceramic microstructure

is also presented and discussed in this chapter.

8.2 Microfabrication of the Ceramic Based 2.5D Micro-model

55 % precursor alumina powders and 45 % polymer binders (a mixture of polyethylene vinyl acetate and polyethylene glycol) were used to prepare a green sample using a torque rheometer. The green sample batch was extruded to produce 3 mm thick green ceramic tape using a custom design tape extruder (I. Schoegl Research Group). The 3 mm thick extruded green tape acts as a molding substrate during the hot embossing process to replicate negative patterns of a master mold. The master mold was fabricated using multi-layer SU-8 lithography and Nickel (Ni) electroforming [52]. A molding pressure of 1.25 Metric tons was applied along with molding temperature of 125^0C for a few seconds and 25^0C as the demolding temperature. Once a negative replica is transformed into a ceramic substrate, a series of solvent extractions as well as thermal debinding processes were performed to remove binder mixture from the ceramic micro-model. Sintering is followed after sealing the embossed ceramic micro-model with a transparent glass slide. The sealing takes place using a thermal fusion bonding method at a fusion temperature of 650^0C to 800^0C. Installation of nano-ports takes place after ceramic sample is completely bonded with glass coverslip. Figure 8.1a shows the 2.5D ceramic rock-based micro-model with fourteen different layers, whereas Figure 8.1b shows close up view of the rectangular in lay of the micro-model. Figure 8.1c shows the shrinkage of green tape sample after sintering. Figure 8.2 shows microscopic images of the 2.5D ceramic rock-based micro-model in which experiment was performed. Figure 8.2a shows an isometric view of the 2.5D ceramic micro-model. Figure 8.2b shows the top view of the micro-model illustrating the inlet and outlet nanoports where experimental fluid was injected and dispensed respectively. Figure 8.2c shows the bottom view (observation/visualization window) of the micro-model through which all the measurements were acquired using an inverted confocal microscope.

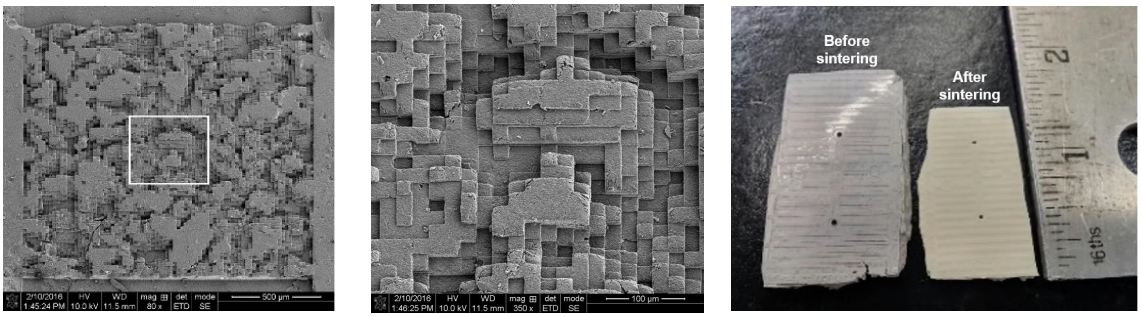

(a) (b) (c)

Figure 8.1: 2.5D rock-based ceramic micro-model showing (a) Scan Electron Microscopic (SEM) image of 2.5D micro-model before sintering and capping (b) close-up view of the ceramic micro-model from white rectangle, and (c) photographic image illustrating shrinkage before and after sintering and capping of the ceramic micro-model

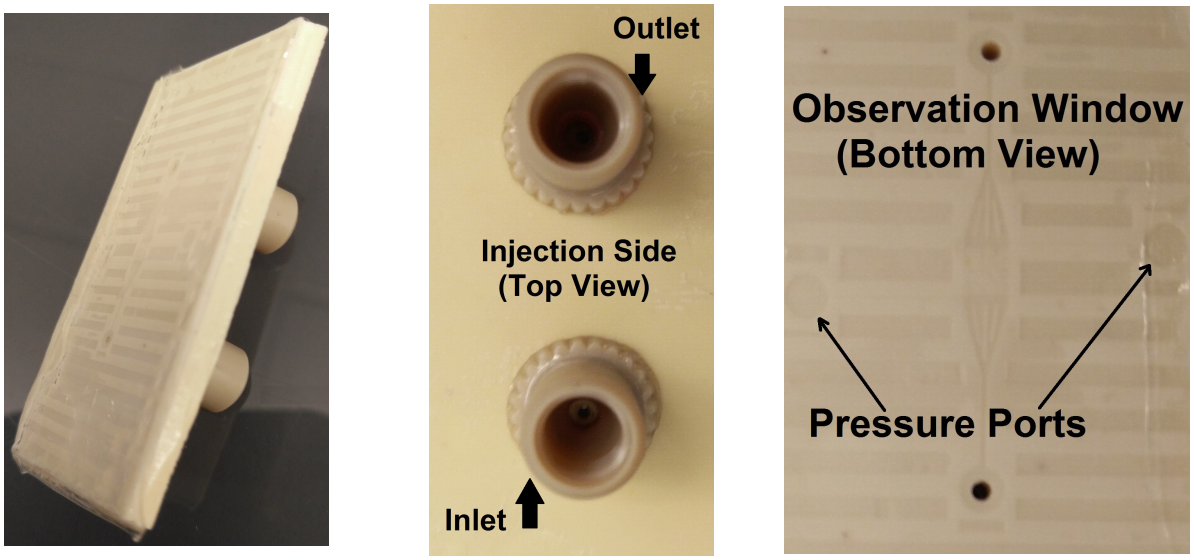

(a) (b) (c)

Figure 8.2: 2.5D rock-based ceramic micro-model (a) isometric view (b) top view; experimental fluid consists of nano-particle is injected through inlet nano-port (b) bottom view; flow visualization occurs through this window and all measurements are recorded using inverted confocal microscope.

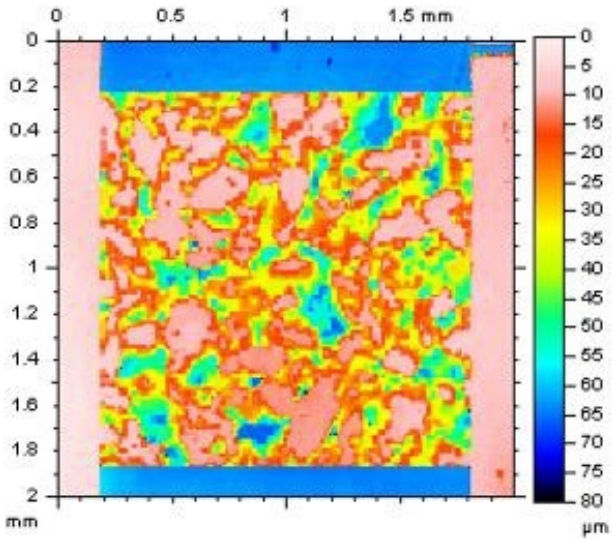

(a)

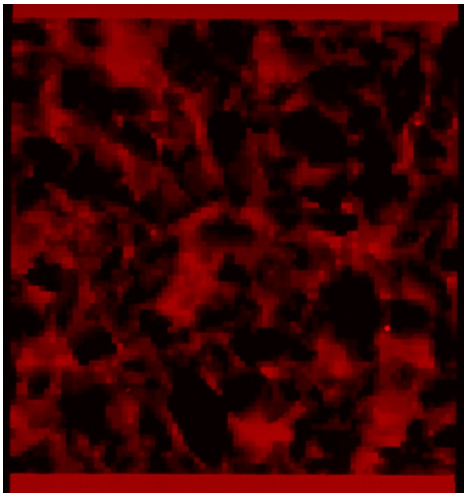

(b)

Figure 8.3: 2.5D ceramic rock based micro-model image (a) from optical scanning of the green sample before sintering and capping and (b) the ceramic micro-model flooded with fluorescence dye.

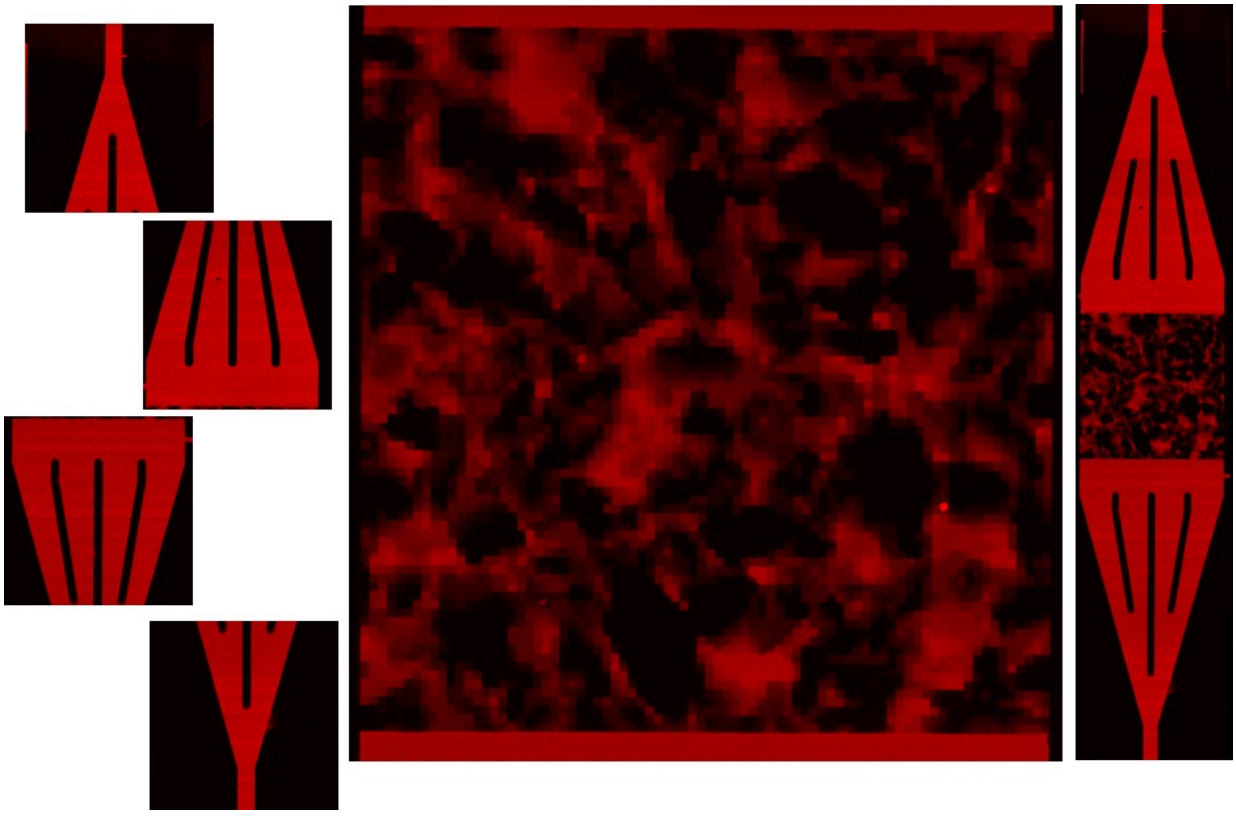

Figure 8.4: Reconstructed full 2.5D ceramic rock based micro-model image from five different segments of the micro-model. Each segment of the micro-model is overlapped with other successive segment of the micro-model.

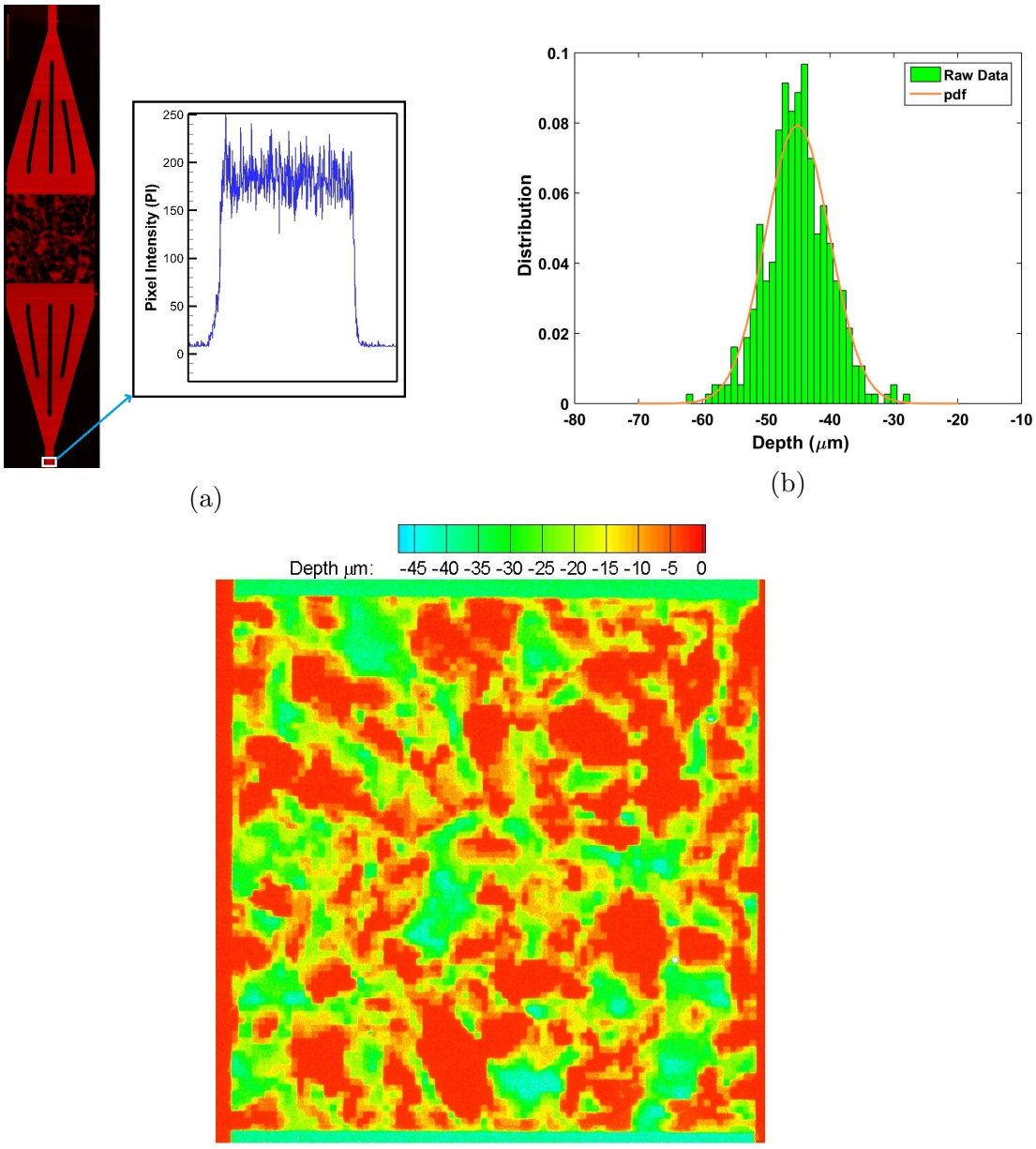

(a) (b) (c)

Figure 8.5: (a) A fluorescence image of the 2.5D ceramic micro-model illustrating inlet depth along with bottom surface roughness at inlet location. Mean depth was measured in Pixel intensity (PI). (b) Probability distribution of inlet location as shown in Figure (a) indicating average depth of the inlet is 45 μm. Gold color line indicated pdf (probability distribution function) of the discretized inlet depth location indicated by Figure (a). (c) Pseudo color rendition of the depth extraction of the 2.5D in-situ ceramic rock-based micro-model from fluorescence intensity.

8.3 In Situ Geometry Extraction Using Fluorescence Based Technology

Figure 8.3a shows depth measurements of the micro-model using optical profilometer prior to capping and sintering. Based on the measurement, the shrinkage varies from 17-20%. Experimental set up and procedure to extract in-situ 3D geometry is explained in detail in chapter 5. Prior to reconstruction of a full image of a ceramic micro-model, various sections of ceramic micro-model are captured and recorded as fluorescence images using a fluorescence microscope in such a way that all the depth lies within the depth of focus of the objective lens. Figure 8.3a shows image of depth scan of a green tape sample before sintering using an optical profilometer. The maximum depth is 65 microns which shows good agreement with the designed micro-model. Figure 8.3b shows a fluorescence image of the sintered ceramic micro-model flooded with rhodamine dye B. Once the fluorescence images are captured by the microscope, a full image of the micro-model was reconstructed. Figure 8.4 shows a reconstructed complete image of the ceramic micro-model synthesized from five different sections of the ceramic micro-model flooded with rhodamine dye. Once a full image is reconstructed, the fluorescence signal at the inlet channel is compared with the calibrated depth of the inlet channel. Inlet depth pixel intensity was used to extract pixels to a calibrated depth coefficient. Figure 8.5a shows a reconstructed image of the micro-model flooded with dye and a depth profile of the inlet channel of the micro-model in terms of pixel intensity. Figure 8.5b shows probability distribution function (pdf) of depth at the inlet channel of the micro-model which measures an average depth of 45 μm within a standard deviation of $\pm 5\mu$m. Figure 8.1b and 8.5a show roughness of the ceramic micro-model. From a prior experiment, it is known that the correlation between pixel intensity of light emitted from a dye and the calibrated depth is linear; assuming a linear co-relation exists in this experiment, we have reconstructed a 3D image of the ceramic micro-model. Figure 8.5c shows a color map of depth extracted from a 2D fluorescence image into a 3D image. The color bar indicates depths at various locations in the ceramic

micro-model.

8.4 3D Velocity Distribution

Inlet

The mean velocity distribution is generated by averaging 449 pairs of instantaneous velocity fields generated using micro-PIV. Figure 8.5a shows an observation location where measurement of nano-particle velocity and concentration were performed. Experimental fluid seeded with 860 nm polystyrene particles (9.54 particles/pL concentration or 0.32 % by volume) coated with fluorescence dye at a flow rate of 30 nL/min was injected through a nanoport into the ceramic micro-model. Figure 8.6 represents nano-particles velocity distribution at the inlet channel with an increment of 5 μm in depth. Figure 8.6a shows the inlet velocity distribution close to the flat coverslip and acts as a reference plane for all other measurements. As we move deeper into the channel, the magnitude of the velocity field increases along the depth until the mid-plane. And also, as we move further away from the mid-plane to the bottom wall of the channel, the velocity magnitude decreases accordingly. The particle behavior near the bottom wall is predominantly non-uniform as the roughness of the bottom wall is comparatively higher than the flat transparent glass slip. Due to low particle concentrations flowing along the plane close to the bottom wall of the micro-model, correlation between two successive image frames is hindered, which results in higher velocity deviation from its mean velocity. Besides the occurrence of particle trapping between free spaces, rough surfaces also adversely affect velocity measurements close to the enclosed walls. These effects can be clearly visualized in the velocity distribution close to walls, especially in the bottom walls of the micro-model. Therefore flow rate, roughness and particle seeding in experimental fluid are important factors to be considered while measuring and characterizing nano-particle behavior in a high resolution channel. From Figures 8.6e and 8.6f, it is clear that the boundary effect is minimum close to the midplane of the rectangular channel which behaves with approximately parabolic flow distribution in the channel. The deviation of the velocity field from parabolic distribution close to walls

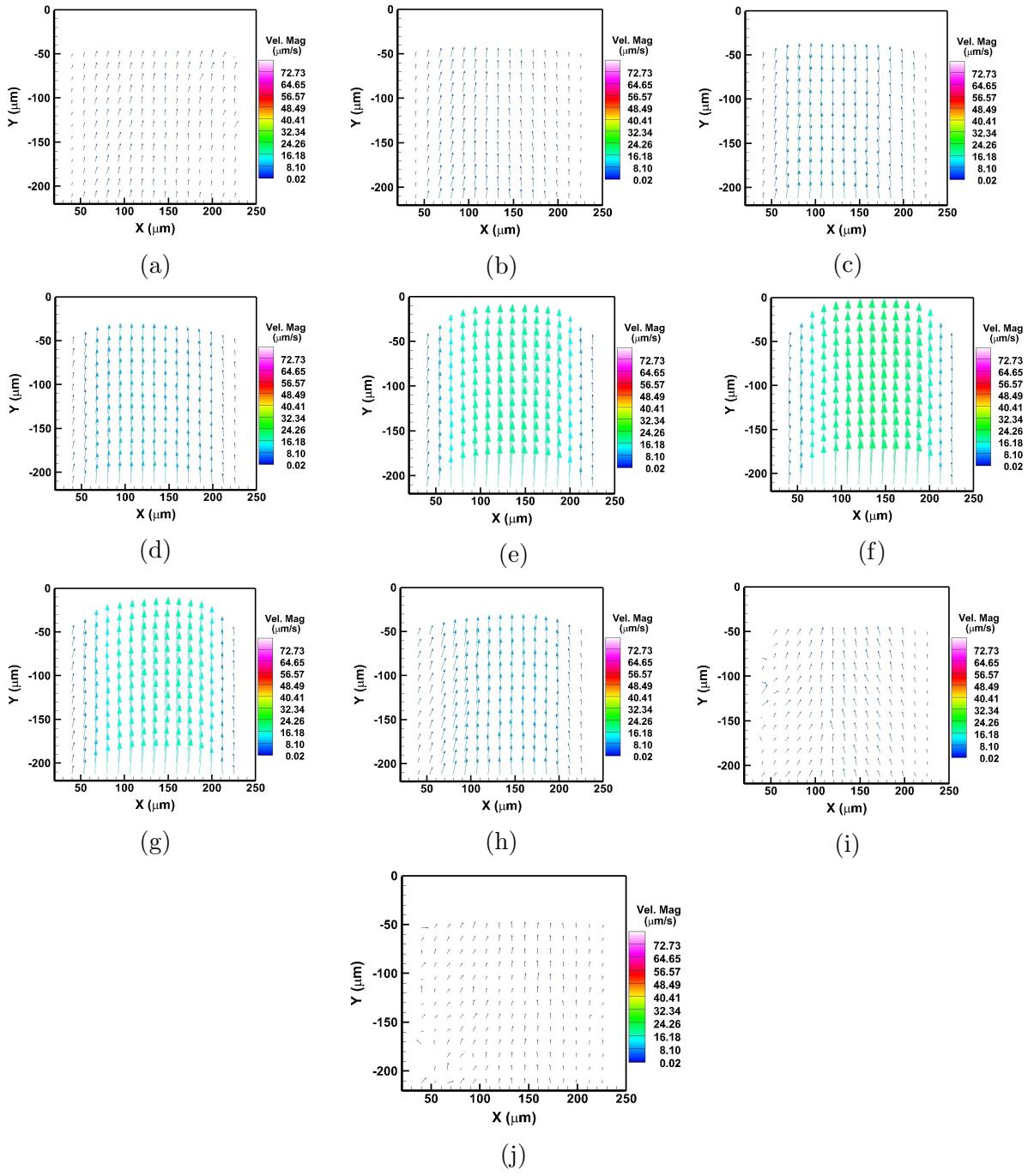

Figure 8.6: Sequence of images illustrating the depth-wise velocity distribution at inlet channel indicated in Figure 8.5a. Depth is measured from inside wall of the visualization window starting at (a) Z = 0 μm progressing at 5 μm increments through (j) Z = 45 μm which is the bottom of the micro-model.

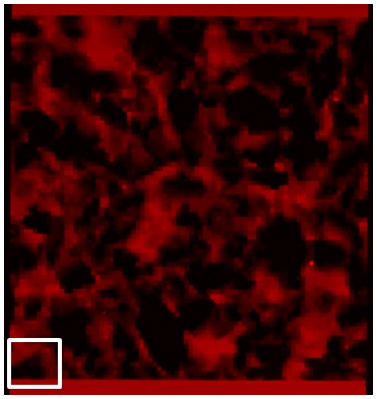

Figure 8.7: Ceramic micro-model flooded with rhodomine dye illustrating region of interest I, indicated by white rectangular box. Each box represents 212 x 212 μm^2.

are the effect of roughness of the walls, particle trapping and low particle seeding close to walls.

Internal Region of Interests (ROIs)

- **Region of Interest I**

Figure 8.7 shows an observation location in the internal domain of the ceramic micro-model where the measurements were taken. This observation location is one of the most favorable principal flow paths in the micro-model, where the velocity is comparatively higher than other locations in the micro-model. 3D velocity measurement of nano-particle at the internal observation location as shown in Figure 8.7 is presented in Figure 8.8. Figure 8.8 shows velocity distributions along depth with an increment of 5 μm from the flat cover slip to bottom of the micro-model. Figure 8.8a shows planar velocity distribution close to the flat coverslip and acts as a reference for all other measurements in that location. Some velocity vectors are sparse on the edge of the structures, which illustrates an effect of low velocity, roughness as well as particle trapping in the velocity distribution in those locations. The velocity magnitude increases with the increase in the depth until the mid-plane and gradually decreases as we move deeper to the bottom of the micro-model. Depth-wise high velocities are observed at approximately 15 μm through the throats. This indicates mid-way depth range between two throats at the lower right. The highest velocities are observed in this plane because of its smaller cross-sectional area. Similar to the velocity

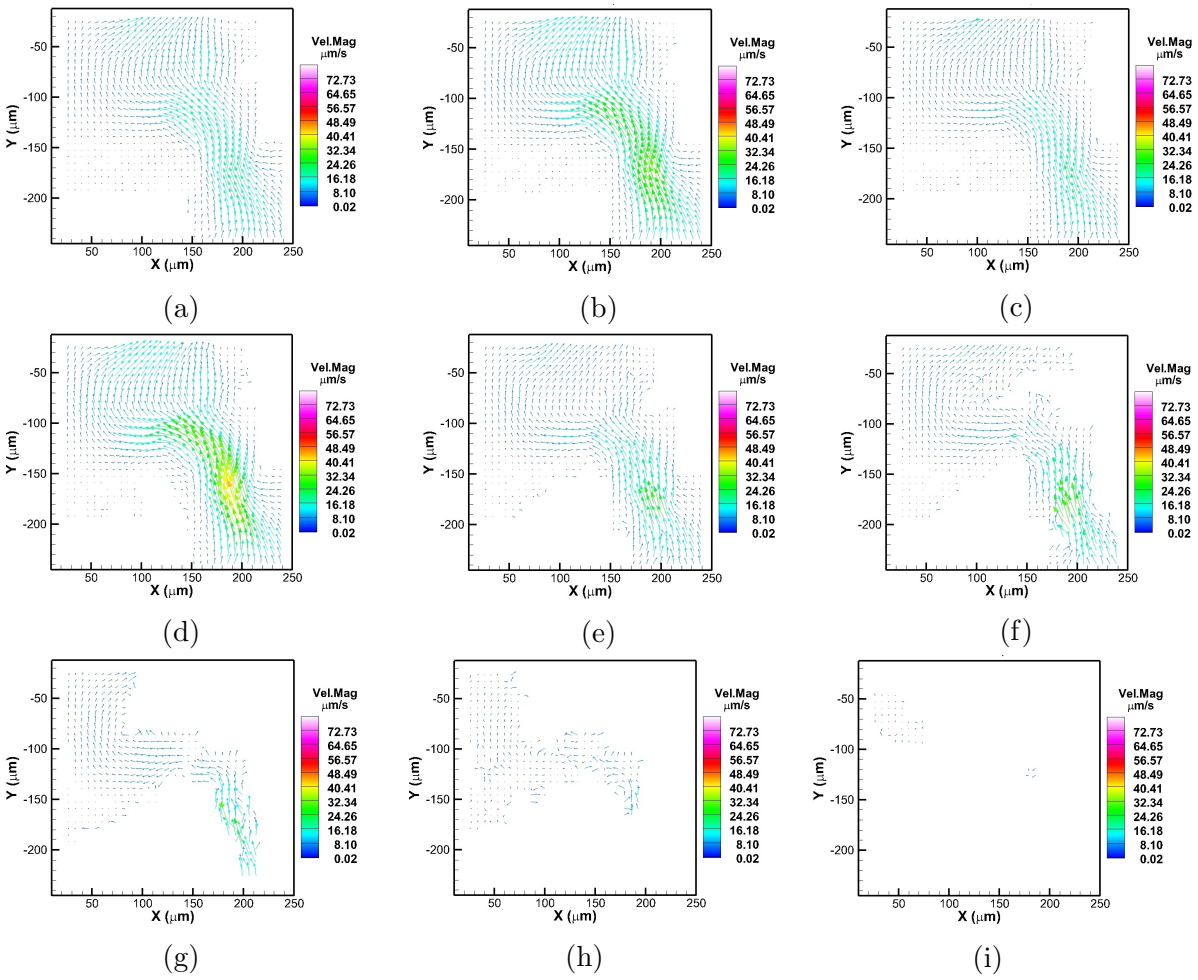

Figure 8.8: Sequence of images illustrating the depth-wise velocity distribution at region of interest I indicated in Figure 8.7. Depth is measured from inside wall of the visualization window starting at (a) Z = 0 μm progressing at 5 μm increments through (i) Z = 40 μm which is the bottom of the micro-model.

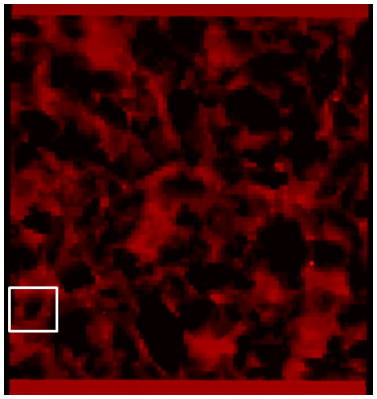

Figure 8.9: Ceramic micro-model flooded with rhodomine dye illustrating region of interest II, indicated by white rectangular box. Each box represents 212 x 212 μm^2.

distribution to the bottom walls of the inlet channel, the velocity distributions close to the bottom wall are often erratic directional velocity vectors. This results because of trapping due to surface roughness and low particle seeding in a very low Reynolds number flow. In addition, this effect becomes more predominant as we move closer to internal solid walls of the ceramic micro-model from liquid domain. This measurement opens a new area of interest in understanding trapping of nano-particles in a ceramic based surface. Most of the rock structures are rough in nature, and these measurements directly aid in understanding natural behavior of nano-particles in natural rock based structures in-order to predict flow behavior efficiently in the oil and gas industries.

- **Region of Interest II**

Figure 8.9 shows observation location II, which is a continuous downstream flow location of observation location I of the ceramic micro-model. This observation location shows predominant high flow field in the micro-model as it flows through a narrow cross-sectional throat of the system. Because of the favorable principal flow path, most of the nano-particles injected from the inlet domain flow though this domain.

Figure 8.10 shows 3D velocity distribution along depth wise with an increment of 5 μm from the flat glass coverslip. Figure 8.10a shows the velocity field close to the flat glass coverslip and acts as a reference plane for all the measurement in observation location II. As nano-particles enter observation location II, flow distributes into two paths: one on the

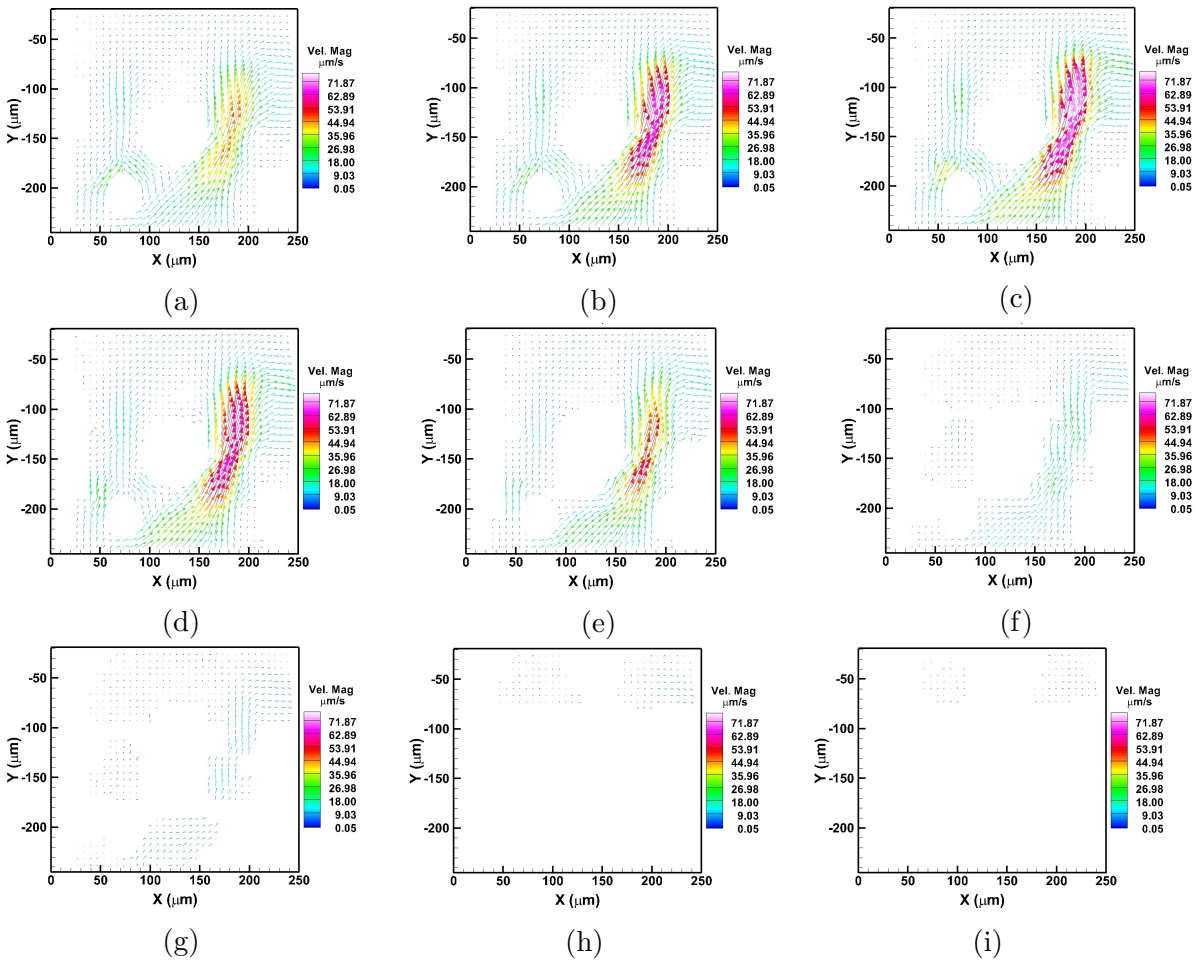

Figure 8.10: Sequence of images illustrating the depth-wise velocity distribution at region of interest II indicated in Figure 8.9. Depth is measured from inside wall of the visualization window starting at (a) Z = 0 μm progressing at 5 μm increments through (i) Z = 40 μm which is the bottom of the micro-model.

left corner close to the side wall of the ceramic micro-model and the other on the right side of the location. Flow on the right is further forged and most of the flow dominates the right path of the system. Further away from the exit location, the presence of micro-structures hinder the flow and a sudden turn on the right corner of the location is observed. Due to a large cross sectional area of the throat in the right side of the system where it makes a right angled turn, the velocity of the nano-particles decelerates. As we move deeper into the micro-model, the velocity magnitude increases significantly on the right throat compared to other locations. The maximum velocity magnitude occurs at the right throat in between 10-15 μm, which is the mid-plane of the throat. Flows close to the bottom walls are more erratic and inconsistent, similar to previous locations, as an effect of low seeding, rough surface and particle trapping in void spaces of the bottom surfaces.

8.5 3D Particle Concentration Distribution

Inlet

The particle concentration distribution at an observation location shown in Figure 8.5a of the inlet channel is presented in Figure 8.11 for all depths, starting close to the observation window (flat coverslip) with an increment of 5 μm all the way to the bottom of the inlet channel. The depth wise spatial resolution is 5 μm. At each figure, the line represents continuous particle concentration within the plane for 29.25 secs. Peak particle concentration is observed in an approximately 20 μm plane and declined progressively along the depth of the channel. Figure 8.12 shows average particle concentration per unit volume along the depth. The particle concentration increases rapidly from the observation plane close to the flat coverslip to 5 μm of the channel, remains steady till midway of the channel, and then decreases drastically as we move close to the bottom of the channel. Because of the design, the injection of the nano-particles in the channel have to turn perpendicular and may have an impingement effect on the flow. As a result, a sudden jump on the particle concentration occurs from 0 μm to 5 μm plane.

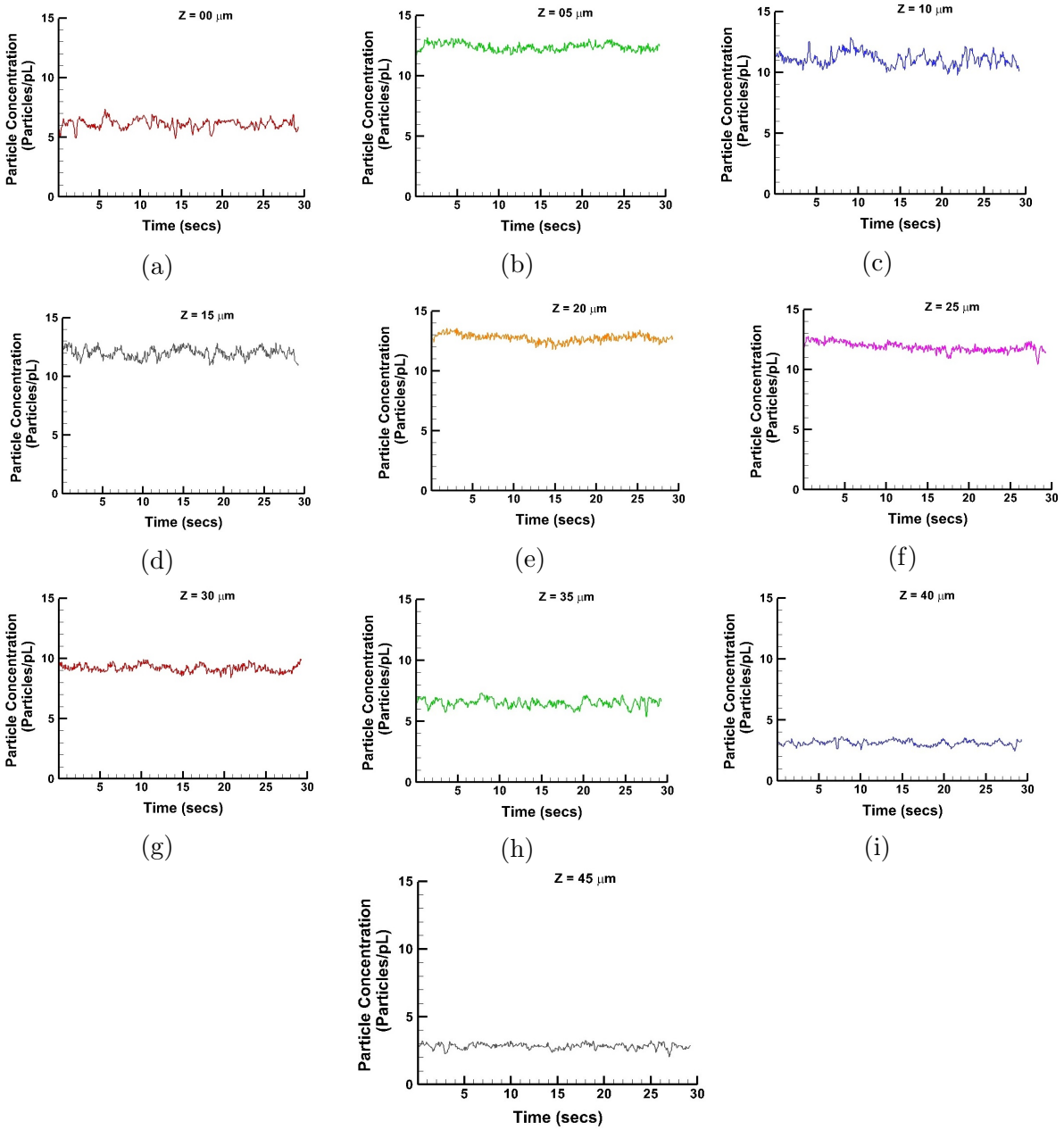

Figure 8.11: Sequence of images illustrating the depth-wise Particle concentration distribution at inlet channel indicated in Figure 8.5a. Depth is measured from inside wall of the visualization window starting at (a) Z = 0 μm progressing at 5 μm increments through (j) Z = 45 μm which is the bottom of the micro-model.

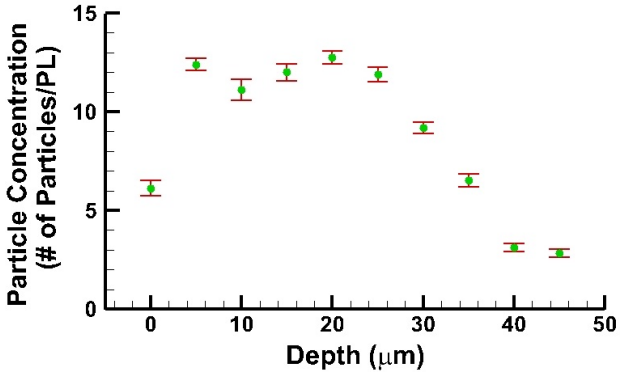

Figure 8.12: Depth-wise average particle concentration distribution at inlet of micro-model indicated in Figure 8.5a. Depth is measured from inner wall of the visualization window.

Internal Region of Interests (ROIs)

- **Region of Interest I**

Figure 8.13 shows instantaneous particle concentration distribution of nano-particles flowing into the ceramic micro-model at an observation location as shown in Figure 8.7. Figure 8.13a shows nano-particle concentration flowing close to the flat coverslip and shows higher particle density compared to other depths on the same location. Since layers 12 and 13 have the most nano-particles flow paths compared to other layers in the design, the particle concentrations flowing on those layers are predominantly higher than the bottom of the micro-model. As we move deep towards the bottom of the micro-model, flow path of the nano-particles decreases accordingly. Figure 8.14 shows average nano-particle distribution along depth in the observation location I. The nano-particle concentration declines as we move away from the flat coverslip to the bottom of the micro-model. Principal flow path of the nano-particle plays a significant role on particle concentration flowing in that domain which is also illustrated by Figure 8.14.

- **Region of Interest II**

Figure 8.15 shows instantaneous particle concentration distribution of nano-particles flowing into the ceramic micro-model at observation location II as shown in Figure 8.9. As similar to observation location I, Figure 8.15a shows nano-particle concentration flowing close to the flat coverslip and shows higher particle density compared to the other depths

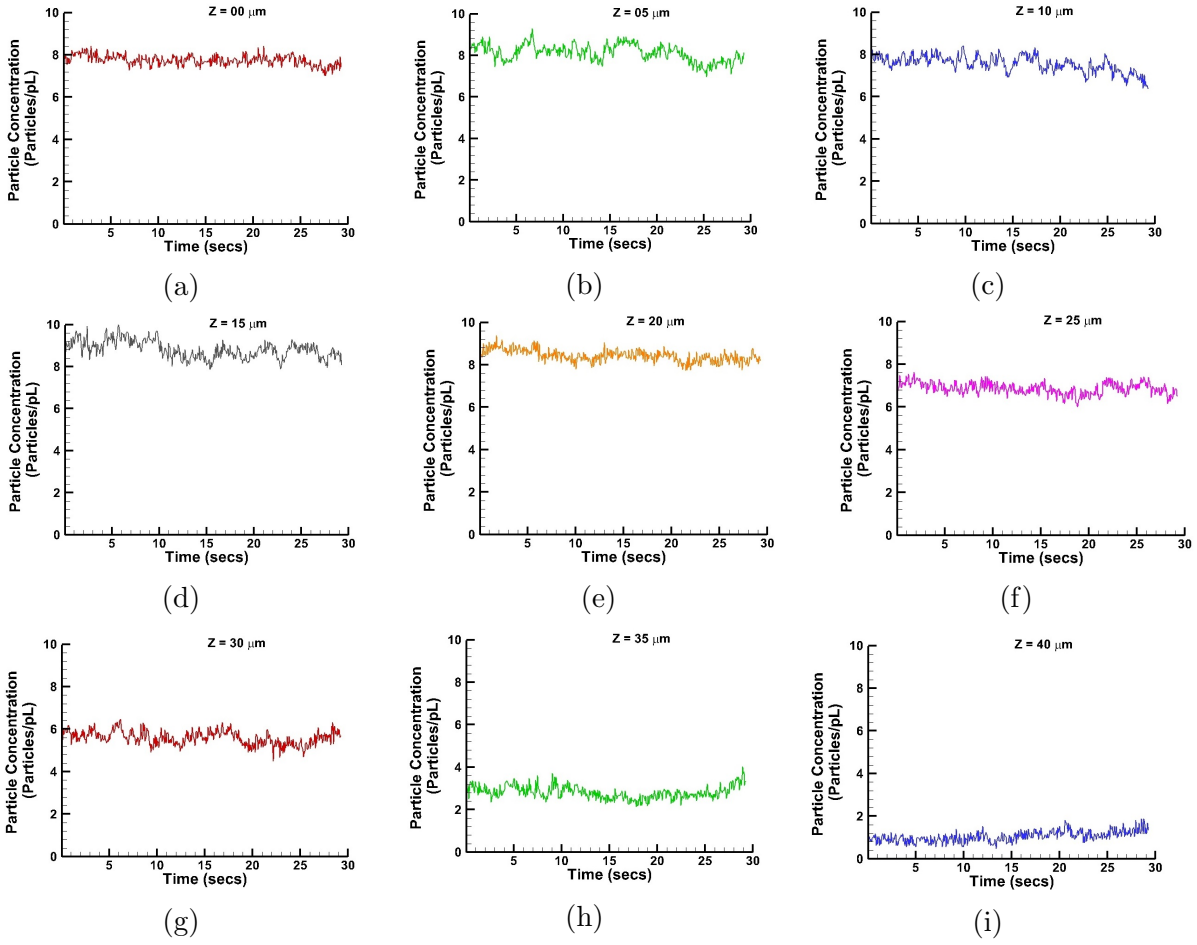

Figure 8.13: Sequence of images illustrating the depth-wise Particle concentration distribution at region of interest I indicated in Figure 8.7. Depth is measured from inside wall of the visualization window starting at (a) Z = 0 μm progressing at 5 μm increment through (i) Z = 40 μm which is the bottom of the micro-model.

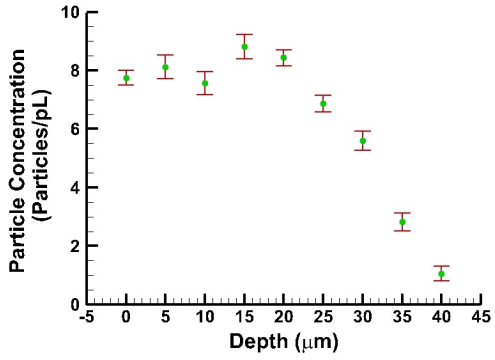

Figure 8.14: Depth-wise average particle concentration distribution at ROI I of micro-model indicated in Figure 8.7. Depth is measured from inner wall of the visualization window.

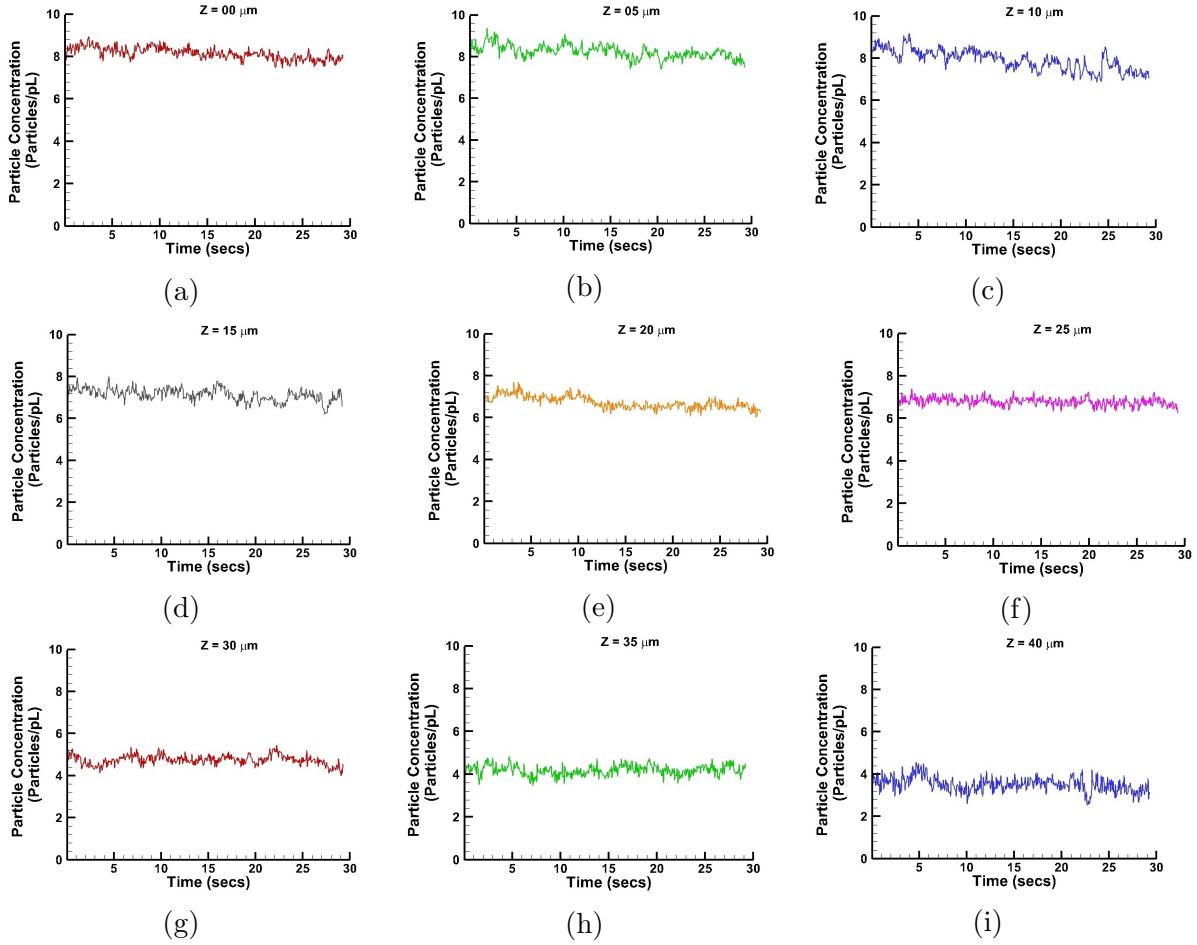

Figure 8.15: Sequence of images illustrating the depth-wise Particle concentration distribution at region of interest II indicated in Figure 8.9. Depth is measured from inside wall of the visualization window starting at (a) Z = 0 μm progressing at 5 μm increments through (i) Z = 40 μm which is the bottom of the micro-model.

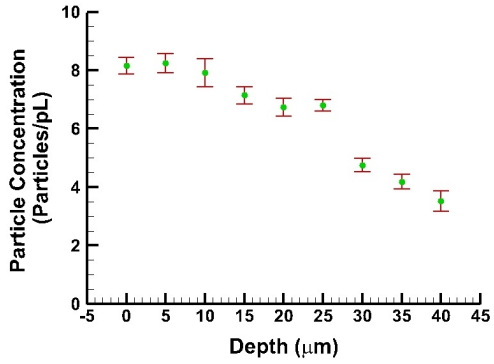

Figure 8.16: Depth-wise average particle concentration distribution at ROI II of micro-model indicated in Figure 8.9. Depth is measured from inner wall of the visualization window.

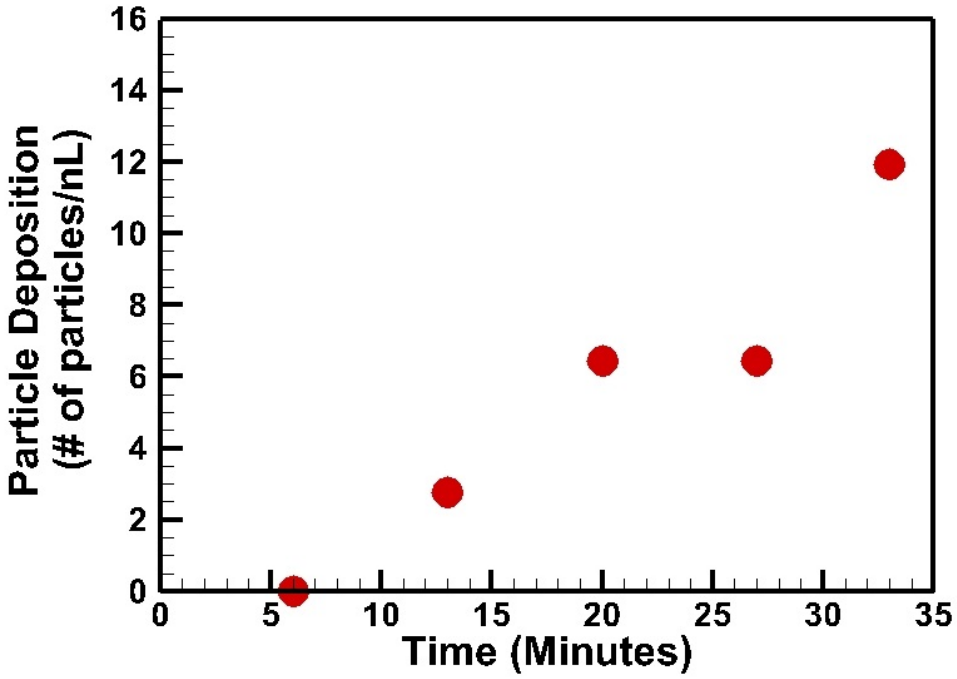

Figure 8.17: Nano-particle particle deposition rate at observation location II as shown in Figure 8.9.

on the same observation location. Similar to observation location I, layers 12 and 13 have the most favorable flow path compared to the other layers in the design, so the particle concentrations flowing on those layers are predominantly higher than the bottom of the micro-model. As we move deep towards the bottom of the micro-model, the flow path of the nano-particles decreases accordingly, and so does particle concentration. Figure 8.16 shows nano-particle distribution along the depth in the observation location II. The nano-particle concentration declines as we move away from the flat coverslip to the bottom of the micro-model because nano-particles flow is significantly hindered by geometrical constrains. As we move deeper, the nano-particles flow path decreases, which results in a low velocity domain with lower particle concentration.

8.6 Particle Deposition Rate

Deposition evolution over a period of time measured at observation location II shown in Figure 8.9 is presented in Figure 8.17. The deposition includes nano-particles deposited

on the side walls, top wall and bottom wall of the micro-model in observation location II. As time elapses, particle deposition on all walls increases. The measurement shown in the Figure 8.17 was during the first approximately 35 mins after the injected particle reached the entrance region of the rock-based structures of the micro-model. The figure also indicates the initial deposition rate is significantly high until approximately 20 mins. Some deposited nano particles are detaching from the wall surface of the micro-model after 20 mins. This phenomenon is shown around approximately 25 mins in Figure 8.17. Once the nano-particle deposition rate is higher than the detaching rate of the nano-particles from the system, then deposition dominates over particle detaching phenomenon. This shows deposition and segregation of nano-particles from walls are continuous processes. At an earlier stage, the deposition rate dominates detachment rate but as time progress, deposition slow down and detachment of nano-particles from the surface increases.

8.7 Conclusion

In this chapter, we have briefly introduced a microfabrication process of a ceramic based micro-model using a hot embossing technique. Using a novel fluorescence based geometry extraction technique, we have reconstructed in-situ 3D geometry of a ceramic micro-model. We have successfully captured the flow field of the inlet channel as well as behavior of nano-particle at two different observation locations. 3D measurements of nano-particle velocity, concentration and particle deposition have been studied. Time evolved particle velocity has also been studied and can be found in detail in appendix F. Because of the side walls and bottom wall roughness some velocity vectors near those walls are erratic and introduce bias in the velocity measurement. Velocities close to the reference plane are more uniform due to the smooth coverslip as well as higher flow permeability. Velocity distribution close to the bottom wall of the micro-model are distorted as there exist a lack of flow connectivity in the plane and stationary flow exists. Due to the stationary flow, Brownian motion dominates nano-particle motion.

Similarly, particle concentration evolution has also been studied which shows a logarith-

mic increase in particle concentration from early stages to the saturation stage but required more experiments to verify it. Similar to the velocity distribution, particle concentration distributions substantially decrease as we move deeper in the micro-model. From experiments, it is illustrated that most of the nano-particle flow from reference plane to mid-plane of the observation location. This effect is due to a favorable principle flow path that comes from flow connectivity of the microporous structures in the micro-model. The other potential effect might be an infringement effect when the flow has to turn perpendicular from the injection direction to the direction of flow in the channel.

Particle deposition evolution is also presented in this chapter. It shows that particle deposition rate at an earlier stage is substantially heavier than a later stage. As time elapses, most of the particles deposited on all walls escape from deposited region either breaking a bond with the wall if it exists or overcoming an energy barrier. After significant time elapses, particle deposition and segregation take place side by side in the ceramic micro-model similar to the PMMA micro-model.

Chapter 9
3D Measurement of Nano-Particles Transport in 2.5D High Resolution PMMA Micro-Model*

This chapter briefly describes microfabrication of a 2.5D rock-based micro-model using a SU-8 lithography technique to produce high resolution features followed by nickel electroplating to produce a master nickel mold along with detailed 3D measurements of nano-particle transport in a high resolution rock-based micro-model. The details of microfabrication process are found in [52]. Multilayered SU-8 lithography, control UV exposure dose, baking time, nickel electroforming, and hot embossing processes are involved in the microfabrication process to fabricate a high resolution micro-model ($\approx$5 μm resolution features). Use of SU-8 enables us to generate multilayer high resolution features with an accuracy of $\pm$ 1.5 μm. Prior to hot embossing, a master mold was created using a nickel electroforming process to replicate mirror features of the 2.5D micro-model. Once the master mold is fabricated, hot embossing techniques was engaged to replicate micro-model structures in wide variety of materials such as ceramics, thermoplastic polymers, *etc.*. A new technique of geometry extraction using fluorescence microscopy is described in this chapter to investigate flow path as well as in situ 3D geometry extraction of a 2.5D PMMA micro-model. Besides 3D geometric investigation, transport of nano-particles is also studied and presented in this chapter. This study aids in understanding nano-particles behavior in a high resolution micro-model micro-model(equivalent resolution of x-ray CT image of Boise sandstone). In this chapter, we present 3D velocity distribution along with particle distribution and particle deposition at one of the principal flow paths of the system.

*some of the materials are republished with permission from "Fabrication of 2.5D Rock-Based micromodels With High Resolution Features", by Daniel S. Park, J. Upadhyay, V. Singh, Karsten E. Thompson and Dimitris E. Nikitopoulos, Paper No. IMECE2015-50657 by ASME.

9.1 Necessity of High Resolution Micro-models

The original Boise rock sandstone was scanned at 5.07 μm resolution using an X-ray micro-CT scan, and the void spaces maintain most of the flow connectivity. Mikael has studied 14 different morphologic and flow (dynamic) parameters in digitally scanned 3D Boise rock sandstone and has optimized those parameters to design a high resolution 2.5D micro-model [52, 25]. Due to limitations in micro-fabrication using micro milling, a low resolution micro-model was developed with minimum features of 25 μm, that represents a low resolution Boise rock-based micro-model. Although the flow characteristics in low resolution are very close to those in high resolution micro-models suggested by Saade Alexis Bou-Mikael, the low resolution results in subtle differences in local flow. This could alter local adsorption/deposition of nano-particles in reservoir applications[52]. Local adsorption/deposition propagates and affects global nano-particle transport in the micro-model. Hence, a new fabrication process is realized to develop a high resolution optimal design, which can fully conform to the actual pore dimension of scanned Boise rock. With the advancement in micro-fabrication technology, a high resolution micro-model with a minimum 5 μm resolution as suggested by Bou-Mikael is adapted so that it can fully imitate actual pore dimensions to study nano-particles transport behavior in rock-based micro-models.

9.2 Fabrication of High Resolution Micro-Model

The 2.5D micro-model obtained from optimizing fourteen different flow as well as morphological parameters along with a depth averaging process with a minimum feature of 5 μm was used to fabricate a nickel master mold. The detail of this microfabrication process can be found in [52]. Since the scaled down version of the micro-model consists of thirteen different layers, it is essential to create thirteen different layered optical masks in order to proceed within the multilayer lithography process. Prior to fabricating the optical masks, a set of alignment marks were designed and marked in the mask for alignment of different layers of optical mask to the substrate. Once the design process is completed, using laser writing with a resolution of 2.5 μm, a set of 13 optical masks were fabricated at the Univer-

sity of Texas in Dallas. A metallic seed layer with chromium(Cr)/Gold(Au)/chromium(Cr) (20nm/50nm/20nm) was deposited on the surface of the silicon (Si) substrate using an electron beam evaporator. Chromium in the seed layer is used as an adhesive layer between the SU-8 and the Au layers. Gold in the seed layer is used for nickel electroforming. SU-8 2005 is poured into the substrate and a target of 5 μm is obtained using spin coating at 2250 rpm for 30 secs. The coated sample is prebaked on hot plate at 65°C for two minutes, 95°C for 6 minutes and 65°C for 2 minutes. Once the sample is prebaked, it is in contact with optical marks using pressuring system. Once the sample is firmly in contact with the optical mask, it is exposed to UV light at an exposure dose of 210-250 mJ/cm^2. The prebaked and UV exposed SU-8 is further baked for 2 minutes at 65^0C, 6 minutes at 95°C and 2 minutes at 65°C. After post baking, the sample is allowed to cool down for 30 minutes prior to the developing process. The developing phase includes treating the sample with SU-8 developer for a minute and rinsing it with isopropanol. Further the developed sample is air dried and hard baked for 5 minutes at 150°C. The exposed portion of Cr is etched out using Cr etchant so that Au is exposed to the nickel salt solution for nickel electroforming. From the second layer onward, SU-8 2010 was used for spin coating at 500 rpm for 30 seconds. The sample follows the same procedure of prebaking, three minutes at 65°C, five minutes at 95°C, three minutes at 65°C. The spin coating at 500 rpm for 30 seconds produces an average of thickness 60 μm SU-8. Excess SU-8 is flycut into a desired thickness of 5 μm in multiple steps. Once the second layer of SU-8 meets target thickness, it is further baked for an hour at 65°C for smoothing the traces of flycutting bit. The same process was repeated until the 13^{th} layers of the micro-model are fabricated. Once the SU-8 mold is ready, electroforming takes place to replicate a final nickel mold insert. Nickel electroforming takes place using an in-house electroplating system which is comprised of two electroplating tank compartments along with a dummy compartment. A DC power supply and temperature controller are attached to this system so that current density and temperature can be controlled as required by the system. The nickel salt solu-

tion consists of 180 gm/L sulfamate nickel mixed with deionized water, Dischem boric acid and Dischem wetting agent. The SU-8 sample is soaked in a wetting agent prior to the electroforming process. Once the gold is exposed to the wetting solution, the electroforming process take place in-house electroplating system. The current density was maintained at 5-10 mA/cm^2 and the temperature of the solution is maintained at 50^{o}C. The current density was increased to 20 mA/cm^2 once the top surface of the SU-8 was covered with electroplated nickel. The electroforming process was continued until the thickness of the nickel mold reached 3.5 mm. The electroplated nickel mold is milled until a 3 mm thick flat surface is achieved. After planarization, the mold was shaped in a circle using pressurized waterjet cutting. A post electroplating process involved removing of silicon substrate using potassium hydroxide, seed layers using Cr/Au etchants and SU-8 treating with microwave plasma asher. Once the etching process was completed, the master mold was laser welded in a stainless steel fixture and acts as a master mold for hot embossing. The hot embossing process is similar to that described in chapter 2. After hot embossing, the sample is cut into the desired size and a thin PMMA sheet (50-125 μm) was used as a flat coversheet to enclose the hot embossed micro-model. Prior to bonding the thin PMMA sheet to the micro-model using a thermal fusion process [57], the inlet and outlet reservoir were drilled through using a 1 mm drill bit for inter fluid connection. Once the micro-model is bonded with the thin PMMA sheet, nano-ports were connected to the inlet and outlet. The inlet of the micro-model is connected to a syringe using a fluorinated ethylene-propylene tube.

9.3 Experimental Set Up

Prior to the particle and dye experiment, the PMMA micro-model sample was connected to a syringe using fluorinated ethylene-propylene tube and underwent an air bubble removal process. The air bubble removal process is described in detail in chapter 3. The difference in this experiment is the injection volumetric flow rate of the test fluid seeded with nano-particles. Initially, a 5 milliliter syringe was used to push water-ethanol at the volumetric flow rate of 5 μl/min for an hour and volumetric flow rate was reduced to 2

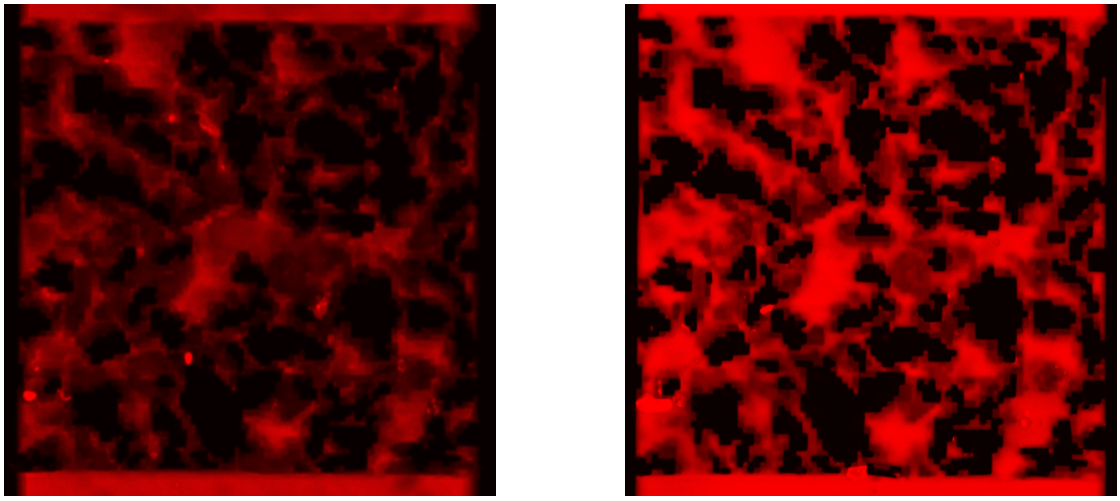

(a) (b)

Figure 9.1: Micro-model flooded with dye is captured by (a) 4 x 0.1 NA objective lens (b) 10 x 0.30 NA objective lens using fluorescence confocal microscope.

μl/min in order to avoid delimitation of PMMA film. Once all the air trapped inside the micro-model was released from the sample, de-ionized water filtered with a 100 nm filter (supplied by GE health care) was injected at volumetric flow rate of 2 μL/min for 12 hrs. The 100 nm filter used in this experiment extracts residue present in de-ionized water, if any exists. The injection of de-ionized water also pushes water-ethanol solution out of the micro-model to avoid any surface modification as well as act as an ideal environment for nano-particle diffusion in the micro-model. After 12 hrs of de-ionized water injection, 100 ppm concentrated Rhodamine B solution, filtered using a 200 nm filter, was injected through the inlet nanoport at a volumetric flow rate of 1 μL/min for 30 minutes before proceeding with image acquisition. Highly sensitive PMTs were used to acquire multiple sequences of images with 2048^2 resolution. Further experimental setup and procedure is described in chapter 5.

9.4 High Resolution 3D Geometry Extraction and The Flow Field

Due to the low magnification and low numerical aperture of the objective lens, most of the light emitted from the dye is diffracted and a blurry image is observed. Figure 9.1a

shows an image flooded with rhodamine dye acquired using a 4 x 0.1 NA objective lens. The benefit of using low magnification and low numerical aperture is that it covers a large depth of field to capture all layers of the micro-model. Similarly, an image acquired by a 10 x 0.3 NA objective lens is presented in Figure 9.1b. Figures 9.1a and 9.1b show indistinguishable features of the micro-model, and it is challenging to measure depth of each layer in the micro-model. The main drawback of using low magnification and low numerical aperture objective lens is that it fails to converge light emitted from high resolution feature of the micro-model. Hence, there is a necessity for a new inexpensive, reliable and time-efficient 3D geometry extraction technique to apprehend high resolution features of 2.5D micro-models. We have therefore proposed a new technique to extract in situ 3D high resolution geometry of the micro-model. The new technique is based on linear superposition of fluorescence images at various depths of the micro-model using high magnification as well as high numerical aperture objective lens. Although high numerical aperture objective lens has low depth of field, we acquire a sequence of multiple high resolution images within the depth of field of the objective lens. The new technique is discussed in detail in this section and aids in in-situ depth measurement as well as 3D geometry extraction of high resolution micro-model.

9.5 Image Acquisition

Preceding to image acquisition, the focal plane of the microscope is focused at the flat wall of the micro-model. Once the focal plane is located near the flat surface of the micro-model, a high resolution image is acquired within the depth of field of the objective lens. In a similar fashion, a series of images were acquired for the entire depth. To maintain the integrity of dye-flooded images of the micro-model, all the acquired images must be below the saturation (maximum) intensity for depth bit of the image. Starting from the top observation window in Figure 9.2 we have presented a series of under saturated images acquired at various depths proceeding to the bottom of the micro-model. These images acquired by confocal microscope are 24 bit true images which consist of 8 bits

of monochromatic red, green and blue channels. Each channel must be under saturated in-order to perfectly represent the geometry of in-situ micro-model. An image as shown in Figure 9.2a shows in-plane fluorescence image captured by a confocal microscope close to the flat observation window whereas the last image indicates in-plane image slightly deeper than the bottom wall of the micro-model. Images presented in Figure 9.2 are under saturated images for a 24 bit image (true depth image). Each image shows fluidic flow path of dye inside the micro-model at various depths.

9.6 Image Segmentation

Image segmentation is a process of image division into different regions having certain properties. Once the image is segmented, pixel intensity of the fluorescence dye can be investigated. Image segmentation is the key step in quantitative analysis of pixel intensity of the fluorescence image. Initially, the true image is segmented based on the monochannels: red, green, and blue, and they are recorded in a 24 bit image depending on emission wavelength of the light. Mathematically, f(x,y) represents an array of monochannels $\{f_1(x,y), f_2(x,y), f_3(x,y)\}$ of an image and (x,y) represents the location of each pixel in the image[104].

$$f(x,y) = \{f_1(x,y), f_2(x,y), f_3(x,y)\} \tag{9.1}$$

The multiple channels of the image is segmented into proper monochannels f_i prior to the second stage of image segmentation. Second stage segmentation of the monochannel is determined by the average intensity of the in-plane image. Based on the average intensity of the monochannel image, threshold values are selected. Second stage segmentation is only required if any impurities exist in the fluorescent image. There is a high chance of impurities being present in the system while handling the microfluidic device, so most of the time second stage segmentation of the monochannel image is required. A Threshold operator is one of the widely used image segmentation techniques, where all the grayscale pixel intensities between threshold values are stored as 1 and rest of them are stored as 0

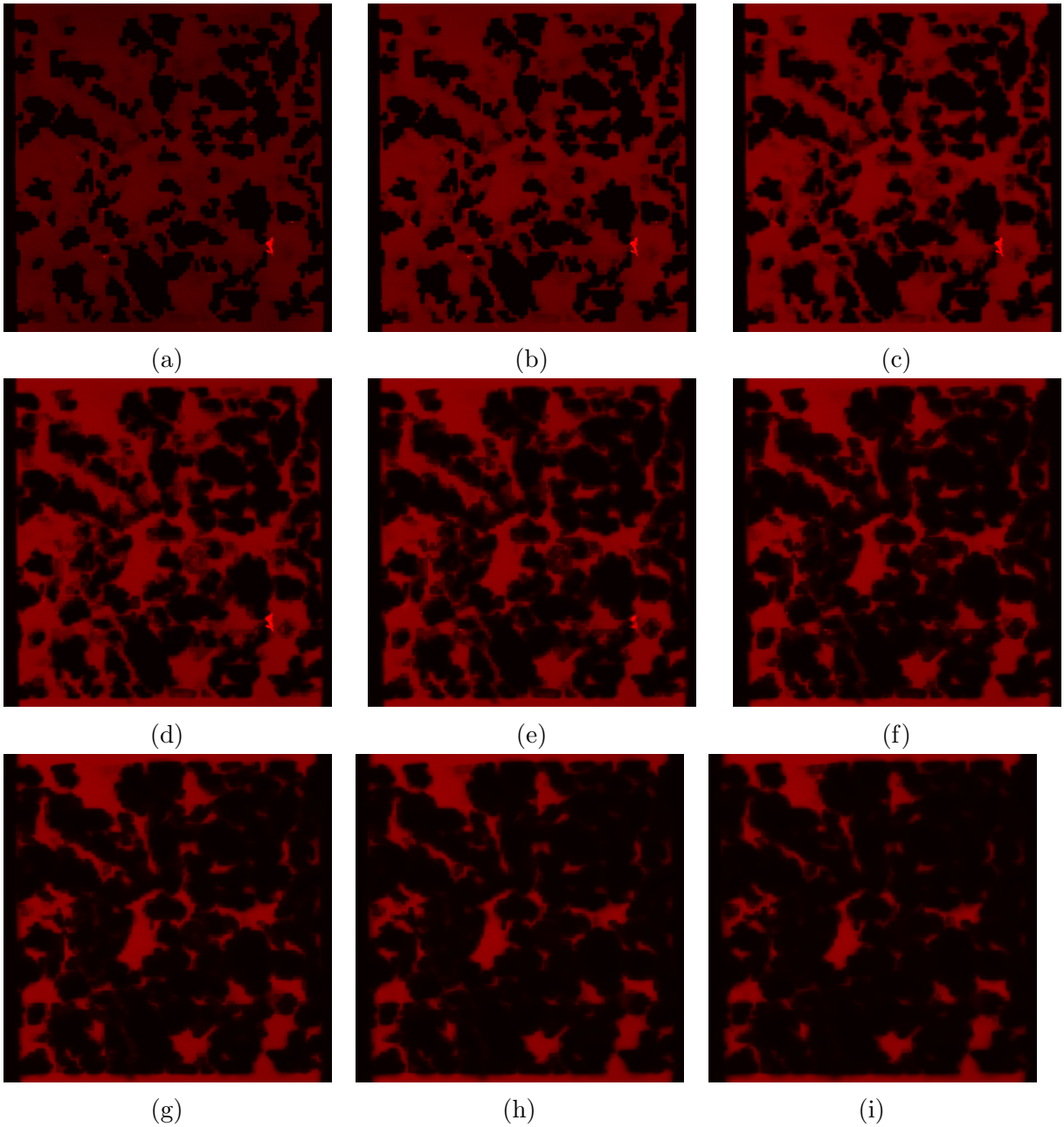

Figure 9.2: Micro-model flooded with dye images at different depth planes starting at (a) top wall to the (r) bottom wall of the micro-model. These images were captured by confocal microscope using water immersion 20x 0.95 NA objective lens (figure cont'd.).

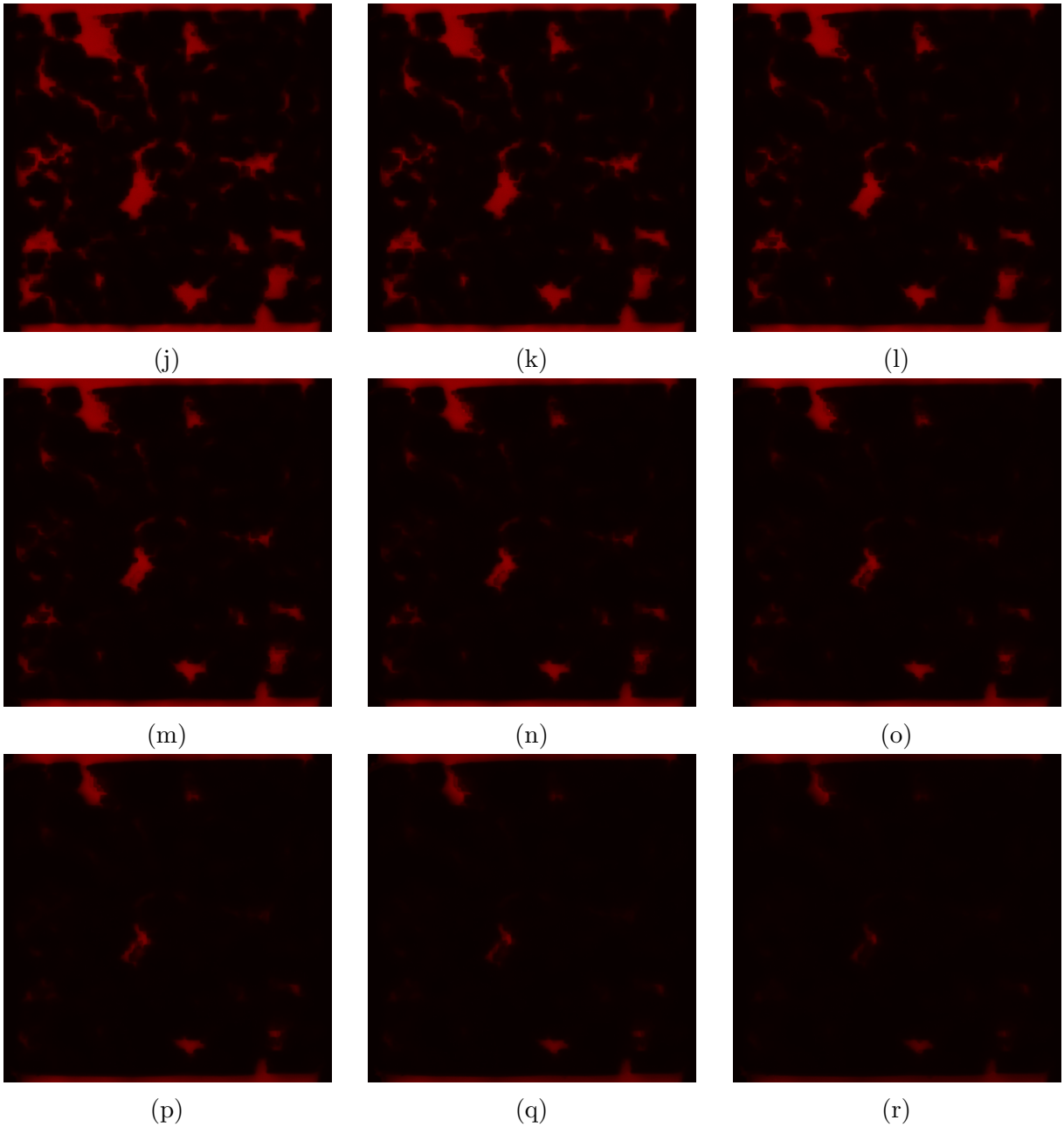

Figure 9.2: Micro-model flooded with dye images at different depth planes starting at (a) top wall to the (r) bottom wall of the micro-model. These images were captured by confocal microscope using water immersion 20x 0.95 NA objective lens.

[104].

$$[Bf_i]_{[t_1,t_2]}(x,y) = \begin{cases} 1, & \text{if } t_1 \leq f_i(x,y) < t_2 \\ 0, & \text{otherwise} \end{cases} \tag{9.2}$$

where $[\mathrm{Bf}_i]_{[t_1,t_2]}$ represents binary data of a grayscale image f_i, and t_1 and t_2 are the minimum and maximum threshold range of image intensity.

Figure 9.3 shows a true color image, segmented into three different monochannels: red, green and blue. The first channel consists of red wavelength signal in term of an 8 bits image (0-255) while the other two channels consist of green and blue signals. Since the fluorescence dye does not emit any light in the wavelength that ranges between green and blue, both channels receive zero signal which is illustrated in Figure 9.3. Using the threshold operator, impurities which are recorded as a brighter signal than the in-plane average signals are segmented out of the raw image assuming that depth of field lies in between the shallow channels. Figure 9.4 shows an image prior to and after the image filter being applied to it. The relatively bright signal represents impurities as shown in Figure 9.4a. Figure 9.4b shows an image after filtering is applied to image shown in Figure 9.4a. Most of the impurities are eliminated from the raw image prior to the next step of the image processing technique.

9.7 Intensity Superposition of In-plane Images

Image analysis includes superposition of a series of under saturated images acquired at various depths of the micro-model. In-plane images at various depths are superimposed to generate high resolution in-depth images. In this application, a superimposed image is generated using intensity superposition of all in-plane images to map depth of the micro-model with the aid of the fluorescence technique. Because of intensity superposition, the signal may exceed the maximum value of 8 bits (gray) image, so a weight function is introduced in such a way that images reconstructed from superposition of various in-planes images should not exceed a maximum value of 8 bits (gray) image. Each image is attenuated with

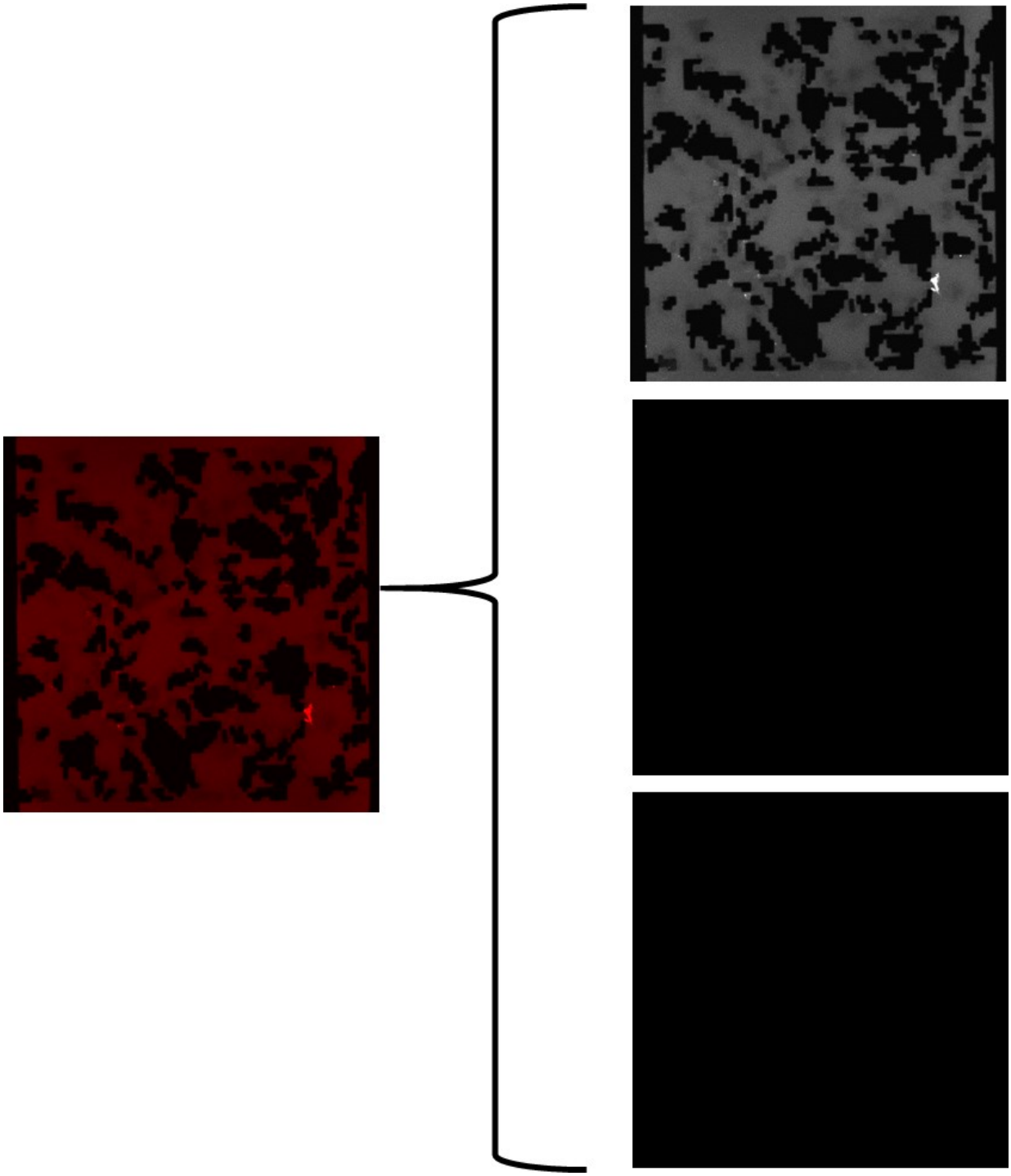

Figure 9.3: Segmentation of 24 bit true image into three monochromatic 8-bits channels (red,green, and blue). First top left image shows red signal, while other two show green and blue signal respectively.

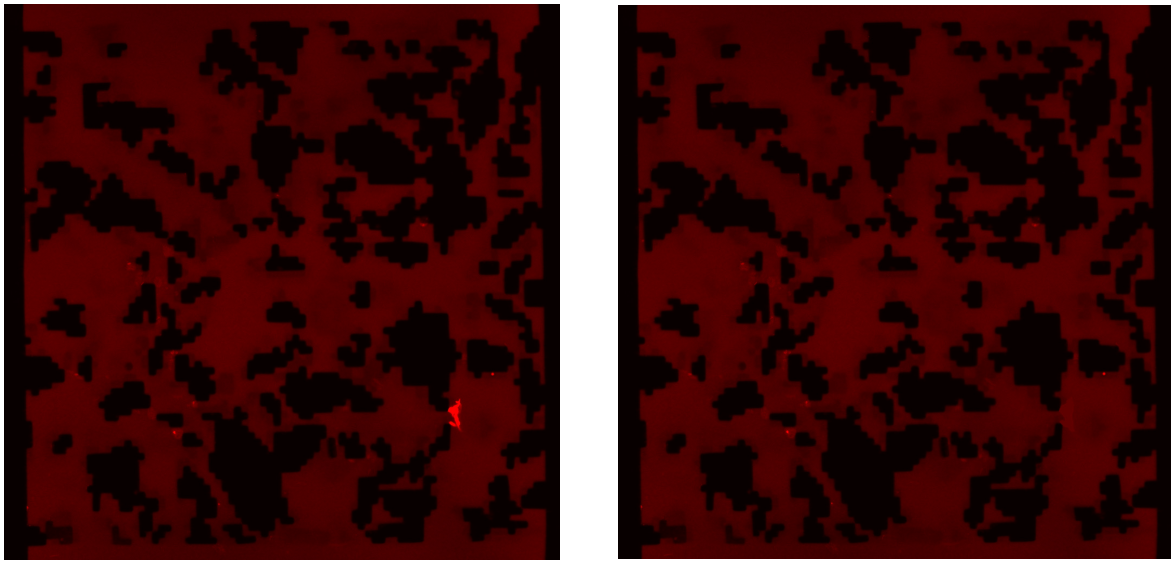

(a) (b)

Figure 9.4: Fluorescence image captured by confocal microscope showing RGB signals (a) Raw image (b) pre-processed image using threshold operator.

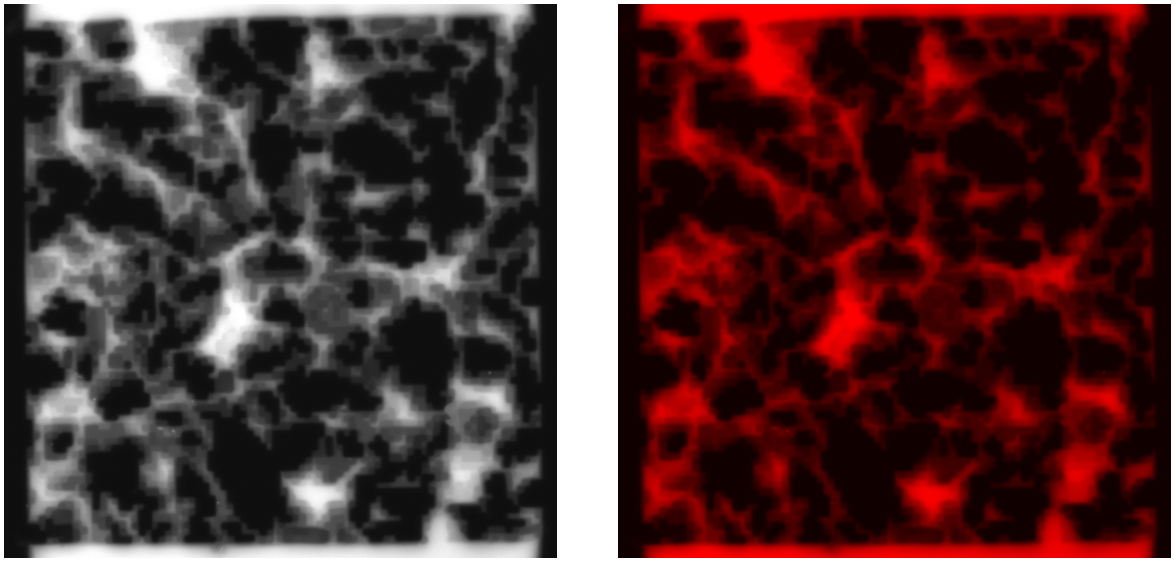

(a) (b)

Figure 9.5: Average of the superposition of fluorescence intensity of all images of dye flooded 2.5D high resolution micro-model, acquired by fluorescence confocal microscope (as shown in Figure 9.2) showing (a) 8-bit grayscale image and (b) 24 bit (true color) image.

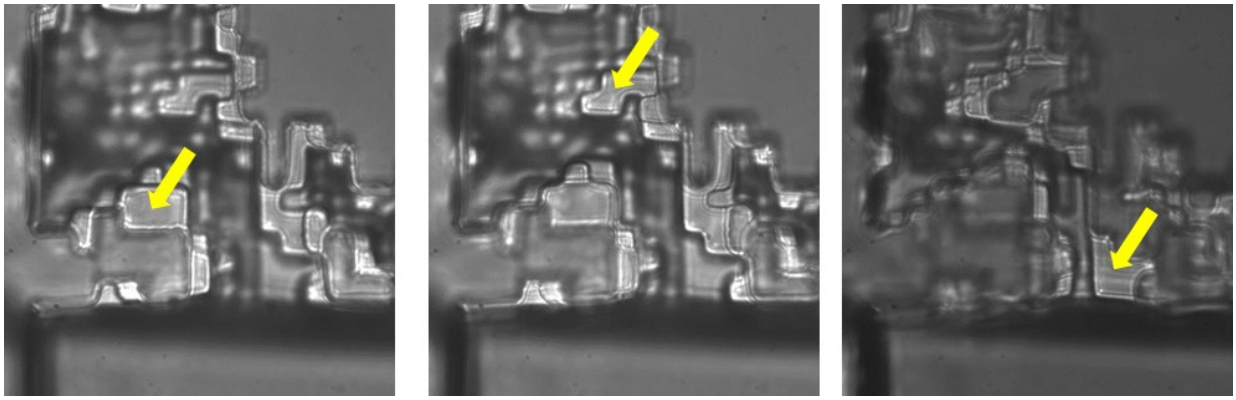

Figure 9.6: Brightfield image capture by confocal microscope using 60x1.49 NA oil immersion objective lens. Yellow arrow indicate depth measurement of the microstructure using confocal system in order to extract depth to calibration co-relation.

the weight function, and the principle of superposition is applied to all images. Figure 9.5 shows reconstructed images after superposition of all raw images.

9.8 Calibration

Similar to the previous depth extraction technique described in chapter 5, five different regions of interest were chosen to measure calibrated depth using a high NA oil immersion objective lens (60 x OI 1.49 NA). The depth of each structures were measured at different planes using a confocal microscope. For each depth, three different measurements were taken prior to analysis of the fluorescence dye image. Yellow arrows shown in the images indicated in Figure 9.6 measure calibrated depths at various planes for in-situ depth extraction of a high resolution micro-model. In similar fashion, 36 different measurements were collected for different structures at various planes.

9.9 Image Analysis

After superposition of all images, pixel intensity of the fluorescence dye at the specific location of the micro-model is calibrated with the calibrated depth of the micro-model. Figure 9.7 illustrates that a linear relationship exits between fluorescence pixel intensity and calibrated depth of the micro-model. The deeper the channel, the higher the signal emitted by fluorescence dye within depth of field. A linear regression model shows a linear relationship exists with more than 99 % correlation and repeatability. The red dotted

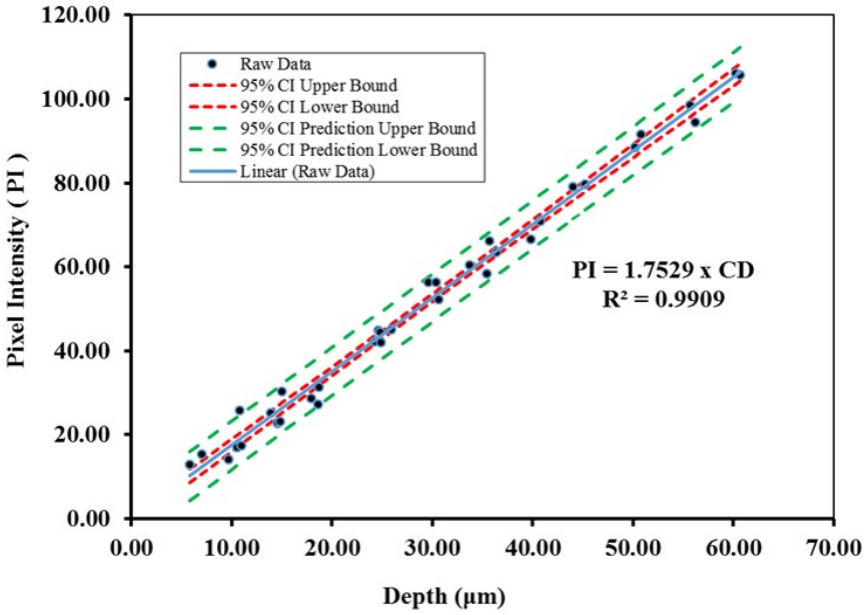

Figure 9.7: Depth correlation between fluorescence intensity measured in pixel intensity and calibrated depth of high resolution micro-model. Red dotted lines indicated 95 % confidential interval while as green dotted line indicated 95 % prediction confidence interval.

lines show a 95 % confidence interval of the model whereas the green dotted lines show a 95 % prediction interval of the linear model. As shown in the Figure 9.7, the linear regression model has less than 1 percent residual error, with a narrow confidence interval and prediction interval. The lower the width of the confidence interval, the higher the accuracy of the model. Based on the relationship between pixel intensity and calibrated depth, one can predict depth of any location with a maximum resolution of approximately 0.57 microns. This calibration equation was used to quantify depth over a high resolution micro-model.

Figure 9.8 shows a depth colormap generated from fluorescent dye image and depth-to-pixel calibration of the micro-model. Figure shows 3D geometry of the fluidic network of the high resolution 2.5D micro-model extracted from Boise rock sandstone. Shallow regions are represented by light brown color whereas the highest depths are represented by deep green color. The depth ranges from a couple of microns to 65 microns of the micro-model. This methodology is inexpensive as well as an efficient method of in-situ depth as well as 3D geometry extraction of a high resolution micro-model. Based on the depth-to-pixel

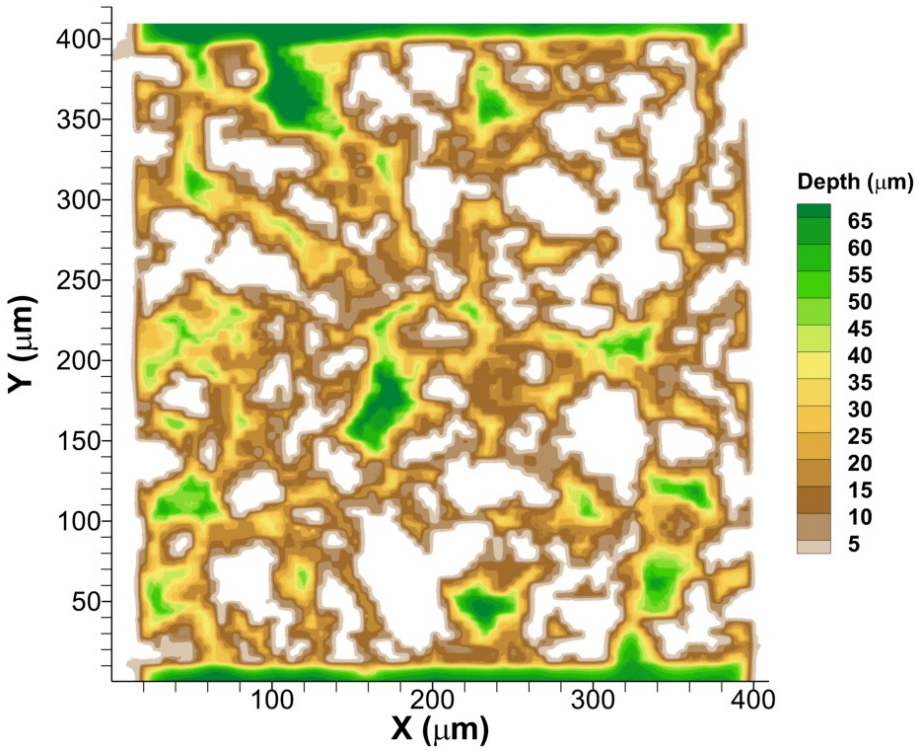

Figure 9.8: Reconstruction of 3D structure of in-situ micro-model using fluorescence based geometry extraction technique. Color map indicates depth of each structure in the micro-model.

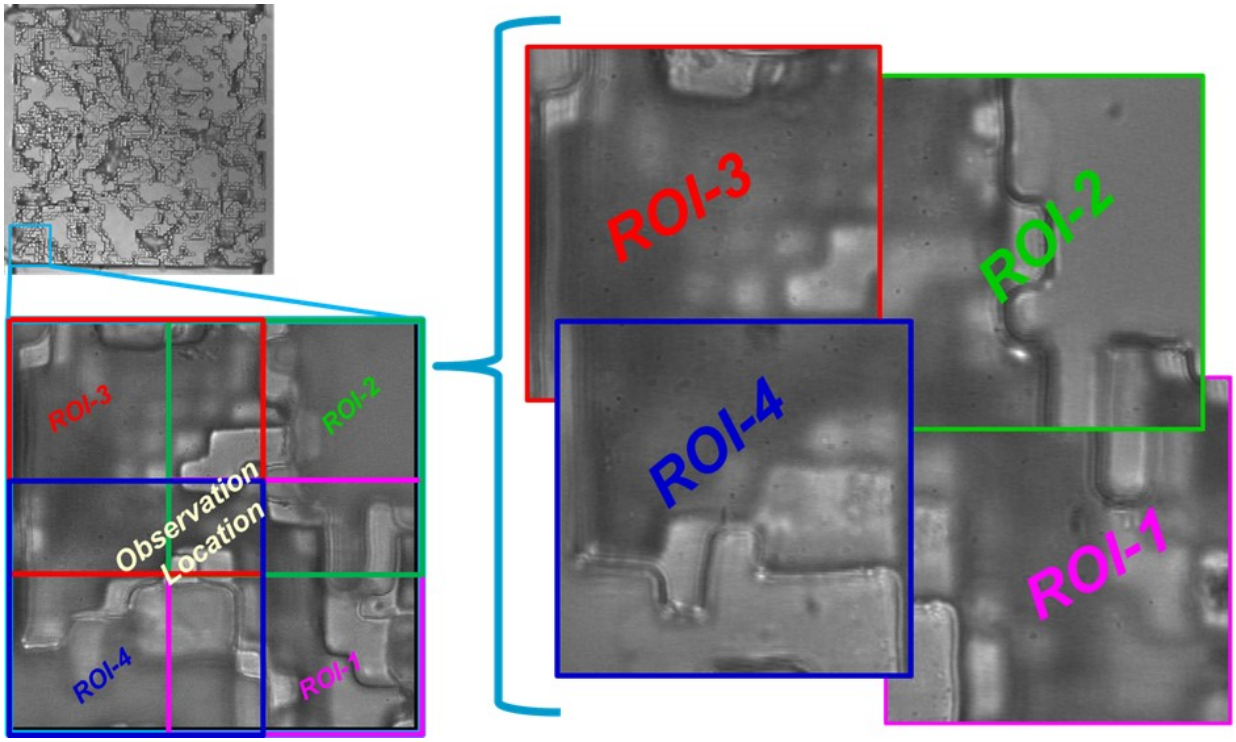

Figure 9.9: Brightfield image of high resolution micro-model filled with deionized water showing discretized region of interests 1,2,3 and 4 where the measurement were focused. Discretized ROIs were reassemble to produce full observation location using patching algorithm described in chapter 4.

intensity calibration relationship, one can segment a fluorescent image into various planes of the micro-model based on depth of the micro-model.

9.10 Velocity Distribution

Figure 9.9 shows an internal observation location of high resolution boise rock-based micro-model where 3D measurement of velocity distributions were measured. The observation location shown in Figure 9.9 consisted of 4 ROIs, the measurements of which were synthesized to cover particle flow domain. The 3D velocity fields of particle velocity measured at the observation location indicated in Figure 9.9 are presented in Figure 9.10 for all depths starting with velocity fields within 2.5 μm from the observation location proceeding in 2.5 μm depth increments all the way to the depth of the first throat of the observation location. The particle experiment was conducted to measure nano-particle velocity, and particle concentration in 3D at an internal observation location. From a prior experiment, it is observed that the observation location has a dominant flow path involving a pore with two throats with good variability in depth and has close velocities to the highest one. The particle transport experiment was initially conducted at 500 pL/min and later changed to 1 nL/min to mitigate difficulties with capturing advection flow over Brownian motion. De-ionized water seeded with neutrally buoyant and electrically neutral 300 nm ($\pm$ 3%) polystyrene fluorescent particles at a concentration 61.3 particles/pL (0.087% by volume) was injected through the inlet nano-port. Experimental procedures have been optimized so that measurements cover the earliest stages of particle flow into the micro-model. The data acquisition process has been optimized to acquire a broad dynamic range of velocities in the observation location with high spatial resolution. The post processing involves extraction of particle velocity and post data analysis to quantify deviation from an average value for each grid point. The process of synthesizing large observation locations from multiple regions of interest without losing any particle information is explained in detail in chapter 5. The spatial resolution is approximately 2.21 μm by 2.21 μm by 2.50 μm for relatively slow velocity fields and approximately 3.86 μm by 3.86 μm by 2.50 μm spatial

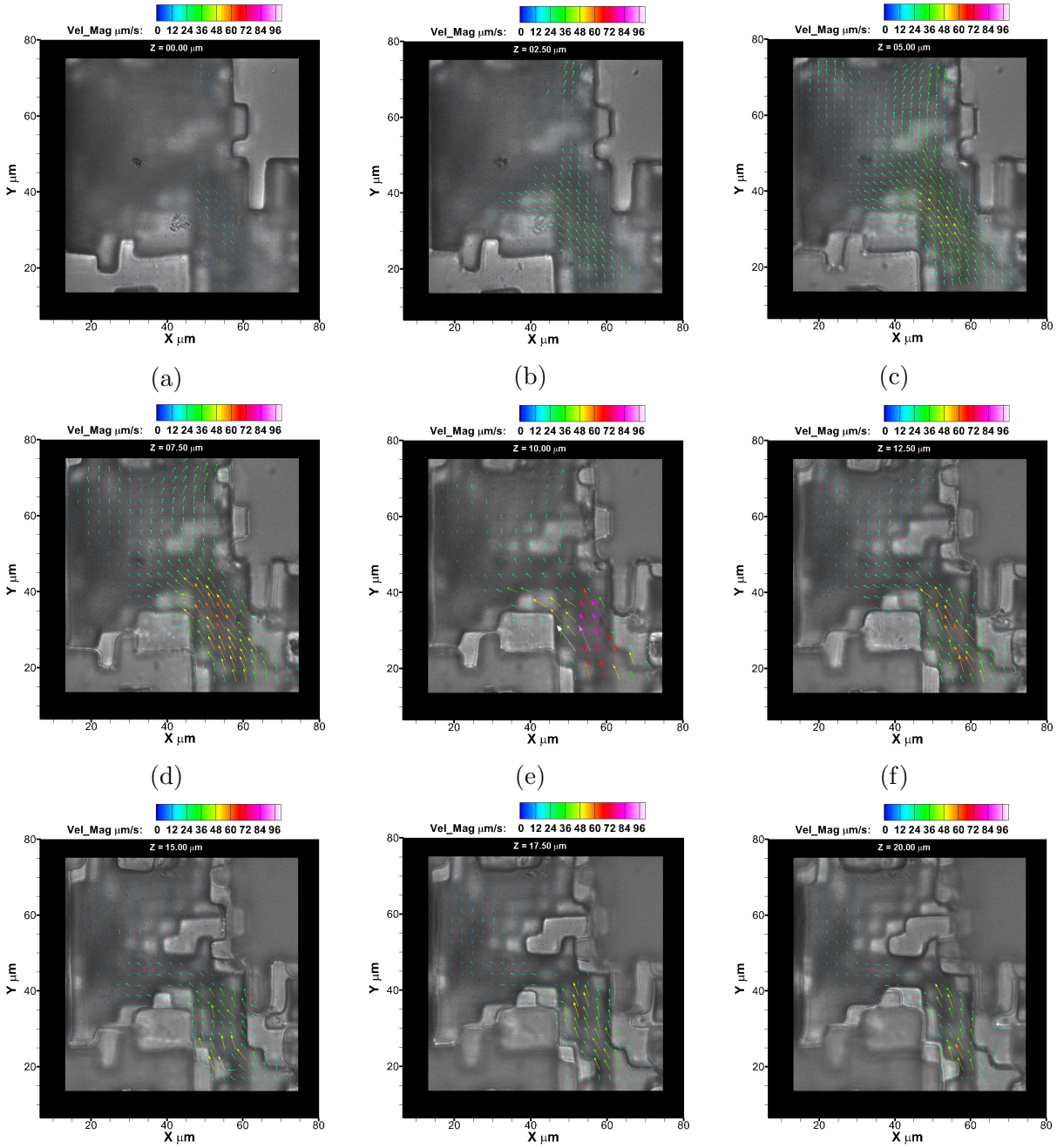

Figure 9.10: Sequences of images illustrating depth-wise velocity distribution at observation location of high resolution micro-model as indicated in Figure 9.9. Depth is measured from inside of the observation window starting at (a) 0 progressing to all the way through (i) 20 μm in an increment of 2.5 μm.Experimental conditions-Polystyrene fluorescent 300 nm particles; net flow rate 1 nL/min; particle concentration: 61.3 particles/pL (0.087% by volume)

resolution for relatively fast nano-particle transport regions. For each grid, each vector is color coded for velocity magnitude in microns per second and superposed in a synthesized bright field image of the observation location at various depths. High velocities are observed within approximately 10 μm through the throat (top half of the first throat). This is the mid-depth of the throat and has the highest velocities because of the nature of its small cross-sectional area. Some erratic velocity vectors are observed inside the narrowest part of the mid-plane and close to the bottom of the first throat of the sample. This is explained the velocity of the particles exceeding the velocity resolution in those depths along with significant low particle concentration compared to the top plane (the plane close to the flat cover sheet). Non-uniform velocity distributions are observed close to the bottom wall of the micro-model due to the fact that demolding of PMMA from the metallic master mold creates roughness near the bottom wall as well as side wall of the micro model. Velocities close to the flat top wall or close to the bottom wall in the observation location exhibit non-zero velocities but tend to zero, because a thin fluid layer may exist between the solid wall and the nano-particles. Velocity distributions close to the top wall are more consistent than the velocity distributions close to bottom wall of the observation location due to dominance of the flow in the system. Most of the fluid flow through the first couple of layers of the micro-model is limited by the throat size and connectivity of the flow as we move deeper into the micro-model close to the bottom of the system.

9.11 Particle Concentration Distribution

Discretization and image processing of raw images is described in detail in chapter 7, along with active area and centroid calculation. Particle concentration per unit pore volume was measured in 3D for observation location shown in Figure 9.9. Figure 9.11 shows 3D particle concentration measurements in nine measured depths for the observation location shown in Figure 9.9. For each depth, particle concentration was extracted at seven span wise locations and seven stream wise locations covering 61.82 μm x 61.82 μm. Each scatter plot is determined by the active flow area of nano-particles in discretized regions

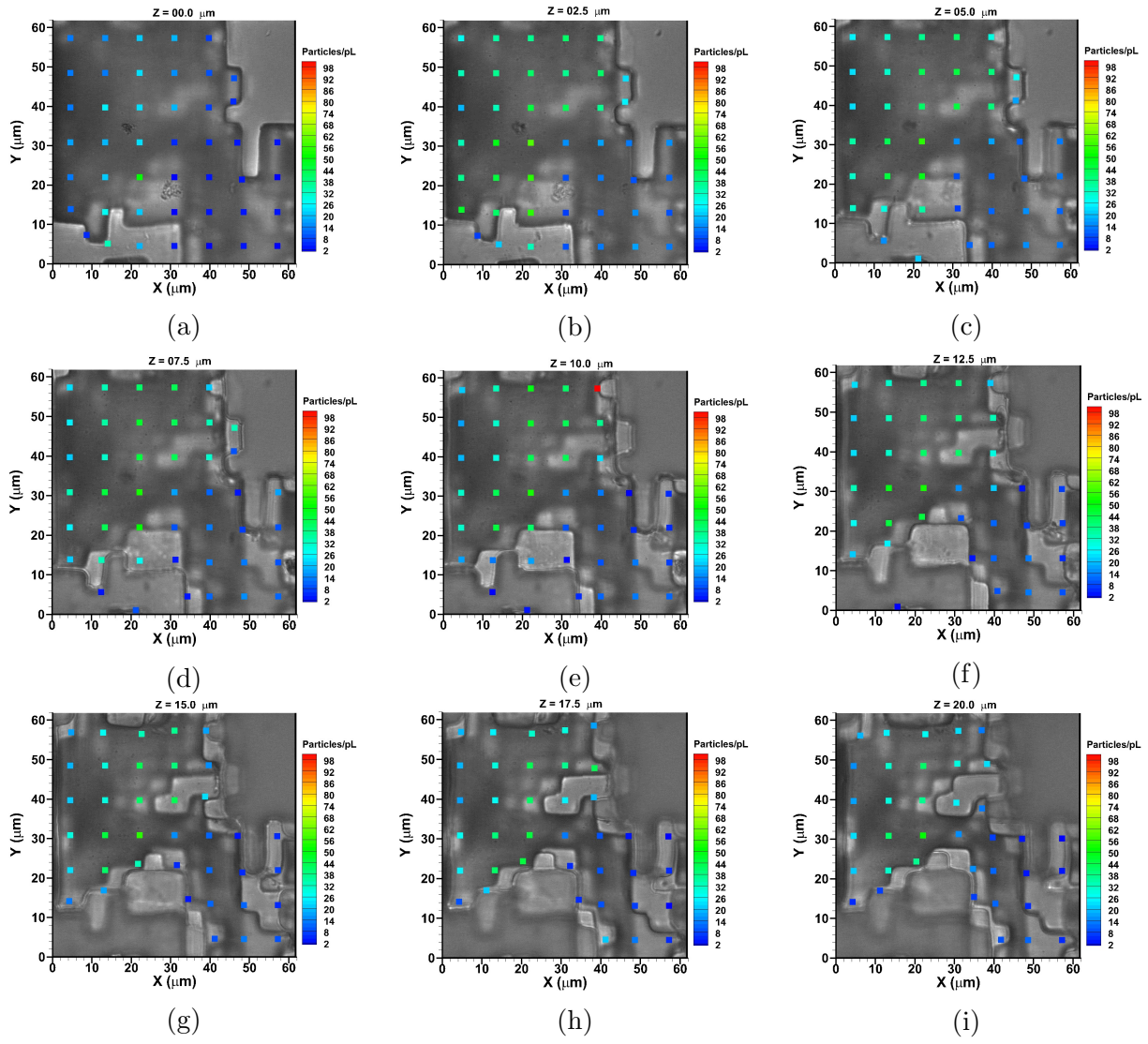

Figure 9.11: Sequences of images illustrating depth-wise velocity distribution at observation location of high resolution micro-model as indicated in Figure 9.9. Depth is measured from inside of the observation window starting at (a) 0 progressing to all the way through (i) 20 μm in an increment of 2.5 μm. Experimental conditions-Polystyrene fluorescent 300 nm particles; net flow rate 1 nL/min; particle concentration: 61.3 particles/pL (0.087% by volume)

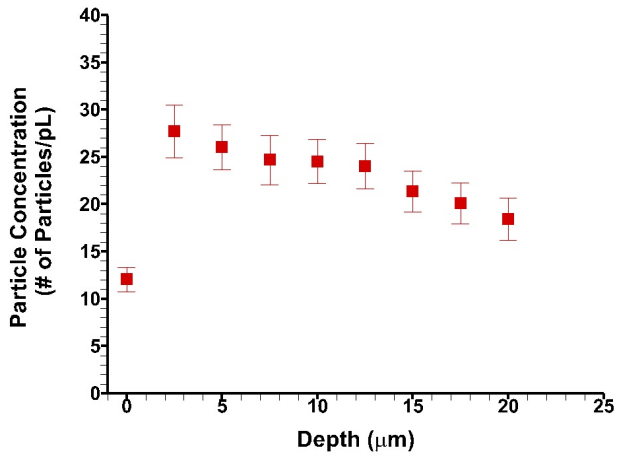

Figure 9.12: Total particle concentration in an observation location shown in Figure 9.9 with respect to depth inside the micro-model.

of 8.83 μm by 8.83 μm. The active flow area is defined as the total planar fluid-filled void area. Each scatter plot is color coded to represent the magnitude of particle concentration in number of particles per pore volume. The particle concentration distribution close to the inlet throat is lower than particle concentration at the outlet region. As we observed from velocity distribution, the highest velocities are observed in the narrow throat compared to the other regions in observation location, while for particle concentration, the highest particle concentration are observed away from the narrow throat location. Particle concentration per unit pore volume seems larger at approximately depth of Z = 2.5 μm while low particle concentration is observed close to the walls. The depth wise particle concentration increases rapidly from Z = 00 μm to Z= 2.5 μm and gradually decreases along depth to the bottom of the micro-model. Figure 9.12 shows depth wise particle concentration distribution which clearly shows particle concentrations close to the walls are much lower than particle concentration away from the walls. Particle concentration distributions on the left side of the observation location covers the largest void area while particle concentration at the right side (inlet region) covers less flow domain. Particle concentration in both domain are uniformly distribution. In a fast moving region, most of the particles enter and exit in a significantly high rate while in slow moving region, most of the particles remain in the observation domain for a longer time. Recapturing of the same particles in images

by confocal system occurs during limited image acquisition time, so recounting of those particles are higher in slow moving regions compare to fast moving regions.

9.12 Particle Deposition

The deposition evolution over time measured at four of these partially overlapping ROIs shown in Figure 9.9 is presented in this section. The experimental fluid consists of deionized water seeded with 300 nm fluorescence nano-particle flowing at a volumetric flow rate of 500 pL/min at a concentration of 61.3 particles/pL (0.087% by volume). Figure 9.13 shows sequences of raw images of nano-particles flowing at ROI 1 at several instantaneous times, acquired by the confocal microscope inside the micro-model close to the top wall, which is also called the Z=0 μm plane. Plane Z=0 μm is defined as the reference plane for all the measurements as well as the innermost plane of the flat observation PMMA sheet. Figure 9.13 consists of three dynamics group of nano-particles, *i.e.* mobile, immobile and waggling in nature. Figure 9.13a shows image of instantaneous nano-particles flowing in ROI 1 at frame 1, while Figure 9.13b shows image of instantaneous nano-particles flowing in the same ROI at frame 2, and Figure 9.13c shows image of instantaneous nano-particles flowing at the same ROI at frame 3. Figure 9.13d shows superposition of all nano-particles flowing in ROI 1 shown in Figure 9.9 at three different instants. Red colored nano-particles in Figure 9.13d indicate all the nano-particles of frame 1, while green colored nano-particles indicate nano-particles of frame 2 and the blue color indicates nano-particles of frame 3. Yellow(mixture of red and green color) signifies nano-particles that shared the same position at frame 1 and frame 2, while cyan(mixture of green and blue color) indicates nano-particles located in the same position at frames 2 and 3. Similarly, magenta(mixture of red and blue color) indicates that nano-particles are at the same position at frame 1 and frame 3. White colored (mixture of red, green and blue color) nano-particles indicate nano-particles remain attached to the same location for all three frames. NP-C1 particle, an immobile group particle appears in all frames (see Figure 9.13a- Figure 9.13c) and remains in the same position firmly which can be visualized by color coded particle in Figure 9.13d.

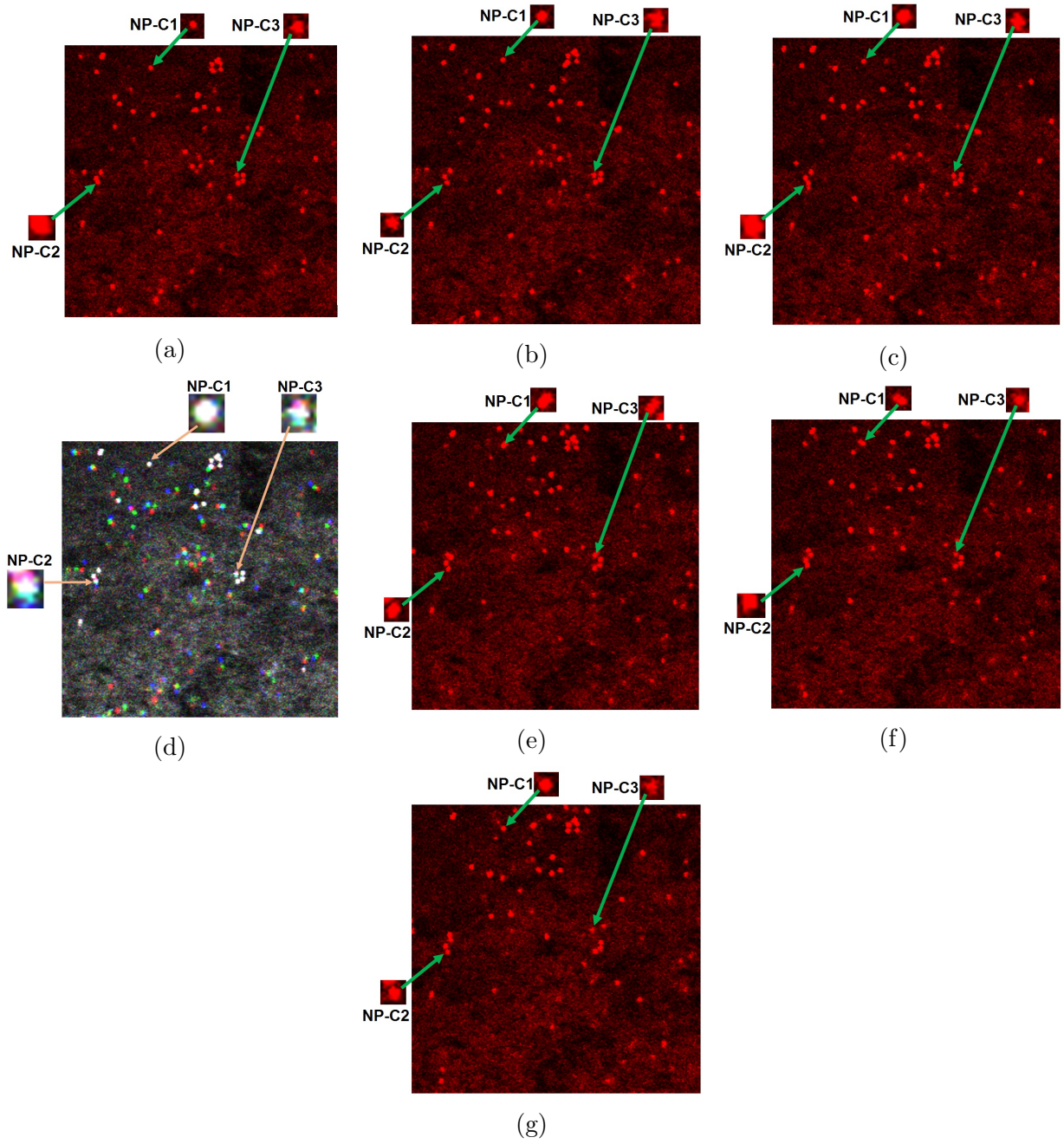

Figure 9.13: Sequences of raw images acquired by confocal microscope at region of interest I of high resolution micro-model as indicated in Figure 9.9 at (a) frame 1 (b) frame 2 (c) frame 3, (e) frame 403, (f) frame 404, and (g) frame 405.Time difference between two successive frame is 65 msecs. Superposition of images of nano-particles of frame 1 (indicated by red color), frame 2 (indicated by green color) and frame 3 (indicated by blue color) is shown in (d). Yellow color indicates partially or fully overlapping of a nano-particle image at fix location at two successive frames 1 and 2, whereas cyan color indicates partially or fully overlapping of a nano-particle image at fix location at two successive frames 2 and 3, and maganta color indicates partially or fully overlapping of a nano-particle image at fix location at two frames 1 and 3. White colored nano-particles in (d) indicates overlapping of a nano-particle image at fix location for all three frames.

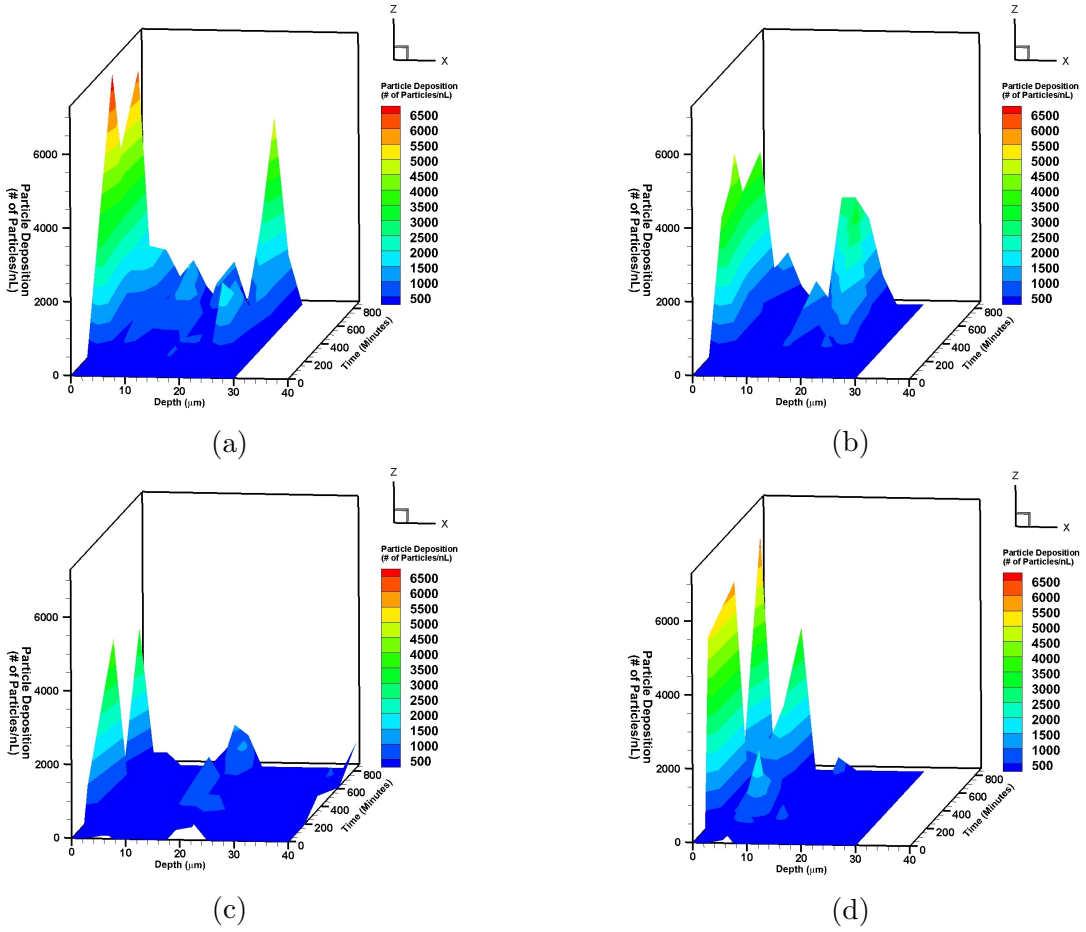

Figure 9.14: Sequences of images illustrating particle deposition over period of time at different planes at (a) ROI 1 (b) ROI 2 (c) ROI 3 (d) ROI 4 as indicated in Figure 9.9. Experimental conditions-Polystyrene fluorescent 300 nm particles; net flow rate 500 pL/min; particle concentration: 61.3 particles/pL (0.087% by volume).

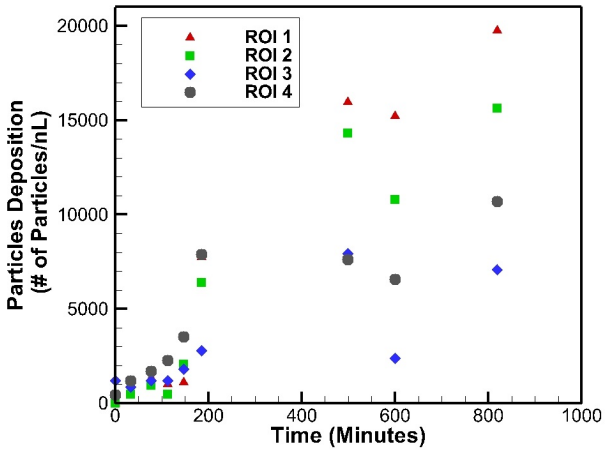

Figure 9.15: Total number of particle deposition in all walls of four different ROIs within the observation location as indicated in Figure 9.9. Experimental conditions-Polystyrene fluorescent 300 nm particles; net flow rate 500 pL/min; particle concentration: 61.3 particles/pL (0.087% by volume).

Similarly, NP-C2 and NP-C3 particles, a waggling group of particles, which have short and waggling motion and do not stay firmly in the same location can also be observed in Figure 9.13. The overlapping region color coded with yellow (mix of red and green color) shows some portion of a NP-C2 particle occupies same position to frame 1 and frame 2, whereas partially red and green color of a nano-particle shows difference in their position with respect to each other at two different frames. Similarly, the overlapping region color coded with magenta shows some portion of a NP-C2 particle occupies the same position in frame 2 and frame 3, whereas the overlapping region color coded with cyan shows some portion of a NP-C2 particle occupies the same position to frame 1 and frame 3. The other group of nano-particles are dynamic or mobile particles. Fully red, green, and blue colored particles shown in Figure 9.13d are dynamic particles and do not show any sign of attachment to the wall of the micro-model. As time proceeds, nano-particles deposit and get attached to the wall. As time passes, nano-particles segregate from the surface of the wall and few deposited particles detached from the surface of the wall and behaved as mobile particles. Figure 9.13e - 9.13g show raw images of nano-particles flowing at frame 403, 404 and 405 respectively. Figure 9.13e and Figure 9.13f show nano-particles NP-C3 is attached to the surface of the micro-model whereas in Figure 9.13g, NP-C3 nano-

particle is detached from the surface and acts as mobile nano-particles. So, deposition of nano-particles on the surface and detachment of nano-particles from the wall surface are continuous and simultaneous processes. There are some nano-particles like NP-C2, waggling in nature but never detached from the surface of the micro-model. The deposition evolution of nano-particles over time measured at four of these partially overlapping ROIs shown in Figure 9.9 is presented in Figure 9.14. Figure 9.14 shows a contour plot of 3D deposited particle counts per pore volume as pore volume is defined as finite fluid filled volume at each plane in four different ROIs. Figure 9.14 shows a contour plot of nano-particle deposition at different planes in four different ROIs. ROI 1 shows a rapid deposition of nano-particles close to the flat wall as it has large pore volume and the most favorable flow path compare to other planes, which results in larger particles concentration flowing on that vicinity compared to other planes in same ROI. Figure 9.15 shows no sign of deposition in all planes for ROI 1 and 2 for approximately 10 minutes after nano-particles enter the entrance throat of the Boise rock structure. As time elapses, particles start depositing on the top wall (flat wall) of the micro-model which is dominant compared to the side and bottom walls. This was measured during the first approximately 880 minutes ($\approx$ 15 hours) after the first particle was visualized in the fluid domain at the entrance of the rock-based structure of the micro-model. Figure 9.13 shows a few firmly deposited particles and few particles which are retained for a few minutes, detached from the walls, and ejected out of the visualization domain. Significant fluctuation of particle deposition and detachment from the surface walls are observed after approximately 200 minutes of the injection of nano-particles in the system as shown in Figure 9.14. Figure 9.15 shows continuous total volumetric particle deposition and detachment in the system at specific locations for approximately 800 minutes after injection of nano-particles in the system. From particle concentration, we know maximum particle flows occur within the first 2-3 layers of the micro-model close to the top flat observation window. The particles flowing close to the flat observation location have a higher affinity to be in contact with the flat

wall and have higher contact surface area compared to particles flowing farther from the flat wall. Therefore, most of the particles are accumulated in the flat wall compared to the other walls. Some particles trapped in the void regions possess Brownian effects due to a negligible pressure gradient and remain in the void region during the experiment.

9.13 Conclusion

In this chapter, we have briefly discussed a micro-fabrication process of a high resolution PMMA micro-model using a LIGA process along with a novel method of measuring in-situ depth, extracting in-situ 3D geometry at the micron level, as well as measuring sub-micron scale dynamics of the nano-particles in a complex high resolution micro-model. Confocal fluorescence microscopy along with a linear depth-to-fluorescence intensity calibration data is used for in-situ 3D geometry extraction of a high resolution Boise rock-based micro-model. The experimental study of 3D measurements of nano-particle velocity, concentration and particle deposition have been presented in this chapter.

Particle deposition over time has been studied, which has opened a new era of studying nano-particle wall interaction and its effects on fluid flow in a micro-nano system. Three dynamic ranges of nano-particles were found during our study: immobile, mobile and semi-mobile (waggling in nature). Immobile nano-particles are firmly attached to the surface of the micro-model whereas mobile particles did not show any sign of attachment to the surface of the wall. Semi-mobile or waggling particles dangle around a position without firm attachment to the surface. Some dangling particles detached from the surface while others attached to the surface of the top wall. The first group of nano-particles attached firmly to the surface of the micro-model signifies that it has higher potential energy compared to energy transfer due to advection in the system. A mobile nano-particle is driven solely by advection, as there is no significant fluctuation of temperature while performing the experiment. The third group of particles, which are waggling in nature are the most unstable nano-particles in the system as their potential energy to the PMMA surface lies within the energy transfer by convection of the fluid. Although the experimental study

in this chapter does not lie in the vicinity of current molecular dynamics simulations as these particles are larger than simulated nano-particle in our group as well as molecular dynamics simulation community, however it provides a basis for qualitative comparison with simulated nano-particles. The experimental results also provide a basis for future investigation of nano-particles in micro-nano systems in order to incorporate particle transport and wall-interaction into current transport models.

References

[1] International Energy Agency, *World energy outlook*. 2007.

[2] U. Energy Information Administration, "Primary energy production," *Monthly Energy Review*, no. November, p. 1, 2015.

[3] M. Cocuzza, C. Pirri, V. Rocca, and F. Verga, "Current and Future Nanotech Applications in the Oil Industry," *American Journal of Applied Sciences*, vol. 9, no. 6, pp. 784–793, 2012.

[4] K. Bullis, "Oil left in the ground," *MIT Technology Review*, 2008.

[5] S. Mokhatab, M. A. Fresky, and M. R. Islam, "Applications of Nanotechnology in Oil and Gas E&P," *Journal of Petroleum Technology*, vol. 58, no. 04, pp. 48–51, 2006.

[6] M. K. Chaudhury, "Spread the word about nanofluids," *Nature*, vol. 423, p. 131, 2003.

[7] D. Wasan, A. Nikolov, and K. Kondiparty, "The wetting and spreading of nanofluids on solids: Role of the structural disjoining pressure," *Current Opinion in Colloid & Interface Science*, vol. 16, no. 4, pp. 344–349, 2011.

[8] D. T. Wasan and A. D. Nikolov, "Spreading of nanofluids on solids.," *Nature*, vol. 423, no. 6936, pp. 156–159, 2003.

[9] B. Moradi, P. Pourafshary, F. Jalali, M. Mohammadi, and M. Emadi, "Experimental study of water-based nanofluid alternating gas injection as a novel enhanced oil-recovery method in oil-wet carbonate reservoirs," *Journal of Natural Gas Science and Engineering*, pp. 1–10, 2015.

[10] A. M. S. Ragab and A. E. Hannora, "An Experimental Investigation of Silica Nano Particles for Enhanced Oil Background of Nano Particles usage for EOR," 2015.

[11] D.-h. Han, A. Nur, and D. Morgan, "Effects of porosity and clay content on wave velocities in sandstones," *Society of Exploration GeoPhysicists*, vol. 51, no. 11, pp. 111–119, 1986.

[12] K. Romanenko, D. Xiao, and B. J. Balcom, "Velocity field measurements in sedimentary rock cores by magnetization prepared 3D SPRITE.," *Journal of Magnetic Resonance*, vol. 223, pp. 120–128, 2012.

[13] D. S. Park, S. Bou-mikael, S. King, K. E. Thompson, C. S. Willson, and D. E. Nikitopoulos, "Design and Fabrication of Rock Based Micromodel," in *International Mechanical Engineering Congress & Expo*, pp. 1–7, 2012.

[14] J. Upadhyay, D. S. Park, , K. E. Thompson, and D. E. Nikitopoulos, "3D Measurements of nano-particle transport in complex 2.5D micro-models," in *International Mechanical Engineering Congress & Expo*, pp. 1–10, ASME, 2015.

[15] W.-C. Tian and E. Finehout, eds., *Microfluidics for Biological Applications*. Springer, 2008.

[16] S. Hardt and F. Schonfeld, eds., *Microfluidic Technologies for Miniaturized Analysis Systems*. Springer, 2007.

[17] D. Sinton, "Energy: the microfluidic frontier," *Lab on a Chip*, vol. 14, no. 17, p. 3127, 2014.

[18] N. C. Wardlaw, "The Effects of pore structure on displacemnet efficiency in reservior rocks and in glass micromodel," *Society of Petroleum Engineers of AIME*, pp. 345–353, 1980.

[19] H. Stone, A. Stroock, and A. Ajdari, "Engineering Flows in Small Devices," *Annual Review of Fluid Mechanics*, vol. 36, no. 1, pp. 381–411, 2004.

[20] J. Zhang, S. Yan, D. Yuan, G. Alici, N.-T. Nguyen, M. Ebrahimi Warkiani, and W. Li, "Fundamentals and Applications of Inertial Microfluidics: A Review," *Lab Chip*, 2015.

[21] N. S. Kumar Gunda, B. Bera, N. K. Karadimitriou, S. K. Mitra, and S. M. Hassanizadeh, "Reservoir-on-a-Chip (ROC): A new paradigm in reservoir engineering," *Lab on a Chip*, vol. 11, no. 22, p. 3785, 2011.

[22] R. Fisher, M. K. Shah, D. Eskin, K. Schmidt, A. Singh, S. Molla, and F. Mostowfi, "Equilibrium gas-oil ratio measurements using a microfluidic technique.," *Lab on a chip*, vol. 13, no. 13, pp. 2623–2633, 2013.

[23] M. a. Nilsson, R. Kulkarni, L. Gerberich, R. Hammond, R. Singh, E. Baumhoff, and J. P. Rothstein, "Effect of fluid rheology on enhanced oil recovery in a microfluidic sandstone device," *Journal of Non-Newtonian Fluid Mechanics*, vol. 202, pp. 112–119, 2013.

[24] M. L. Porter, J. Jiménez-Martínez, R. Martinez, Q. McCulloch, J. W. Carey, and H. S. Viswanathan, "Geo-material microfluidics at reservoir conditions for subsurface energy resource applications," *Lab Chip*, vol. 15, no. 20, pp. 4044–4053, 2015.

[25] S. A. Bou-Mikael, "Design and Optimization of 2.5 Dimension Porous Media Micomodel for Nanosensor Flow Experiments," Master's thesis, Louisiana State University, 2012.

[26] L. Hendraningrat, S. Li, and O. Torsæter, "A coreflood investigation of nanofluid enhanced oil recovery," *Journal of Petroleum Science and Engineering*, vol. 111, pp. 128–138, 2013.

[27] E. Rodriguez Pin, M. Roberts, H. Yu, C. Huh, and S. L. Bryant, "Enhanced Migration of Surface-Treated Nanoparticles in Sedimentary Rocks," *SPE Annual Technical Conference and Exhibition*, p. 124418, 2013.

[28] B. Suleimanov, F. Ismailov, and E. Veliyev, "Nanofluid for enhanced oil recovery," *Journal of Petroleum Science and Engineering*, vol. 78, no. 2, pp. 431–437, 2011.

[29] H. Ehtesabi, M. M. Ahadian, V. Taghikhani, and M. H. Ghazanfari, "Enhanced heavy oil recovery in sandstone cores using TiO2 nanofluids," *Energy and Fuels*, vol. 28, no. 1, pp. 423–430, 2014.

[30] H. Zhang, A. Nikolov, and D. Wasan, "Enhanced oil recovery (EOR) using nanoparticle dispersions: Underlying mechanism and imbibition experiments," *Energy and Fuels*, vol. 28, no. 5, pp. 3002–3009, 2014.

[31] M. J. Jackson, *Microfabrication and Nanomanufacturing*. CRC Taylor and Francis, 2006.

[32] T. Masuzawa and H. Tönshoff, "Three-Dimensional Micromachining by Machine Tools," *CIRP Annals - Manufacturing Technology*, vol. 46, no. 2, pp. 621–628, 1997.

[33] S. Franssila, *Introduction of Microfabrication*. John Wiley & Sons Ltd., second ed., 2010.

[34] M. J. Madou, *Fundamentals of Microfabrication*. CRC Press, 2 ed., 2002.

[35] G. Bissacco, H. N. Hansen, and L. De Chiffre, "Micromilling of hardened tool steel for mould making applications," *Journal of Materials Processing Technology*, vol. 167, no. 2-3, pp. 201–207, 2005.

[36] E. M. Kussul, D. a. Rachkovskij, T. N. Baidyk, and S. a. Talayev, "Micromechanical engineering: a basis for the low-cost manufacturing of mechanical microdevices using microequipment," *Journal of Micromechanics and Microengineering*, vol. 6, no. 4, pp. 410–425, 1996.

[37] J. H. Lee, S. R. Park, and S. H. Yang, "Machining a Micro/Meso Scale Structure Using a Minaturized Machine Tool by Using a Conventional Cutting Process," *Journal of Manufacturing Science and Engineering*, vol. 128, no. 3, p. 820, 2006.

[38] I. Ikawa, R. R. Donaldson, W. Konig, T. H. Aachen, and P. A. McKeown, "Ultraprecision Metal Cutting- The Past, the Present and the Future," *Annals of the CIRP*, vol. 40, no. 2, pp. 587–594, 1991.

[39] A. Aramcharoen and P. Mativenga, "Size effect and tool geometry in micromilling of tool steel," *Precision Engineering*, vol. 33, no. 4, pp. 402–407, 2009.

[40] K. Liu and S. N. Melkote, "Finite element analysis of the influence of tool edge radius on size effect in orthogonal micro-cutting process," *International Journal of Mechanical Sciences*, vol. 49, no. 5, pp. 650–660, 2007.

[41] J. Chae, S. Park, and T. Freiheit, "Investigation of micro-cutting operations," *International Journal of Machine Tools and Manufacture*, vol. 46, no. 3-4, pp. 313–332, 2006.

[42] M. P. Vogler, R. E. DeVor, and S. G. Kapoor, "On the Modeling and Analysis of Machining Performance in Micro-Endmilling, Part I: Surface Generation," *Journal of Manufacturing Science and Engineering*, vol. 126, no. 4, pp. 685–694, 2004.

[43] K. Liu, X. P. Li, and M. Rahman, "Characteristics of high speed micro-cutting of tungsten carbide," *Journal of Materials Processing Technology*, vol. 140, no. 1-3 SPEC., pp. 352–357, 2003.

[44] K. Saptaji, *Handbook of Manufacturing Engineering and Technology*. Springer-Verlag London, a.y.c nee ed., 2015.

[45] D. Dornfeld, S. Min, and Y. Takeuchi, "Recent Advances in Mechanical Micromachining," *CIRP Annals - Manufacturing Technology*, vol. 55, no. 2, pp. 745–768, 2006.

[46] L. Gillespie, *Deburring and Edge Finishing Handbook*. SME Dearborn, 1999.

[47] M. Heckele and W. K. Schomburg, "Review on micro molding of thermoplastic polymers," *Journal of Micromechanics and Microengineering*, vol. 14, no. 3, pp. R1–R14, 2003.

[48] T. Hanemann, M. Heckele, and V. Piotter, "Current Status of Micromolding Technology," *Polymer News*, vol. 25, pp. 224–229, 2000.

[49] S. Yang and L. Nien, "Experimental study on injection compression molding of cylindrical parts," *Advances in Polymer Technology*, vol. 15, no. 3, pp. 205–213, 1996.

[50] H. Becker and U. Heim, "Hot embossing as a method for the fabrication of polymer high aspect ratio structures," *Sensors and Actuators, A: Physical*, vol. 83, no. 1, pp. 130–135, 2000.

[51] R.-D. Chien, "Hot embossing of microfluidic platform," *International Communications in Heat and Mass Transfer*, vol. 33, no. 5, pp. 645–653, 2006.

[52] D. S. Park, J. Upadhyay, V. Singh, K. E. Thompson, and D. E. Nikitopoulos, "Fabrication of 2.5D rock-base micromodels with high resolution features," in *IMECE*, 2015.

[53] R. Moreno-Atanasio, R. A. Williams, and X. Jia, "Combining X-ray microtomography with computer simulation for analysis of granular and porous materials," *Particuology*, vol. 8, no. 2, pp. 81–99, 2010.

[54] E. N. Landis and D. T. Keane, "X-ray microtomography," *Materials Characterization*, vol. 61, no. 12, pp. 1305–1316, 2010.

[55] D. Baker, L. Mancini, M. Polacci, M. Higgins, G. Gualda, R. Hill, and M. Rivers, "An introduction to the application of X-ray microtomography to the three-dimensional study of igneous rocks," *Lithos*, vol. 148, pp. 262–276, 2012.

[56] I. M. Orlov, D. G. Morgan, and R. H. Cheng, "Efficient implementation of a filtered back-projection algorithm using a voxel-by-voxel approach," *Journal of Structural Biology*, vol. 154, no. 3, pp. 287–296, 2006.

[57] T. Park, I. h. Song, D. S. Park, B. H. You, and M. Murphy, "Thermoplastic fusion bonding using a pressure-assisted boiling point control system Lab on a Chip Thermoplastic fusion bonding using a pressure-assisted boiling point control system," no. August 2016, 2012.

[58] Olympus, "Confocal Laser Scanning Biological Microscope.".

[59] M. Minsky, "Memoir on Inverting the Confocal scanning Microscope," *Scanninng*, vol. 10, pp. 128–138, 1998.

[60] J. S. Park, C. K. Choi, and K. D. Kihm, "Optically sliced micro-PIV using confocal laser scanning microscopy (CLSM)," vol. 37, pp. 105–119, 2004.

[61] S. Kimura and C. Munakata, "Depth resolution of the fluorescent confocal scanning optical Microscope," *Applied Optics*, vol. 29, no. 9, pp. 489–494, 1990.

[62] T. Wilson, "Resolution and optical sectioning in the confocal microscope," vol. 244, no. August 2010, pp. 113–121, 2011.

[63] S. Wilhelm, B. Grobler, M. Gluch, and H. Heinz, "Confocal laser scanning microscopy: Principles," tech. rep., 2003.

[64] C. J. Bourdon, M. G. Olsen, and A. D. Gorby, "Power-filter technique for modifying depth of correlation in microPIV experiments," vol. 37, pp. 263–271, 2004.

[65] C. J. Bourdon, M. G. Olsen, and A. D. Gorby, "in Micro-PIV for High Numerical Aperture and Immersion Objectives," vol. 128, no. July 2006, pp. 883–886, 2014.

[66] M. Rossi, R. Segura, C. Cierpka, and C. J. Ka, "On the effect of particle image intensity and image preprocessing on the depth of correlation in micro-PIV," pp. 1063–1075, 2012.

[67] B. M. B. Stoeber, "Effect of linear image processing on the depth of correlation in micro PIV," 2014.

[68] W. Kim, S. Jin, and J. Jeong, "Novel Intra Deinterlacing Algorithm Using Content Adaptive Interpolation," *IEEE Transactions on Consumer Electronics*, vol. 53, no. 3, pp. 1036–1043, 2007.

[69] M. K. Park, M. G. Kang, K. Nam, and S. G. Oh, "New Edge Dependent Deinterlacing Algorithm Based on Horizontal Edge Pattern," *IEEE Transactions on Consumer Electronics*, vol. 49, no. 4, pp. 1508–1512, 2003.

[70] O. Kwon, K. Sohn, and C. Lee, "Deinterlacing using Directional Interpolation and Motion Compensation," *IEEE Transactions on Consumer Electronics*, vol. 49, no. 1, pp. 198–203, 2003.

[71] G. D. E. Haan, S. Member, and E. B. Bellers, "Deinterlacing An Overview," *PROCEEDINGS OF THE IEEE*, vol. 86, no. 9, pp. 1839–1857, 1998.

[72] S. C. Tai, C. S. Yu, and F. J. Chang, "A Motion and Edge Adaptive Deinterlacing Algorithm," in *IEEE International Conference on Multimedia and Expo (ICME)*, pp. 659–662, 2004.

[73] H. Kim, S. Große, G. E. Elsinga, and J. Westerweel, "Full 3D-3C velocity measurement inside a liquid immersion droplet," *Experiments in Fluids*, vol. 51, pp. 395–405, feb 2011.

[74] C. D. Meinhart, S. T. Wereley, and J. G. Santiago, "PIV measurements of a microchannel flow," *Experiments in Fluids*, vol. 27, pp. 414–419, 1999.

[75] Ronald J. Adrian, "Particle-Imaging Techniques for Experimental Fluid Mechanics," *Annual Review of Fluid Mechanics*, vol. 23, pp. 261–304, 1991.

[76] S. Devasenathipathy, J. G. Santiago, S. T. Wereley, C. D. Meinhart, and K. Takehara, "Particle imaging techniques for microfabricated fluidic systems," *Experiments in Fluids*, vol. 34, pp. 504–514, mar 2003.

[77] J. G. Santiago, S. T. Wereley, C. D. Meinhart, D. J. Beebe, and R. J. Adrian, "A particle image velocimetry system for microfluidics," *Experiments in Fluids*, vol. 25, pp. 316–319, sep 1998.

[78] A. Melling, "Tracer particles and seeding for particle image velocimetry," *Measurement Science and Technology*, vol. 8, pp. 1406–1416, 1997.

[79] J. Fredrich, "3D Imaging of Porous Media using Laser Scanning Confocal Microscopy with Application to Microscale Transport Processes," *Phys. Chern. Earth (A)*, vol. 24, no. 7, pp. 551–561, 1999.

[80] S. D. Peterson, H.-s. Chuang, and S. T. Wereley, "Three-dimensional particle tracking using micro-particle image velocimetry hardware," *Measurement Science and Technology*, vol. 19, 2008.

[81] S. a. Klein, J. L. Moran, D. H. Frakes, and J. D. Posner, "Three-dimensional three-component particle velocimetry for microscale flows using volumetric scanning," *Measurement Science and Technology*, vol. 23, p. 085304, aug 2012.

[82] L. Kajitani and D. Dabiri, "A full three-dimensional characterization of defocusing digital particle image velocimetry," *Measurement Science and Technology*, vol. 16, pp. 790–804, mar 2005.

[83] K. C. Kim, "Advances and applications on micro-defocusing digital particle image velocimetry (μ-DDPIV) techniques for microfluidics," *Journal of Mechanical Science and Technology*, vol. 26, pp. 3769–3784, jan 2013.

[84] S. J. Lee and S. Kim, "Advanced particle-based velocimetry techniques for microscale flows," *Microfluidics and Nanofluidics*, vol. 6, pp. 577–588, jan 2009.

[85] H. Kim, J. Westerweel, and G. E. Elsinga, "Comparison of Tomo-PIV and 3D-PTV for microfluidic flows," *Measurement Science and Technology*, vol. 24, feb 2012.

[86] H. Kinoshita, S. Kaneda, T. Fujii, and M. Oshima, "Three-dimensional measurement and visualization of internal flow of a moving droplet using confocal micro-PIV," *Lab on a Chip*, vol. 7, pp. 338–346, 2006.

[87] R. Lima, S. Wada, M. Takeda, K.-i. Tsubota, and T. Yamaguchi, "In vitro confocal micro-PIV measurements of blood flow in a square microchannel: the effect of the haematocrit on instantaneous velocity profiles.," *Journal of biomechanics*, vol. 40, pp. 2752–7, jan 2007.

[88] Y. Sugii, R. Okuda, and K. Okamoto, "Velocity measurement of both red blood cells and plasma of in vitro blood flow using high-speed micro PIV technique," *Measurement Science and Technology*, vol. 16, pp. 1126–1130, 2005.

[89] T. a. Ooms, R. Lindken, and J. Westerweel, "Digital holographic microscopy applied to measurement of a flow in a T-shaped micromixer," *Experiments in Fluids*, vol. 47, pp. 941–955, jun 2009.

[90] Y. U. Min and K. C. Kim, "Hybrid micro-/nano-particle image velocimetry for 3D3C multi-scale velocity field measurement in microfluidics," *Measurement Science and Technology*, vol. 22, p. 064001, jun 2011.

[91] D. Liu, S. V. Garimella, and S. T. Wereley, "Infrared micro-particle image velocimetry in silicon-based microdevices," *Experiments in Fluids*, vol. 38, pp. 385–392, feb 2004.

[92] D. Sen, D. S. Nobes, and S. K. Mitra, "Optical measurement of pore scale velocity field inside microporous media," *Microfluidics and Nanofluidics*, vol. 12, pp. 189–200, aug 2011.

[93] K. Ogawa, T. Matsuka, and S. Hirai, "Three-dimensional velocity measurement of complex interstitial flows through water-saturated porous media by the tagging method in the MRI technique," *Measurement Science and Technology*, vol. 12, pp. 172–180, 2001.

[94] B. Bijeljic, A. Raeini, P. Mostaghimi, and M. J. Blunt, "Predictions of non-Fickian solute transport in different classes of porous media using direct simulation on pore-scale images," vol. 013011, pp. 1–9, 2013.

[95] G. Silva, N. Leal, and V. Semiao, "Chemical Engineering Research and Design Determination of microchannels geometric parameters using micro-PIV," *chemical Engineering Research and Design*, vol. 87, no. August, pp. 298–306, 2009.

[96] K. Kikuchi and O. Mochizuki, "Micro PIV measurement of slip flow on a hydrogel surface," *Measurement Science and Technology*, vol. 25, 2014.

[97] P. A. Walsh, V. M. Egan, and E. J. Walsh, "Novel micro-PIV study enables a greater understanding of nanoparticle suspension flows : nanofluids," *Microfluid Nanofluid*, vol. 8, pp. 837–842, 2010.

[98] J. Chen and J. Katz, "Elimination of peak-locking error in PIV analysis using the correlation mapping," *Measurement Science and Technology*, vol. 16, pp. 1605–1618, 2005.

[99] D. P. Hart, "PIV error correction," *Experiments in Fluids*, vol. 29, pp. 13–22, 2000.

[100] R. D. Keane and R. J. Adrian, "Theory of cross-correlation analysis of PIV images RICHARD D. KEANE & RONALD J. ADRIAN," *Applied Scientific Reserach*, vol. 49, pp. 191–215, 1992.

[101] H. Nobach and Æ. E. Bodenschatz, "Limitations of accuracy in PIV due to individual variations of particle image intensities," *Experiments in Fluids*, vol. 47, pp. 27–38, 2009.

[102] K. Sharmin, *FABRICATION AND CHARACTERIZATION OF MINIATURIZED COMPONENTS BASED ON EXTRUDED CERAMIC-FILLED POLYMER BLENDS*. PhD thesis, Louisiana State University, 2015.

[103] B. R. Knitter, W. Bauer, and D. Göhring, "Manufacturing of Ceramic Microcomponents by a Rapid Prototyping Process Chain," *Advanced Engineering Materials*, no. 1, pp. 49–54, 2001.

[104] P. Soille, *Morphological Image Analysis: Principles and Applications*. Springer Science & Business Media, 2 ed., 2013.

Appendix A
Comparision of X-ray Tomography and In-situ Depth Measurement Techniques

This appendix covers depth measurements of various planes of 2.5D micromodel using X-ray tomography and in-situ depth measurement technique described in chapter 4. Fluorescence image of Boise rock-based micromodel captured by confocal image is segmented using pixel-to-depth calibration which is experimentally determined, is used to segment fluorescence to extract various depth planes of fluidic domain. Colored coded region in design CAD drawing represents void region of 2.5D micromodel whereas white color indicates solid structures. In fluorescence image, black color coded region indicates solid region where no fluid can penetrate whereas white region indicates fluid filled region. In other word, fluid filled region denotes void region in 2.5D micromodel. The x-ray tomography images are shown as gray image where solid structures are clearly visualized. Figure A.1 - A.12 compares images of 2.5D micromodel at various depth using x-ray tomography technique and fluorescence based depth extraction technique.

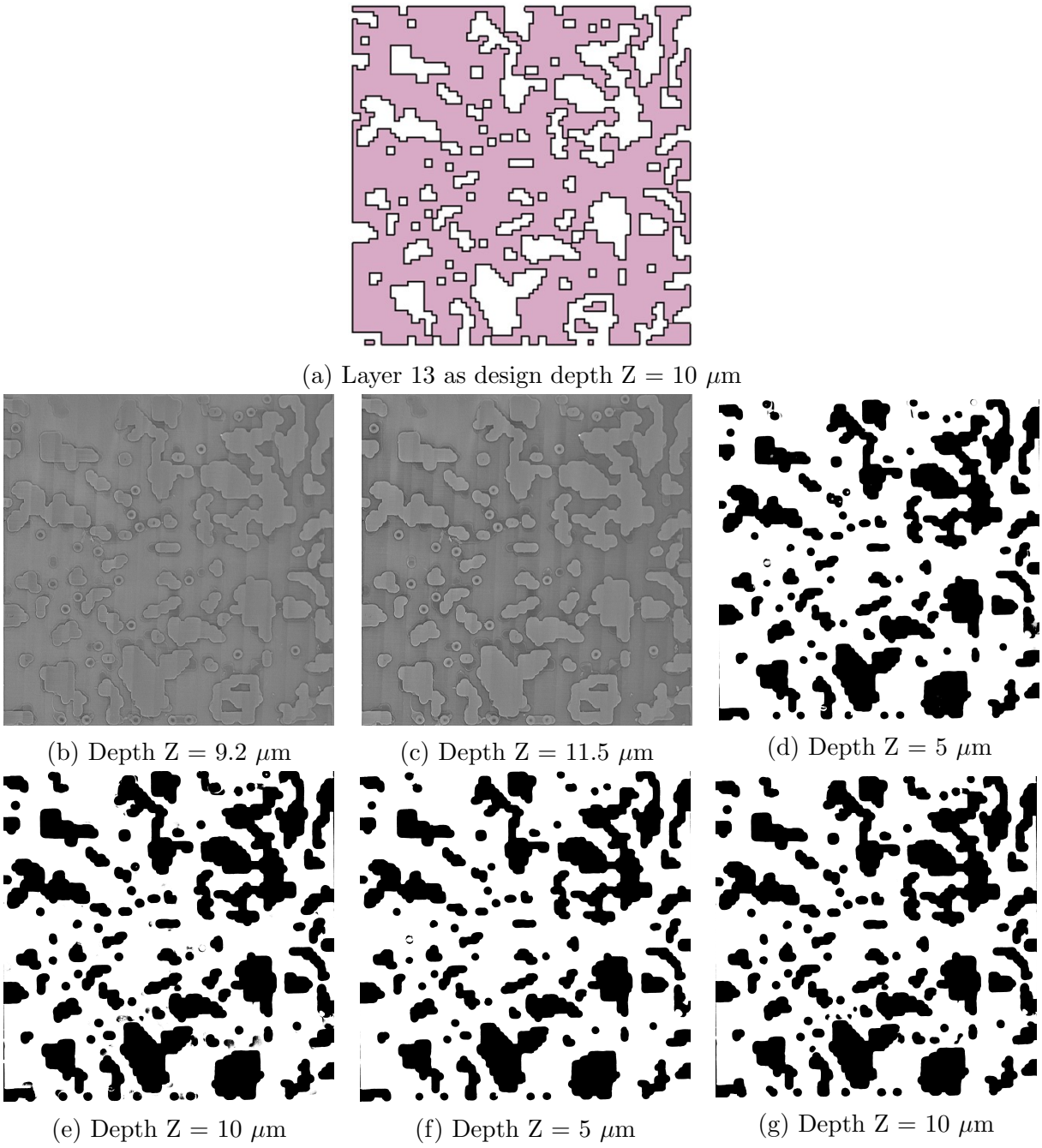

(a) Layer 13 as design depth Z = 10 μm

(b) Depth Z = 9.2 μm

(c) Depth Z = 11.5 μm

(d) Depth Z = 5 μm

(e) Depth Z = 10 μm

(f) Depth Z = 5 μm

(g) Depth Z = 10 μm

Figure A.1: Comparision of Depth Measurement using Fluorescence and X-ray Tomography Techniques at layer 13. Design drawing is represented in (a) whereas (b) and (c) are CT X-ray images at their respective depth and (d) and (e) represents raw fluorescence images at respective depth using fluorescent techniques and (f) and (g) are fluorescence images after applying filter to image (d) and (e).

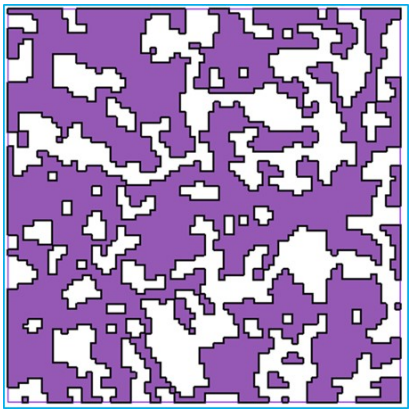

(a) Layer 12 as design depth Z = 20 μm

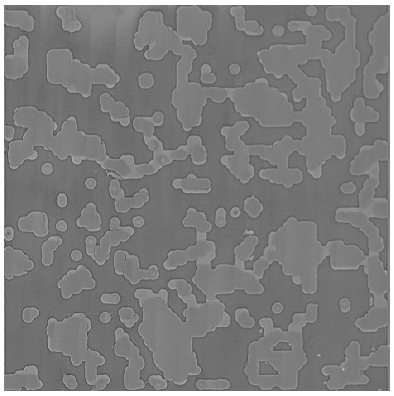

(b) Depth Z = 18.4 μm

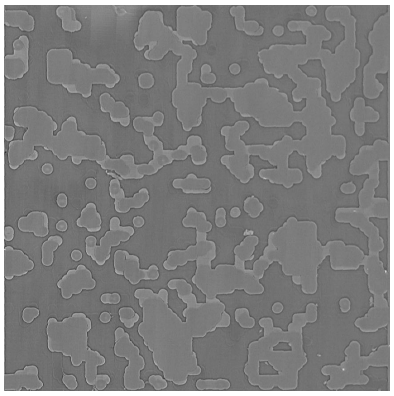

(c) Depth Z = 20.7 μm

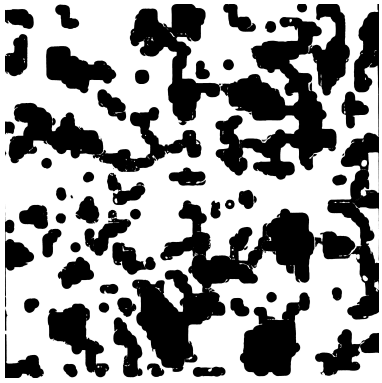

(d) Depth Z = 15 μm

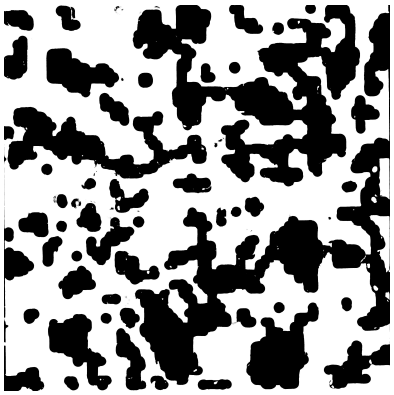

(e) Depth Z = 20 μm

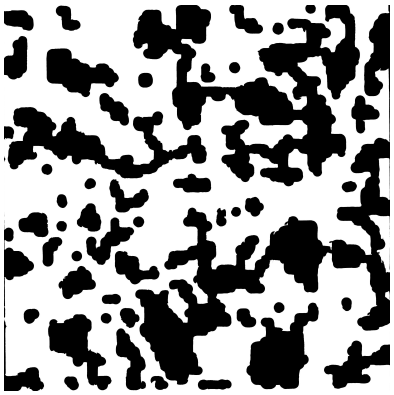

(f) Depth Z = 15 μm

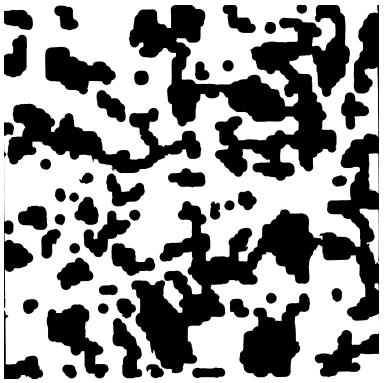

(g) Depth Z = 20 μm

Figure A.2: Comparision of Depth Measurement using Fluorescence and X-ray Tomography Techniques at layer 12. Design drawing is represented in (a) whereas (b) and (c) are CT X-ray images at their respective depth and (d) and (e) represents raw fluorescence images at respective depth using fluorescent techniques and (f) and (g) are fluorescence images after applying filter to image (d) and (e).

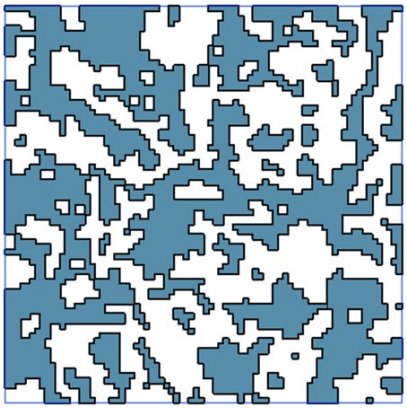

(a) Layer 11 as design depth Z = 30 μm

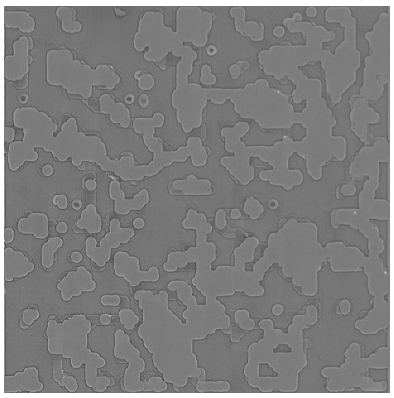

(b) Depth Z = 29.9 μm

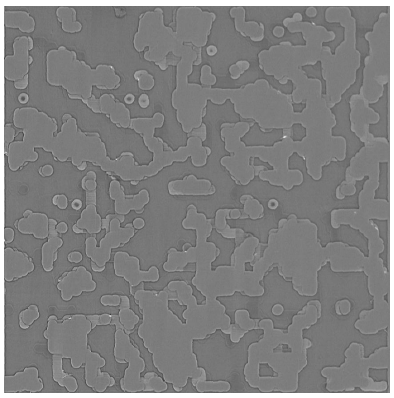

(c) Depth Z = 32.2 μm

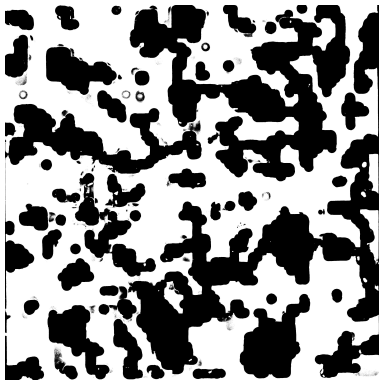

(d) Depth Z = 25 μm

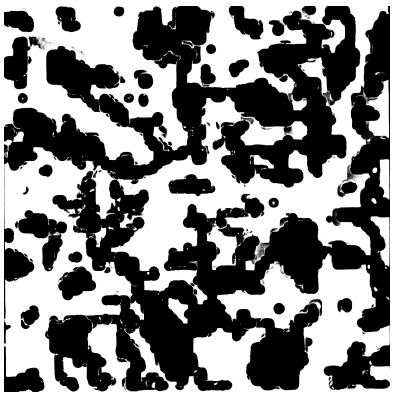

(e) Depth Z = 30 μm

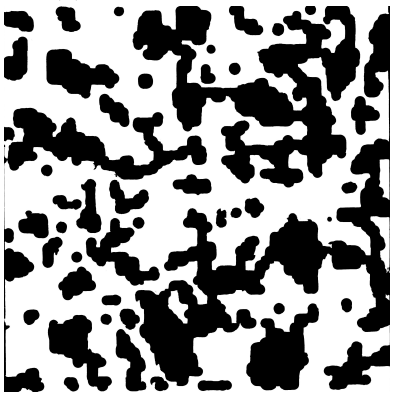

(f) Depth Z = 25 μm

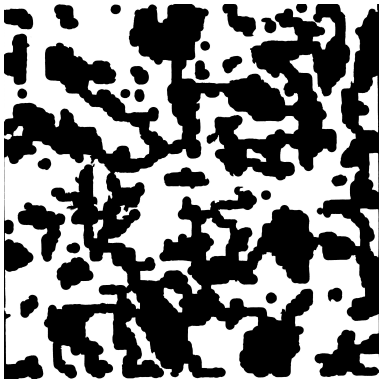

(g) Depth Z = 30 μm

Figure A.3: Comparision of Depth Measurement using Fluorescence and X-ray Tomography Techniques at layer 11. Design drawing is represented in (a) whereas (b) and (c) are CT X-ray images at their respective depth and (d) and (e) represents raw fluorescence images at respective depth using fluorescent techniques and (f) and (g) are fluorescence images after applying filter to image (d) and (e).

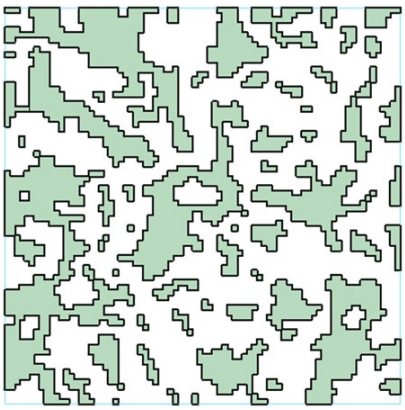

(a) Layer 10 as design depth Z = 40 μm

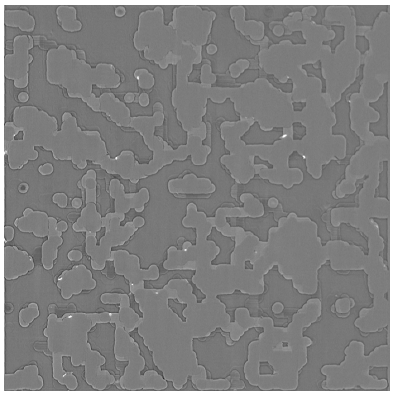

(b) Depth Z = 39.1 μm

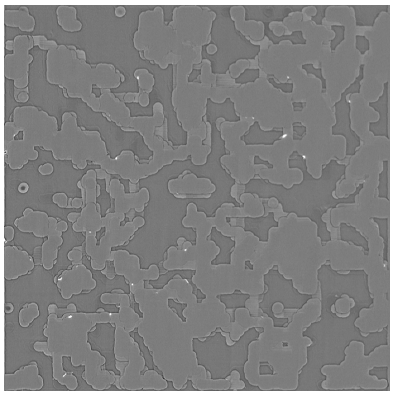

(c) Depth Z = 41.4 μm

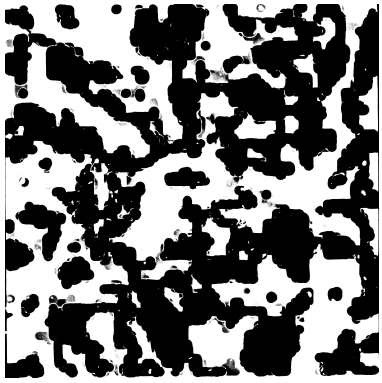

(d) Depth Z = 35 μm

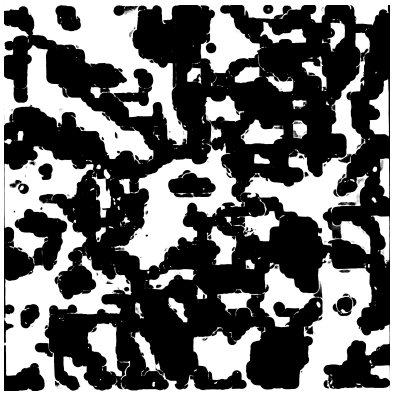

(e) Depth Z = 40 μm

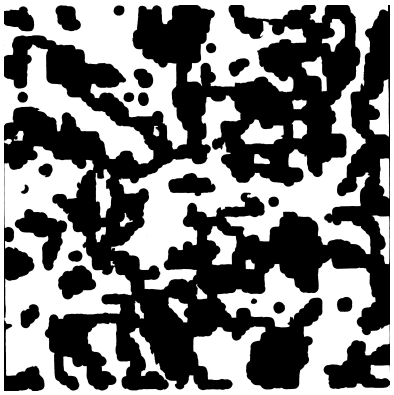

(f) Depth Z = 35 μm

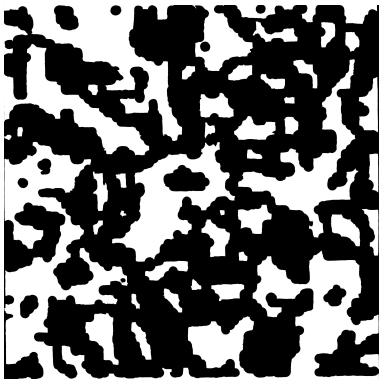

(g) Depth Z = 40 μm

Figure A.4: Comparision of Depth Measurement using Fluorescence and X-ray Tomography Techniques at layer 10. Design drawing is represented in (a) whereas (b) and (c) are CT X-ray images at their respective depth and (d) and (e) represents raw fluorescence images at respective depth using fluorescent techniques and (f) and (g) are fluorescence images after applying filter to image (d) and (e).

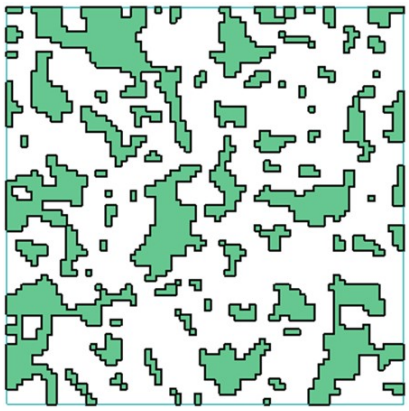

(a) Layer 9 as design depth Z = 50 μm

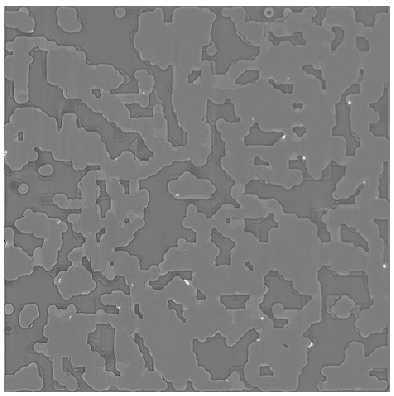

(b) Depth Z = 48.3 μm

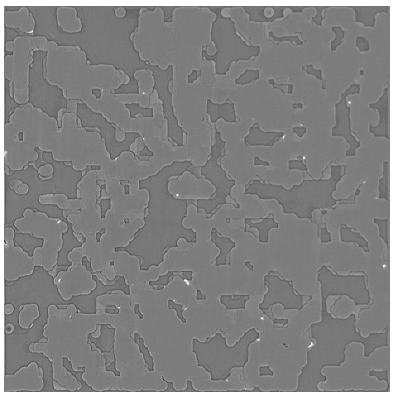

(c) Depth Z = 50.6 μm

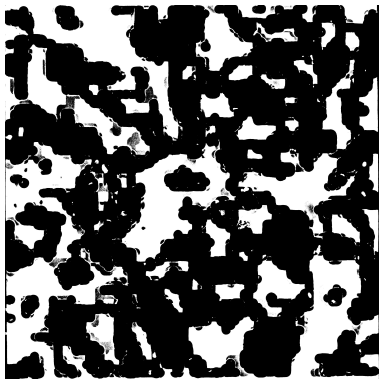

(d) Depth Z = 45 μm

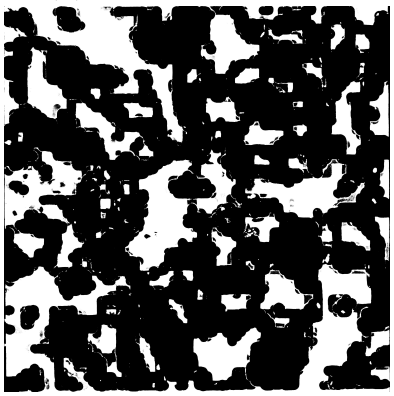

(e) Depth Z = 50 μm

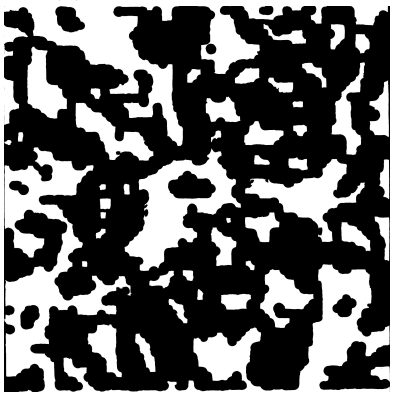

(f) Depth Z = 45 μm

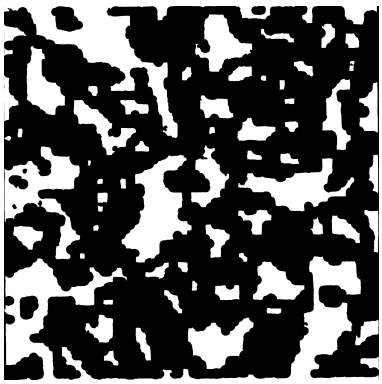

(g) Depth Z = 50 μm

Figure A.5: Comparision of Depth Measurement using Fluorescence and X-ray Tomography Techniques at layer 9. Design drawing is represented in (a) whereas (b) and (c) are CT X-ray images at their respective depth and (d) and (e) represents raw fluorescence images at respective depth using fluorescent techniques and (f) and (g) are fluorescence images after applying filter to image (d) and (e).

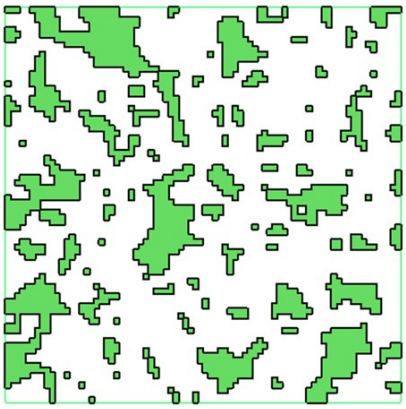

(a) Layer 8 as design depth Z = 60 μm

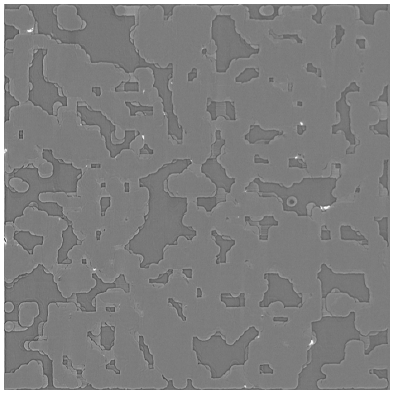

(b) Depth Z = 59.8 μm

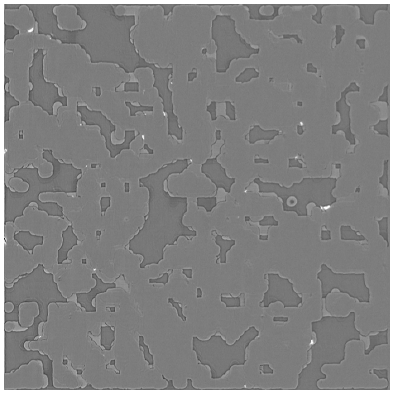

(c) Depth Z = 62.1 μm

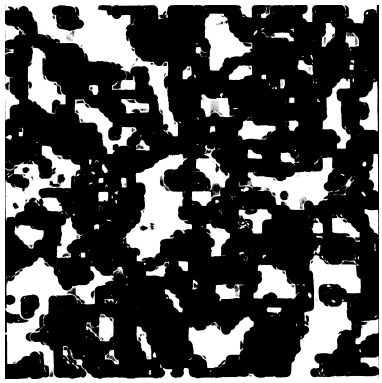

(d) Depth Z = 55 μm

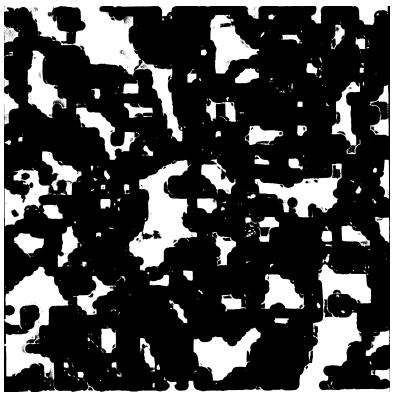

(e) Depth Z = 60 μm

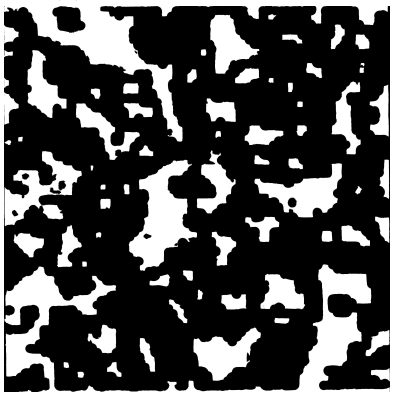

(f) Depth Z = 55 μm

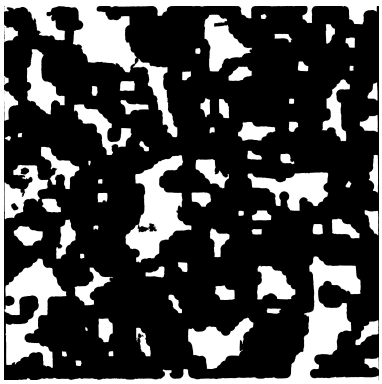

(g) Depth Z = 60 μm

Figure A.6: Comparision of Depth Measurement using Fluorescence and X-ray Tomography Techniques at layer 8. Design drawing is represented in (a) whereas (b) and (c) are CT X-ray images at their respective depth and (d) and (e) represents raw fluorescence images at respective depth using fluorescent techniques and (f) and (g) are fluorescence images after applying filter to image (d) and (e).

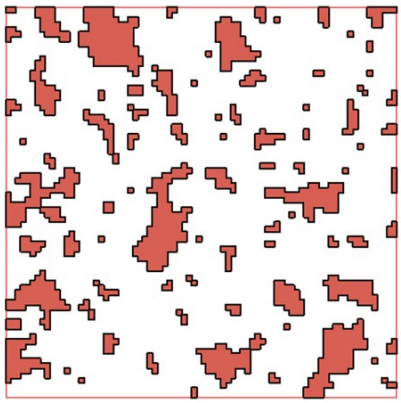

(a) Layer 7 as design depth Z = 70 μm

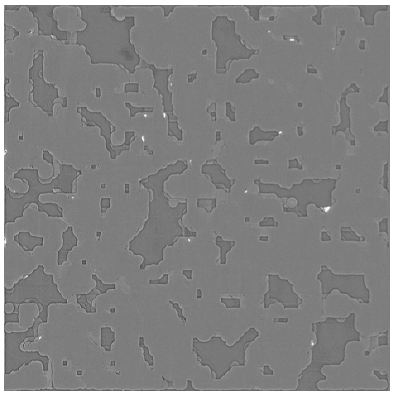

(b) Depth Z = 69 μm

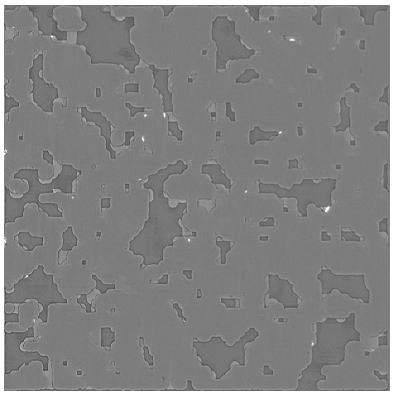

(c) Depth Z = 71.3 μm

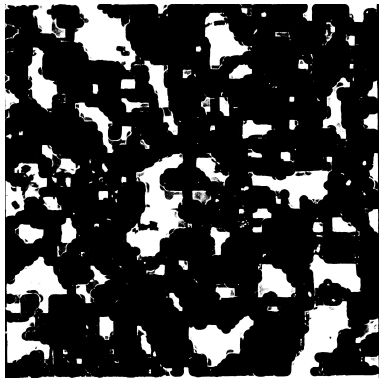

(d) Depth Z = 65 μm

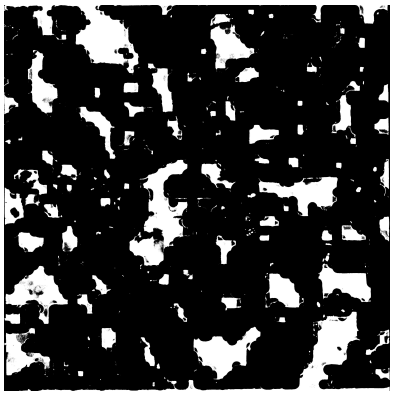

(e) Depth Z = 70 μm

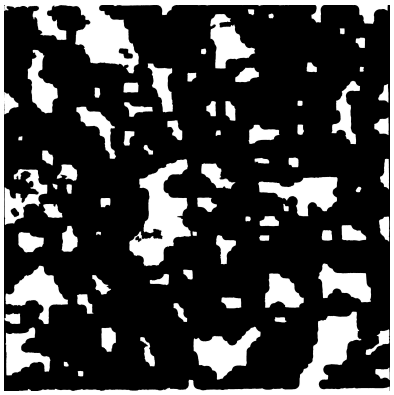

(f) Depth Z = 65 μm

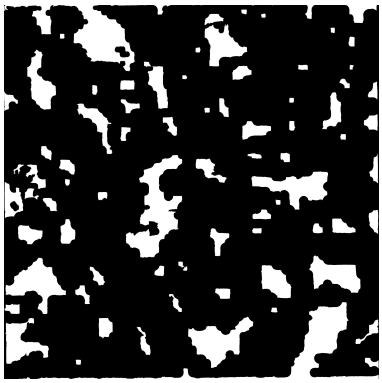

(g) Depth Z = 70 μm

Figure A.7: Comparision of Depth Measurement using Fluorescence and X-ray Tomography Techniques at layer 7. Design drawing is represented in (a) whereas (b) and (c) are CT X-ray images at their respective depth and (d) and (e) represents raw fluorescence images at respective depth using fluorescent techniques and (f) and (g) are fluorescence images after applying filter to image (d) and (e).

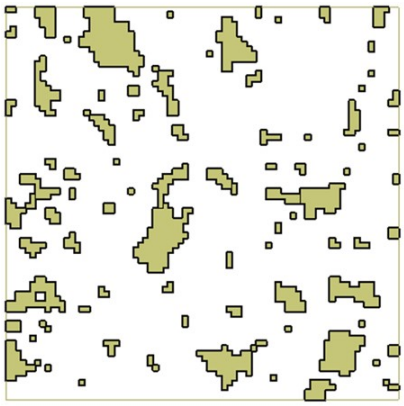

(a) Layer 6 as design depth Z = 80 μm

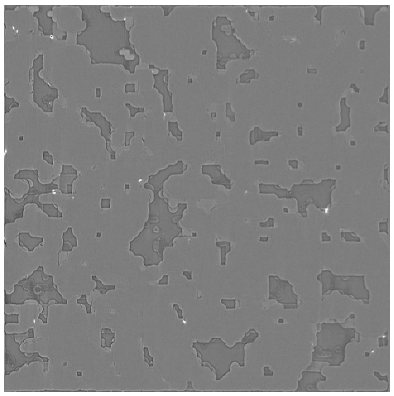

(b) Depth Z = 78.2 μm

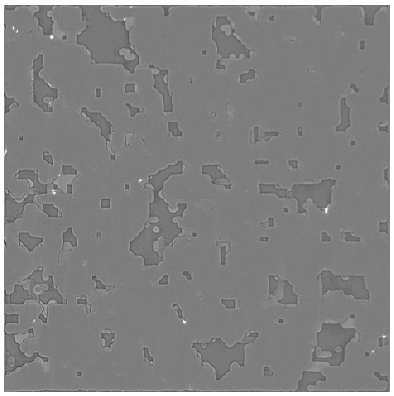

(c) Depth Z = 80.5 μm

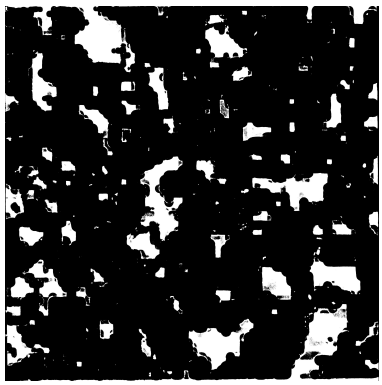

(d) Depth Z = 75 μm

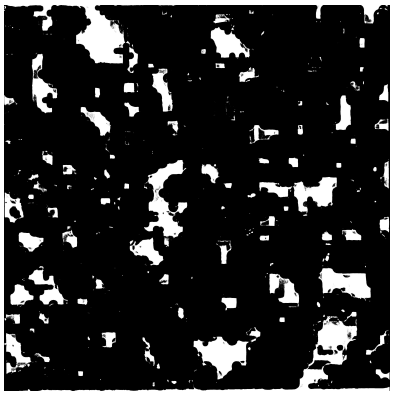

(e) Depth Z = 80 μm

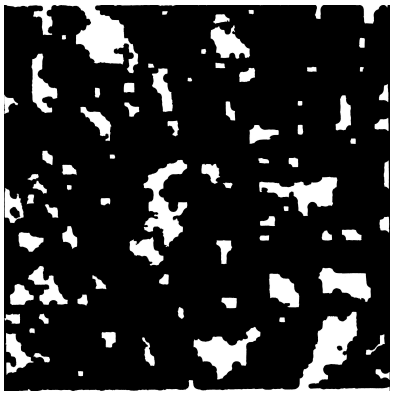

(f) Depth Z = 75 μm

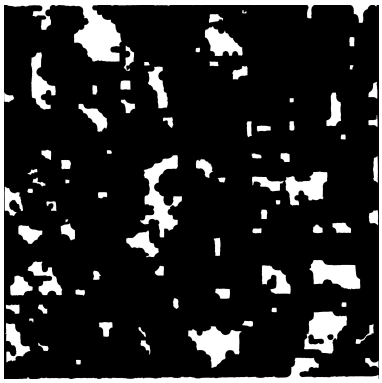

(g) Depth Z = 80 μm

Figure A.8: Comparision of Depth Measurement using Fluorescence and X-ray Tomography Techniques at layer 6. Design drawing is represented in (a) whereas (b) and (c) are CT X-ray images at their respective depth and (d) and (e) represents raw fluorescence images at respective depth using fluorescent techniques and (f) and (g) are fluorescence images after applying filter to image (d) and (e).

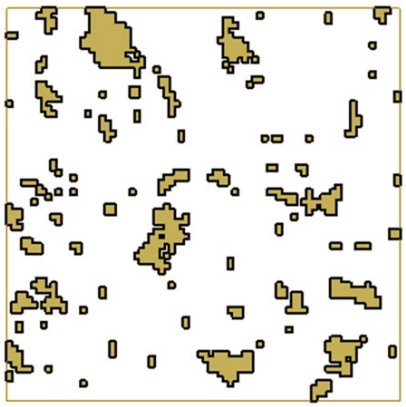

(a) Layer 5 as design depth Z = 90 μm

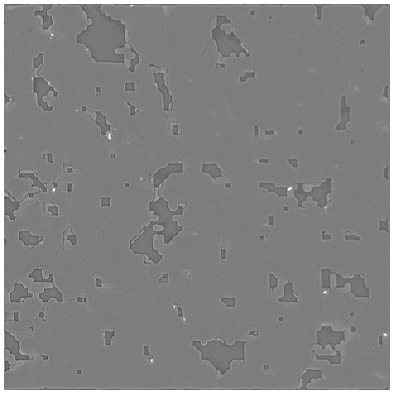

(b) Depth Z = 89.7 μm

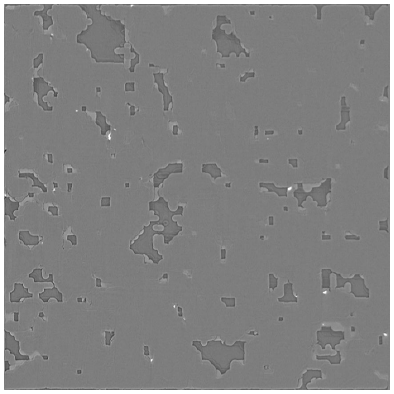

(c) Depth Z = 92 μm

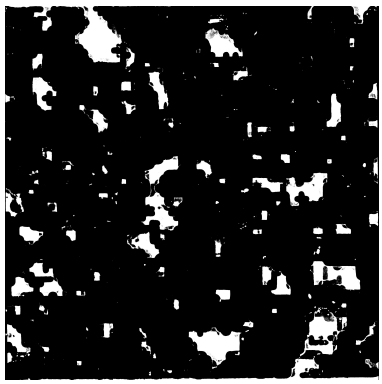

(d) Depth Z = 85 μm

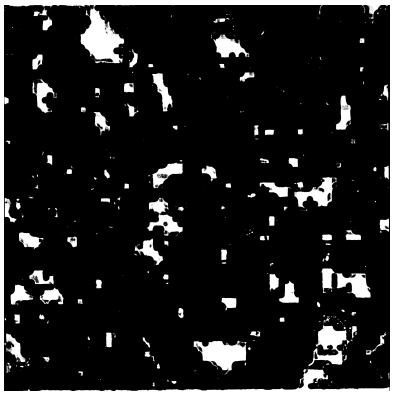

(e) Depth Z = 90 μm

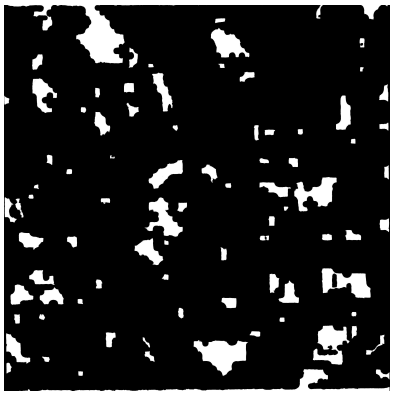

(f) Depth Z = 85 μm

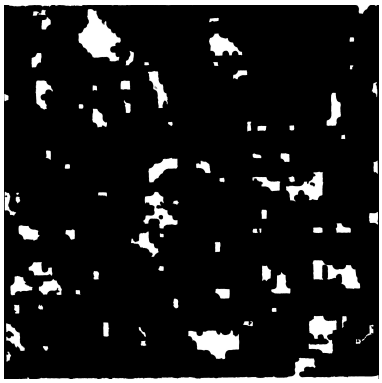

(g) Depth Z = 90 μm

Figure A.9: Comparision of Depth Measurement using Fluorescence and X-ray Tomography Techniques at layer 5. Design drawing is represented in (a) whereas (b) and (c) are CT X-ray images at their respective depth and (d) and (e) represents raw fluorescence images at respective depth using fluorescent techniques and (f) and (g) are fluorescence images after applying filter to image (d) and (e).

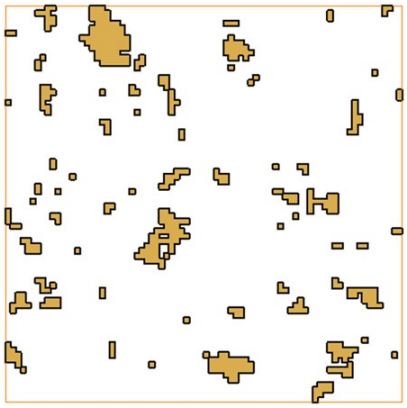

(a) Layer 4 as design depth Z = 100 μm

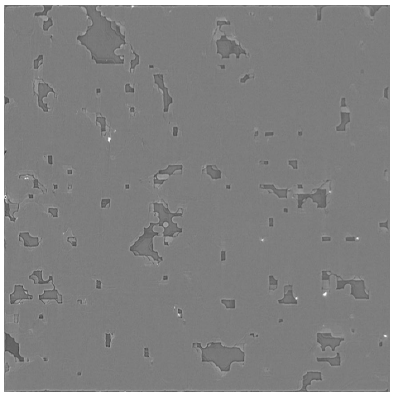

(b) Depth Z = 98.9 μm

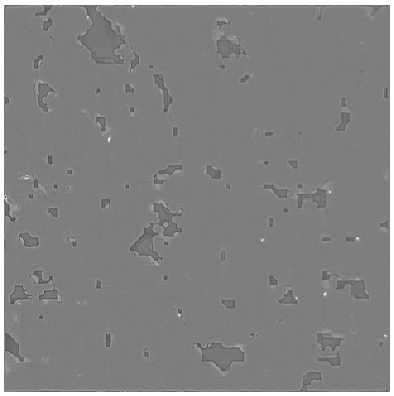

(c) Depth Z = 101.2 μm

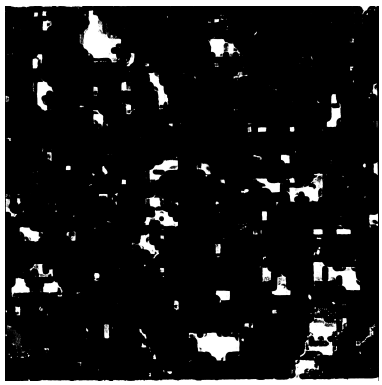

(d) Depth Z = 95 μm

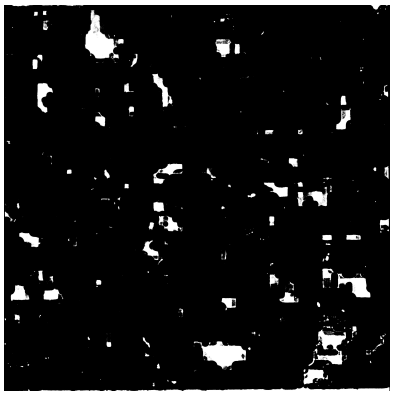

(e) Depth Z = 100 μm

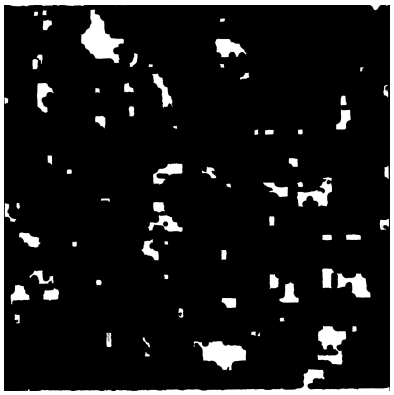

(f) Depth Z = 95 μm

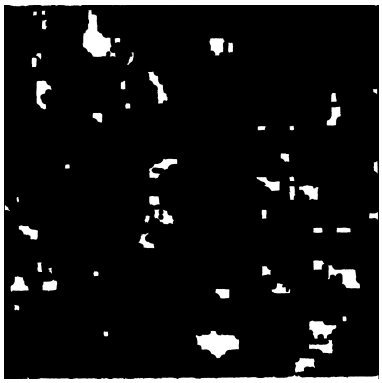

(g) Depth Z = 100 μm

Figure A.10: Comparision of Depth Measurement using Fluorescence and X-ray Tomography Techniques at layer 4. Design drawing is represented in (a) whereas (b) and (c) are CT X-ray images at their respective depth and (d) and (e) represents raw fluorescence images at respective depth using fluorescent techniques and (f) and (g) are fluorescence images after applying filter to image (d) and (e).

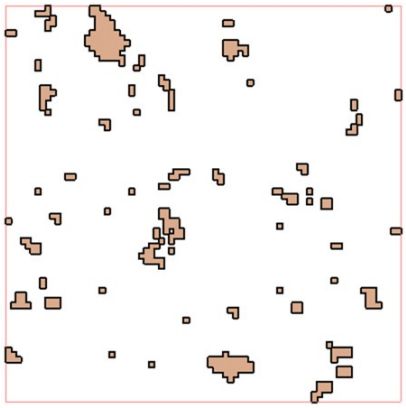

(a) Layer 3 as design depth Z = 110 μm

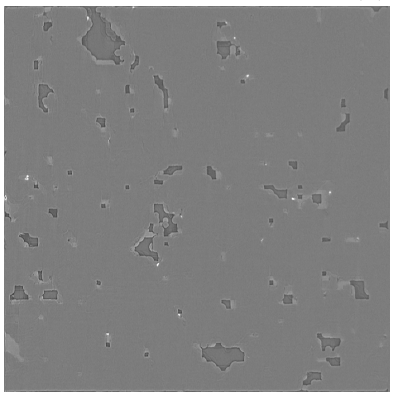

(b) Depth Z = 108.1 μm

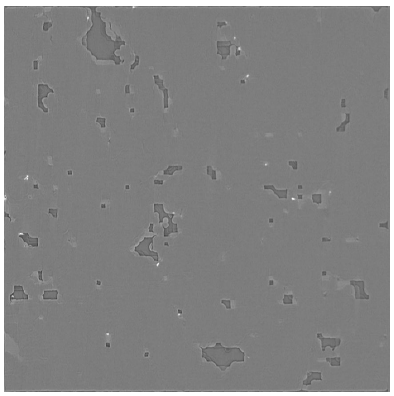

(c) Depth Z = 110.4 μm

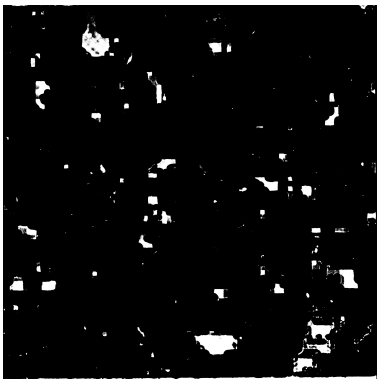

(d) Depth Z = 105 μm

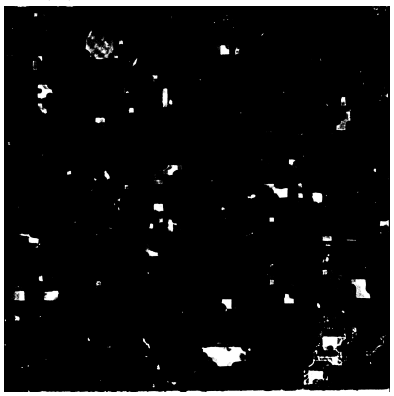

(e) Depth Z = 110 μm

(f) Depth Z = 105 μm

(g) Depth Z = 110 μm

Figure A.11: Comparision of Depth Measurement using Fluorescence and X-ray Tomography Techniques at layer 3. Design drawing is represented in (a) whereas (b) and (c) are CT X-ray images at their respective depth and (d) and (e) represents raw fluorescence images at respective depth using fluorescent techniques and (f) and (g) are fluorescence images after applying filter to image (d) and (e).

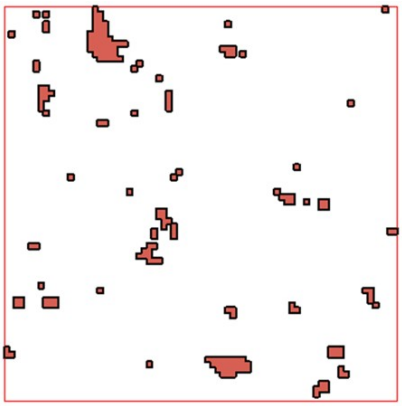

(a) Layer 2 as design depth Z = 120 μm

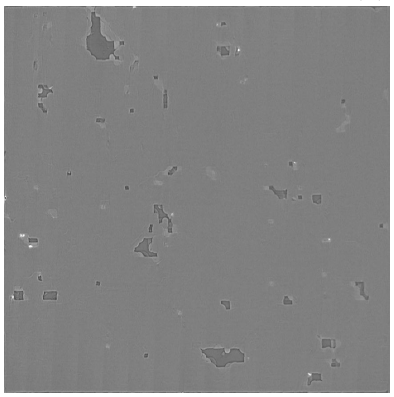

(b) Depth Z = 119.6 μm

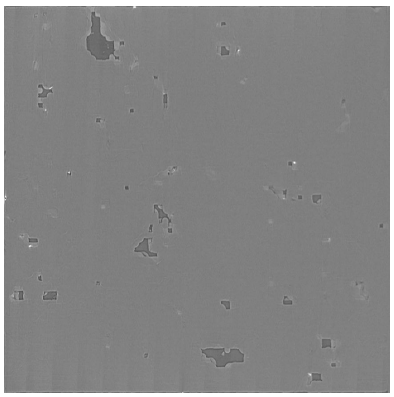

(c) Depth Z = 121.9 μm

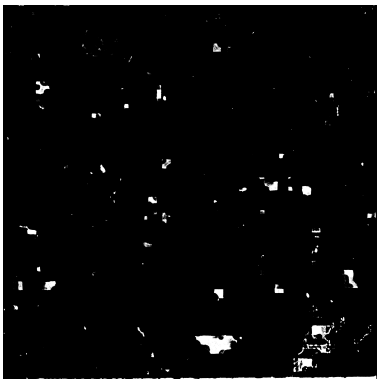

(d) Depth Z = 115 μm

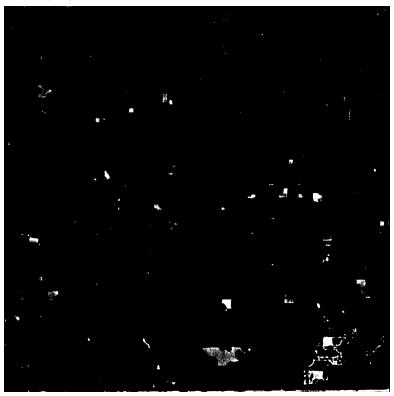

(e) Depth Z = 120 μm

(f) Depth Z = 95 μm

(g) Depth Z = 120 μm

Figure A.12: Comparision of Depth Measurement using Fluorescence and X-ray Tomography Techniques at layer 2. Design drawing is represented in (a) whereas (b) and (c) are CT X-ray images at their respective depth and (d) and (e) represents raw fluorescence images at respective depth using fluorescent techniques and (f) and (g) are fluorescence images after applying filter to image (d) and (e).

Appendix B
3D Nano-particle Velocity Measurements along the Path of Principal Flow

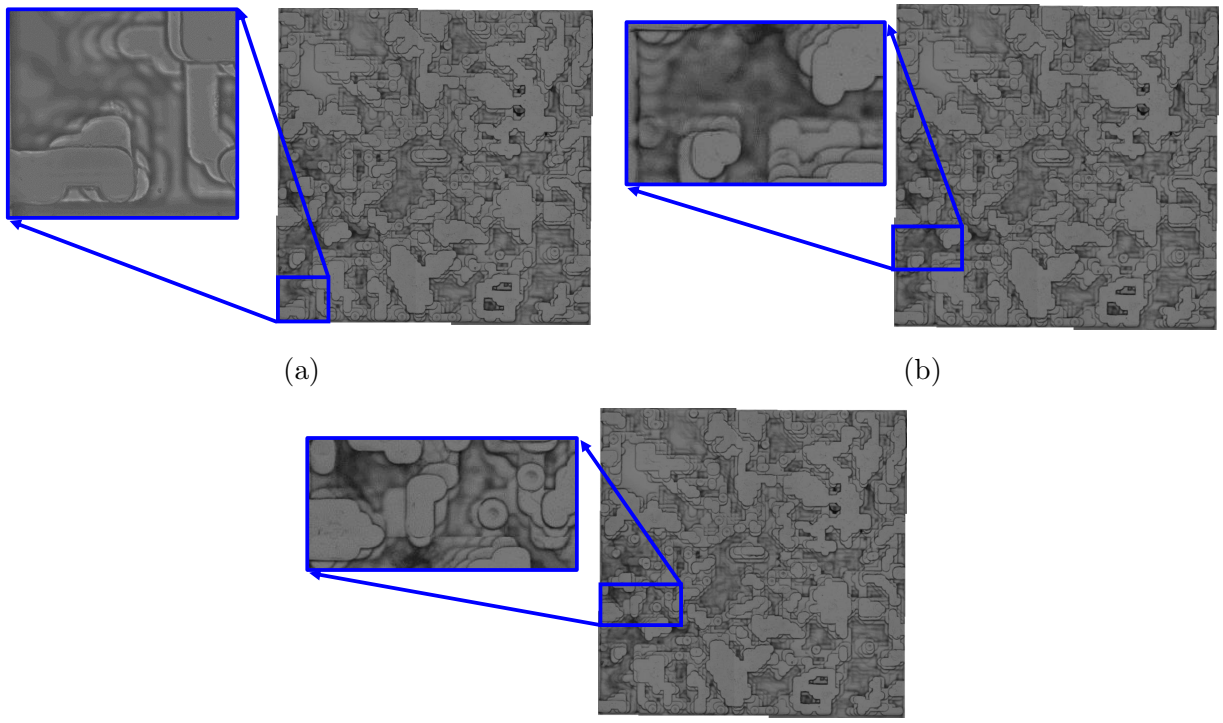

(a) (b)

(c)

Figure B.1: Principal flow path in Boise rock-based low resolution PMMA 2.5D micro-model.(a) Nine overlapping ROIs were used to cover first entrance observation location, (b) twelve overlapping ROIs were used to cover third observation location, and (c) twelve overlapping ROIs were used to cover fourth entrance observation location. Each ROI was 105.98 μm x 105.98 μm

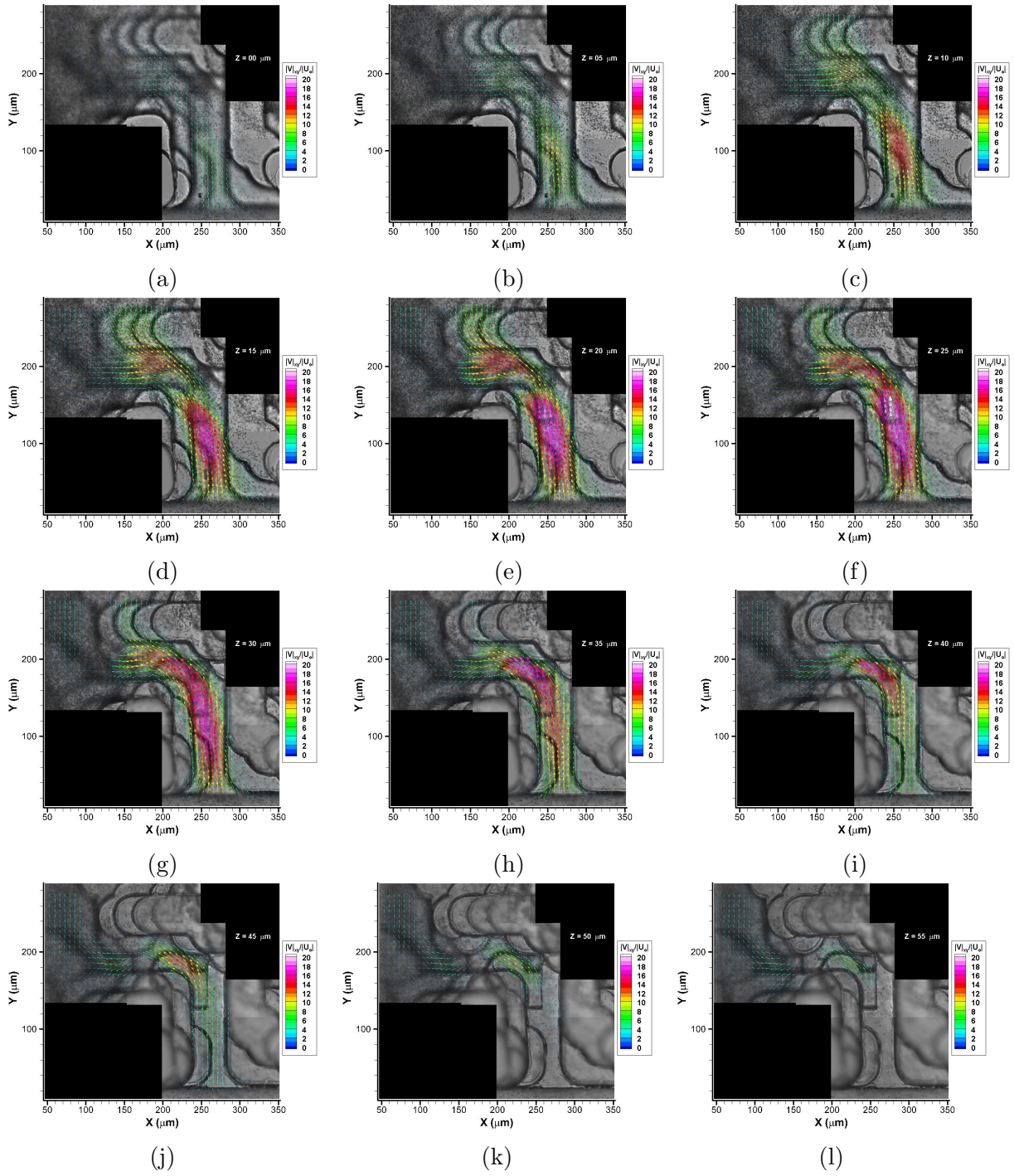

Figure B.2: Sequence of images illustrating depth- wise planar velocity distribution from observation location of the micro-model indicated in Figure B.1a. Depth is measured from inner wall of the observation window starting at 0 (a) progressing in 5 μm increments through (q) which is at the local depth of 80 μm. The special resolution of the velocity is 6.62 μm x 6.62 μm x 5 μm in X,Y and Z planes respectively. Experimental conditions- polystyrene fluorescent 860 nm particles; net flow rate 10 nL/min; particle concentration of 9.54 particles/pL (0.32% by volume) (figure cont'd.).

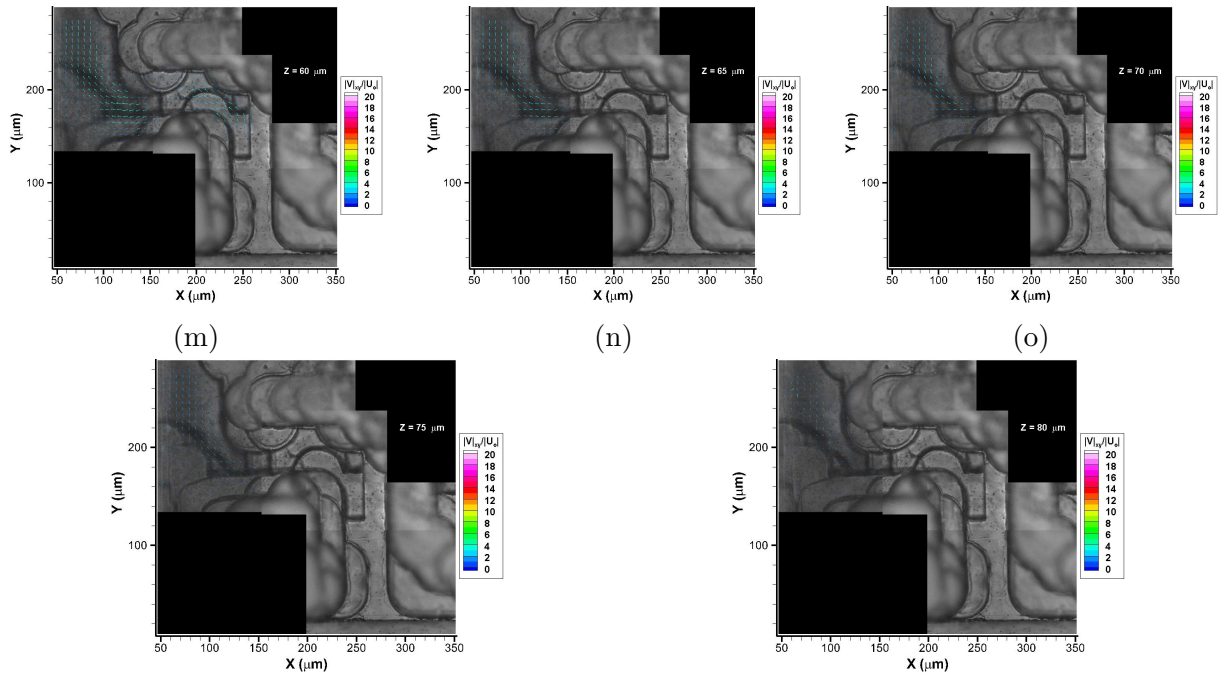

Figure B.2: Sequence of images illustrating depth- wise planar velocity distribution from observation location of the micro-model indicated in Figure B.1a. Depth is measured from inner wall of the observation window starting at 0 (a) progressing in 5 μm increments through (q) which is at the local depth of 80 μm. The special resolution of the velocity is 6.62 μm x 6.62 μm x 5 μm in X,Y and Z planes respectively. Experimental conditions- polystyrene fluorescent 860 nm particles; net flow rate 10 nL/min; particle concentration of 9.54 particles/pL (0.32% by volume).

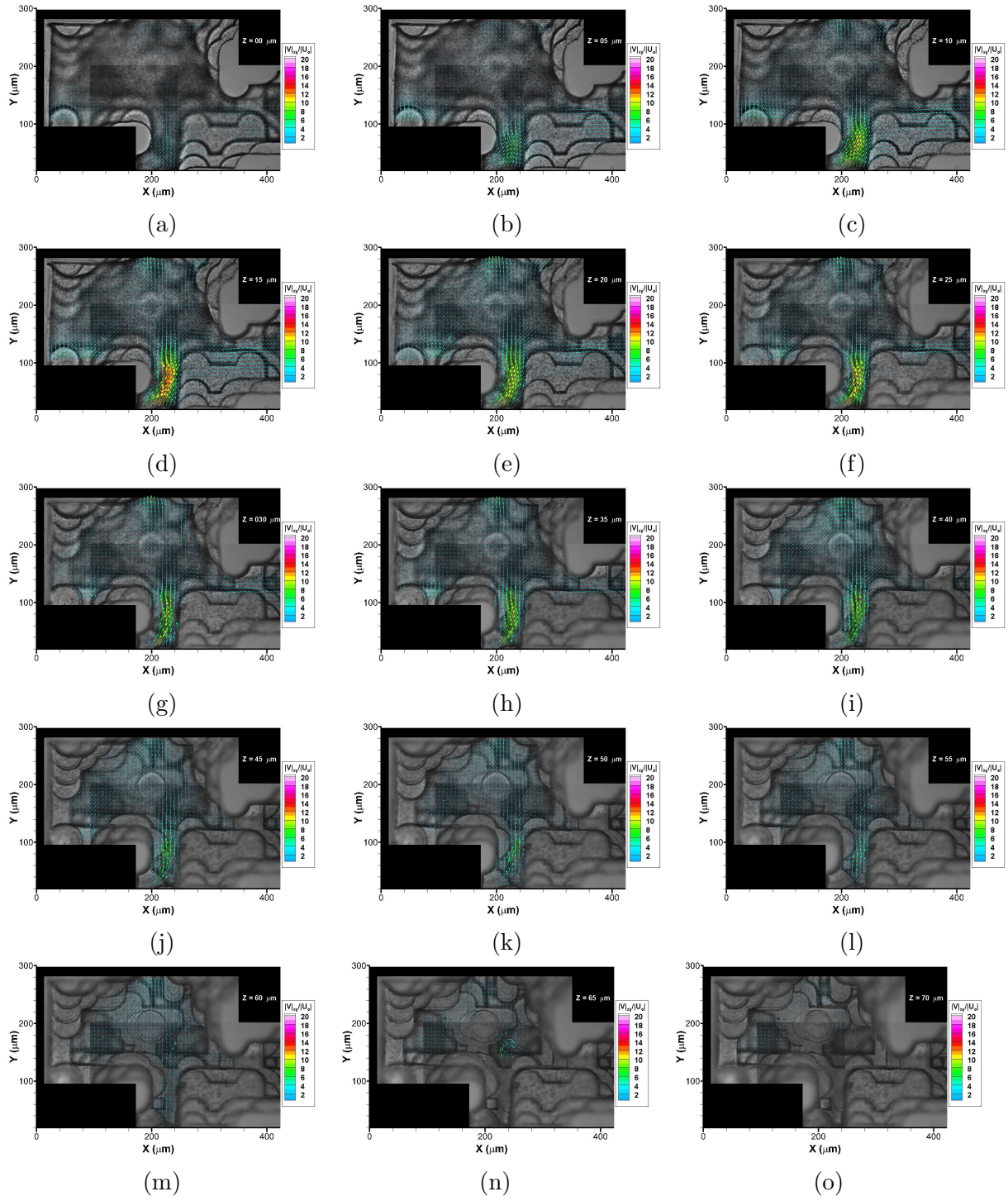

Figure B.3: Sequence of images illustrating depth- wise planar velocity distribution from observation location of the micro-model indicated in Figure B.1b. Depth is measured from inner wall of the observation window starting at 0 (a) progressing in 5 μm increments through (q) which is at the local depth of 80 μm. The special resolution of the velocity is 6.62 μm x 6.62 μm x 5 μm in X,Y and Z planes respectively. Experimental conditions- polystyrene fluorescent 860 nm particles; net flow rate 10 nL/min; particle concentration of 9.54 particles/pL (0.32% by volume) (figure cont'd.).

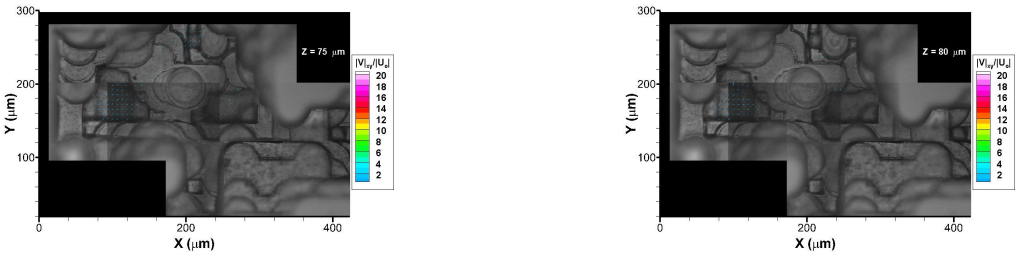

(p) (q)

Figure B.3: Sequence of images illustrating depth- wise planar velocity distribution from observation location of the micro-model indicated in Figure B.1b. Depth is measured from inner wall of the observation window starting at 0 (a) progressing in 5 μm increments through (q) which is at the local depth of 80 μm. The special resolution of the velocity is 6.62 μm x 6.62 μm x 5 μm in X,Y and Z planes respectively. Experimental conditions- polystyrene fluorescent 860 nm particles; net flow rate 10 nL/min; particle concentration of 9.54 particles/pL (0.32% by volume).

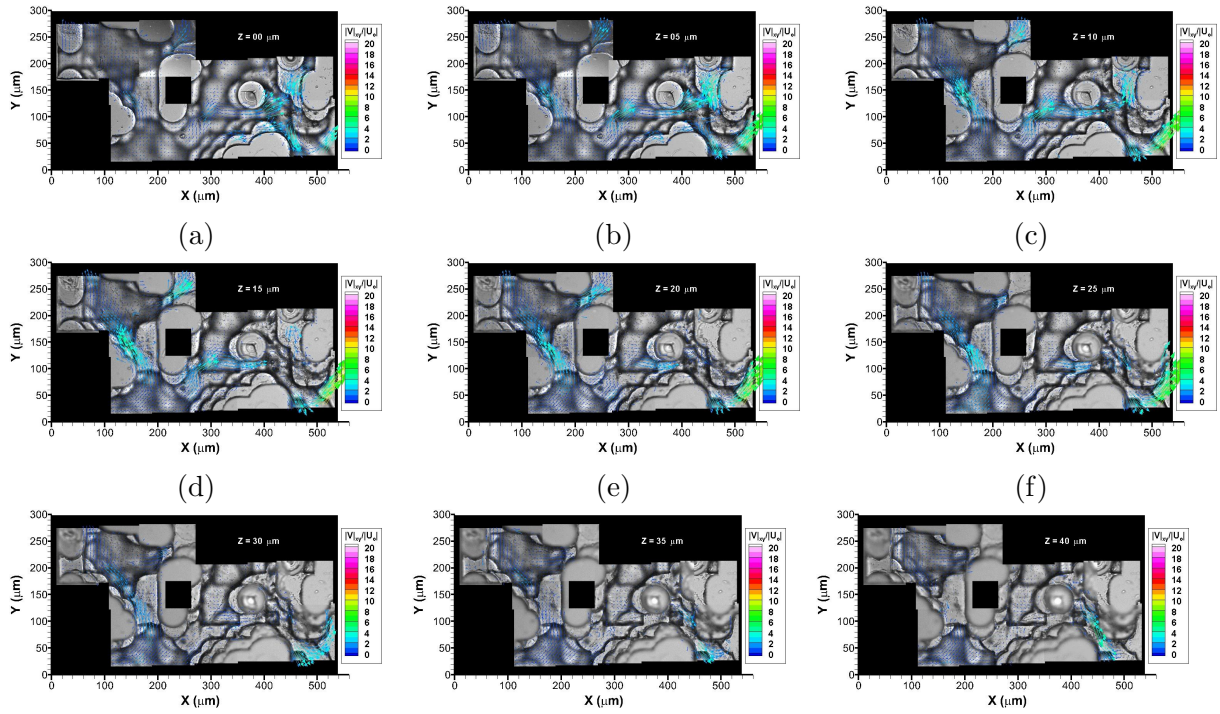

(a) (b) (c)

(d) (e) (f)

(g) (h) (i)

Figure B.4: Sequence of images illustrating depth- wise planar velocity distribution from observation location of the micro-model indicated in Figure B.1c. Depth is measured from inner wall of the observation window starting at 0 (a) progressing in 5 μm increments through (y) which is at the local depth of 120 μm. The special resolution of the velocity is 6.62 μm x 6.62 μm x 5 μm in X,Y and Z planes respectively. Experimental conditions- polystyrene fluorescent 860 nm particles; net flow rate 10 nL/min; particle concentration of 1.92 particles/pL (0.06% by volume) (figure cont'd.).

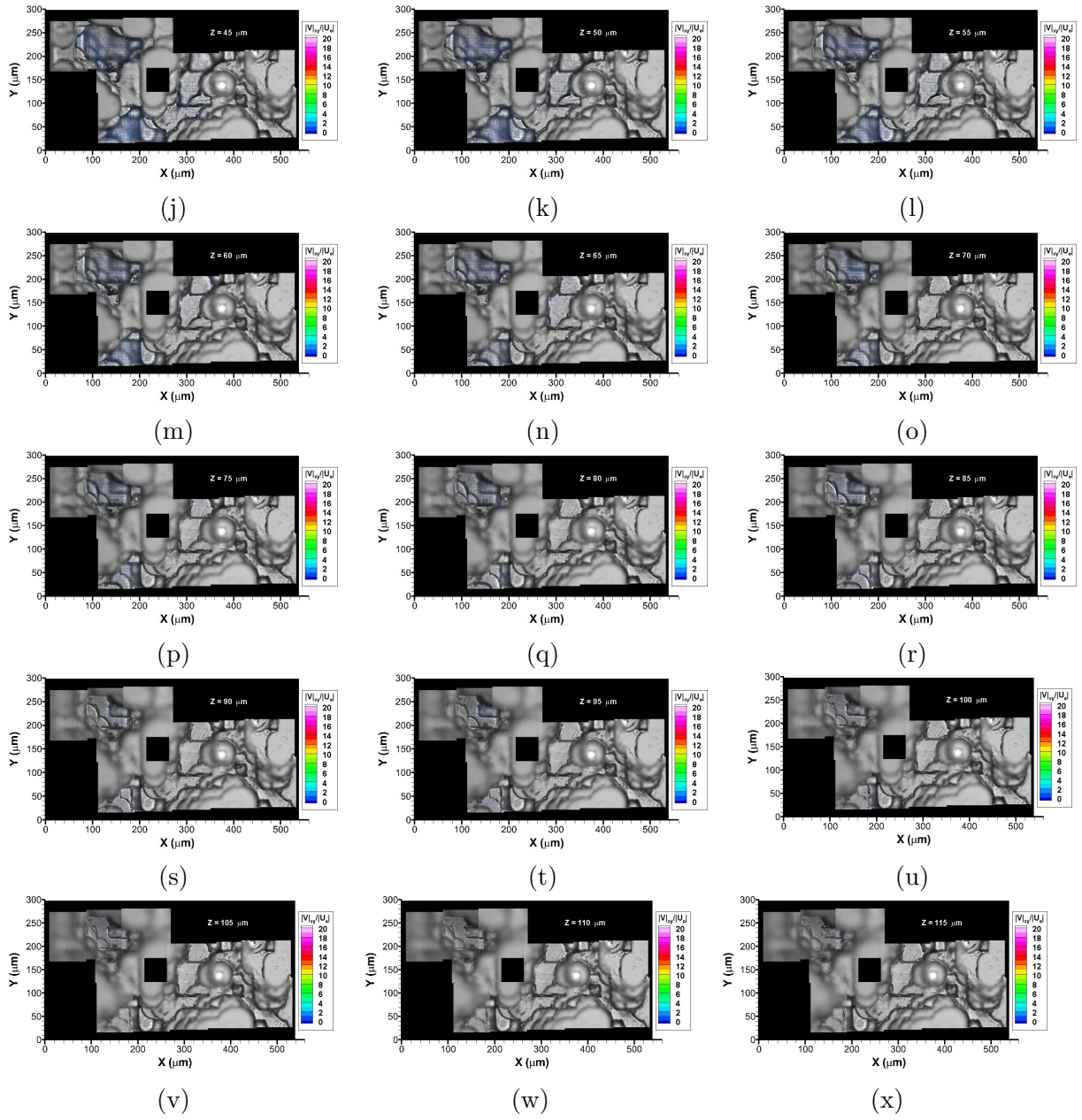

Figure B.4: Sequence of images illustrating depth- wise planar velocity distribution from observation location of the micro-model indicated in Figure B.1c. Depth is measured from inner wall of the observation window starting at 0 (a) progressing in 5 μm increments through (y) which is at the local depth of 120 μm. The special resolution of the velocity is 6.62 μm x 6.62 μm x 5 μm in X,Y and Z planes respectively. Experimental conditions- polystyrene fluorescent 860 nm particles; net flow rate 10 nL/min; particle concentration of 1.92 particles/pL (0.06% by volume) (figure cont'd.).

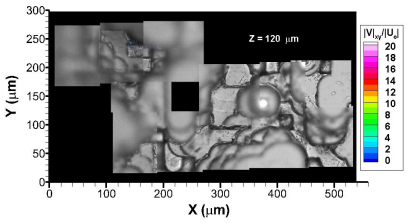

(y)

Figure B.4: Sequence of images illustrating depth- wise planar velocity distribution from observation location of the micro-model indicated in Figure B.1c. Depth is measured from inner wall of the observation window starting at 0 (a) progressing in 5 μm increments through (y) which is at the local depth of 120 μm. The special resolution of the velocity is 6.62 μm x 6.62 μm x 5 μm in X,Y and Z planes respectively. Experimental conditions- polystyrene fluorescent 860 nm particles; net flow rate 10 nL/min; particle concentration of 1.92 particles/pL (0.06% by volume).

Appendix C
3D Nano-particle Concentration Distribution Measurements along the Path of Principal Flow

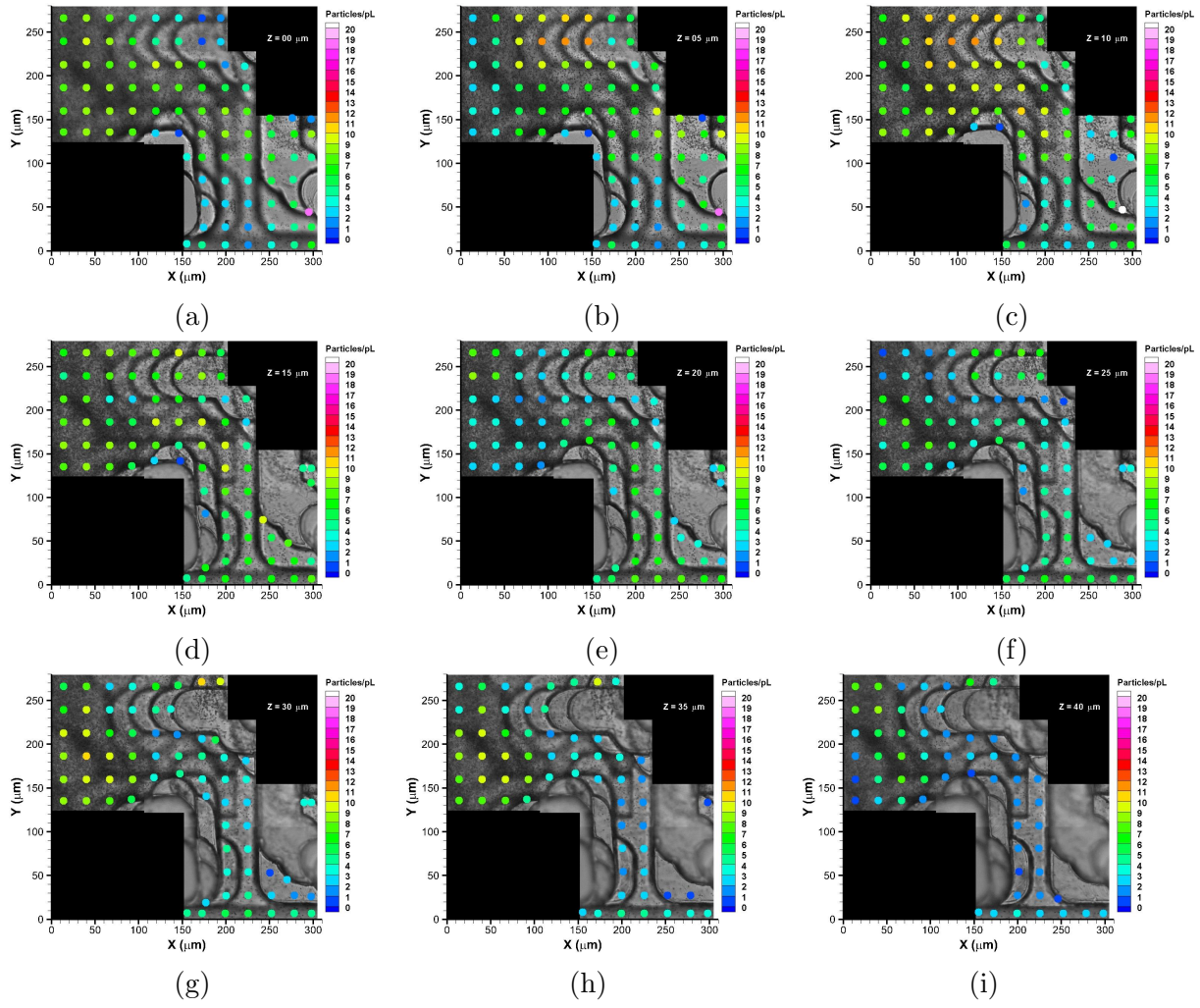

Figure C.1: Sequence of images illustrating depth- wise planar particle concentration distribution from observation location of the micro-model indicated in Figure B.1a. Depth is measured from inner wall of the observation window starting at 0 (a) progressing in 5 μm increments through (q) which is at the local depth of 80 μm. The special resolution of the Concentration is 6.62 μm x 6.62 μm x 5 μm in X,Y and Z planes respectively. Experimental conditions-polystyrene fluorescent 860 nm particles; net flow rate 10 nL/min; particle concentration of 9.54 particles/pL (0.32% by volume) (figure cont'd.).

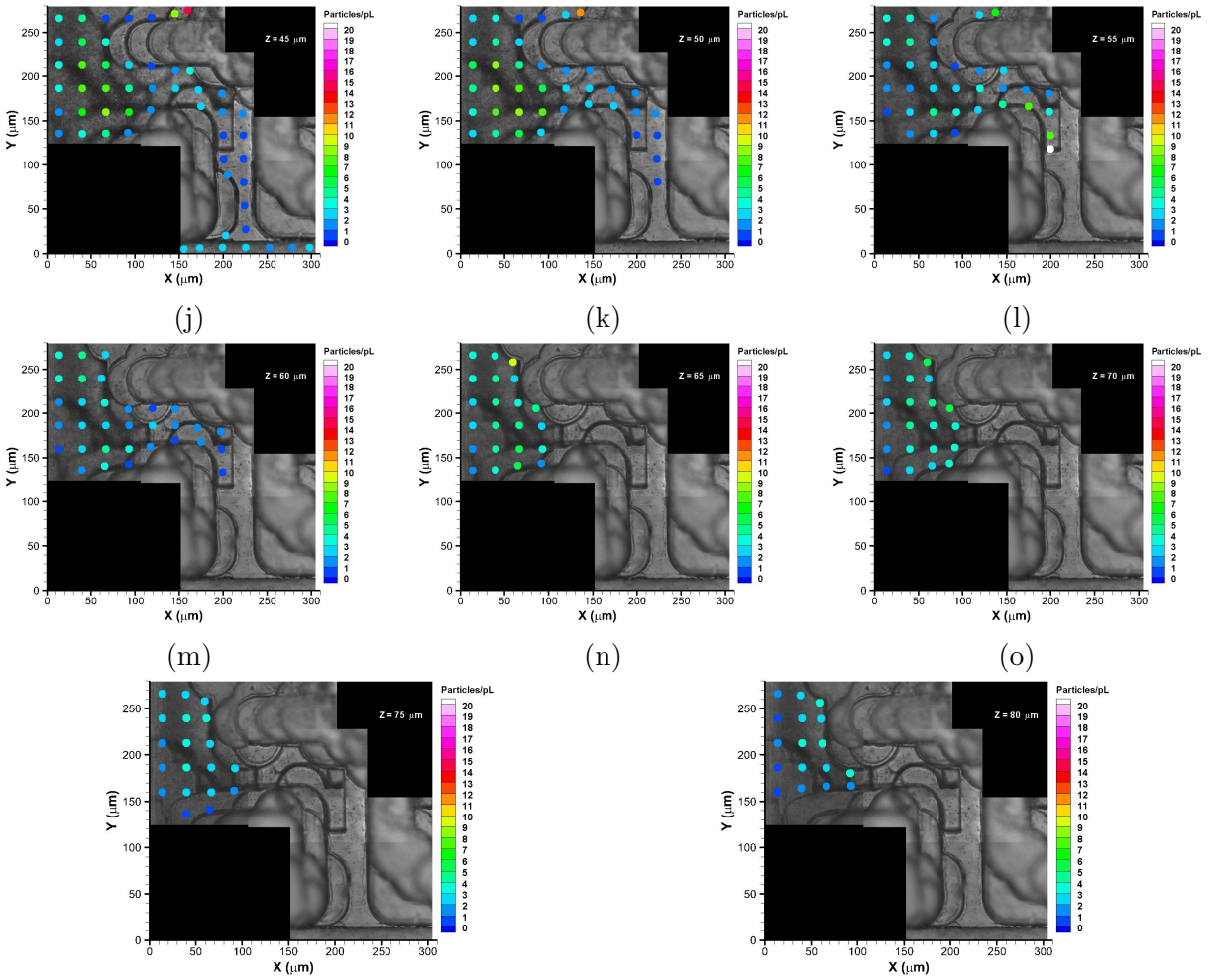

Figure C.1: Sequence of images illustrating depth- wise planar particle concentration distribution from observation location of the micro-model indicated in Figure B.1a. Depth is measured from inner wall of the observation window starting at 0 (a) progressing in 5 μm increments through (q) which is at the local depth of 80 μm. The special resolution of the Concentration is 6.62 μm x 6.62 μm x 5 μm in X,Y and Z planes respectively. Experimental conditions-polystyrene fluorescent 860 nm particles; net flow rate 10 nL/min; particle concentration of 9.54 particles/pL (0.32% by volume).

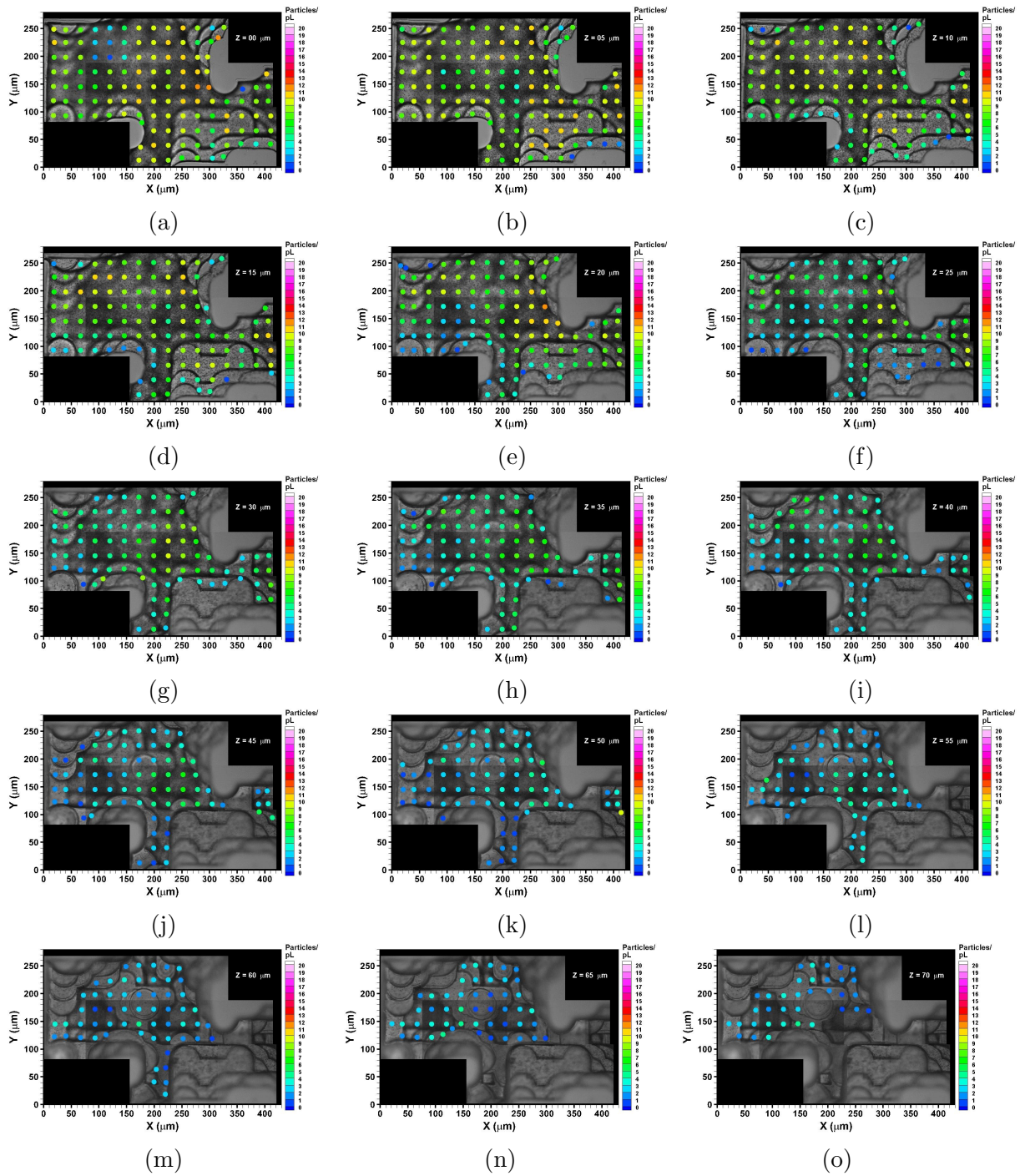

Figure C.2: Sequence of images illustrating depth- wise planar particle concentration distribution from observation location of the micro-model indicated in Figure B.1b. Depth is measured from inner wall of the observation window starting at 0 (a) progressing in 5 μm increments through (q) which is at the local depth of 80 μm. The special resolution of the Concentration is 6.62 μm x 6.62 μm x 5 μm in X,Y and Z planes respectively. Experimental conditions-polystyrene fluorescent 860 nm particles; net flow rate 10 nL/min; particle concentration of 9.54 particles/pL (0.32% by volume)(figure cont'd.).

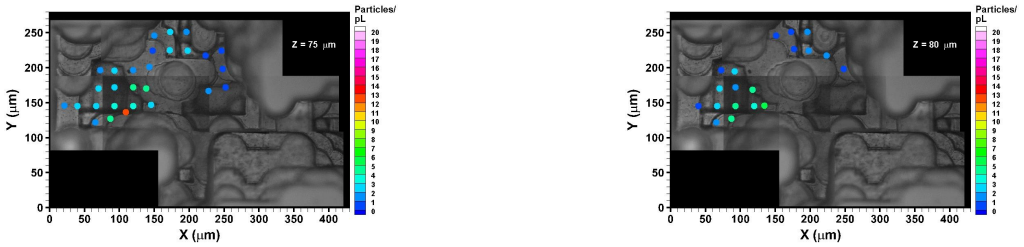

(p) (q)

Figure C.2: Sequence of images illustrating depth- wise planar particle concentration distribution from observation location of the micro-model indicated in Figure B.1b. Depth is measured from inner wall of the observation window starting at 0 (a) progressing in 5 μm increments through (q) which is at the local depth of 80 μm. The special resolution of the Concentration is 6.62 μm x 6.62 μm x 5 μm in X,Y and Z planes respectively. Experimental conditions-polystyrene fluorescent 860 nm particles; net flow rate 10 nL/min; particle concentration of 9.54 particles/pL (0.32% by volume).

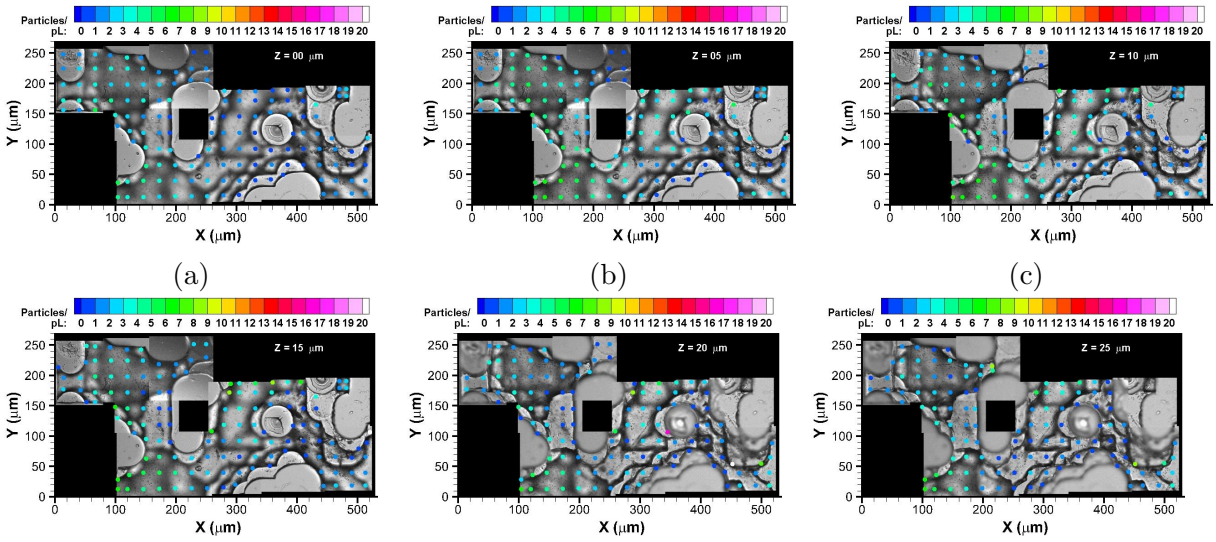

(a) (b) (c)

(d) (e) (f)

Figure C.3: Sequence of images illustrating depth- wise planar particle concentration distribution from observation location of the micro-model indicated in Figure B.1c. Depth is measured from inner wall of the observation window starting at 0 (a) progressing in 5 μm increments through (y) which is at the local depth of 120 μm. The special resolution of the Concentration is 6.62 μm x 6.62 μm x 5 μm in X,Y and Z planes respectively. Experimental conditions-polystyrene fluorescent 860 nm particles; net flow rate 10 nL/min; particle concentration of 1.92 particles/pL (0.06% by volume)(figure cont'd.).

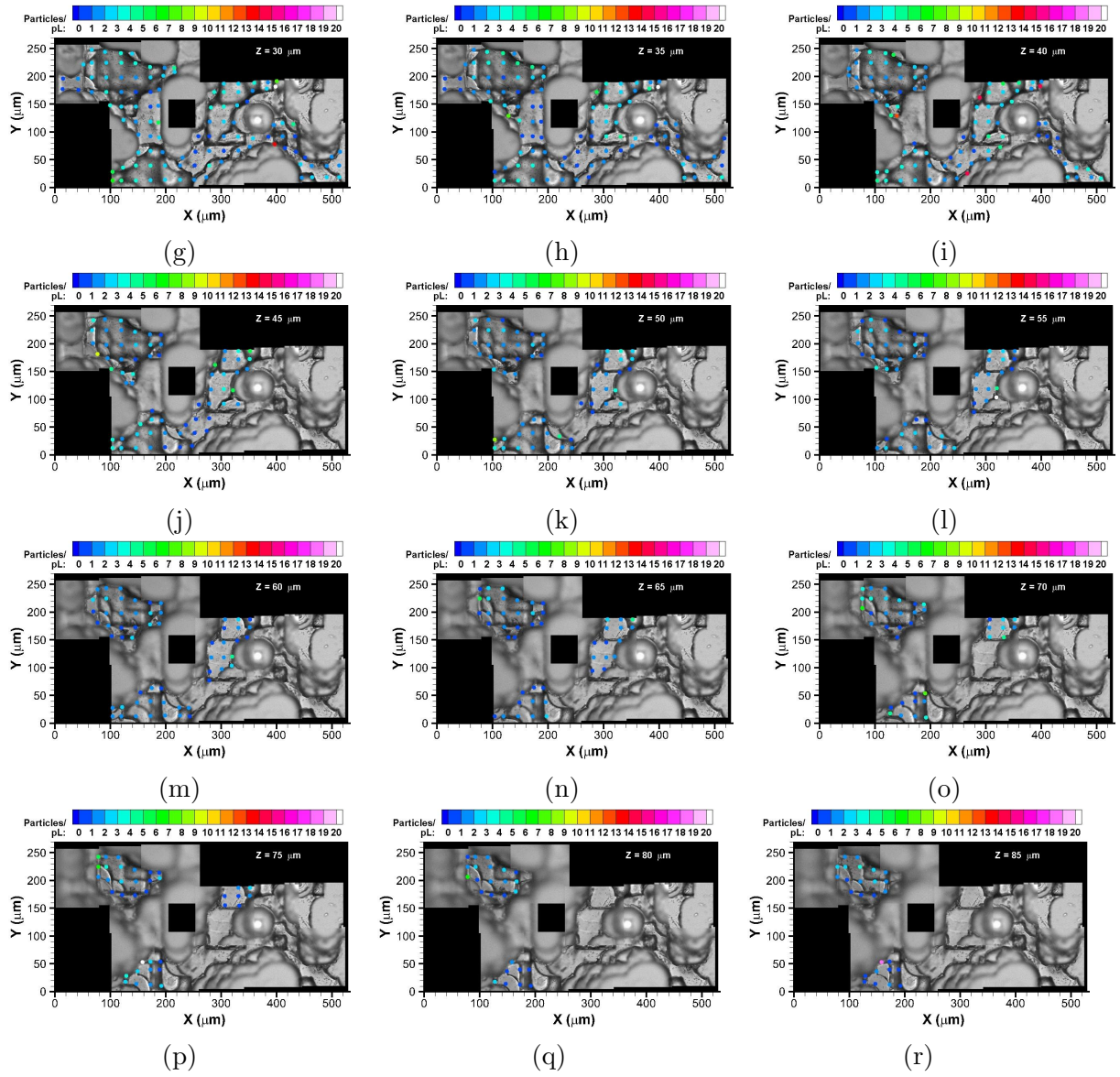

Figure C.3: Sequence of images illustrating depth- wise planar particle concentration distribution from observation location of the micro-model indicated in Figure B.1c. Depth is measured from inner wall of the observation window starting at 0 (a) progressing in 5 μm increments through (y) which is at the local depth of 120 μm. The special resolution of the Concentration is 6.62 μm x 6.62 μm x 5 μm in X,Y and Z planes respectively. Experimental conditions-polystyrene fluorescent 860 nm particles; net flow rate 10 nL/min; particle concentration of 1.92 particles/pL (0.06% by volume)(figure cont'd.).

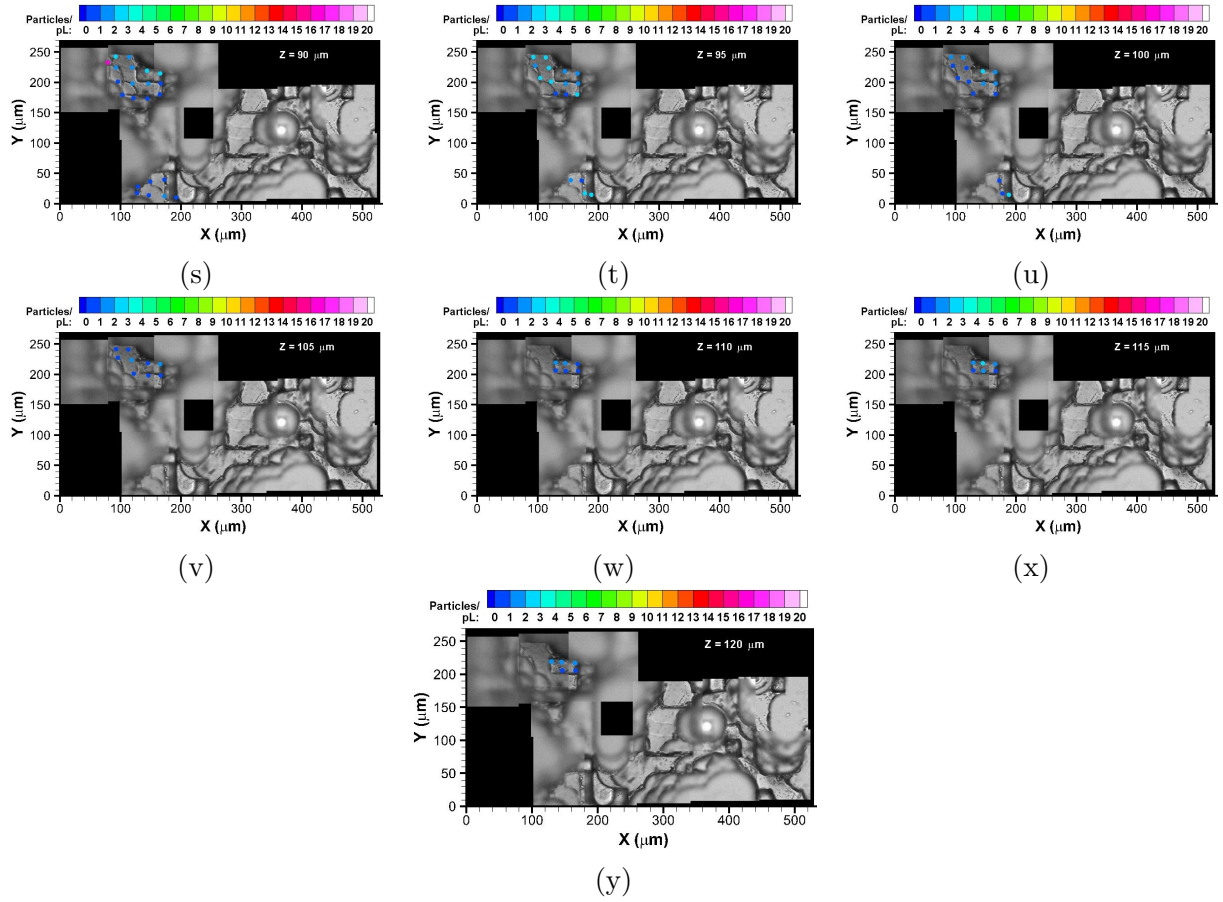

Figure C.3: Sequence of images illustrating depth- wise planar particle concentration distribution from observation location of the micro-model indicated in Figure B.1c. Depth is measured from inner wall of the observation window starting at 0 (a) progressing in 5 μm increments through (y) which is at the local depth of 120 μm. The special resolution of the Concentration is 6.62 μm x 6.62 μm x 5 μm in X,Y and Z planes respectively. Experimental conditions-polystyrene fluorescent 860 nm particles; net flow rate 10 nL/min; particle concentration of 1.92 particles/pL (0.06% by volume).

Appendix D
3D Nano-particle Deposition Measurements at Selected ROIs along the Path of Principal Flow

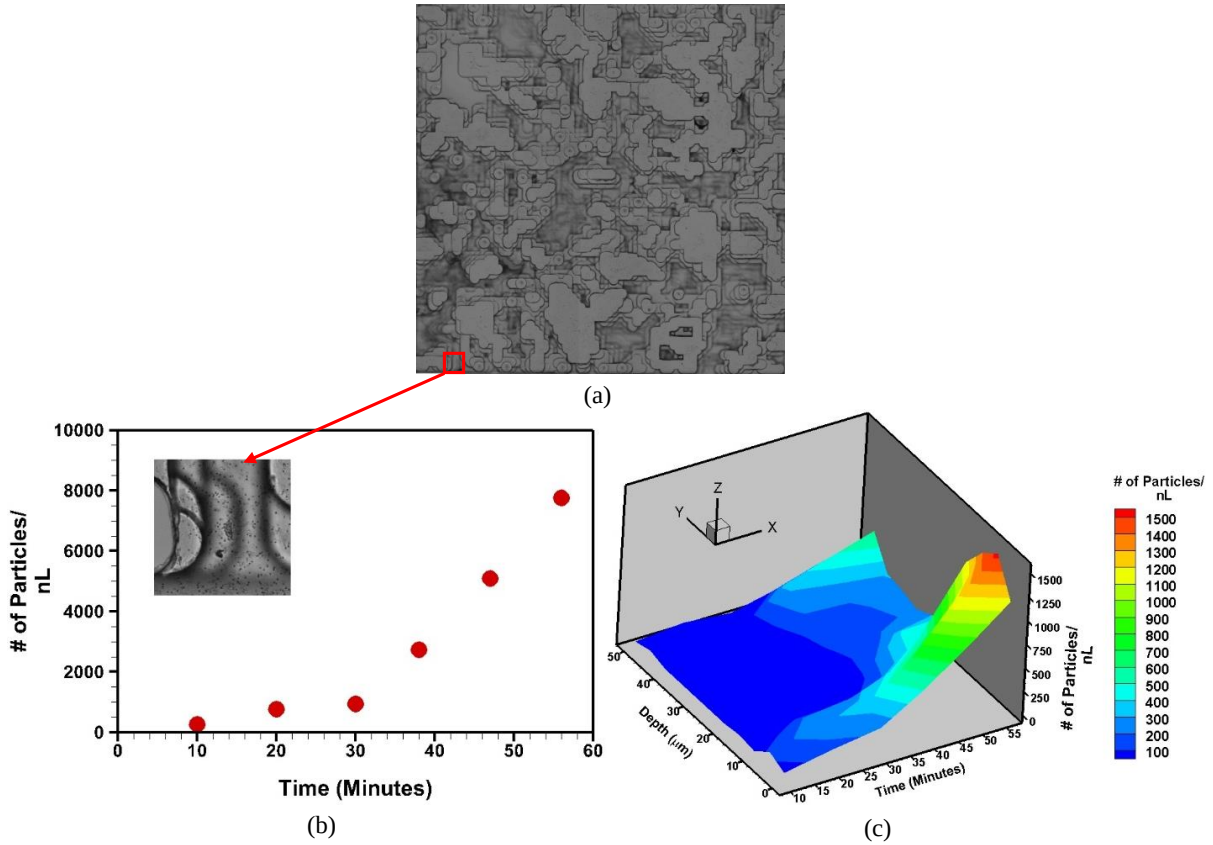

Figure D.1: (a) shows region of interest where particle deposition measurements were taken. (b) Illustrates time sequence of total number of particle deposition at location (a), and (c) shows detail deposition of nanoparticles at various planes over time. Experimental conditions-polystyrene fluorescent 860 nm particles; net flow rate 10 nL/min; particle concentration of 9.54 particles/pL (0.32% by volume).

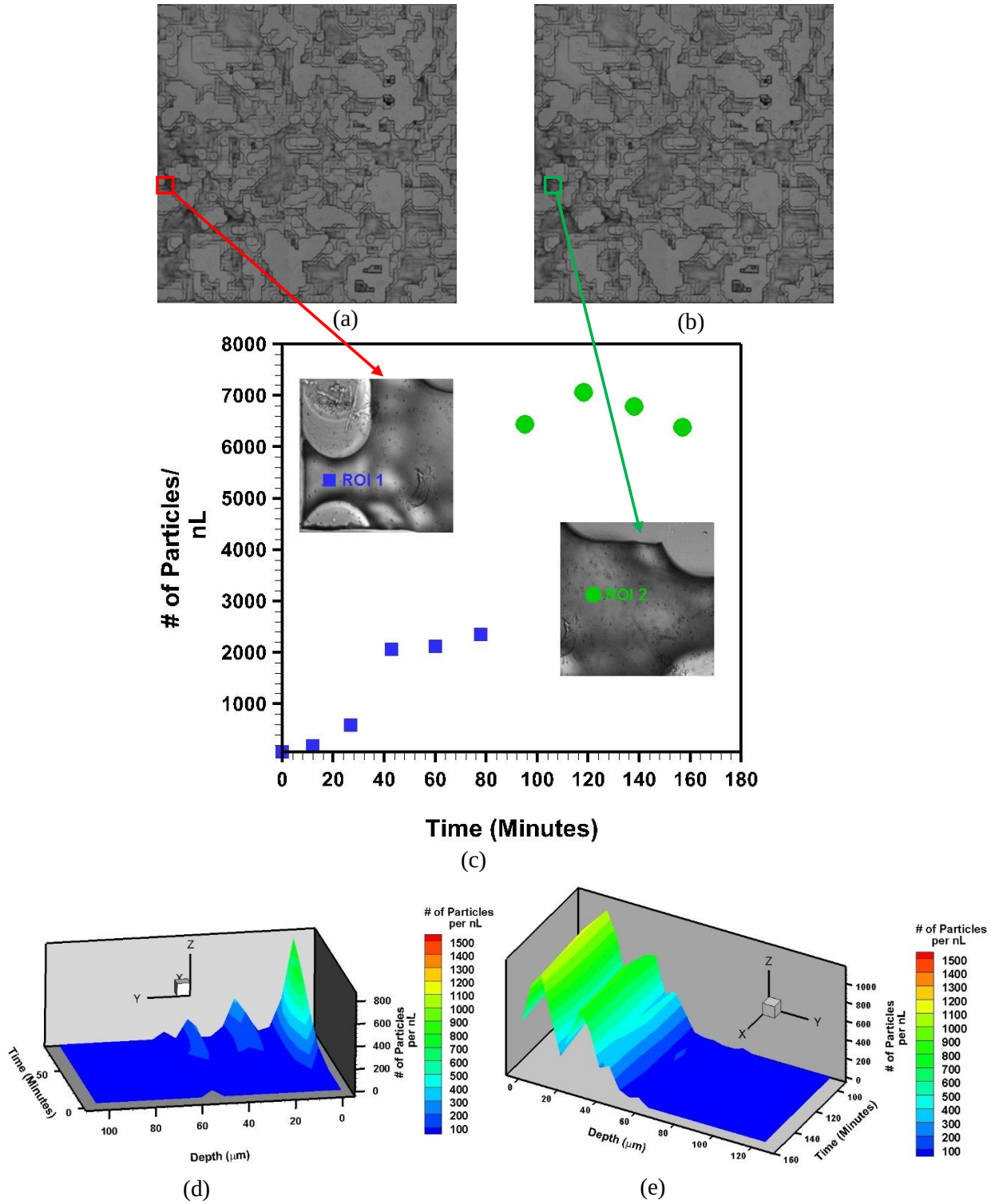

Figure D.2: (a), (b) show region of interests where particle deposition measurements were taken. (c) indicates total number of particle deposition over time at location (a) and (b). (d) and (e) show detail deposition of nanoparticles at different planes over time at location shown in Figure (a) and (b). Experimental condition - polystyrene fluorescent 860 nm particles; net flow rate 10 nL/min; particle concentration of 1.92 particles/pL (0.06% by volume).

Appendix E
Computation Fluid Dynamics Simulation in In-situ geometry

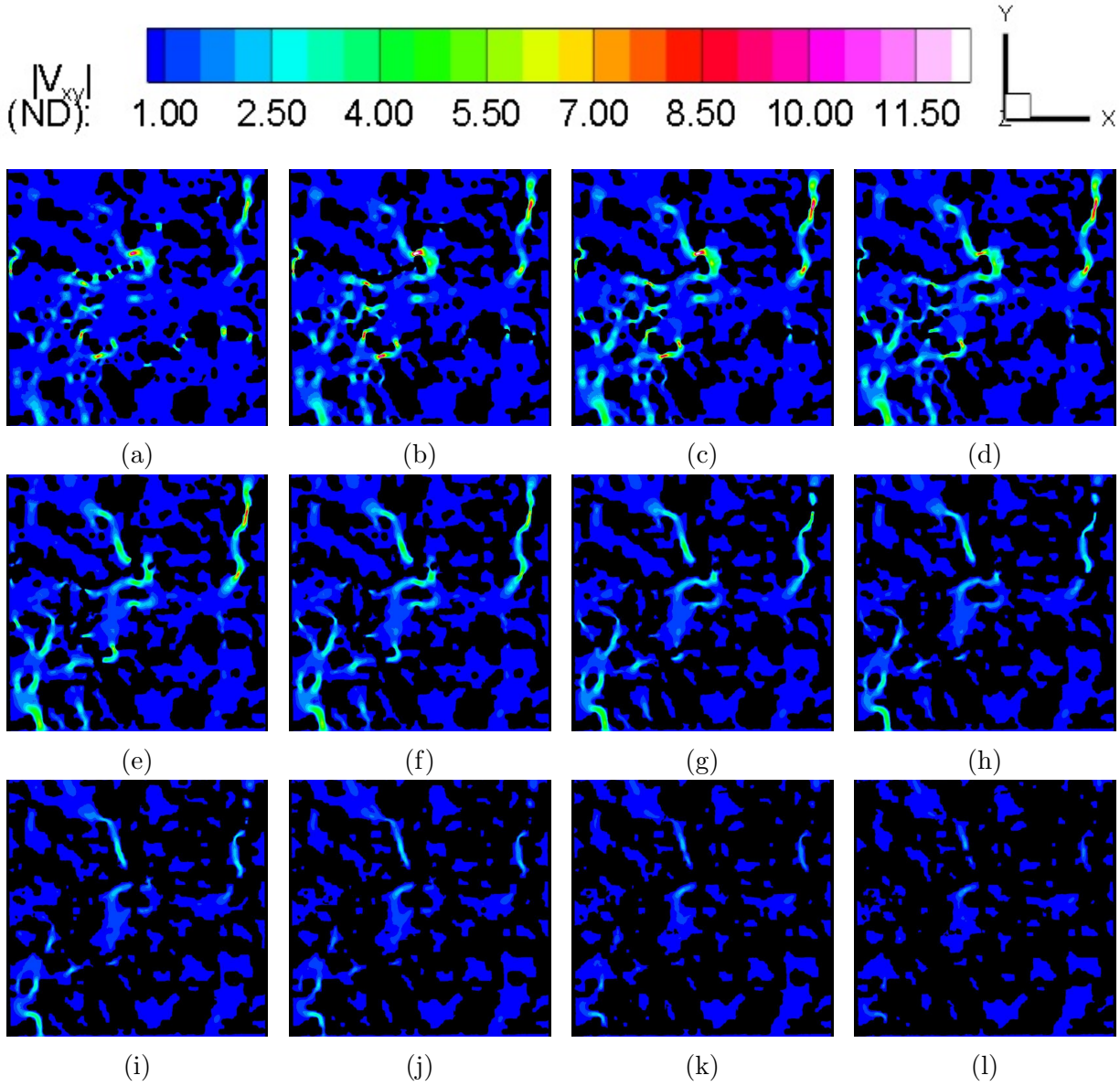

Figure E.1: Sequence of images illustrating depth-wise velocity distribution from Computational Fluid Dynamics simulation of in-situ geometry of micro-model indicated in Figure 4.8. Depth is measured from inner wall of the observation window starting at 5 μm (a) progressing in 5 μm increments through (x) which is at the local depth of 120 μm. Computational conditions as indicated in Figure 7.6 (figure con'd.).

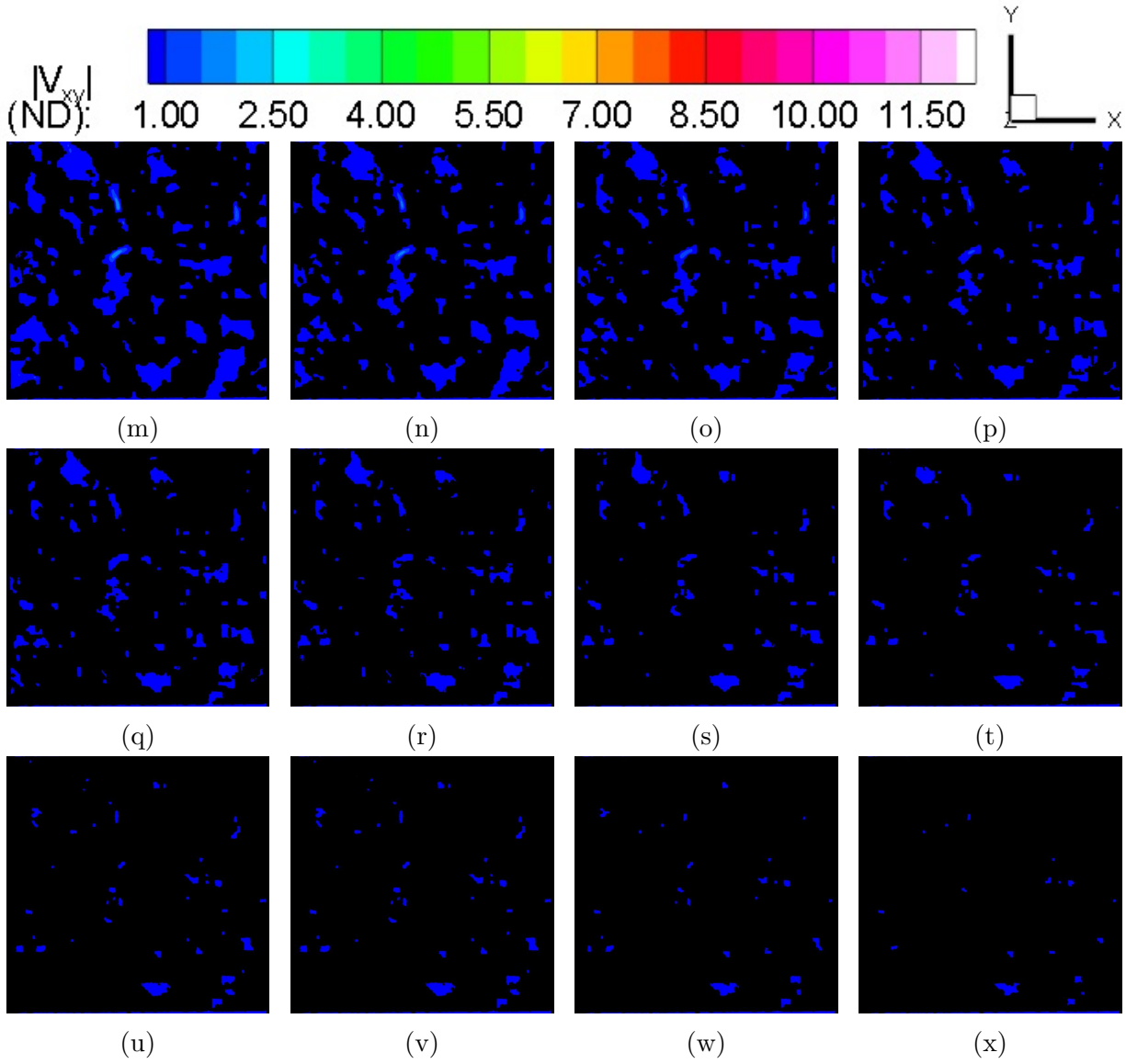

Figure E.1: Sequence of images illustrating depth-wise velocity distribution from Computational Fluid Dynamics simulation of in-situ geometry of micro-model indicated in Figure 4.8. Depth is measured from inner wall of the observation window starting at 5 μm (a) progressing in 5 μm increments through (x) which is at the local depth of 120 μm. Computational conditions as indicated in Figure 7.6.

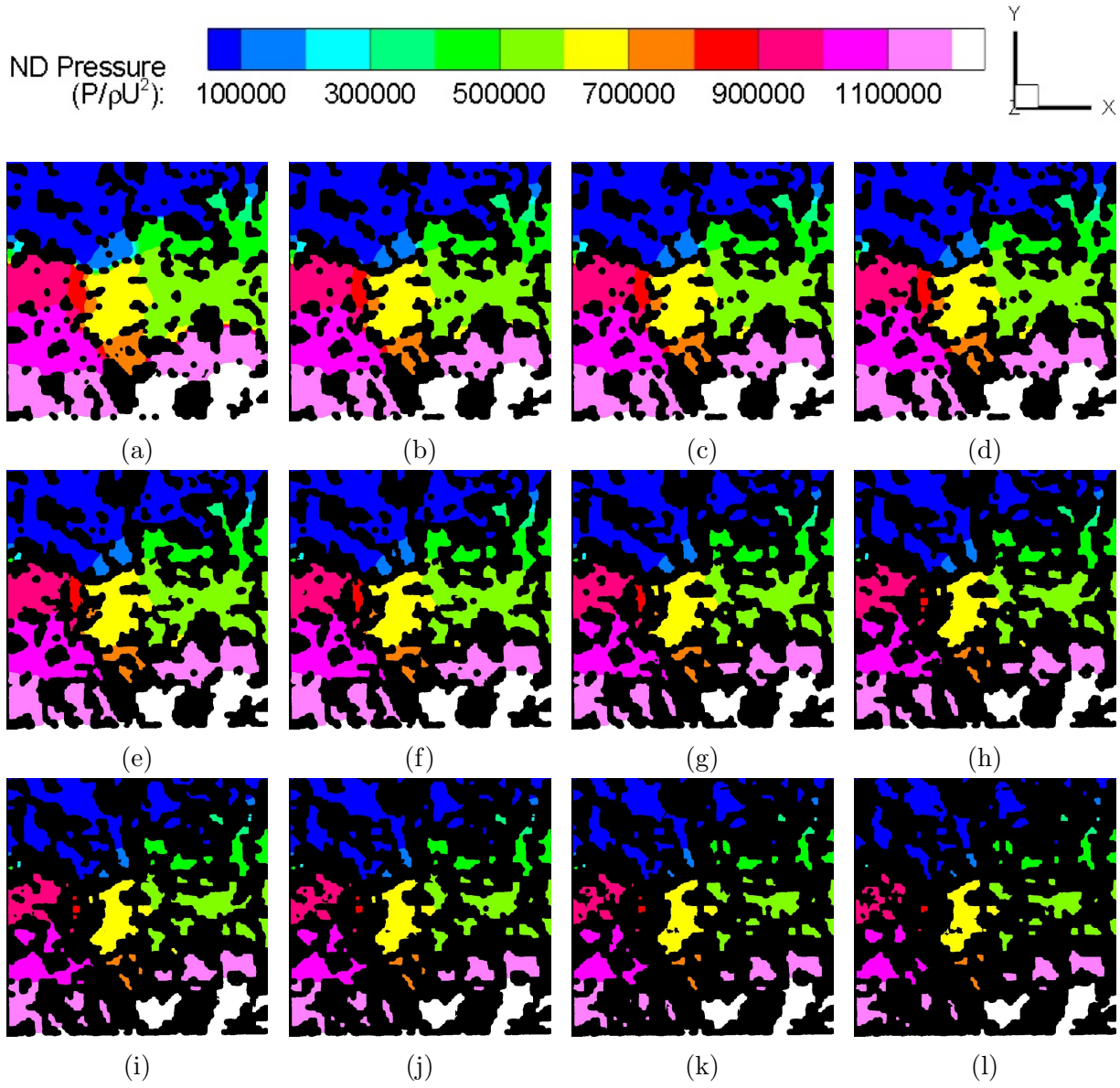

Figure E.2: Sequence of images illustrating depth-wise pressure distribution from Computational Fluid Dynamics simulation of in-situ geometry of micro-model indicated in Figure 4.8. Depth is measured from inner wall of the observation window starting at 5 μm (a) progressing in 5 μm increments through (x) which is at the local depth of 120 μm. Computational conditions as indicated in Figure 7.6(figure cont'd.).

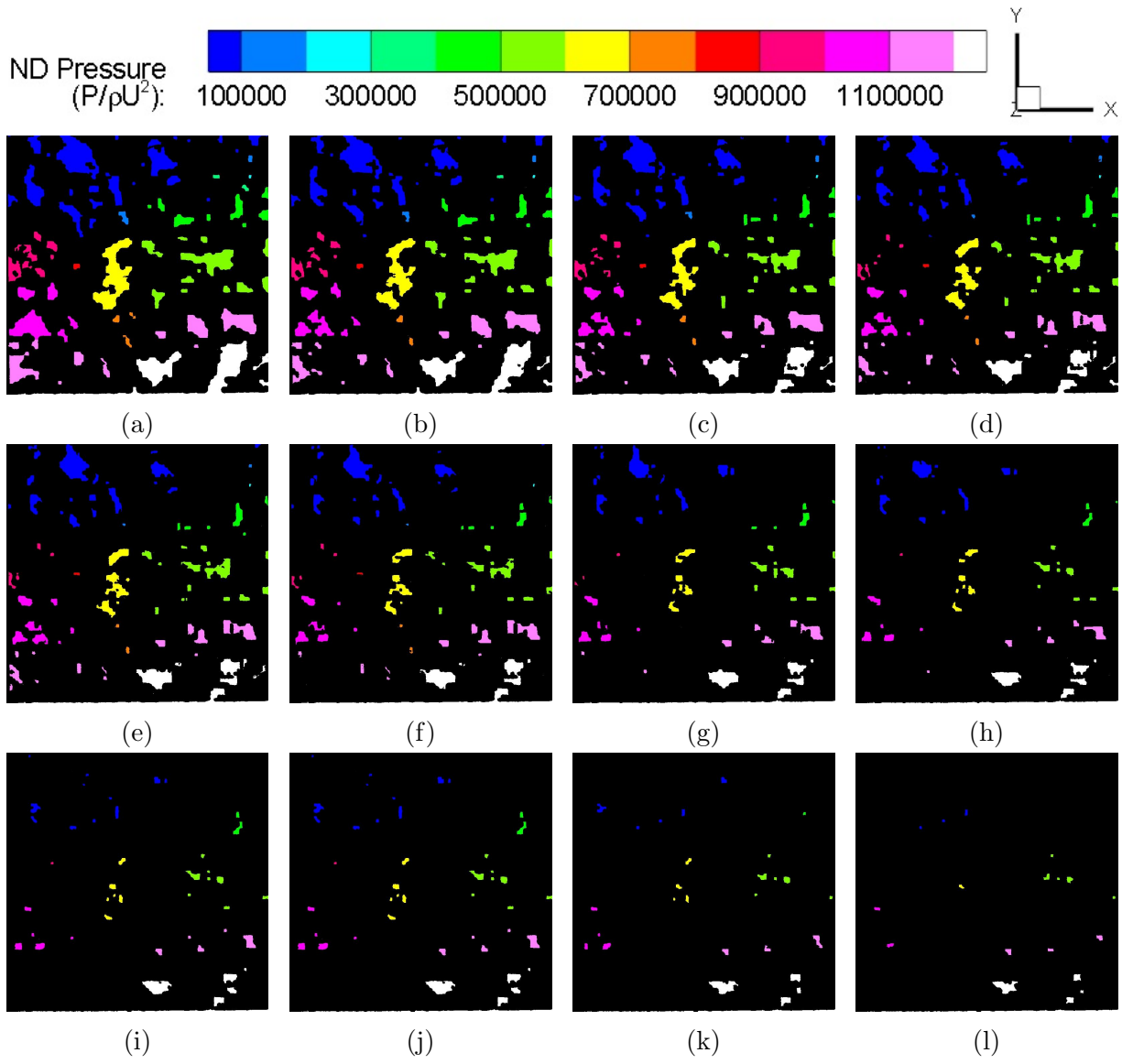

Figure E.3: Sequence of images illustrating depth-wise pressure distribution from Computational Fluid Dynamics simulation of in-situ geometry of micro-model indicated in Figure 4.8. Depth is measured from inner wall of the observation window starting at 5 μm (a) progressing in 5 μm increments through (x) which is at the local depth of 120 μm. Computational conditions as indicated in Figure 7.6.

Appendix F
3D Nano-particle Instantaneous Velocity Measurements in 2.5D Ceramic Micro-models

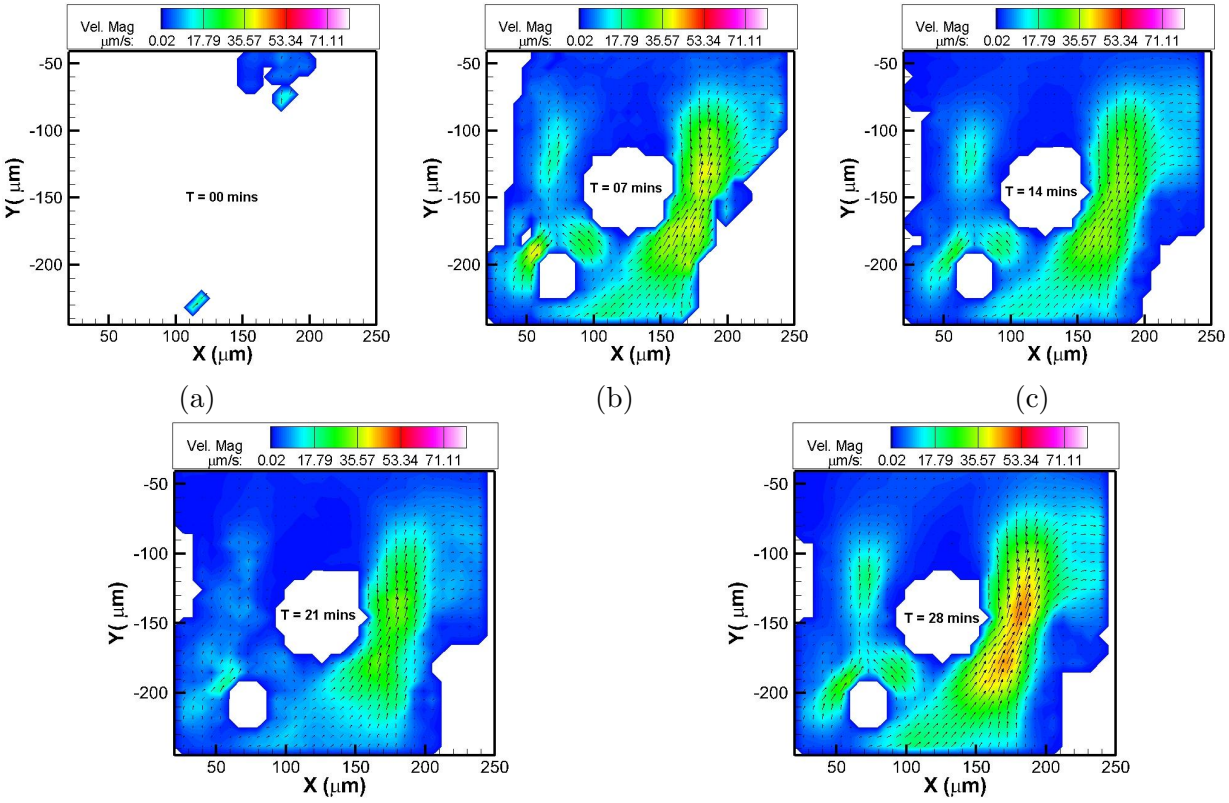

(a) (b) (c)

(d) (e)

Figure F.1: Intantaneous velocity measurements at location shown in Figure 8.9 in ceramic micromodel at (a) 00 mins, (b) 07 mins,(c) 14 mins,(d) 21 mins, and(e) 28 mins at Z = 00 μm plane. Experimental conditions as same as Figure 8.9.

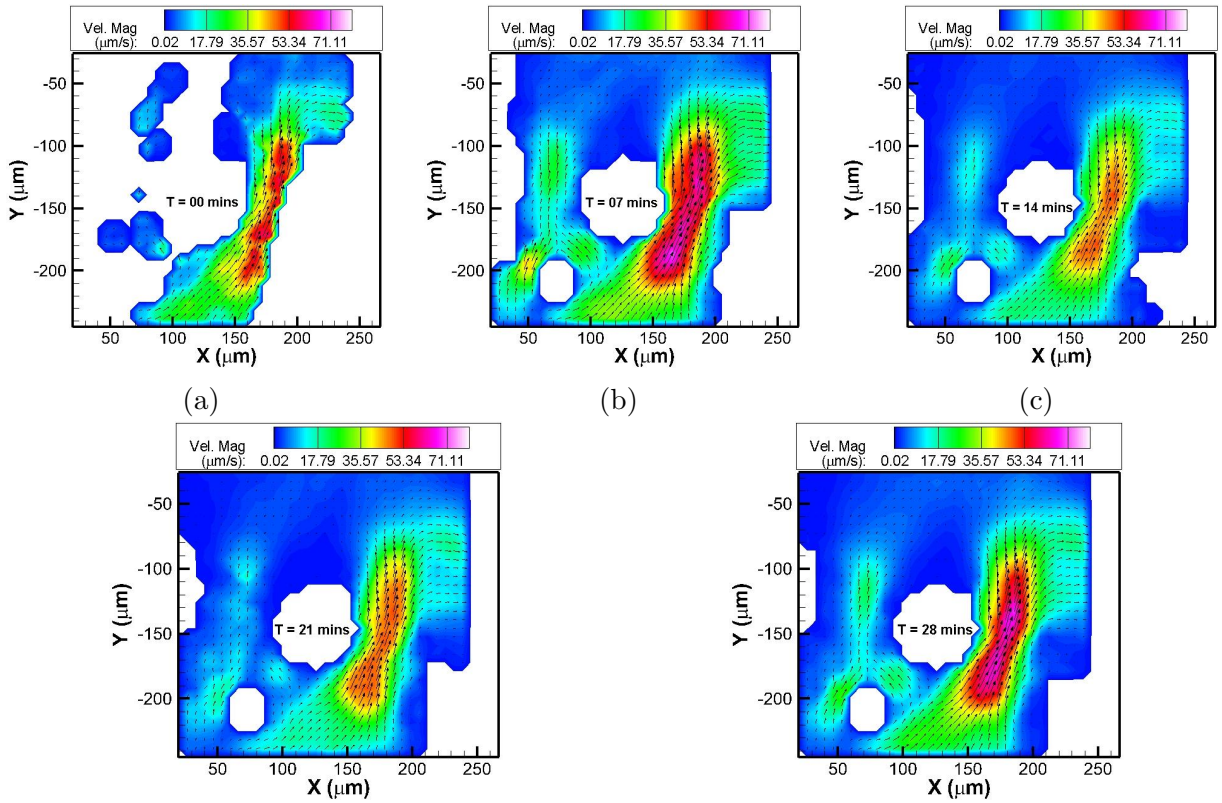

(a) (b) (c)

(d) (e)

Figure F.2: Intantaneous velocity measurements at location shown in Figure 8.9 in ceramic micromodel at (a) 00 mins, (b) 07 mins,(c) 14 mins,(d) 21 mins, and(e) 28 mins at Z = 05 μm plane. Experimental conditions as same as Figure 8.9.

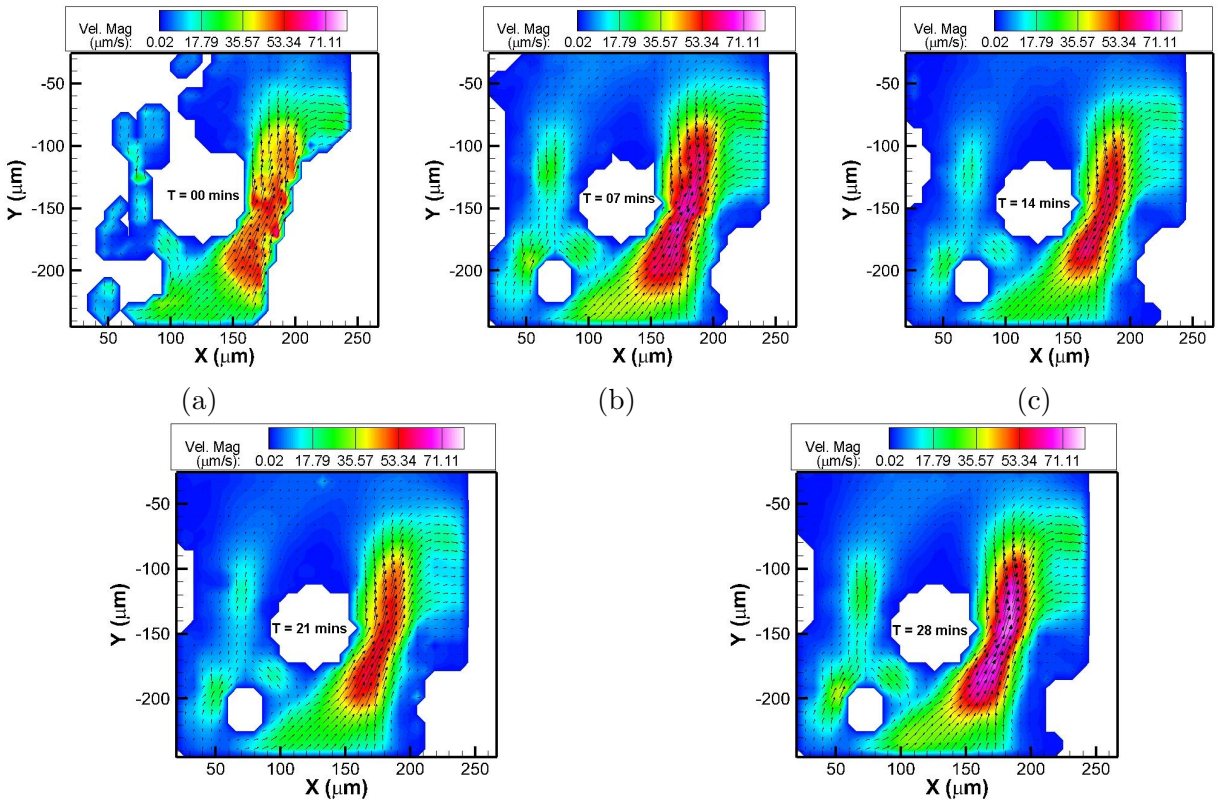

Figure F.3: Intantaneous velocity measurements at location shown in Figure 8.9 in ceramic micromodel at (a) 00 mins, (b) 07 mins,(c) 14 mins,(d) 21 mins, and(e) 28 mins at Z = 10 μm plane. Experimental conditions as same as Figure 8.9.

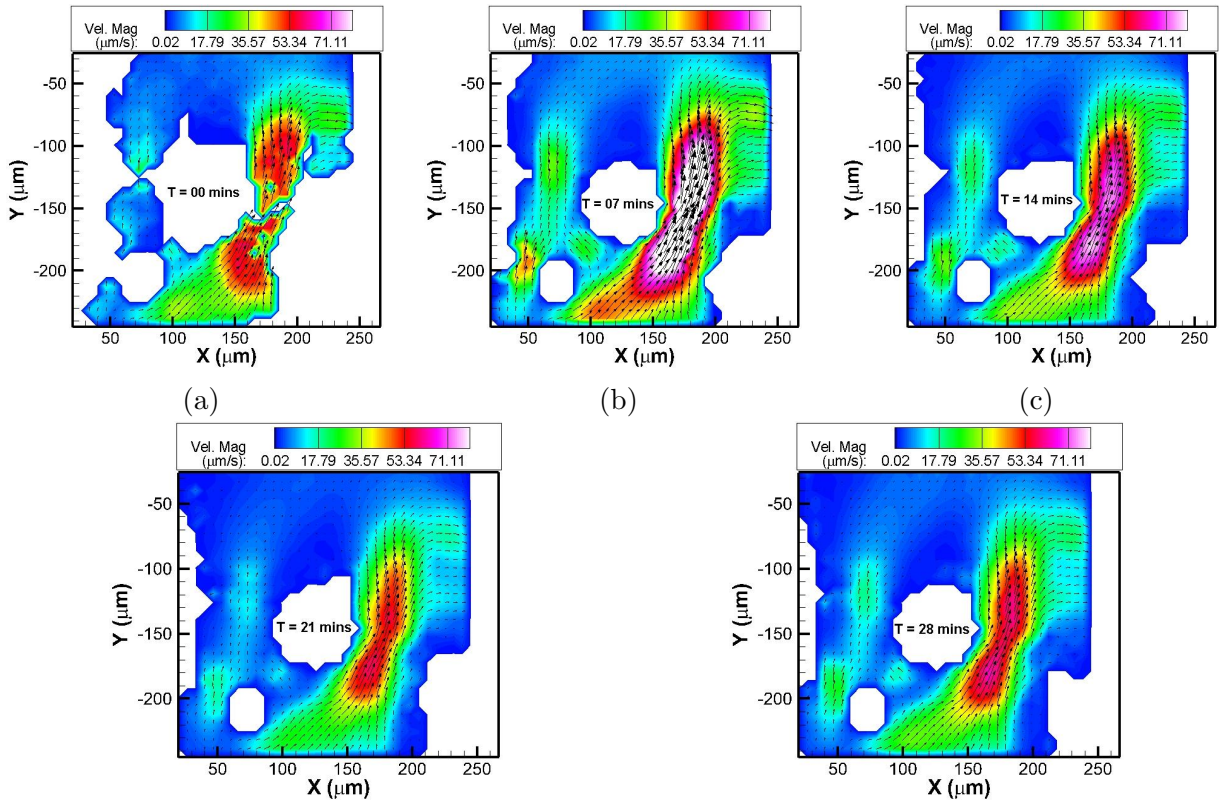

(a) (b) (c)

(d) (e)

Figure F.4: Intantaneous velocity measurements at location shown in Figure 8.9 in ceramic micromodel at (a) 00 mins, (b) 07 mins,(c) 14 mins,(d) 21 mins, and(e) 28 mins at Z = 15 μm plane. Experimental conditions as same as Figure 8.9.

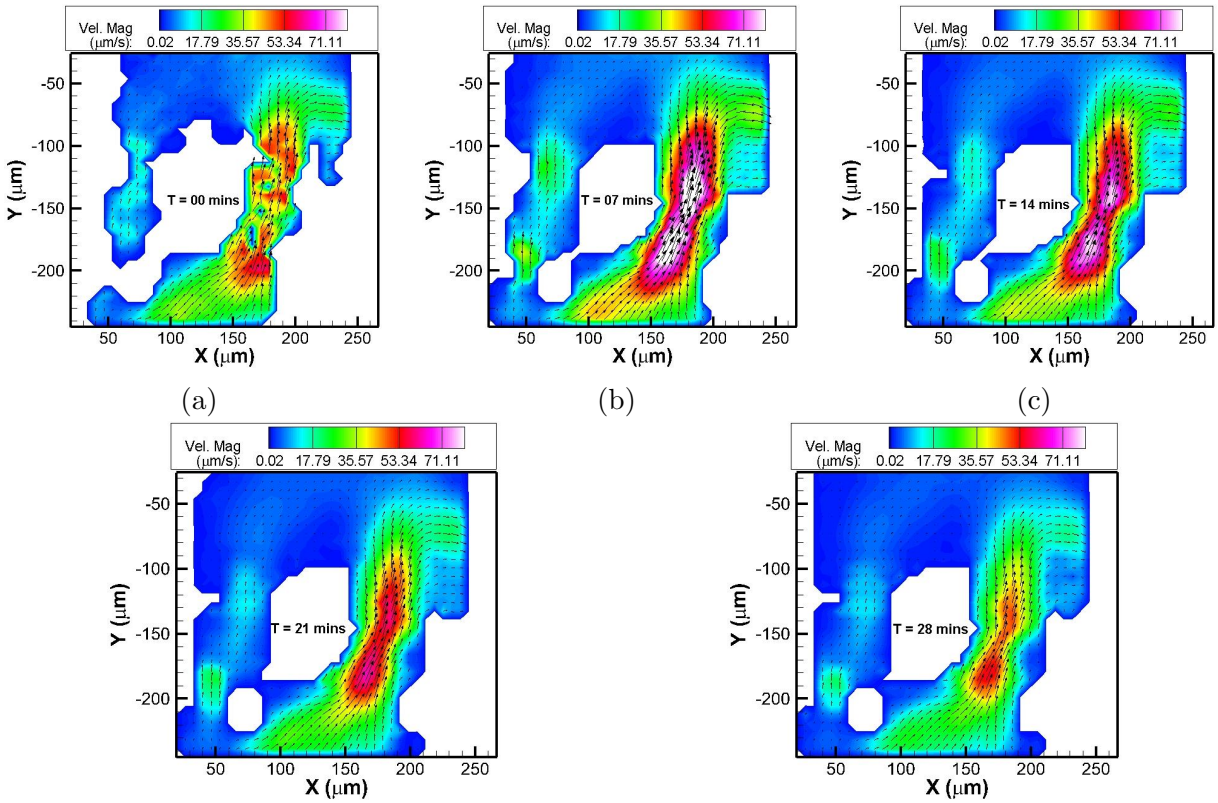

(a) (b) (c)

(d) (e)

Figure F.5: Intantaneous velocity measurements at location shown in Figure 8.9 in ceramic micromodel at (a) 00 mins, (b) 07 mins,(c) 14 mins,(d) 21 mins, and(e) 28 mins at Z = 20 μm plane. Experimental conditions as same as Figure 8.9.

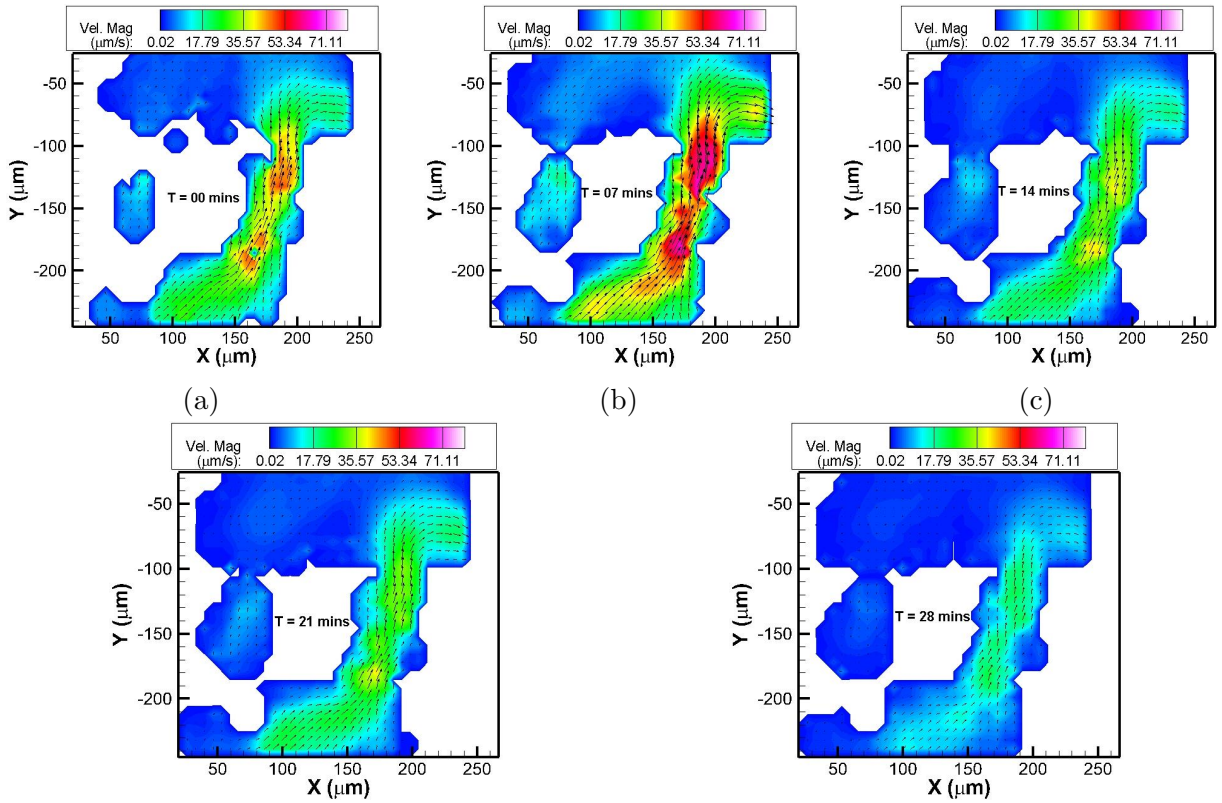

Figure F.6: Intantaneous velocity measurements at location shown in Figure 8.9 in ceramic micromodel at (a) 00 mins, (b) 07 mins,(c) 14 mins,(d) 21 mins, and(e) 28 mins at Z = 25 μm plane. Experimental conditions as same as Figure 8.9.

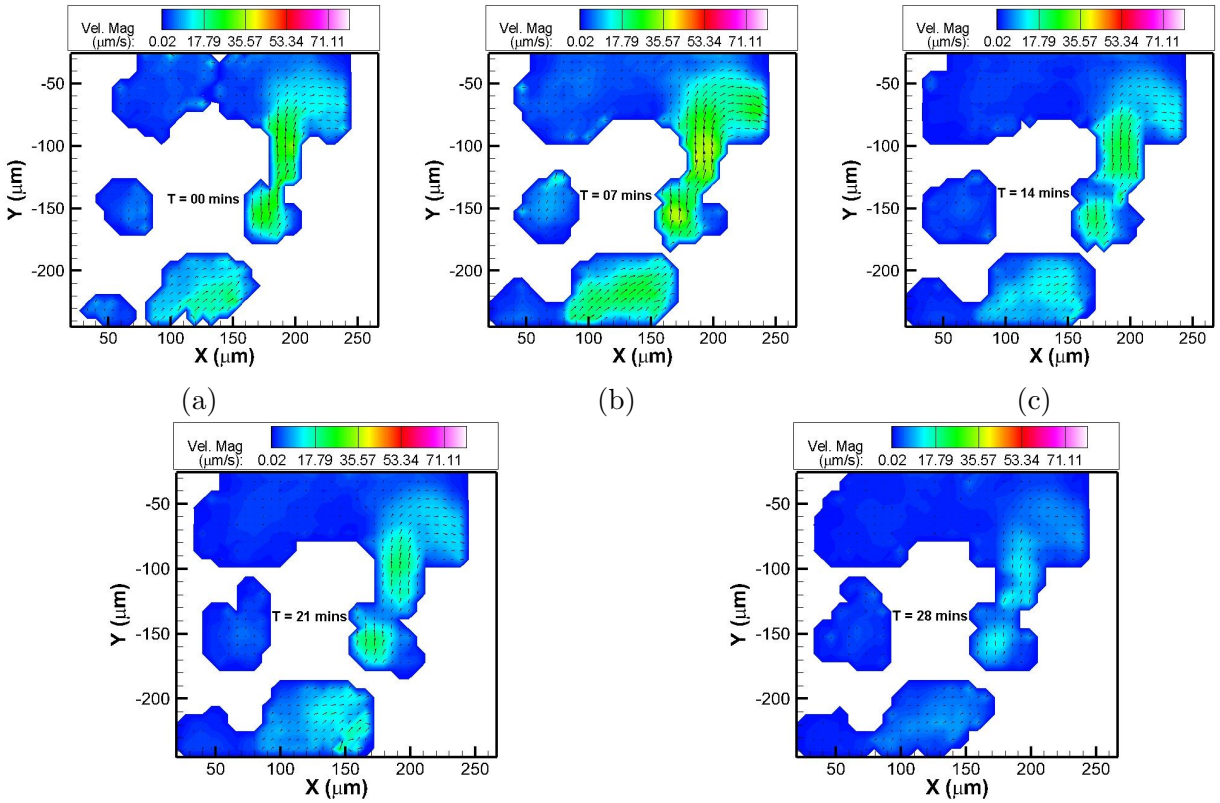

Figure F.7: Intantaneous velocity measurements at location shown in Figure 8.9 in ceramic micromodel at (a) 00 mins, (b) 07 mins,(c) 14 mins,(d) 21 mins, and(e) 28 mins at Z = 30 μm plane. Experimental conditions as same as Figure 8.9.

Appendix G
Permission to Republish Materials

RE: Permission to republish for my PhD. Dissertation

Beth Darchi <DarchiB@asme.org>

Mon 10/30/2017 3:07 PM

To: Jagannath Upadhyay <jupadh1@lsu.edu>;

Dear Mr. Upadhyay:
This permission has been revised to reflect all requests. It is our pleasure to grant you permission to use the following ASME materials:

- **Figures 1, 4** from "Design and Fabrication of Rock-Based Micromodel," by Daniel S. Park, Saade Bou-Mikael, Sean King, Karsten E. Thompson, Clinton S. Willson and Dimitris E. Nikitopoulos, Paper No. IMECE2012-88501
- **Image Processing section and Figure 5** from "3D Measurements of Nano-Particle Transport in Complex 2.5D Micro-Models," by Jagannath Upadhyay, Daniel S. Park, Karsten E. Thompson and Dimitris E. Nikitopoulos, Paper No. IMECE2015-50635
- **Section** " Multilayer Lithography of SU-8", **Figures 5, 6, and 7** from "Fabrication of 2.5D Rock-Based Micromodels With High Resolution Features," by Daniel S. Park, J. Upadhyay, V. Singh, Karsten E. Thompson and Dimitris E. Nikitopoulos, Paper No. IMECE2015-50657

cited in your letter for inclusion in a doctoral dissertation entitled Mobility of Nano-particles in rock based micro-models, in Mechanical Engineering to be published at Louisiana State University.

As is customary, we request that you ensure full acknowledgment of this material, the author(s), source and ASME as original publisher. Acknowledgment must be retained on all pages printed and distributed.

Many thanks for your interest in ASME publications.

Sincerely,

Beth Darchi
Publishing Administrator
ASME
2 Park Avenue
New York, NY 10016-5990
Tel 1.212.591.7700

RE: Permission to republish in my PhD. Dissertation

Beth Darchi <DarchiB@asme.org>

Wed 1/31/2018 2:44 PM

To: Jagannath Upadhyay <jupadh1@lsu.edu>;

Dear Prof. Upadhyay,
It is our pleasure to grant you permission to use the following ASME materials:

- **Figures 2,3,5** from "Fabrication for and Flow Visualization in 2.5D Rock-Based Ceramic Micromodels," by Daniel S. Park, J. Upadhyay, K. Sharmin, J. F. Robbins, I. Schoegl, K. E. Thompson and D. E. Nikitopoulos, Paper No. IMECE2017-71639
- **Figures 2,3,4,5,6,8,10** from "Flow Visualization and 3D Measurements of Nano-Particle Transport in Rock-Based 2.5D Ceramic Micro-Models," by Jagannath Upadhyay, Daniel S. Park, Khurshida Sharmin, Ingmar Schoegl, Karsten E. Thompson and Dimitris E. Nikitopoulos, Paper No. IMECE2017-71698

cited in your letter for inclusion in a doctoral dissertation entitled Mobility of Nano-particles in rock based micro-models to be published by Louisiana State University.

Permission is granted for the specific use as stated herein and does not permit further use of the materials without proper authorization. Proper attribution must be made to the author(s) of the materials. **Please note:** if any or all of the figures and/or Tables are of another source, permission should be granted from that outside source or include the reference of the original source. ASME does not grant permission for outside source material that may be referenced in the ASME works.

As is customary, we request that you ensure full acknowledgment of this material, the author(s), source and ASME as original publisher. Acknowledgment must be retained on all pages where figure is printed and distributed.

Many thanks for your interest in ASME publications.

Sincerely,

Beth Darchi
Publishing Administrator
ASME
2 Park Avenue
New York, NY 10016-5990
darchib@asme.org

From: Jagannath Upadhyay [mailto:jupadh1@lsu.edu]
Sent: Tuesday, January 30, 2018 1:35 PM
To: permissions@asme.org
Subject: Permission to republish in my PhD. Dissertation

Vita

Jagannath Upadhyay was born in Rajapur 4 Kha, Bardiya, Nepal. He completed his School Leaving Certifcate from Ganesh Baba School, Tikapur, Kailali, Nepal. Then he joined Kathmandu Model Higher Secondary School, Bagbazaar, Kathmandu to complete his high school in physics. Later, he was admitted to Grambling State Univeristy for his undergraduate degree in physics in 2007. Later on, he joined Louisiana State University in the Mechanical Engineering Program in 2009 and completed his bachelorette in Mechanical Engineering with cum lauda in 2012. He then joined the graduate progam in 2012 for his doctorate in Mechanical Engineering and he is receiving his doctorate degree in spring 2018.